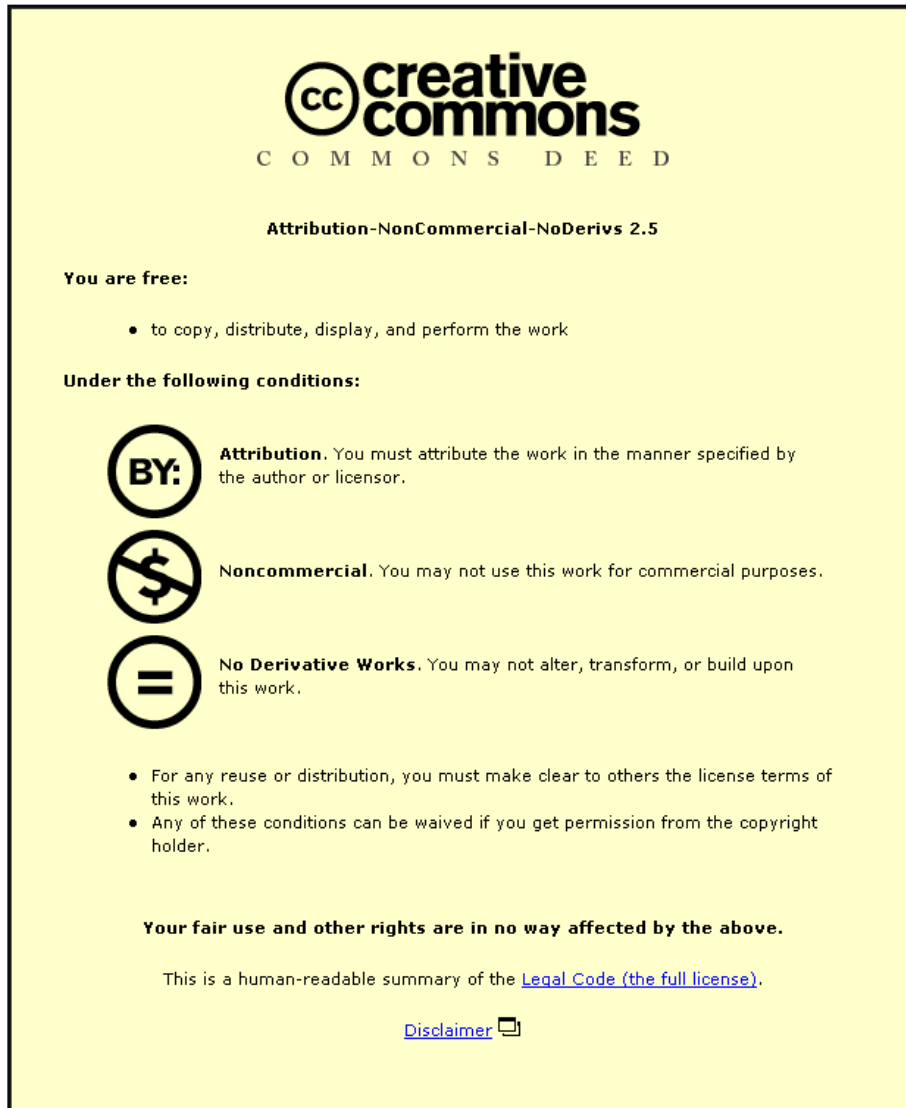


This item was submitted to Loughborough's Institutional Repository (<https://dspace.lboro.ac.uk/>) by the author and is made available under the following Creative Commons Licence conditions.



CC creative commons
COMMONS DEED

Attribution-NonCommercial-NoDerivs 2.5

You are free:

- to copy, distribute, display, and perform the work

Under the following conditions:

BY: **Attribution.** You must attribute the work in the manner specified by the author or licensor.

Noncommercial. You may not use this work for commercial purposes.

No Derivative Works. You may not alter, transform, or build upon this work.

- For any reuse or distribution, you must make clear to others the license terms of this work.
- Any of these conditions can be waived if you get permission from the copyright holder.

Your fair use and other rights are in no way affected by the above.

This is a human-readable summary of the [Legal Code \(the full license\)](#).

[Disclaimer](#) 

For the full text of this licence, please go to:
<http://creativecommons.org/licenses/by-nc-nd/2.5/>

**TURBULENT FLOW AROUND BLUFF BODIES AT THE
FLOODPLAIN EDGE**



Fiona Heatlie

Department of Civil and Building Engineering

Loughborough University

A Doctoral Thesis Submitted in Partial Fulfillment of the
Requirements for the Award of

Doctor of Philosophy

September 2010

© by Fiona Heatlie (2010)

Abstract

Key words: compound channel flow, floodplain vegetation, one line vegetation, bluff body drag, surface-piercing cylinder, surface mounted cylinder

This thesis examines the flow around bluff bodies placed at the floodplain edge in a compound, open channel. The floodplain edge location is associated with a strong shear layer between lower velocity floodplain flow and high velocity flow in the main channel. The drag force exerted by a bluff body is dependant on the way in which the flow separates around the body and subsequently recovers but the drag coefficients typically used to represent the effects of bluff bodies are based on experiments on bodies in geometrically simple channels. The differences induced in the wake structures and therefore in the drag coefficients of bluff bodies when they are placed in the shear layer at the floodplain edge are little understood.

In this study, experimental data is gathered that allows direct comparison of the wakes of identical bluff bodies, both emergent (surface-piercing) and submerged, in simple and compound open channels. For the compound channel scenarios, for both single and multiple block arrangements, turbulence data is also reported. These results are augmented using a computational model based on the solution of the 3D Reynolds Averaged Navier Stokes equations, using a non-linear turbulence model.

The results show that the changes induced in the wake structures due to their location at the floodplain edge of the compound channel can have a significant effect on the drag coefficient. For the emergent bodies, the proximity of the deep main channel flow is shown to impact in a complex manner upon the processes of reattachment and re-separation, changing the formation of vorticity in the wake. For the submerged bodies, this is complicated by asymmetry in the same processes on the block top. For both body types, separation on the main channel side results in the creation of a strong axial circulation at the floodplain edge and the decay of the wake is asymmetrically affected by the differing behaviour of the turbulence on the two sides.

For Brian, who never had the chance.

Acknowledgements

This thesis is the fruition of a long cherished dream, the achievement of which is due in no small part to the following courageous souls:

I offer thanks to my husband, Matthew, for his selfless hard work in keeping the wolves from the door and my sanity intact, to my parents, for their long years of material abstinence for the sake of my education and for bringing me up to have an open mind and an open heart and to my remaining family, on both sides of the border, for hot meals, warm words and sanctuary from myself.

I pay my respects to my supervisors; Dr Scott, for his clear perspective and magical nudges in the right direction and Prof Shiono, whose patience, attentiveness and unwavering positivity I can only hope to emulate. I also thank Prof Ishigaki of Kansai University, whose thoughtfulness ensured that my time in Osaka was both comfortable and productive.

I owe a great debt of thanks to all of those individuals who assisted me in the practice of this work; Jie Xin Huang and Rene Wackrow in Loughborough and Kazuhiko Hattori, Ryuji Kawanaka and Yoshihiro Fukushima in Osaka. From the team at the Loughborough laboratory, I would also like to thank Mick Barker in particular, for support both practical and moral.

Finally, I gratefully acknowledge the financial support of the British Council in funding my time in Japan.

Contents

Contents	iv
List of Tables	ix
List of Figures	x
Nomenclature	xxii
1 Introduction	1
1.1 Aims and Objectives	2
1.2 Contribution to Knowledge	4
1.3 Structure of Thesis	5
2 Literature Review	7
2.1 Introduction	7
2.2 Turbulence in open channel flow	7
2.2.1 Flow in non-circular ducts	8
2.2.2 Flow in simple, open channels	11
2.2.3 Flow in compound, open channels	13
2.2.4 Summary	15
2.3 Vegetation in open channel flow	16
2.3.1 Vegetation as surface roughness	16
2.3.2 Wake Theory & Two-Dimensional Analyses	18
2.3.3 Fully 3D Approaches	20

2.3.3.1	Emergent Vegetation in a Simple Open Channel . . .	21
2.3.3.2	Submerged Vegetation in a Simple Open Channel . .	21
2.3.3.3	Vegetation on the Floodplain of a Compound Channel	23
2.3.3.4	One Line Vegetation at the Floodplain Edge	25
2.3.3.5	Three-Dimensional Numerical Modelling	26
2.3.4	Summary	27
2.4	Turbulent flow around isolated obstacles	28
2.4.1	Two-dimensional flow around bluff bodies	28
2.4.2	Surface mounting effects	31
2.4.3	End Effects - Submerged Bluff Bodies	34
2.4.4	End Effects - Emergent Bluff Bodies	37
2.4.5	Tandem Bluff Bodies	39
2.4.6	Summary	41
2.5	The Research Gap	42
3	Methodology	52
3.1	Physical Experiments	52
3.1.1	Loughborough Experiments	52
3.1.1.1	Experimental Equipment & Set-Up	52
3.1.1.2	Experimental Series - Set-Up Details	63
3.1.2	Kansai Experiments	68
3.1.2.1	Experimental Equipment & Set-Up	68
3.1.2.2	Experimental Series - Set-Up Details	74
3.2	Numerical Modelling	76
3.2.1	Basic Concepts & Equations	76
3.2.2	Turbulence Modelling	79
3.2.2.1	The K- ϵ model	79
3.2.2.2	Higher Order Turbulence Closures	81
3.2.3	Boundary Conditions	84
3.3	Summary	87

4	Experimental Results	103
4.1	Emergent Cases	104
4.1.1	Kansai - Single, large aspect ratio block in a simple channel (S4 CIII)	104
4.1.1.1	Upstream Conditions	104
4.1.1.2	Wake Structure	106
4.1.2	Kansai - Single, large aspect ratio block at the floodplain edge (S4 CI)	108
4.1.2.1	Upstream Conditions	108
4.1.2.2	Wake Structure	110
4.1.2.3	Emergent Block in Simple & Compound Channels - Comparison of Drag Coefficients	112
4.1.3	Loughborough - Single, large aspect ratio block at the flood- plain edge (S2 CI)	115
4.1.3.1	Upstream Conditions	115
4.1.3.2	Wake Structure - Mean Flow	117
4.1.3.3	Wake Structure - Turbulence Statistics	122
4.1.3.4	Summary	126
4.1.4	Loughborough - Multiple, small blocks at the floodplain edge (S1 CII)	128
4.2	Submerged Cases	132
4.2.1	Kansai - Single, large aspect ratio block in simple channel (S4 CIV)	132
4.2.1.1	Upstream Conditions	132
4.2.1.2	Wake Structure	133
4.2.2	Kansai - Single, large aspect ratio block at the floodplain edge (S4 CII)	135
4.2.2.1	Upstream Conditions	135
4.2.2.2	Wake Structure	135

4.2.2.3	Submerged blocks in simple & compound channels - Comparison of Drag Coefficients	137
4.2.3	Loughborough - Single, large aspect ratio block at the flood- plain edge (S2 CII)	139
4.2.3.1	Upstream Conditions	139
4.2.3.2	Wake Structure - Mean Flow	140
4.2.3.3	Wake Structure - Turbulence Statistics	142
4.2.3.4	Summary	144
4.2.4	Loughborough - Multiple, small blocks at the floodplain edge (S1 CI & III)	145
4.3	Summary	148
5	Computational Modelling	197
5.1	Model Testing - Simple Scenarios	197
5.2	Model Testing - Experimental Scenarios	201
5.2.1	Emergent Cases	201
5.2.1.1	Emergent, Low Aspect Ratio In-line Blocks (S1CII) .	201
5.2.1.2	Single, Emergent, Large Aspect Ratio Block at the Floodplain Edge (S2CI)	204
5.2.2	Submerged Cases	207
5.2.2.1	Submerged, Low Aspect Ratio, In-line Blocks (S1CI)	207
5.2.2.2	Submerged, Single, Large Aspect Ratio Block at the Floodplain Edge (S2CII)	209
5.2.3	Model Testing - Summary	211
5.3	Model Results - Emergent Cases	212
5.3.1	Variation of Block Aspect Ratio (AR)	212
5.3.2	Multiple blocks	218
5.4	Model Results - Submerged Cases	221
5.4.1	Variation of Block Aspect Ratio	222
5.4.2	Multiple Blocks	224

CONTENTS

5.5 Summary	226
6 Conclusion	262
6.1 Summary of Research Findings	262
6.2 Suggestions for Future Research	270
6.3 Final Comment	272
References	274

List of Tables

3.1	Rotation Angles ($^{\circ}$) applied to the velocity vectors measured with the ADV	56
3.2	Velocity statistics at sampling frequencies of 25 and 50Hz	60
3.3	Experimental Conditions	65
3.4	Rotation Angles ($^{\circ}$) applied to the velocity vectors measured with the EMV	71
4.1	Flow Parameters and Drag Coefficients for Single, Emergent Blocks in Simple and Compound Channels	113
4.2	Flow Parameters and Drag Coefficients for Single, Submerged Blocks in Simple and Compound Channels	138
5.1	Flow Parameters for Emergent Cases	214
5.2	Flow Parameters for Blocks 1 and 4 in Multiple, Emergent, High AR Block Case	219
5.3	Flow Parameters for Submerged Cases	222
5.4	Flow Parameters for Cylinders 1 and 4 in Multiple, Submerged, High AR Block Case	225
5.5	Equivalent Manning's Coefficient Values for Blocks representing Vegetation	227

List of Figures

1.1	Clockwise from top left: River Derwent at Eaton Bank, River Churnet at Westwood, River Hamps at Onecote, River Lune at Borrow Beck Confluence, River Dove at Milldale, River Petteril at M6 bridge, River Severn at Ironbridge, Field Drain nr. Peterborough	3
2.1	(a) contours of streamwise vorticity and (b) isovels in the top right quadrant of a square duct from Brundrett and Baines (1964)	43
2.2	Isovels of streamwise velocity and vectors of secondary circulations in the left half of a rectangular channel of $AR = 3.94$, (Tominaga <i>et al.</i> , 1989)	44
2.3	Schematic of vertically orientated vortices at the floodplain edge, (Fukuoka and Fujita, 1989)	44
2.4	(a) Contours of streamwise velocity and (b) velocity vectors of secondary circulations from Tominaga and Nezu (1991)	45
2.5	Schematic of flow in a straight, compound channel from Shiono and Knight (1991)	46
2.6	Distribution of Boundary Shear Stress in a compound channel with $D_r = 0.5$, adapted from Tominaga and Nezu (1991)	46
2.7	Spanwise variation of mean streamwise velocity across a partially vegetated channel, from Nezu and Onitsuka (2001). z/B is the spanwise position and α is the vegetation density.	47

LIST OF FIGURES

2.8	Secondary currents in a rectangular, compound channel with vegetated floodplain ($D_r = 0.5$, Vegetation density = $0.25m^{-1}$), Kang and Choi (2006)	47
2.9	Contours of mean streamwise velocity, normalised with U_m , in a trapezoidal channel with one line of emergent blocks at the main channel/floodplain interface, Sun (2006)	48
2.10	Variation of Drag Coefficient C_D with Reynolds number Re for a 2D circular cylinder in a uniform freestream with low turbulence, Zdravkovich (1997)	48
2.11	Streamwise variation of (a) Mean streamwise velocity, (b) streamwise turbulent intensity and (c) spanwise turbulent intensity on the centreline of the wake of a square 2D block, where all variables are normalised with U_m . Adapted from Lyn <i>et al.</i> (1995)	49
2.12	Spanwise orientated vortices upstream of a surface mounted circular cylinder, (Baker, 1980)	50
2.13	Flow fields around submerged circular cylinders, (Kawamura <i>et al.</i> , 1984)	50
2.14	Schematic of flow around a surface mounted cube, (Martinuzzi and Tropea, 1993)	51
2.15	Schematic of flow around a surface piercing circular cylinder, (Chaplin and Teigen, 2003)	51
3.1	(a) Plan view of the Loughborough flume and (b) cross-section schematic	88
3.2	Channel survey results in Loughborough flume for (a) the main channel bed and (b) the floodplain bed	89
3.3	The ADV, (a) Acoustic transducers and (b) operational schematic . . .	90
3.4	Mean spanwise velocity vs. Yaw angle in the simple open channel . .	90
3.5	Flow statistics vs. Velocity Range for the main channel position (left column) and the position behind the block (right column)	91

LIST OF FIGURES

3.6	(a) Raw and (b) filtered data sets at $x = 3.5$ and $y = 1.86$ for the multiple, deep submerged, small AR case (S1CI)	92
3.7	Data sets collected behind the block after filtering using linear interpolation at sampling frequencies of (a) 200, (b) 100, (c) 75 , (d) 50 and (e) 25Hz	93
3.8	Arrangement at flume inlet (a) with board and (b) without board . .	94
3.9	Mean streamwise velocity at 0.01m from the floodplain bed for (a) the 'with board' case and (b) the 'without board' case	95
3.10	Experimental Series 1 - Multiple, small blocks (a) experiment set-up and (b) measurement positions	96
3.11	Plan Measurement grid for single, large AR, emergent block (S2CI). White circles are measured points and black circles are assumed, extrapolated or interpolated points.	96
3.12	Cross-section Measurement grid for single, large AR, emergent block (S2CI). White circles are measured points and black circles are assumed, extrapolated or interpolated points.	97
3.13	Plan Measurement grid for single, large AR, submerged block (S2CII). White circles are measured points and black circles are assumed, extrapolated or interpolated points.	97
3.14	Cross-section Measurement grid for single, large AR, submerged block (S2CII). White circles are measured points and black circles are assumed, extrapolated or interpolated points.	98
3.15	(a) Photograph of the Kansai flume and (b) cross-section schematic .	98
3.16	Centreline channel survey results for the main channel bed, Kansai flume	99
3.17	Kansai flume floodplain section - (a) upstream set-up, (b) glass test section	99
3.18	Calibrating the Pitot-static tube - (a) calibration set-up, (b) calibration curve	100

LIST OF FIGURES

3.19	Water Surface measured with Ultrasonic Level Meter upstream of the single, large AR, submerged block in a simple channel (S4CIV) .	101
3.20	Measurement grid for the single, large aspect ratio blocks in the compound channel in the Kansai flume (S4CI&II)	101
3.21	Measurement grid for the single, large aspect ratio blocks in the simple channel in the Kansai flume (S4CIII&IV)	102
3.22	$E(Rr)$ from the experimental data of (Nikuradse, 1932)	102
4.1	Mean (a) streamwise velocity contours (U) and (b) spanwise velocity contours (V) upstream of the large aspect ratio, emergent block in the simple channel (S4CIII)	150
4.2	Distribution of boundary shear stress upstream of the large aspect ratio, emergent block in the simple channel (S4CIII)	151
4.3	Mean (a) streamwise velocity contours (U) and (b) spanwise velocity contours (V) downstream of the large aspect ratio, emergent block in the simple channel (S4CIII)	152
4.4	Vertical distribution of streamwise velocity U at the block centreline upstream and downstream of the large aspect ratio, emergent block in the simple channel (S4CIII)	153
4.5	Distribution of boundary shear stress at all sections for the large aspect ratio, emergent block in the simple channel (S4CIII)	153
4.6	Difference between downstream water level and average upstream water level, normalised with block width for large aspect ratio, emergent blocks in both simple and compound channels (S4CIII,S4CI) . .	154
4.7	Mean (a) streamwise velocity contours (U) and (b) spanwise velocity contours (V) upstream of the large aspect ratio, emergent block in the compound channel (S4CI)	155
4.8	Distribution of boundary shear stress upstream of the large aspect ratio, emergent block in the compound channel (S4CI)	156

4.9 Mean (a) streamwise velocity contours (U) and (b) spanwise velocity contours (V) downstream of the large aspect ratio, emergent block in the compound channel (S4CI) 157

4.10 Vertical distribution of streamwise velocity U at the block centreline upstream and downstream of the large aspect ratio, emergent block in the compound channel (S4CI) 158

4.11 Distribution of boundary shear stress at all sections for the large aspect ratio, emergent block in the compound channel (S4CI) 158

4.12 (a) Mean streamwise velocity contours (U) and (b) mean turbulent kinetic energy contours (K) upstream of the large aspect ratio, emergent block in the compound channel (S2CI) 159

4.13 Mean streamwise velocity contours (U) (a) around ($z = 1$) and (b) downstream ($x = 2.7$) of the large aspect ratio, emergent block in the compound channel (S2CI) 160

4.14 Mean (a) spanwise velocity contours (V) and (b) vertical velocity contours (W) around ($z = 1$) the large aspect ratio, emergent block in the compound channel (S2CI) 161

4.15 Vortex stretching of vertical vortices downstream ($x, z = 2.7, 1.0$) of the large aspect ratio, emergent block in the compound channel (S2CI) 162

4.16 Vectors of secondary circulations downstream ($x = 2.7$) of the large aspect ratio, emergent block in the compound channel (S2CI) 162

4.17 (a) Axial vorticity and (b) contributions to axial vorticity production downstream ($x = 2.7$) of the large aspect ratio, emergent block in the compound channel (S2CI) 163

4.18 Normalised mean turbulent kinetic energy (K/U_m^2) in the wake of the large aspect ratio, emergent block in the compound channel (S2CI) 164

4.19 Mean streamwise normal Reynolds stress contours ($\overline{u'u'}$) (a) around ($z = 1$) and (b) downstream ($x = 2.7$) of the large aspect ratio, emergent block in the compound channel (S2CI) 165

4.20 Mean spanwise normal Reynolds stress contours ($\overline{v'v'}$) (a) around ($z = 1$) and (b) downstream ($x = 2.7$) of the large aspect ratio, emergent block in the compound channel (S2CI) 166

4.21 Mean vertical normal Reynolds stress contours ($\overline{w'w'}$) (a) around ($z = 1$) and (b) downstream ($x = 2.7$) of the large aspect ratio, emergent block in the compound channel (S2CI) 167

4.22 Components of and total turbulent kinetic energy production at ($x, z = 2.7, 1.0$) for the large aspect ratio, emergent block in the compound channel (S2CI) 168

4.23 Mean Reynolds shear stress contours ($-\overline{u'v'}$, $-\overline{u'w'}$, $-\overline{v'w'}$) around ($z = 1.0$) the large aspect ratio, emergent block in the compound channel (S2CI) 169

4.24 Mean velocity components around small, emergent block in the multiple block arrangement in the compound channel (S1CII) (a) U and (b) Vectors of V and W 170

4.25 Turbulent kinetic energy and normal turbulent stresses around small, emergent block in the multiple block arrangement in the compound channel (S1CII) (a) K , (b) $\overline{u'u'}$, (c) $\overline{v'v'}$ and (d) $\overline{w'w'}$ 171

4.26 Turbulent shear stresses around small, emergent block in the multiple block arrangement in the compound channel (S1CII) (a) $-\overline{u'v'}$, (b) $-\overline{u'w'}$ and (c) $-\overline{v'w'}$ 172

4.27 Mean (a) streamwise velocity contours (U) and (b) spanwise velocity contours (V) upstream of the large aspect ratio, submerged block in the simple channel (S4CIV) 173

4.28 Distribution of boundary shear stress at the upstream section for the large aspect ratio, submerged block in the simple channel (S4CIV) . . 174

4.29 Mean (a) streamwise velocity contours (U) and (b) spanwise velocity contours (V) downstream of the large aspect ratio, submerged block in the simple channel (S4CIV) 175

4.30 Vertical distribution of streamwise velocity U at the block centre-line upstream and downstream of the large aspect ratio, submerged block in the simple channel (S4CIV) 176

4.31 Distribution of boundary shear stress at all sections for the large aspect ratio, submerged block in the simple channel (S4CIV) 176

4.32 Difference between downstream water level and average upstream water level, normalised with block width, for the large aspect ratio, submerged blocks in the simple and compound channel (S4CIV,S4CII) 177

4.33 Mean (a) streamwise velocity contours (U) and (b) spanwise velocity contours (V) upstream of the large aspect ratio, submerged block in the compound channel (S4CII) 178

4.34 Distribution of boundary shear stress upstream of the large aspect ratio, submerged block in the compound channel (S4CII) 179

4.35 Mean (a) streamwise velocity contours (U) and (b) spanwise velocity contours (V) downstream of the large aspect ratio, submerged block in the compound channel (S4CII) 180

4.36 Vertical distribution of streamwise velocity U at the block centre-line upstream and downstream of the large aspect ratio, submerged block in the compound channel (S4CII) 181

4.37 Distribution of boundary shear stress at all sections for the large aspect ratio, submerged block in the compound channel (S4CII) . . . 181

4.38 (a) Mean streamwise velocity contours (U) and (b) mean turbulent kinetic energy contours (K) upstream of the large aspect ratio, submerged block in the compound channel (S2CII) 182

4.39 Mean streamwise velocity contours (U) (a) around ($z = 1$) and (b) downstream ($x = 2.7$) of the large aspect ratio, submerged block in the compound channel (S2CII) 183

4.40 Mean (a) spanwise velocity contours (V) and (b) vertical velocity contours (W) around ($z = 1.0$) the large aspect ratio, submerged block in the compound channel (S2CII) 184

4.41	Vectors of secondary circulations downstream ($x = 2.7$) of the large aspect ratio, submerged block in the compound channel (S2CII) . . .	185
4.42	Mean vorticity components downstream ($x, z = 2.7, 1.0$) of the large aspect ratio, submerged block in the compound channel (S2CII) . . .	185
4.43	Normalised mean turbulent kinetic energy (K/U_m^2) in the wake of the large aspect ratio, submerged block in the compound channel (S2CII)	186
4.44	Mean streamwise normal Reynolds stress contours ($\overline{u'u'}$) (a) around ($z = 1$) and (b) downstream ($x = 2.7$) of the large aspect ratio, submerged block in the compound channel (S2CII)	187
4.45	Mean spanwise normal Reynolds stress contours ($\overline{v'v'}$) (a) around ($z = 1$) and (b) downstream ($x = 2.7$) of the large aspect ratio, submerged block in the compound channel (S2CII)	188
4.46	Mean vertical normal Reynolds stress contours ($\overline{w'w'}$) (a) around ($z = 1$) and (b) downstream ($x = 2.7$) of the large aspect ratio, submerged block in the compound channel (S2CII)	189
4.47	Mean Reynolds shear stress contours ($-\overline{u'v'}$, $-\overline{u'w'}$, $-\overline{v'w'}$) around ($z = 1.0$) the large aspect ratio, submerged block in the compound channel (S2CII)	190
4.48	Mean velocity components around small, deep submerged block in the multiple block arrangement in the compound channel (S1CI) (a) U and (b) Vectors of V and W	191
4.49	Mean velocity components around small, shallow submerged block in the multiple block arrangement in the compound channel (S1CIII) (a) U and (b) Vectors of V and W	192
4.50	Turbulent kinetic energy and normal turbulent stresses around small, deep submerged block in the multiple block arrangement in the compound channel (S1CI) (a) K , (b) $\overline{u'u'}$, (c) $\overline{v'v'}$ and (d) $\overline{w'w'}$. . .	193

LIST OF FIGURES

4.51 Turbulent kinetic energy and normal turbulent stresses around small, shallow submerged block in the multiple block arrangement in the compound channel (S1CIII) (a) K , (b) $\overline{u'u'}$, (c) $\overline{v'v'}$ and (d) $\overline{w'w'}$. . . 194

4.52 Turbulent shear stresses around small, deep submerged block in the multiple block arrangement in the compound channel (S1CI) (a) $-\overline{u'v'}$, (b) $-\overline{u'w'}$ and (c) $-\overline{v'w'}$ 195

4.53 Turbulent shear stresses around small, shallow submerged block in the multiple block arrangement in the compound channel (S1CIII) (a) $-\overline{u'v'}$, (b) $-\overline{u'w'}$ and (c) $-\overline{v'w'}$ 196

5.1 Square Duct Simulation - Grid Profile (a) Cross Section (b) Plan Section 229

5.2 Square duct flow results from $k - \epsilon$ model (a) Contours of U and (b) K and (c) Secondary Flow Vectors 230

5.3 Square duct flow results from Speziale model (a) Contours of U , (b) Contours of K and (c) Secondary Flow Vectors 231

5.4 Square duct flow results from K&H model (a) Contours of U , (b) Contours of K and (c) Secondary Flow Vectors 232

5.5 Compound Channel Simulation - Grid Profile (a) Cross Section (b) Plan Section 233

5.6 Compound channel flow results from $k - \epsilon$ model (a) Contours of U and (b) K and (c) Secondary Flow Vectors 234

5.7 Compound channel flow results from K&H model (a) Contours of U , (b) Contours of K and (c) Secondary Flow Vectors 235

5.8 Experimental and modelled results for multiple, low aspect ratio, emergent blocks (S1CII), downstream of fourth block at $(x,z) = (+3.5, +0.5)$ (a) U , (b) V , (c) W and (d) K 236

5.9 Modelled results around fourth emergent low aspect ratio block in series, (S1CII), Contours of U and secondary flow vectors for (a) & (b) the streamwise block centre and (c) & (d) the downstream station ($x = +3.5$) 237

5.10 Experimental and modelled results at Station Three ($(x, z) = (1.3, 1.0)$), Single, large aspect ratio, emergent block (S2CI) (a) U , (b) V , (c) W and (d) K 238

5.11 Experimental and modelled results at Station Five ($(x, z) = (4.0, 1.0)$), Single, large aspect ratio, emergent block (S2CI) (a) U , (b) V , (c) W and (d) K 239

5.12 Experimental and modelled results at Station Seven ($(x, z) = (6.7, 1.0)$), Single, large aspect ratio, emergent block (S2CI) (a) U , (b) V , (c) W and (d) K 240

5.13 Longitudinal variation in the average percentage difference between measured and modelled values of mean streamwise velocity U , Emergent & submerged single, large aspect ratio blocks at the floodplain edge (S2CI&II) 241

5.14 Experimental and modelled results for multiple, low aspect ratio, submerged blocks (S1CI), downstream of fourth block at $(x, z) = (+3.5, +0.5)$ (a) U , (b) V , (c) W and (d) K 242

5.15 Modelled results around fourth submerged, low aspect ratio block in series, (S1CI), Contours of U and secondary flow vectors for (a) & (b) the upstream station ($x = -3.5$) and (c) & (d) the downstream station ($x = +3.5$) 243

5.16 Experimental and modelled results at Station Three ($(x, z) = (1.3, 1.0)$), Single, large aspect ratio, submerged block (S2CII) (a) U , (b) V , (c) W and (d) K 244

5.17 Experimental and modelled results at Station Five ($(x, z) = (4.0, 1.0)$), Single, large aspect ratio, submerged block (S2CII) (a) U , (b) V , (c) W and (d) K 245

5.18	Experimental and modelled results at Station Seven ($(x, z) = (6.7, 1.0)$), Single, large aspect ratio, submerged block (S2CII) (a) U , (b) V , (c) W and (d) K	246
5.19	Variation of Emergent Block Aspect Ratio - Series Inlet Conditions (a) Contours of U and (b) Vectors of Secondary Circulations	247
5.20	Mean streamwise velocity recovery downstream of emergent blocks of varying aspect ratio at floodplain edge	248
5.21	Modelled U at Station Five ($x = 4$), Single emergent blocks of vary- ing aspect ratio (a) $AR = 1$, (b) $AR = 2$, (c) $AR = 3$ and (d) $AR = 5$	249
5.22	Modelled V and W at Station Five ($x = 4$), Single emergent blocks of varying aspect ratio (a) $AR = 1$, (b) $AR = 2$, (c) $AR = 3$ and (d) $AR = 5$	250
5.23	Modelled U at ($z = 1$), Single emergent blocks of varying aspect ratio (a) $AR = 1$, (b) $AR = 5$	251
5.24	Modelled results for $AR = 1$ at streamwise block centreline (a) U , (b) V and W	252
5.25	Mean streamwise velocity recovery downstream of first and fourth emergent blocks in multiple block arrangement at the floodplain edge (a) model results only and (b) model results and prediction of Petryk (1969)	253
5.26	Modelled U for multiple, emergent, high aspect ratio blocks at $x' =$ 5.5 for (a) Block 1 and (b) Block 4	254
5.27	Modelled results at $z = 2.0$ for Block 4 in multiple, emergent, high aspect ratio block case, (a) U and (b) K	255
5.28	Mean streamwise velocity recovery downstream of submerged blocks of varying aspect ratio at floodplain edge	256
5.29	Modelled U at Station Five ($x = 4$), Single submerged blocks of varying aspect ratio (a) $AR = 1.5$, (b) $AR = 3.5$ and (c) $AR = 4.5$	257
5.30	Modelled V and W at Station Five ($x = 4$), Single submerged blocks of varying aspect ratio (a) $AR = 1.5$, (b) $AR = 3.5$ and (c) $AR = 4.5$	258

LIST OF FIGURES

5.31 Mean streamwise velocity recovery downstream of first and fourth submerged blocks in multiple block arrangement at the floodplain edge 259

5.32 Modelled U for multiple, submerged, high aspect ratio blocks at $x' = 5.5$ for (a) Block 1 and (b) Block 4 260

5.33 Summary of drag coefficient values calculated with numerical model 261

Nomenclature

Roman Symbols

AR_{bl}	Aspect ratio of blocks (H_{bl}/W_{bl})
d_{pst}	Diameter of Pitot-static tube
AR_{ch}	Aspect ratio of channels (W_{ch}/H_{ch})
C_1	Coefficient in the Kimura and Hosoda (2003) turbulence model
C_2	Coefficient in the Kimura and Hosoda (2003) turbulence model
C_3	Coefficient in the Kimura and Hosoda (2003) turbulence model
C_D	Drag coefficient
C_L	Lift coefficient
$C_{\epsilon 1}$	Coefficient in $k - \epsilon$ equation set
$C_{\epsilon 2}$	Coefficient in $k - \epsilon$ equation set
C_{μ}	Coefficient in $k - \epsilon$ equation set
D_{ch}	Channel depth (Equivalent to Channel Height)
D_{fl}	Floodplain depth
D_r	Relative depth

NOMENCLATURE

E	Roughness Parameter
f_d	Drag force
f_{sa}	ADV Sampling Frequency
f_{sh}	Shedding frequency
Fr	Froude number
g	Gravitational Acceleration
H_{ch}	Channel height
H_{bl}	Block height
I_e	Energy Slope
K	Turbulent kinetic energy
l	Turbulent length scale
L	Characteristic length for calculation of Strouhal number
L_{ch}	Channel length
n	Manning's roughness coefficient
n^+	Dimensionless distance from channel wall
p	Wetted perimeter position
P	Static Pressure
P_D	Dynamic Pressure
P_K	Production of Turbulent Kinetic Energy
P_{Ω_x}	Production of Axial Vorticity

NOMENCLATURE

R_r	Roughness parameter from Jayatilke (1969)
Re_{ch}	Channel Reynolds number $\rho UW_{ch}/\mu$
Re_D	Local Block Reynolds number $\rho UW_{bl}/\mu$
s	Distance between the centre of tandem blocks
S_o	Channel bed slope
T	ADV Recording Period
T_u	Freestream Turbulence Level
u	Streamwise instantaneous velocity
u^+	Dimensionless Velocity at Wall
U	Streamwise mean velocity
U_x	Streamwise Velocity Component on ADV output files
U_a	Approach Velocity - Depth-averaged mean streamwise velocity of freestream at cylinder centreline
U_m	Bulk Mean Velocity - Cross-sectional spatial average of mean streamwise velocity
U_*	Shear Velocity
u'	Streamwise turbulent velocity
$\overline{u'u'}$	Reynolds normal stress in streamwise direction
$\overline{u'v'}$	Reynolds shear stress in horizontal (xy) plane
$\overline{u'w'}$	Reynolds shear stress in transverse (xz) plane
v	Spanwise instantaneous velocity

NOMENCLATURE

V	Spanwise mean velocity
U_y	Spanwise Velocity Component on ADV output files
v'	Spanwise turbulent velocity
$\overline{v'v'}$	Reynolds normal stress in spanwise direction
$\overline{v'w'}$	Reynolds shear stress in cross-sectional (yz) plane
w	Vertical instantaneous velocity
W	Vertical mean velocity
U_z	Vertical Velocity Component on ADV output files
w'	Vertical turbulent velocity
$\overline{w'w'}$	Reynolds normal stress in vertical direction
W_{ch}	Channel width
W_{fl}	Floodplain width
W_{bl}	Block width
X	Streamwise coordinate
X_C	Streamwise coordinate of block centre
x	Normalised streamwise coordinate
Y	Spanwise coordinate
Y_C	Spanwise coordinate of block centre
y	Normalised spanwise coordinate
y_r	Mean height of boundary roughness

Z	Vertical coordinate
Z_0	Vertical coordinate of block base
z	Normalised vertical coordinate

Greek Symbols

α_1	Coefficient in the Kimura and Hosoda (2003) turbulence model
α_2	Coefficient in the Kimura and Hosoda (2003) turbulence model
α_3	Coefficient in the Kimura and Hosoda (2003) turbulence model
δ^*	Displacement Thickness
δ_{ij}	Kronecker Delta
ϵ	Turbulent kinetic energy dissipation rate
θ	Bed Slope Angle
κ	Von Kármán Constant
μ	Molecular Viscosity
μ_t	Turbulent Viscosity
ν	Kinematic Viscosity
ρ	Fluid Density
σ_K	Coefficient in $k - \epsilon$ equation set
σ_ϵ	Coefficient in $k - \epsilon$ equation set
τ_b	Boundary shear stress
τ_{bed}	Bed shear stress

τ_{wall}	Wall shear stress
τ_{uv}	Reynolds shear stress in horizontal (xy) plane
τ_{uw}	Reynolds shear stress in transverse (xz) plane
τ_{vw}	Reynolds shear stress in cross-sectional (yz) plane
Ω_x	Streamwise Vorticity
Ω_y	Spanwise Vorticity
Ω_z	Vertical Vorticity

Abbreviations and Acronyms

2D	Two-dimensional
3D	Three-dimensional
ADV	Acoustic Doppler Velocimeter
ASM	Algebraic Stress Model
CDS	Central Differencing Scheme
DNS	Direct Numerical Simulation
EMV	Electromagnetic Velocimeter
FFT	Fast Fourier Transform
HSV	ADV Height of Sampling Volume
LDA	Laser Doppler Anemometer
LES	Large Eddy Simulation
LT	ADV Velocity Range

NOMENCLATURE

PIV Particle Image Velocimetry

RANS Reynolds Averaged Navier Stokes

RSM Reynolds stress model

SERC - FCF Science & Engineering Research Council - Flood Channel Facility

SGS Sub-grid Scale Model

SIP Strongly Implicit Method

UDS Upwind Differencing Scheme

VR ADV Velocity Range

CHAPTER 1

Introduction

The attractions of river floodplains for human colonisation cannot be disputed but our encroachment onto them has left our lives and property vulnerable to the risk of flooding. In order to mitigate this risk, it is essential that a sufficient understanding of the characteristics of river flow be achieved. A river, however, cannot be considered in isolation from its wider environment so that the modern management of rivers and their floodplains is necessarily directly concerned with the role of vegetation. Sub-dividing this taxon by size into small, flexible vegetation and large, rigid vegetation and concerning ourselves solely with the latter, we can identify a phenomenon within the UK river environment that is worthy of further attention.

Figure 1.1 shows various examples of the pattern in question, namely that trees can be commonly found growing at the edge of UK rivers in relatively straight lines and often with the remainder of the floodplain area bereft of other such large obstacles. In rural areas, we may speculate that this pattern is the result of common agricultural practice, where the riverbank marks the field boundary and the trees form part of the hedgerow system that characterises the British countryside, whilst also offering the channel sides some degree of protection from erosion. Whatever the genesis of this pattern however, the thrust of current environmental policy in Europe, as embodied by the Water Framework Directive, is to restore or enhance

the aquatic environment wherever possible. As such, the wholesale removal of riparian trees is unlikely and their effects must be understood.

Despite their obvious ecological functions, riparian trees and other vegetation have a large impact on flood hydraulics. The presence of vegetation tends to reduce the conveyance capacity of a river and its floodplain, raising local flood levels. Although some would advocate the use of vegetated areas of floodplain on a catchment scale to attenuate flood flow peaks, in areas where lower flood levels are desirable, effective management of the vegetation, informed by science, is a necessity.

In order to improve guidance on the establishment or removal of riparian vegetation, it is necessary to understand how the presence of vegetation provides resistance to the flow. In fact, this process is twofold; the vegetation provides direct resistance to the passage of the water and also tends to affect the sedimentation processes in such a way as to reduce the cross sectional area of the channel. However, this programme of research will concentrate on the former of these components.

1.1 Aims and Objectives

The overarching aim of this programme of research is to better understand the characteristics of compound open channel flow in which rigid vegetation is situated at the floodplain edge of a compound channel. Under the umbrella of this general aim, four specific objectives were identified and are summarised below.

- To identify the bulk changes in the wake structure around an identical obstacle when moved from the centre of a symmetrical, open channel of simple cross-section to the floodplain edge of a compound, open channel, for both submerged and emergent (surface piercing) obstacles, and the resultant effects on the drag coefficient.

1.1 Aims and Objectives



Figure 1.1: Clockwise from top left: River Derwent at Eaton Bank, River Churnet at Westwood, River Hamps at Onecote, River Lune at Borrow Beck Confluence, River Dove at Milldale, River Petteril at M6 bridge, River Severn at Ironbridge, Field Drain nr. Peterborough

- To reveal the detailed structure of the mean and turbulent fields around submerged and surface piercing obstacles at the floodplain edge of a compound, open channel. Specifically, by what processes the changes identified in the bulk flow characteristics and the drag coefficient come about.
- To examine how the structures and processes identified in the previous step affect the flow patterns in the wider channel and how these are linked to the secondary circulation patterns observed by other researchers.
- To investigate how the trends identified change with the changing geometry of the obstacle and how they are affected by the arrangement of multiple obstacles in a single line at the floodplain edge.

1.2 Contribution to Knowledge

The contribution to knowledge from this project can be summarised as the following:

- The current approaches to the analysis of compound, open channel flow with vegetation at the floodplain edge have been shown to be limited by the lack of consideration of the effects of the strong shear layer that exists in this location between the main channel and the floodplain. This highly three-dimensional flow environment has been shown to significantly affect the formation of the wake structures around blocks representing vegetation in this position and therefore to affect the drag force exerted on the flow by the presence of the vegetation.
- For both emergent and submerged block cases, it has been demonstrated that the floodplain edge location causes complex deformations and asymmetries in the processes of separation, reattachment, re-separation and recovery around the blocks, leading to significant alterations in their drag coefficients from the equivalent blocks in simple open channel flows.

- In testing a numerical model against the experimental results collected as part of this project, it has been demonstrated that solution of the 3D RANS equations, using a non-linear $k - \epsilon$ turbulence closure is of some use in interrogating this flow type and can reproduce some of the key features associated with the complications of the wake structure due to the floodplain edge location.
- It has been shown that the impact on the wake structures of cylindrical obstacles placed at the floodplain edge persists for a range of block geometries and distributions, although the precise changes induced in the wakes and the resultant changes in the drag coefficient vary strongly with the block aspect ratio and relative depth of the floodplain flow. The arrangement of multiple blocks along the floodplain edge also revealed how the vorticity created in the separation zones around each block is reinforced in the multiple block arrangement, gradually causing significant alteration to the structure of the flow in the wider channel.

1.3 Structure of Thesis

This thesis has a total of six chapters, the contents of which can be summarised as follows:

- *Chapter 1* describes the motivation behind the research and presents its structure.
- *Chapter 2* describes the review of literature and sets out the specific points of interest of the research in relation to this body of work.
- *Chapter 3* describes the methods by which data was collected and created, specifically the details of the physical experiments and the basis of the numerical model.

- *Chapter 4* presents the results from the two series of experiments carried out at Loughborough and Kansai universities respectively.
- *Chapter 5* compares and contrasts the experimental results with those from the numerical simulations and presents further computational results encompassing variations of block geometry.
- *Chapter 6* summarises and discusses the conclusions of the programme of research and gives suggestions for future work.

CHAPTER 2

Literature Review

2.1 Introduction

This section will describe the knowledge base from which this project will draw, including current understanding of the turbulent structure of flow in simple and compound open channels, the history of the analysis of the effects of vegetation in open channel flow, work done on the flow around single and tandem pairs of bluff bodies and the numerical methods that have been developed to analyse these flows.

The following axes convention will be adhered to in all subsequent equations and figures, unless otherwise indicated; X represents the streamwise direction, Y , the spanwise direction and Z , the vertical.

2.2 Turbulence in open channel flow

It is now well recognised that the structure of flow in open channels is inherently three-dimensional in nature and that without an understanding of the turbulence field a full description of the flow cannot be achieved.

The advent of hot wire anemometer technology in the 1950's allowed researchers to directly measure the internal structure of flows in detail for the first time. The

anemometer and its successors have since been used extensively in ducts and open channels to understand how turbulence acts to retard the flow in the streamwise direction.

2.2.1 Flow in non-circular ducts

It had been observed in the former half of the last century that the nature of flow in circular and non-circular pipes was fundamentally different. Prandtl (1927) predicted that the deformations observed in the streamwise velocity profiles in non-circular pipes were due to the presence of circulations in the transverse plane. He differentiated between this type of circulation, which he attributed to the action of turbulence, and the circulations seen in curved pipes and channels, which are due to the centrifugal force on the fluid body.

One experimental study on the flow in non-circular ducts using hot wire technology was completed by Brundrett and Baines (1964), the results of which seemed to confirm Prandtl's theory. Mathematical analysis of the flow was also performed using the streamwise vorticity equation, through which the authors sought to identify the processes by which streamwise vorticity (Ω_x) is created, convected and diffused.

The experimental measurements for fully developed square duct flow showed the presence of secondary circulation cells in the transverse plain, which act to significantly distort the isovels of mean streamwise velocity (U). The turbulence measurements agreed with the proposal that these secondary circulation cells are created and controlled by the anisotropy of the normal turbulent stresses ($\overline{v'^2} - \overline{w'^2}$) and, to a lesser degree, by the magnitude of the turbulent shear stress ($\overline{v'w'}$).

The presence of a solid surface will act to limit the length scale of the turbulent fluctuations of velocity that are perpendicular to it. The parallel component will not be similarly damped by this process so that the lateral $\overline{v'^2}$ and vertical $\overline{w'^2}$ normal turbulent stresses will not act to balance out one another. The resultant deformation of the flow under this stress is the main source of the angular

2.2 Turbulence in open channel flow

momentum that constitutes the secondary circulations.

The streamwise vorticity equation is a useful tool in analysing the source of axial angular momentum in a flow and indeed, its analogous equations in the spanwise and vertical directions can be put to a similar purpose. The laminar equation (Equation 2.1) is constructed as follows; terms on the left hand side represent the convection of vorticity by the mean flow, whilst the fourth term on the right hand side is the diffusion of vorticity. The first three terms on the right hand side represent the interaction of the vorticity in all three Cartesian directions with the rate of strain. The first of these is the action of vortex stretching, whilst the remaining two are tilting contributions (Libby, 1996).

$$\rho U \frac{\partial \Omega_x}{\partial x} + \rho V \frac{\partial \Omega_x}{\partial y} + \rho W \frac{\partial \Omega_x}{\partial z} = \rho \Omega_x \frac{\partial U}{\partial x} + \rho \Omega_y \frac{\partial U}{\partial y} + \rho \Omega_z \frac{\partial U}{\partial z} + \mu \left(\frac{\partial^2 \Omega_x}{\partial x^2} + \frac{\partial^2 \Omega_x}{\partial y^2} + \frac{\partial^2 \Omega_x}{\partial z^2} \right) \quad (2.1)$$

For the fully developed turbulent uniform flow case, where the derivatives in X are zero and the tilting contributions balance one another out, the equation can be simplified to the form shown in equation 2.2. From this equation, we can see that the forces driving the streamwise vorticity are the difference in the spanwise and vertical normal Reynolds stresses and the Reynolds shear stress.

$$\rho V \frac{\partial \Omega_x}{\partial y} + \rho W \frac{\partial \Omega_x}{\partial z} = \frac{\partial^2}{\partial z \partial y} (\overline{\rho w'^2} - \overline{\rho v'^2}) + \left(\frac{\partial^2}{\partial y^2} - \frac{\partial^2}{\partial z^2} \right) (\overline{\rho v'w'}) + \mu \left(\frac{\partial^2 \Omega_x}{\partial y^2} + \frac{\partial^2 \Omega_x}{\partial z^2} \right) \quad (2.2)$$

Brundrett and Baines (1964)'s experiments showed that the imbalance in the normal stresses, or the turbulent anisotropy, is greatest away from any axis of symmetry or solid boundary. The diffusion of vorticity, being associated with viscous stresses, was shown to be greatest in the duct corners so that the secondary circulations act to convect vorticity from regions of production to regions of diffusion. The action of the secondary currents to transport low momentum fluid away from the wall regions and high momentum fluid away from the channel centre causes the

2.2 Turbulence in open channel flow

isovels of mean streamwise velocity to bulge towards the duct corners. This phenomenon is shown in Figure 2.1. The flow structure highlighted by these studies has since been repeatedly observed by a number of other researchers, e.g. Melling and Whitelaw (1976), where the relative strength of these circulations has been found to be 1 – 4% of the bulk mean velocity (U_m).

Boundary shear stress (τ_b) is an important flow parameter since its magnitude and distribution dominates the geomorphological processes that affect rivers. An average value of boundary shear force can be used to calculate the flow resistance of different surface roughnesses. Profiles of boundary shear stress and information about its maximum value can be used in sediment transport work. Knight *et al.* (1984) measured profiles of boundary shear stress in closed channels of varying aspect ratios. Their work shows that the boundary shear stress is always at a minimum in the corner and increases towards the channel centreline. For a channel aspect ratio of $W_{ch}/H_{ch} > 5$, the maximum is at the channel centreline, whilst for $1 < W_{ch}/H_{ch} < 5$, the maximum value is shifted a little further towards the corner and the centreline value is slightly lessened.

By integrating the streamwise momentum equation for uniform flow (i.e. $\frac{\partial}{\partial x} = 0$) and applying the appropriate boundary conditions, Nezu and Nakagawa (1993) derive equations 2.3 and 2.4 to describe the bed shear stress (τ_{bed}) and wall shear stress (τ_{wall}) respectively. These derivations illustrate that the magnitude of the boundary shear stress at any point is a function of the energy slope, the secondary currents and the Reynolds stresses. As such, the differences in the boundary shear stress profiles observed by Knight *et al.* (1984) for the range of channel aspect ratios can be attributed to the changing patterns of the secondary currents.

$$\frac{\tau_{bed}}{\rho} = gI_e H_{ch} - \frac{\partial}{\partial y} \int_0^{H_{ch}} \left(UV + \frac{\tau_{uv}}{\rho} \right) dz \quad (2.3)$$

$$\frac{\tau_{wall}}{\rho} = gI_e \frac{W_{ch}}{2} - \frac{\partial}{\partial z} \int_0^{\frac{W_{ch}}{2}} \left(UW - \frac{\tau_{uw}}{\rho} \right) dy \quad (2.4)$$

2.2.2 Flow in simple, open channels

For the study of flow in rivers, the most natural extension of this field of research was to study the influence of the free surface for similar phenomena in open channels. Tominaga *et al.* (1989) used a hot film anemometer to extend the experimental measurement of the effects of turbulence in creating secondary circulations to flows in straight, open channels with aspect ratios in the range of 2 to 7, showing that the free surface acts to distort the relative sizes and positions of the vortices in comparison to the duct flow case.

From the results of their experiments in a half-channel, they detected the existence of two vortices, flowing towards the side wall, separated at approximately 60% of the total flow depth. The authors named the upper vortex the 'free surface vortex' and the lower vortex the 'bottom vortex'. This regime is shown in Figure 2.2.

Where there is a free surface, the vertical velocity component (w) should be zero in its vicinity. This condition on the vertical turbulent component (w') has the consequence that it is damped throughout the entire domain but also alters the distribution of turbulent length scale (l). The result of these changes is that turbulent anisotropy and therefore, streamwise vorticity production is strongly positive near the free surface and near the bed, while the region of zero production is shifted towards the channel side wall. Next to the sidewall itself, lies a region where $\overline{v'^2}$ is greater than $\overline{w'^2}$ and the sign of the anisotropy is reversed.

The effect of these changes is to alter the distribution of streamwise velocity as shown in Figure 2.2. The free surface vortex transports high momentum fluid away from the free surface and brings in low momentum fluid from the channel edges, acting to depress the region of maximum streamwise velocity. This phenomenon is often called the 'velocity dip effect' (Nezu and Nakagawa, 1993). As opposed to closed duct flow, the isovels tend to bulge towards the side wall.

In fact, this phenomenon had already been studied via numerical modelling (Naot and Rodi, 1982) so that the experimental results published in the late '80's

2.2 Turbulence in open channel flow

and early '90's (Nezu and Rodi, 1993; Tominaga *et al.*, 1989) served to confirm what had previously been demonstrated.

The model results also showed two counter-rotating vortices in the cross-sectional plane, with the relative strength of these being dependent on the channel aspect ratio, as defined by the ratio of channel width to depth (W_{ch}/H_{ch}). At $W_{ch}/H_{ch} = 2$, the free surface vortex dominated the channel, growing in size with the aspect ratio to occupy a space equivalent to twice the depth. The bottom vortex however was limited to the corner of the channel. The experimental results of Tominaga *et al.* (1989) confirmed these trends.

More recent modelling studies (Kang and Choi, 2006) have also identified a small vortex in the corner of the rectangular channel, at the point where the wall and free surface meet. Rotating in the same manner as the bottom vortex with a strength of approximately 1% of the mean streamwise velocity, this structure has a recognisable impact on the isovel pattern in this corner. However, because of its size, it has seldom been recognised in experimental work.

The strength of the larger vortex structures was measured by Tominaga *et al.* (1989) to be approximately 1.5% of the mean streamwise velocity. Beyond the edges of this pair of vortices in the central channel region, much weaker circulations are present but not deemed to be of significance to the alteration of the streamwise velocity profile.

The experimental and numerical results obtained by the above researchers served to demonstrate that the channel geometry has a strong influence on the turbulent intensity field. In particular, the changing relationship between the spanwise and vertical turbulent intensities was seen to strongly influence the streamwise vorticity and therefore the cross-sectional profile of mean streamwise velocity.

With reference to Equations 2.3 and 2.4, it is also to be expected that the profiles of boundary shear stress will differ between a closed channel and open channel set-up. The evidence of Knight *et al.* (1984) suggests that the differences between the two distributions are quite small for aspect ratios of less than approximately 5. However above this value, a distinct bump can be seen in the bed shear stress

profile for the open channel close to the sidewall. The data of Tominaga *et al.* (1989) also includes a plot of bed shear stress for an open channel flow of aspect ratio $W_{ch}/H_{ch} = 3.94$, which although slightly lower than Knight *et al.* (1984)'s threshold, clearly shows the secondary peak in question. This pattern is attributed to the action of the bottom vortex.

2.2.3 Flow in compound, open channels

In order to study the structure of flow in a flooding river, it is necessary to consider the case of a compound channel, i.e. a combination of a deep main channel and a shallower floodplain. Although a gross simplification of the naturally occurring geometry of river beds and floodplains, the combination of a straight main channel and floodplain is an essential building block in our understanding of more complex flows.

As such, Tominaga and Nezu (1991) used a Laser Doppler Anemometer (LDA) to investigate the internal structure of fully developed flow in a straight, compound open channel. The authors concentrated on investigating the structure for rectangular main channels. Other researchers have also investigated this phenomenon, such as Shiono and Knight (1989), who took similar measurements for trapezoidal main channel profiles as part of an extensive programme of testing at the UK's Science and Engineering Research Council Flood Channel Facility (SERC - FCF).

The geometry of a compound channel is such that the mean streamwise velocity of the floodplain flow, affected as it is by the retarding bed shear force of the floodplain bed, must be less than the mean streamwise velocity of the main channel flow at the same depth. Thus, straight, compound channel flow is distinguished by a large difference in streamwise velocity between the main channel and floodplain. This large lateral velocity gradient is, in effect, a strong shear layer where large values of the $\overline{(u'v')}$ Reynolds stress component are to be expected.

This shear force should produce angular momentum about the vertical axis, (Ω_z) and indeed, large vortices with vertical axes have been observed by a number

2.2 Turbulence in open channel flow

of researchers (Fukuoka and Fujita, 1989; Sellin, 1964; Tamai *et al.*, 1986), acting to transfer momentum between the main channel and the floodplain. The strength of these vortices becomes weaker as the overall water depth increases and the difference between the mean velocity at equivalent depths in the floodplain and main channel diminishes. Fukuoka and Fujita (1989)'s schematic representation of these vortices, seen as a plan view on the water surface is presented in Figure 2.3.

From equation 2.1, it can be seen that the contributions of the large value of $\frac{\partial U}{\partial y}$ and the vertical vorticity Ω_z described above will result in the production of streamwise vorticity Ω_x at the floodplain edge. Using a cross-sectional geometry argument, one can also deduce the origins of the streamwise vorticity patterns from the turbulent stresses. The lateral normal Reynolds stress $\overline{v'^2}$ has its cross-sectional maximum on the floodplain bed, whilst the vertical normal Reynolds stress $\overline{w'^2}$ has its maximum on the floodplain wall. Either side of the diagonal that bisects the corner therefore, are two large peaks in turbulent anisotropy, which drive the flow upwards and outwards.

The results of the experiments of Tominaga and Nezu (1991) show that the transition from a simple rectangular channel to a compound channel results in the creation of two additional streamwise vortices. The authors name these the 'main channel vortex' and the 'floodplain vortex', describing their respective zones of influence. A schematic of the positions of these vortices is shown in Figure 2.4, where the experiments were conducted in a half-channel. The action of these streamwise vortices is to transport low momentum fluid from the floodplain bed and main channel sidewall into the body of the main channel, creating a characteristic bump in the contour plot of streamwise velocity.

The maximum strength of these vortices in the experiments of Tominaga and Nezu (1991) was approximately 4% of the maximum streamwise velocity. However, the relative strength and size of these vortices was shown to depend on the relative depth of flow on the floodplain (D_{fl}) to flow in the main channel (D_{ch}), a variable commonly symbolised by D_r . For low values of D_r , the main channel

vortex extends in the spanwise direction and becomes flatter. For high values of D_r , the main channel vortex shrinks in size and the floodplain vortex becomes dominant.

Shiono and Knight (1991) proposed a schematic of the flow structure of straight, compound channel flow, which is shown in Figure 2.5. The interaction of the streamwise and vertically orientated vortices and the relative influence of the component parts of this flow structure under different flow and geometry conditions is still a contentious matter but it is sufficient to say that the distribution of velocities and forces in a compound channel are significantly more complex than those in a simple open channel. One may therefore hypothesise that the wake formed behind large, rigid vegetation at the floodplain edge may differ in size and form from that behind such obstacles in a simple flow and it is this idea that will be examined in more detail in subsequent sections.

Their influence on the distribution of boundary shear stress has been examined by Tominaga and Nezu (1991), whose measurements are shown in Figure 2.6. On the main channel bed, the profile is similar to that of an open channel, with the secondary peak associated with the bottom vortex being observed. On the floodplain bed, the most pertinent feature of the profile is an increase towards the floodplain edge. With reference to equation 2.3, this increase in bed shear stress can be attributed to the large spanwise gradient in $\overline{u'v'}$ and the action of the secondary current W .

2.2.4 Summary

Through all of this experimental and numerical work, it has been clearly demonstrated that the structure of flow in square and rectangular ducts and channels is inherently 3D in nature. The relative influences of the solid boundaries and free surface, where it exists, act to change the relationship between the normal Reynolds stresses and it is primarily through this mechanism that axial vorticity is created. For the special case of the compound channel, the strong shear layer at the

floodplain edge creates both axial and vertically orientated vorticity, such that the streamwise velocity profile and boundary shear stress distributions are significantly affected.

2.3 Vegetation in open channel flow

All of the research effort mentioned above and subsequent studies into the structure of flow in asymmetric and meandering compound channels has been of great interest to river engineers and has prompted the creation of improved modelling systems with which the commercial engineer can analyse the real environment. However, more recently interest has turned to attempts to include more complex elements of the real river system, including vegetation. The following sections will describe the approaches commonly taken to examine the influence of vegetation on flooding river systems. These briefly comprise the following; vegetation as surface roughness, 2D wake analysis and 3D consideration of bulk matrices of vegetation.

2.3.1 Vegetation as surface roughness

Section 2.2 describes the progress that has been made in understanding the important phenomena at work in open channel flows and although the description of the research above has not explicitly included it, in fact, many of the studies extend their analyses to the examination of the effect of varying boundary roughness on the flow structures. This constitutes one method for modelling the effects of vegetation in the river corridor and is, by virtue of its simplicity, the method by which vegetation is commonly accounted for by today's practising engineer.

One thread of the research effort for improving flow modelling therefore concentrates on attempts to estimate the contribution of vegetation to an increase in flow resistance in terms of standard flow resistance formulae, e.g. the increase in Manning's coefficient (n).

2.3 Vegetation in open channel flow

Studies of this type (Jordanova *et al.*, 2006; Petryk and Bosmajian, 1975; Sellin and Beeston, 2002) can provide useful information about seasonal and species-related changes in overall flow resistance but any attempt to account for the effects of floodplain vegetation by varying the Manning's 'n' value alone is extremely limited, particularly since Manning's roughness parameter is formulated only to make allowance for surface roughness.

Despite their simplicity, the experiments of Petryk and Bosmajian (1975) highlighted the dominant features of the vegetation structure that affect the bulk properties of the flow, namely:

- *Density*, specifically the ratio of projected area of vegetation to total flow area,
- *Flexibility*, in that the bending of vegetation acts to reduce its projected area,
- *Depth of inundation*, since completely submerged vegetation affects flow in a different way to emergent vegetation and
- *Distribution*, which is especially influential in compound channels

Of these parameters, this study will only consider three, since the flexibility of vegetation adds a considerable layer of complexity. For sufficiently large and rigid vegetation such as mature trees, this factor may justifiably be neglected as a first step. However, the three D's - density, depth of inundation and distribution - are easier to manipulate and have been the subject of a number of investigations. By eliminating the flexibility of vegetation, we can reduce the plant stems and trunks to rigid, bluff bodies in the flow. On this basis, much work has been done using a variety of approaches to measure and model the effects of bulk matrices of vegetation on open channel flow.

2.3.2 Wake Theory & Two-Dimensional Analyses

As computing resources become more efficient, two dimensional analyses are becoming more commonplace in the world of commercial modelling. Although the effects of vegetation are still commonly accounted for by changes in roughness parameters within these models, the additional dimension provides the opportunity of using more sophisticated approaches. The development of an accurate two-dimensional model of vegetated channel flow would be of considerable and immediate benefit.

In one of the earliest attempts to analyse vegetated channel flow in this way, Petryk (1969) investigated the range of drag forces (f_d) on individual emergent circular cylinders in different multi-cylinder arrangements under a variety of open-channel flow conditions in rectangular channels. Measuring wake decay and spread rates behind the cylinders, Petryk (1969) used 2D idealised wake theory as a basis to analyse his experimental data and to develop and validate an analytical model for the prediction of depth-averaged velocity in such a flow. The rates of wake spread and decay that he observed were considerably higher than those predicted by the theory but he derived Equation 2.5 empirically for open channel flow to calculate the maximum depth averaged velocity deficit decay rate, where the velocity deficit is defined as the difference between the local velocity and a reference free stream velocity U_o . To enable the analysis of flows containing multi-cylinder arrangements, the principle of linear superposition of wakes was used to extend this formula.

$$\frac{ud_{max}}{U_o} = -0.90 \left(\frac{x}{C_D d} \right)^{-0.7} \left(\frac{1}{1 + \frac{gxS_o}{\frac{U_o^2}{2}}} \right)^{\frac{3}{2}} \quad (2.5)$$

To solve this Equation 2.5, Petryk (1969) assumed that where no aeration occurred behind the cylinder, the 2D idealised drag co-efficient (C_D) of 1.2 (Schlicht-

ing, 1968) was still valid. However, he acknowledged that his experimental set-up differed from the 2D theory by being influenced by:

- open channel turbulence,
- a non-uniform streamwise velocity profile,
- the free surface and
- blockage caused by the channel walls.

This 2D empirical approach has been extended and modified by more recent researchers (Järvelä, 2002; Li and Shen, 1973; Linder, 1991; Mertens, 1989; Nuding, 1991; Pasche and Rouvé, 1985) with varying results. This work has essentially focussed on finding an appropriate drag coefficient value to include the effects listed above and those induced by multiple cylinder arrangements. Linder (1991), for example, determined an equation for the drag co-efficient of the cylinders, suggesting that C_D is dependent on the narrowing effect of neighbouring cylinders and the resistance due to the gravitational force. Mertens (1989) and Nuding (1991) undertook analyses concluding that a blanket C_D value of 1.5 was adequate. More recently, Järvelä (2002) extended this to investigate the influence of type, density and combination of vegetation, flow depth, velocity, Reynolds number and vegetal characteristics on C_D .

Two-dimensional depth averaged approaches to modelling partially vegetated open channels remain popular. Wu *et al.* (2005) built such a model for the modelling of flow through matrices of vegetation using a drag coefficient based upon the restricted streamwise velocity in the matrix. This drag coefficient was deemed to vary little with cylinder density and Reynolds number and was therefore more generally applicable. Wilkerson (2007) developed an analytical model to handle submerged and emergent vegetation in rectangular and trapezoidal compound channels. This is an extension of Petryk (1969)'s method for the compound channel case but does not take account of the three dimensional nature of the velocity field in that channel.

All of the studies mentioned above offer simplified analyses of the flow scenario of vegetation in open channels and as such, put forward models that may be of practical use. In investigating the appropriate values of C_D to be used, these studies have also sought to identify the relationships between the drag force created by the vegetation and its density and distribution. However, a common feature of the approaches detailed above is the neglect of the three-dimensional nature of the open channel flow itself, as has been emphasised in Section 2.2. Only with an understanding of the three-dimensional effects of open channel turbulence and the non-uniform streamwise velocity profile which is its consequence can we understand the processes that are affecting C_D and create a truly widely applicable 2D approximation of them.

2.3.3 Fully 3D Approaches

The three major consequences of the introduction of vegetation to open channel flow are summarised as the production of additional drag forces, an increase in the production of turbulent kinetic energy (K) and a change in the length scale and anisotropy of the turbulent field (Naot *et al.*, 1996). Yang *et al.* (2007) recently published results of experiments, measuring the three velocity components in a compound, trapezoidal channel flow with a vegetated floodplain. Contrasting the resultant vertical velocity profiles with those from a non-vegetated channel, the authors note that the nature of the secondary circulations is radically altered and that the effects of this change may be significant. If a full understanding of this flow type is to be achieved therefore, an appreciation of the interaction between the turbulent wake behind a bluff body and the turbulence in the free stream passing around it is essential. Several researchers have performed physical experiments and numerical modelling exercises to look at the changes to the turbulent field of an open channel, when vegetation is introduced into it.

2.3.3.1 Emergent Vegetation in a Simple Open Channel

Pasche and Rouvé (1985), Tsujimoto (1992a), Tsujimoto (1992b), Naot *et al.* (1996) and Nepf and Vivoni (2000) have all examined the case of a rectangular open channel partially filled with emergent vegetation. The nature of the flow in such a channel was concluded to be heavily influenced by the shear layer that develops at the edge of the vegetated zone, since the flow within the vegetation is decelerated compared to that in the non-vegetated zone. In fact, Naot *et al.* (1996) created a hydrodynamic model for the case and more specifically identified that it is the difference between this shear layer and the shear layer at the solid boundary on the other side of the channel that acts to distort the internal structure of the flow. At low vegetation densities, it was shown that the presence of the vegetation introduces a measure of asymmetry to the contours of streamwise velocity, with a peak in turbulent kinetic energy near the channel bed at the lateral interface. At intermediate densities, the turbulent energy peak was spread throughout the water depth at the edge of the vegetated zone and the streamwise contours showed a more symmetrical profile. Finally, at very high densities, the secondary current patterns were heavily altered and acted to convect the turbulent kinetic energy peak from the junction zone into the non-vegetated zone.

It is clear from these results that the wakes from the vegetation interact not only with each other but also with the flow in the non-vegetated zone to produce a range of different patterns of turbulence generation and transmission. The details of how these interactions act to create the patterns identified still requires investigation.

2.3.3.2 Submerged Vegetation in a Simple Open Channel

Tsujimoto *et al.* (1992) gave details of turbulence measurements in a rectangular channel with submerged vegetation uniformly distributed across the whole channel bed. Concentrating on the variation of the velocity and turbulence parameters over the water depth, they concluded that the flow in the vegetation layer was highly influenced by the velocity and depth of the flow in the upper layer. Turbulent

intensities and Reynolds shear stresses were observed to peak at the top of the vegetation. Nepf and Vivoni (2000) later stated that the inflection in the vertical profile of the streamwise velocity at the top of the vegetation causes large eddies with streamwise orientation to be generated in this location.

Naot *et al.* (1996) supplemented these results by examining a similar flow via numerical modelling, this time with submerged vegetation present only in the channel corner. In this flow, a shear layer is not only present at the top of the vegetation, as noted by Tsujimoto *et al.* (1992), but also at the side of the vegetated zone.

Nezu and Onitsuka (2001) used both a PIV system and a LDA to take turbulence measurements for such a case, i.e. a rectangular open channel with half of the channel width covered in submerged, rigid vegetation. With the PIV, a plan sheet of data was collected at an elevation above the height of the vegetation, the density of which was varied. The results of these measurements showed that an inflection point exists in the spanwise profile of streamwise velocity at the spanwise edge of the vegetation zone, as shown in Figure 2.7. The generation of the vertically orientated coherent vortices that were observed is attributed to this inflection. As the density of the vegetation was increased, these structures were consolidated. Although the presence of vertically orientated coherent vortices may lead one to draw analogies with the simple compound channel case, the mechanism by which they are generated must be dissimilar, since the inflected profile of streamwise velocity would not be expected in the compound channel case, where the secondary currents act to create a dip in the streamwise velocity at the junction point, as described in Section 2.2.3.

The LDA measurements of a single cross-section highlighted the secondary current pattern of this partially vegetated case, showing that it was quite different from that described for the compound open channel case. Large velocity vectors were measured at the interface, flowing strongly towards the layer above the vegetation, whilst analysis of the turbulent anisotropy term showed a large positive

peak in anisotropy just under the free surface near the interface position. The generation of turbulent kinetic energy was shown to peak at the junction position, at the side and top of the vegetation, being partly attributed to the wake structures behind that vegetation.

These experiments therefore showed that all of the important flow variables, such as streamwise velocity and boundary shear stress, are affected in a complex manner by the addition of vegetation to the channel as the wakes from the vegetation interact with the freestream turbulence.

2.3.3.3 Vegetation on the Floodplain of a Compound Channel

Naot *et al.* (1996), Rameshwaran and Shiono (2007), Sun (2006) and Kang and Choi (2006) are among the small number of researchers who have extended these analyses to compound channels with vegetated floodplains.

Detailed experimental results for the case of emergent vegetation on the floodplain of a compound channel can be found in Sun (2006), who performed tests in a straight, trapezoidal, compound channel using an Acoustic Doppler Velocimeter (ADV) to measure the velocity distribution. For all the floodplain vegetation cases that were examined, it was noted that the presence of the vegetation caused the streamwise velocity on the floodplain to be significantly reduced, thus accentuating the spanwise gradient in U from the smooth channel case. However, the actions of the secondary currents add further complexity to the streamwise velocity contours. For the emergent case, Sun (2006) recorded a circulation in the main channel being driven by a strong flow into the main channel from the floodplain edge near the free surface. This circulation pattern was also found by Kang and Choi (2006), who used Reynolds Stress Modelling (RSM), incorporating the vegetation by way of a drag term in the momentum equations, to perform numerical simulations of flow in a rectangular compound channel with a fully vegetated floodplain. Their results are shown in Figure 2.8.

Testing this scenario with a range of vegetation densities, Kang and Choi (2006) observed that the main channel vortex grows in size and influence as the vegetation

2.3 Vegetation in open channel flow

density increases and measured a range of maximum strengths of the secondary currents of 3.4% – 5.1% of the maximum streamwise velocity, increasing with vegetation density. The intensity of the turbulence and the turbulent kinetic energy were observed by both Sun (2006) and Kang and Choi (2006) to peak at the main channel/floodplain interface. As with Pasche and Rouvé (1985), Sun (2006) also identified large vertically orientated eddies at the interface and attributed them to the lateral shear caused by the wakes from the vegetation.

Sun (2006) also performed experiments with submerged vegetation at two flow depths such that at one depth, the vegetation was slightly submerged and at the other, deeply submerged. In these cases, there was strong flow towards the main channel along the height of the vegetation at the floodplain edge. In the shallow submerged case, the circulation described for the emergent case was also partially visible. For the deeply submerged case, the strong flow into the main channel then formed a circulation flowing back onto the floodplain, above the top of the vegetation layer. Sun (2006) measured a maximum strength of the secondary currents of about 10% of the maximum streamwise velocity. The intensity of the turbulence and the kinetic energy again peaked at the main channel/floodplain interface but in these cases, there was also a secondary peak in the streamwise and spanwise turbulent intensities at the top of the vegetation.

Sun (2006) showed that the anisotropy of the turbulence also peaked at the floodplain edge but having performed a vorticity balance, concluded that in the vegetated floodplain case, the Reynolds shear stress was of a similar magnitude and therefore much more important for the creation of streamwise vorticity than in the smooth channel case. This was very clear for the submerged cases but the results were less conclusive for the emergent case.

In both submerged and emergent cases, all three Reynolds shear stresses were found to peak at the floodplain edge. However, the peak of τ_{uv} was generally larger than that of τ_{uw} and τ_{vw} , which were of analogous magnitudes. For the emergent case, the peak of τ_{uv} at the floodplain edge was negative and of the smallest magnitude of the three cases. τ_{vw} also had the lowest peak magnitude of

the three cases. For the deep submergence case, the pattern of τ_{uv} was complex, with a negative region on the slanting surface of the main channel wall. In the shallow submergence case, the pattern of τ_{uv} was similar to that of the emergent case but with a greater peak magnitude than the other two cases.

In analysing these results, the above authors have attributed the changes in Reynolds stress and velocity distributions and the creation of axial and vertically orientated vorticity to the action of the wakes from the vegetation elements. However, as yet, there appears to have been no attempt to study the structure of these wakes in detail nor to predict how the changes in freestream conditions will impact upon them and therefore upon the flow structure more generally.

2.3.3.4 One Line Vegetation at the Floodplain Edge

Sun (2006) also extended his experiments to the case of a single line of emergent vegetation placed at the floodplain edge of a compound channel with $D_r = 0.52$. Since the velocities in this case were measured with a Pitot tube, only the stream-wise velocity profile could be directly recorded. Measurements were made at the centre of the gap between adjacent rods, where the spacing between rods was set to $4.44W_{bl}$. The results showed the creation of two velocity maxima, either side of the vegetation, as shown in Figure 2.9. This also implies the existence of two transverse shear layers, the combined width of which was twice that of the single shear layer in the smooth floodplain case. Of course, the spanwise gradient of U is shown to be greater on the main channel side than on the floodplain side. Using a Preston tube, it was also shown that the presence of the vegetation acted to significantly reduce the overall boundary shear stress and in particular, to reduce it on the floodplain. Despite these revelations, no secondary current or turbulence data were collected. It is therefore unknown how the wakes from the vegetation interact with the compound channel turbulence and the possible distribution of coherent vortices that may result from this interaction.

2.3.3.5 Three-Dimensional Numerical Modelling

Whilst these experimentalists have been revealing the structures and patterns of vegetated flow, other researchers have been attempting to replicate their results by way of three dimensional numerical modelling. The focus of much of this work has been the search for suitable values of drag coefficient but the alteration of other model coefficients has also been proposed. Numerical modelling of these flow scenarios has commonly been attempted by combining a drag coefficient approach with the solution of the three-dimensional Reynolds-averaged Navier Stokes equations and the $k - \epsilon$ turbulence model.

Shimizu and Tsujimoto (1994) and Lopez and Garcia (1997) both analysed flow through vegetation arrays using the Reynolds-averaged approach, opting to include a sink term for the vegetal drag in all of the equations and to calibrate their model by changing two of the five coefficients of the standard $k - \epsilon$ model. Fischer-Antze *et al.* (2001) adapted this approach, choosing not to modify the $k - \epsilon$ model at all on the assumption that the values of K and ϵ in the vegetation layer did not affect the velocity. More recently, this approach was also used by Wilson *et al.* (2006) to model the affects of willow stands in a natural river geometry. All of these models make assumptions about the appropriate value of drag co-efficient to be used to calculate the drag force exerted per vegetation element. Fischer-Antze *et al.* (2001) and Wilson *et al.* (2006) used a universal value of 1.0, although the latter also tested the use of a value of 1.5, as espoused by Mertens (1989) and Nuding (1991).

Although the $k - \epsilon$ model has been used successfully to produce a variety of interesting results for open channels containing vegetation, it is well recognised that this two-equation turbulence model is unreliable for the prediction of turbulence in open channel flows since it cannot predict the difference between the spanwise and vertical normal turbulent stresses. The $k - \epsilon$ model is also limited when applied to the flow around bluff bodies, since it cannot predict the normal turbulent stresses, which dominate in the stagnation zones.

A limited amount of work has therefore been done on extending the 3D numerical modelling of vegetated channels through the use of algebraic stress models (ASM's) and Reynolds stress models (RSM's), both of which attempt to include the influence of the transport of Reynolds stresses and therefore the anisotropy of the turbulent field. Naot *et al.* (1996) used an algebraic stress model with the drag co-efficient approach. In this case, not only were the drag forces incorporated into the momentum equations but the $k - \epsilon$ equations were modified to take into account the direct contribution of the vegetation to the turbulent intensity and scale and also the presence of the free shear layer at the edge of the vegetated zone. Finally, the algebraic stress model equations were extended by assuming that the turbulence produced by the vegetation was distributed among the individual component directions according to an anisotropy matrix. Kang and Choi (2004, 2006) performed similar simulations using a full RSM, also using the drag coefficient approach to include the vegetation. Comparing their results to those of Naot *et al.* (1996), the authors noted that although agreement between the two sets of data was reasonably good, the Reynolds stress technique allows the turbulent anisotropy near the free surface to be better predicted. Consequently, the velocity dip effect is more clearly observed in the Reynolds stress model results.

2.3.4 Summary

The work described in this section has clearly shown that the addition of vegetation to an open channel flow has wide ranging effects on the flow structure. These effects are directly dependent on the three D's: vegetation density, distribution and depth of inundation. All of the above researchers have concluded that the wakes behind the vegetation elements cause additional turbulent kinetic energy to be generated and then convected into the non-vegetated parts of the channel. For all cases, it is also apparent that the shear layers existing at the top and sides of the vegetated zones cause axial and vertical vorticity to be generated, altering the streamwise velocity and boundary shear stress distributions from those of their

2.4 Turbulent flow around isolated obstacles

smooth channel equivalents. These studies almost universally concentrate on the bulk effect on open channel flow structures of the addition of large matrices of vegetation to those channels. Very little has yet been revealed about the effects of a single line of vegetation at the floodplain edge, which has been identified in Section 1 as an important growth pattern in UK river systems. Moreover, the manner in which the wakes behind the vegetation elements interact with the turbulent structures of the compound channel is yet to be studied at all.

2.4 Turbulent flow around isolated obstacles

2.4.1 Two-dimensional flow around bluff bodies

Much of the investigative effort into the effects of vegetation on the flow structure in open channels has been directed at observation of its bulk effects, e.g. experiments on rows or matrices of vegetation elements, inclusion of vegetation in numerical models using the drag co-efficient approach. Although these approaches have yielded important information about the effects of the wakes from the vegetation on the overall flow structure, they do not give any detailed information about how the wakes and the free stream flow are interacting to create these effects. Analysis based upon wake theory on the other hand, has been limited to a two dimensional depth-averaged approach and has been based on assumptions that may significantly limit its application to open channel flow.

If we reduce the vegetation to the status of a rigid bluff body in the flow, by ignoring the presence of branches and leaves and eliminating the flexibility, we then allow ourselves to draw analogies between the flow around floodplain vegetation and the large knowledge base that has been built up by aerodynamicists and hydraulicists with regards to the nature of flow around bluff bodies.

Much of the basic understanding of the nature of these flows was found by performing experiments on two-dimensional bluff bodies in uniform free streams, in which free stream turbulence was purposefully suppressed. The exact structure

2.4 Turbulent flow around isolated obstacles

of the wake behind such a body is determined by its local Reynolds number (Re_D), its geometry (cylindrical, sharp-edged) and the nature of the free stream in which it sits.

For a two-dimensional circular cylinder in a uniform free stream with low turbulence, Zdravkovich (1997) gives a summary of the changing wake structure throughout the Reynolds number range. All flows around bluff bodies feature boundary layers on the body's surface, a wake region downstream of the body and shear layers bounding this wake. The creation and decay of the coherent structures often seen in the wake depend upon the flow state of each of these regions.

In the case of floodplain vegetation, the local Reynolds number (i.e. approach velocity \times vegetation diameter / kinematic viscosity) is likely to be in the range of 1×10^5 (laboratory flume scale) to 1×10^6 (natural river channel). In this range, for Zdravkovich's 2D circular cylinder, if the free stream turbulence is controlled and the flow is uniform, the wake region would be turbulent and transition to turbulence is also likely to have occurred in the free shear layers. Transition in the boundary layer attached to the cylinder surface may also be underway. At the bottom of this range, we would already expect the cylinder to be shedding turbulent eddies with the same orientation as the cylinder, commonly known as a von Kármán vortex street. Although the long time averaged flow may be steady, the vortices are shed alternately from each side of the cylinder, with a frequency described by the dimensionless Strouhal number, which is defined as:

$$St = \frac{f_{sh}L}{U_m} \quad (2.6)$$

where f_{sh} is the shedding frequency and L is a characteristic length. As the Reynolds number increases and transition occurs in the free shear layers, alternating eddies also appear in this region. With further increases, the boundary layers become turbulent through a complex process, in which the shedding of eddies is at some points retarded and at other points promoted.

2.4 Turbulent flow around isolated obstacles

The drag force of the cylinder is made up of friction drag from fluid passing over its surface and pressure drag, which emanates from the unequal pressure distribution across the cylinder. Throughout the transitions mentioned above, the pressure distribution and therefore the drag coefficient is constantly fluctuating. This is shown clearly in Figure 2.10. It follows from this that the free stream conditions in which a bluff body is sitting can have far reaching effects on the drag force that it exerts.

Due to modelling constraints, this research is concerned with the flow around square sectioned bluff bodies. Although the circular cylinder is intuitively preferable to model the effect of trees on compound channel flow, in reality, the cross section of such vegetation is rarely simple and since much of the same theory is applicable to the square sectioned case as for the circular section case, it is reasonable to interchange between the two. The aim of the work is, after all, to investigate the interaction of the compound channel environment and the wake flow from an obstruction and compare this to what we might expect in a simple channel environment. These conclusions can be drawn equally for both section shapes.

Although much of the same theory applies for a sharp-edged bluff body, much less research effort has been expended on understanding this flow type. Researchers such as Durao *et al.* (1988) and Bearman and Trueman (1972) were amongst the first to examine the case of a square and rectangular block respectively. A more detailed experiment was carried out by Lyn *et al.* (1995) using a LDV to take measurements in the wake of a square block. Lyn *et al.* (1995) used these results to make a comparison of the flow around a square block with that around an equivalent circular cylinder.

Unlike the circular cylinder, where the point of flow separation moves around the circumference, separation always occurs at the sharp edges of a square block producing a wider wake than in the circular case. Streamwise and spanwise coordinates are normalised using the block width ($x = X/W_{bl}$, $y = Y/W_{bl}$) and vertical co-ordinates are normalised with the block height, where the block height is equal to the floodplain depth in the emergent cases ($z = Z/H_{bl}$ or $z = Z/D_{fl}$)

2.4 Turbulent flow around isolated obstacles

). Unless otherwise indicated, these conventions will be used to describe all of the following results.

Measuring the wake at $x = 1$, Lyn *et al.* (1995) observed peaks in the Reynolds shear stress $\overline{u'v'}$ showing the shear layers to be at approximately $y = \pm 0.75$. This implies and the experiments confirmed that the recovery of the centreline velocity is slower for a square block than for a circular one. The recirculation region was measured to be of length $1.4W_{bl}$, which is more clearly shown in Figure 2.11. The experiments also showed that turbulent intensities in the wake are larger for the square case and these values are also plotted in Figure 2.11.

From the detailed measurements of Lyn *et al.* (1995), this 2D wake structure resulted in a Strouhal number of 0.13 and a time-averaged drag coefficient of 2.1 at a block Reynolds number of 21,400. Based on a scaling argument, Lyn *et al.* (1995) therefore proposed the following relationship between drag coefficients for the circular and square blocks.

$$\frac{(C_D)_{sq}}{(C_D)_{circ}} \approx 1.7 \quad (2.7)$$

2.4.2 Surface mounting effects

Reviewing the details of the flow around two-dimensional bluff bodies gives us important information about what to expect from all bluff body flows, ie. flow separation, the creation of vorticity and a gradual recovery. It also serves to demonstrate the important influence of freestream conditions on these processes. However, the 2D approach has its obvious limitations since nearly all engineering applications will involve three-dimensional flow. For the case of riparian vegetation, we must consider the influence of the bed and either the free surface or the flow over the top of the body. We must also consider the freestream turbulence and non-uniformity of the oncoming flow. In other words, we must take account of the three-dimensional nature of the flow and of the vegetation.

2.4 Turbulent flow around isolated obstacles

The first addition to the complexity of flow around a bluff body in an open channel flow is the necklace or horseshoe vortex, which is created when any bluff body is mounted onto a solid surface. A review by Simpson (2001) reveals that this system has been measured and modelled for various applications by many researchers. Despite the differences of body shape and Reynolds number, the common feature of the system is the formation of two axially orientated vortices on the bed in the body wake, which rotate towards its central axis.

These vortices originate in the stagnation zone upstream of the body, where a complex process of 3D separation is occurring due to the adverse pressure gradient that the presence of the body induces. In an early study on a set of large aspect ratio circular cylinders, Baker (1980) used flow visualisation to reveal the time averaged stagnation pattern on the bed. There occur two stagnation points, from which two sets of separation lines extend around the bluff body. Although indistinguishable from the experimental results, it is concluded that there must be an attachment between these separation points.

Martinuzzi and Tropea (1993) confirmed this pattern in their experiments on a surface mounted cube. They also concurred with Baker (1980) that as the turbulent boundary layer on the channel bed enters the stagnation zone, a system of four vortices with spanwise orientation are created. These vortices are shown in Figure 2.12, of which the vortex labelled (1) is the dominant structure. It is this vorticity, which is swept around the sides of the body and consolidated by vortex stretching to form the horseshoe vortex.

In fact, at the Reynolds numbers encountered in open channel flow, the horseshoe vortex system has become highly unsteady and its instantaneous structure may be very different from that described above. In common with researchers looking at the flow around aerofoils, Martinuzzi and Tropea (1993) found that there were two distinct modes of system behaviour, with switching occurring between the two modes at a low frequency unrelated to the Von Kármán shedding frequency. The features of this unsteady phenomenon will not be described in detail here but it is important to note that this process results in the creation of high

2.4 Turbulent flow around isolated obstacles

turbulent kinetic energy and turbulent stresses in the stagnation zone.

For bodies of sufficient height, i.e. $H_{bl}/W_{bl} > 1.5$, Baker (1980) found that the only factors influencing the horseshoe vortex system were the Reynolds number and the relative width of the body and the boundary layer (W_{bl}/δ^*), noting that as these factors increased, the primary stagnation point moves closer to the body. Importantly, he did not record any change in the vertical dimensions of the vortices with changing (W_{bl}/δ^*).

Spezzy and Bearman (1992) investigated the effects of the block aspect ratio H_{bl}/W_{bl} on the two-dimensionality of the flow around a circular cylinder mounted between two end plates. Focusing on the changing nature of the Von Kármán vortex shedding as opposed to the detailed interaction between it and the horseshoe vortex systems, they performed a set of experiments with a constant blockage ratio of $A_{bl}/A_{ch} = 7.7\%$ and a freestream turbulence level of $T_u < 0.05\%$. Although the experiments covered differing behaviours over a range of Reynolds numbers, only the results from the top of the range, i.e. at $Re = 1.3 \times 10^5$ are pertinent to our interests.

At this Reynolds number, for aspect ratios of approximately $H_{bl}/W_{bl} = 5$ and above, the fluctuating coefficient of lift (i.e. the spanwise force coefficient) at the centre of the cylinder height was found to be constant. Below this value, C_L increased towards a peak at approximately $H_{bl}/W_{bl} = 2.5$ before experiencing a large drop at values lower than this. At these lowest values of aspect ratio, the drop in lift coefficient is attributed to the near complete suppression of the vortex shedding. When considering the mean drag coefficient at the mid-height position, the value was again approximately constant for $H_{bl}/W_{bl} > 5$ and increased toward a peak for values below this. Putting the flow behaviour at very low aspect ratios to one side, the conclusion from this data is that the flow is more two-dimensional at lower aspect ratios. When the shedding cycle is in phase over the entire height of the cylinder, the fluctuating lift and the mean drag will be at their greatest. At high aspect ratios, small disturbances along the greater height of the cylinder disrupt the regular shedding cycle, and therefore weaken its long time averaged effects.

2.4.3 End Effects - Submerged Bluff Bodies

Baker (1980) performed his experiments on a submerged cylinder and defined $H_{bl}/W_{bl} = 1.5$ as a threshold of aspect ratio above which the position of the spanwise vortices in which the horseshoe vortex originates is stable. This insinuates that the flow passing over the top of the cylinder does not penetrate low enough into the wake to have an influence on the horseshoe vortex. This flow does however, have a significant effect on the Von Kármán vortices that are being formed around the shaft of the bluff body. According to the experimental work of Kawamura *et al.* (1984) and Kappler (2002), the end effects for such a cylinder change the vortex shedding system considerably. Suggesting the pattern shown in Figure 2.13, they claimed that for high aspect ratio cylinders, some degree of regular vortex shedding is preserved around the lower portion of the body, but for aspect ratios of 2 or less, vortex shedding is completely suppressed.

For the former case, the results of the Large Eddy Simulation (LES) of Fröhlich and Rodi (2004) are useful in demonstrating the complexities of the flow structure. The simulation mimics an experiment of Kappler (2002), in which the flow around a circular cylinder of $H_{bl}/W_{bl} = 2.5$ was measured. At this aspect ratio, a small region of vortex shedding is expected. The drag coefficient for a surface mounted cylinder is a function of the cylinder aspect ratio H_{bl}/W_{bl} , the cylinder width and boundary layer thickness ratio W_{bl}/δ^* , the freestream turbulence level T_u and the blockage ratio A_{bl}/A_{ch} . The experiment was performed in a water tunnel at a cylinder Reynolds number of 43,000, where $W_{bl}/\delta^* = 4$. By these measures, this flow is similar to that in which we are interested. The suppression of the freestream turbulence in the experiment to ($T_u = 2\%$) differs from the higher turbulence level that we might expect. Finally, the blockage ratio (A_{bl}/A_{ch}) in this case was 7.3%.

Both the experimental and numerical results revealed the following features of the flow. At the top of the cylinder, the flow separates from the top front edge rolling up into a system of spanwise orientated vortices and reattaching at approximately the centre of the top surface. At the rear edges, the separation is very

2.4 Turbulent flow around isolated obstacles

complex but results in two tip vortices, which reach downward into the wake. Immediately at the rear edge, these tip vortices form part of an arch vortex structure, which appears in the long time-averaged results and sits directly behind the cylinder.

Directly below the top rear edge, the tip vortices highly distort the flow separating around the shaft of the cylinder so that no regularity can be identified. Moving away from the top of the cylinder, the vortices being shed around the shaft become larger and more regular and as the position falls below ($z = 0.6$), occasional alternate eddy shedding behaviour can be observed.

Long time averages of the three-dimensional recirculation region directly behind the cylinder show that it is narrower at the top and widens out towards the bottom. In the lower regions, the pattern of Reynolds stresses nearly follows that of the 2D case in a qualitative sense, so that $\overline{(u'^2)}$ and $\overline{(u'v')}$ peak in the shear layers whilst $\overline{(v'^2)}$ and $\overline{(w'^2)}$ peak in the central region of the wake. However, the wake is wider than that measured in an analogous 2D case and the peak of $\overline{(v'^2)}$ is smaller in magnitude and slightly off-centre. Near the top, the similarity to the 2D case breaks down further and the magnitude of all of the normal stresses is lessened. As there is no shedding behaviour, the recirculation region is smaller.

Moving downstream of the recirculation zone, the vorticity associated with the tip vortices diminishes and disappears at approximately one diameter downstream of the cylinder, only to be replaced with streamwise orientated vorticity emanating from the downward flow over the top of the cylinder. These secondary currents peak in magnitude at $x = 2$ and then steadily decrease in strength. Examination of the eddies being shed from the shaft further downstream from the cylinder reveals that a distorted Von Kármán vortex street develops. However, the shedding of vortices is highly sporadic and the eddies are angled downwards as they are affected by the downward flow over the top of the cylinder. Finally, evidence of a small horseshoe vortex was also observed around the base of the cylinder.

Since this study was concerned with a circular cylinder, quantitative comparisons with the 2D case described above cannot be made. However, it has been

2.4 Turbulent flow around isolated obstacles

observed in experiments, e.g. Kawamura *et al.* (1984), that the drag coefficient reduces with the cylinder aspect ratio so that the influence of the flow over the top of the cylinder and the suppression of the regular vortex shedding mechanism acts to reduce the drag. It is therefore reasonable to assume that the wake structure described here will result in a lower relative drag coefficient than in the purely 2D case. In comparing their calculated values of drag coefficient with the results from previous experiments, Fröhlich and Rodi (2004) make the point that the final drag force exerted by the cylinder is strongly dependent on the blockage ratio.

As the aspect ratio of a submerged bluff body is reduced, the length over which shedding can take place is destroyed. The ultimate example of this is flow over a cube, which has been studied in detail by a number of researchers including Castro and Robins (1977), Schofield and Logan (1990), Martinuzzi and Tropea (1993) and Shah and Ferziger (1997). Using flow visualisations and static pressure measurements of flows at Reynolds numbers in the range of 8×10^5 to 1.2×10^6 and a low blockage ratio of 0.02, Martinuzzi and Tropea (1993) proposed the schematic shown in Figure 2.14 of the flow over a surface mounted cube.

In common with its taller counterpart, the cube causes the creation of a horseshoe vortex, although its influence on the downstream flow patterns must be proportionally greater. Again, the flow separates at the leading edges of the top of the cube and reattaches onto the top surface. Separation at the rear of the cube continues to result in an arch vortex structure with recirculation vortices with the same orientation. Figure 2.14 would seem to suggest that the axial velocity observed downstream of the cube emanates purely from the horseshoe vortex. This is disputed by others including (Schofield and Logan, 1990), who attribute the vorticity to a number of sources including a horseshoe vortex with its source in the recirculation region, i.e. the same conclusion drawn by Fröhlich and Rodi (2004) for the taller circular cylinder.

2.4.4 End Effects - Emergent Bluff Bodies

For large floodplain obstacles such as trees, perhaps the more significant scenario is that of the emergent bluff body, where there is no flow over the top but where the deformation of the free surface exerts its influence on the wake. Indeed, for shallow submerged obstacles, the influence of the free surface must also be included. Flow past surface-piercing bluff bodies has long been the domain of naval architects. Chaplin and Teigen (2003) conducted experiments on a smooth, surface piercing circular cylinder in a towing tank and compared their results to the existing experimental database in this field, including Hay (1947), Hseih (1964) and Hogben (1974). Of these, the only experimental set-up in which the cylinder was fixed to the channel bed was that of Hseih (1964).

When a free surface is introduced, the drag force exerted on the flow consists of three mechanisms. In addition to those elucidated above, i.e. friction drag and pressure drag, the generation of the surface wave must now also be considered. A general description of the surface of an open channel flowing around a bluff body is shown in figure 2.15. It is characterised by a positive slope of the water surface upstream of the obstacle, followed by a depression in water level downstream. As the Froude number increases, the amplitude of this wave increases until eventually, the entire rear face of the body is exposed to the air.

Chaplin and Teigen (2003) measured the pressure on the surface of a smooth circular cylinder being towed through a water tank at a constant speed by way of a ring of pressure taps inserted into the body of the cylinder. Pressure distributions at different relative depths were found by varying the water depth in the tank. Noting that no evidence of vortex shedding could be identified from the instantaneous pressure measurements, a time averaged value of pressure was found at each tap and these averaged values were integrated around the circumference of the cylinder to calculate sectional drag coefficients. By plotting these drag coefficients as a function of vertical position on the cylinder for a range of Froude numbers, the changing characteristics of the wake were highlighted.

2.4 Turbulent flow around isolated obstacles

At low Froude numbers ($Fr < 0.8$) C_D was almost constant across the depth at a value of approximately 0.95. In the range of ($0.8 < Fr < 1.4$) C_D was observed to increase with increasing vertical position, before sharply turning and falling to zero at the highest point of measurement. This effect was most exaggerated in critical flow, where the maximum value was 1.5. For higher Froude numbers, ($Fr > 1.4$) C_D again becomes constant throughout the depth but at a relatively low value of approximately 0.5.

Inoue *et al.* (1993) took more detailed measurements around a circular cylinder at $Fr = 0.8$ and 1.0 and were able to identify the changes that the presence of the free surface affected on the wake structure with more clarity. The generation of the free surface wave acts to attenuate the shedding of vortices from the cylinder near the surface, whilst the expected vortex shedding behaviour persists at greater depths. Kawamura *et al.* (2002) made further investigations of this flow type via LES and confirmed some of Inoue *et al.* (1993)'s results. The simulations, performed at a cylinder Reynolds number of 2.7×10^4 to match the experiments of Inoue *et al.* (1993), showed that the impact of the free surface on the wake structure was minimal at $Fr = 0.2$ and 0.5 but for $Fr = 0.8$, a noticeable impact was observed. No information on the blockage ratio or freestream turbulence level was attainable.

At the higher Froude number, they observed two strong counter-rotating vortices under the free surface downstream of the cylinder. These vortices acted to alter the vertical profile of the wake so that it was narrowed at a distance approximately 60% of the diameter of the cylinder under the free surface. Above and below this point, the wake became wider. It was concluded that an unstable shear layer exists under the free surface, in which the turbulent fluctuations of velocity are relatively small and random in nature. Deeper under the surface, the fluctuations become more periodic and more closely resemble those to be expected in the wake behind a continuous cylinder. This feature was attributed to the orientation of the separated shear layers, which are aligned straight in the downstream direction in the deep part of the flow but are deflected outwards near the free surface.

2.4 Turbulent flow around isolated obstacles

Consequently, the eddy street normally to be expected downstream of a cylinder is disrupted close to the surface.

Kawamura *et al.* (2002) calculated the total drag coefficient for their bluff body by integrating the stresses on the surface and were able to show a decreasing value of C_D with increasing Froude number so that with an increase in Froude number from 0.2 to 0.8, the drag coefficient dropped by 12%. This correlates well with the trend for the increase in free surface deformation to attenuate the vortex shedding.

2.4.5 Tandem Bluff Bodies

For the study of one-line vegetation at the floodplain edge, we are interested, not simply in the interaction between the compound channel flow and the wake behind a single bluff body but also in the interaction between neighbouring bodies. Since each subsequent body sits in the wake of the previous one, the drag force exerted by a row of vegetation at the floodplain edge will depend not only on the characteristics of the single block wake but also on the changes introduced to the tandem block relationship by its placement at this location.

s is defined as the distance between the body centres and the variable s/W_{bl} is the key determining factor for the structure of the flow around tandem bodies. Havel *et al.* (2001) provides a concise summary of the different flow regimes encountered by both tandem square blocks and tandem cubes, both drawing on the experimental work of previous researchers (Hangan and Vickery, 1999; Martinuzzi and Havel, 2000; Sakamoto and Haniu, 1988) and producing new experimental data. The new data was collected at a block Reynolds number of 2.2×10^4 and a freestream turbulence level of 1.5%. The square blocks had an aspect ratio of $H_{bl}/W_{bl} = 16$ and a blockage ratio of 6.5%. The cubes had a boundary layer thickness ratio of $W_{bl}/\delta^* = 14.3$ and a blockage ratio of less than 2%. The data of Hangan and Vickery (1999) was collected at a similarly low freestream turbulence level for a block of aspect ratio $H_{bl}/W_{bl} = 40$. The data of Sakamoto and Haniu (1988) was collected for a block of much smaller aspect ratio $H_{bl}/W_{bl} = 3$ and a

2.4 Turbulent flow around isolated obstacles

boundary layer thickness ratio of $W_{bl}/\delta^* = 1.25$. Since the block Reynolds number places these experiments in a lower Reynolds number regime than that which we might expect, these results are included as a qualitative guide to the regimes experienced by tandem blocks. Indeed, analogous experiments on circular cylinders have revealed similar flow regimes.

The first regime, found at the lowest values of s/W_{bl} is the 'one body' regime, where the flow separating from the upstream obstacle overshoots the downstream obstacle completely so that the tandem pair can be considered as one. Although this regime can be identified clearly for 2D cases, for the cubes, the flow entering the gap from the top means that this regime is unlikely to exist. For the blocks, the situation at such small spacings is unclear. The 'one body' regime is associated with a low drag coefficient for the upstream obstacle and a negative drag coefficient for its downstream partner.

As the spacing increases, the second regime, referred to as 'bistable' takes over. The title refers to two modes of shedding which occur in this spacing range for both 2D and 3D obstacles; either the shear layers from the first obstacle do not reattach to the second and low frequency shedding from the first obstacle occurs or the shear layers do reattach and the shedding takes place from the second obstacle with a higher frequency. For the 2D cases, the drag profiles described above persist until $s/W_{bl} \approx 2$, where both values dramatically increase due to the roll up of the upstream shear layers into the gap. For the 3D cases, this regime is associated with gradually decreasing drag coefficient on the upstream obstacle and increasing drag coefficient on the downstream obstacle since the reattachment position on the downstream obstacle is affected by the flow over the top.

The third regime, the 'lock-in' regime, describes the situation in which there is consistent shedding from the upstream obstacle at a single frequency but where the upstream shear layers roll up and attach onto the upstream face of the downstream obstacle. For the cube, the shedding occurs at the natural frequency of the gap. For the large aspect ratio block and 2D cases, it is less obvious that this is the case. The vortices being shed from the downstream obstacle have the same frequency as

2.4 Turbulent flow around isolated obstacles

those from the upstream obstacle, since the latter triggers the former. For the 3D cases, this regime is associated with the reduction of the upstream drag coefficient to its minimum value. The drag coefficient for the downstream obstacle continues to gradually increase.

Finally, the 'quasi-isolated' regime is reached, where the process of vortex formation is separated for the two obstacles. Despite this, the up- and downstream obstacles still have the same shedding frequency as the pressure fluctuations in the wake of the upstream obstacle are enough to trigger shedding from the downstream obstacle. In this regime, the shedding frequency gradually increases asymptotically, as do the drag coefficients for both of the obstacles. Eventually, for very large spacings ($s/W_{bl} > 12$) the shedding is completely decoupled.

2.4.6 Summary

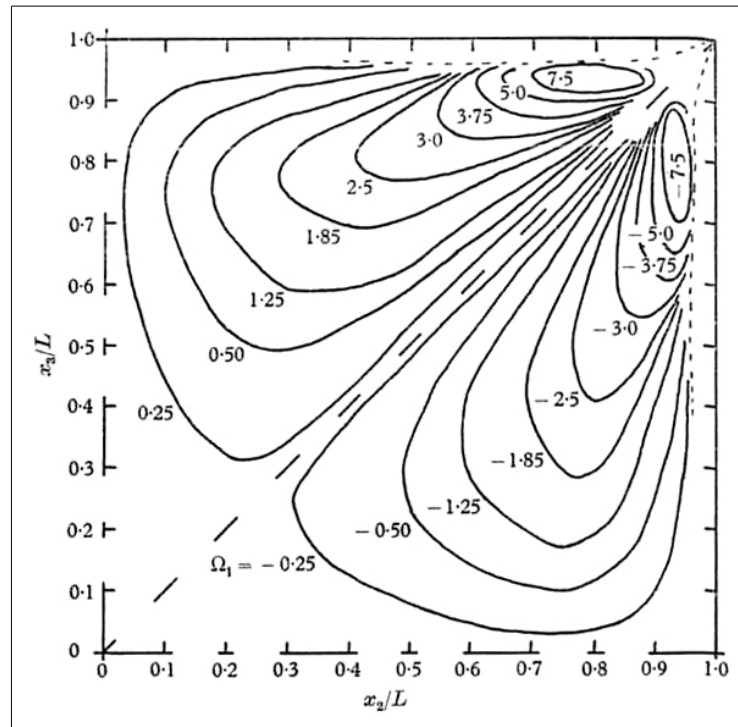
The large volume of work that has been done to understand the wake structures behind cylindrical bluff bodies belies the complexity of the flow scenario in question. Vitally however, it has clearly been shown that the environment into which a bluff body is introduced has a significant impact on the wake structure and therefore the drag force that the body exerts on the flow. Reynolds number, blockage ratio and freestream turbulence levels have been shown to quantitatively affect the size and strength of the wake and the speed of flow recovery but in addition, end effects from solid surface mounting, submergence and free surface interaction have all been shown to retard the vortex shedding phenomenon in various locations and thereby reduce the overall drag coefficient.

In the case of one-line vegetation at the floodplain edge, the location of the blocks in the strong shear layer between the main channel and floodplain may also alter the wake structure and therefore the overall drag coefficient.

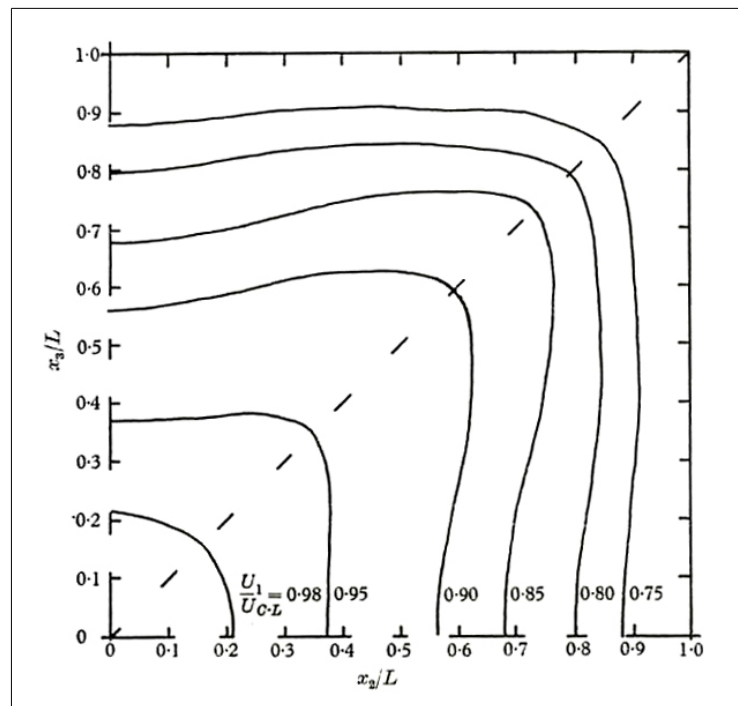
2.5 The Research Gap

A great deal of work has been done to understand the turbulent field in open channel flows and how it is affected by the introduction of areas of vegetation. Simultaneously, the intricate details of flow around individual bluff bodies has been studied, concentrating on simplified freestream conditions. This project will draw together these themes to investigate the following:

- The bulk changes in the wake structure around an identical cylindrical obstacle when moved from the centre of a symmetrical, open channel of simple cross-section to the floodplain edge of a compound, open channel, for both submerged and emergent (surface piercing) obstacles, and the resultant effects on the drag coefficient.
- The detailed structure of the mean and turbulent fields around submerged and surface piercing obstacles at the floodplain edge of a compound, open channel. Specifically, by what processes the changes identified in the bulk flow characteristics and the drag coefficient come about.
- How the structures and processes thus identified affect the flow patterns in the wider channel and how these are linked to the secondary circulation patterns observed by researchers such as Sun (2006).
- How the trends identified change with the changing geometry of the obstacle and how they are affected by the arrangement of multiple obstacles in a single line at the floodplain edge.



(a)



(b)

Figure 2.1: (a) contours of streamwise vorticity and (b) isovels in the top right quadrant of a square duct from Brundrett and Baines (1964)

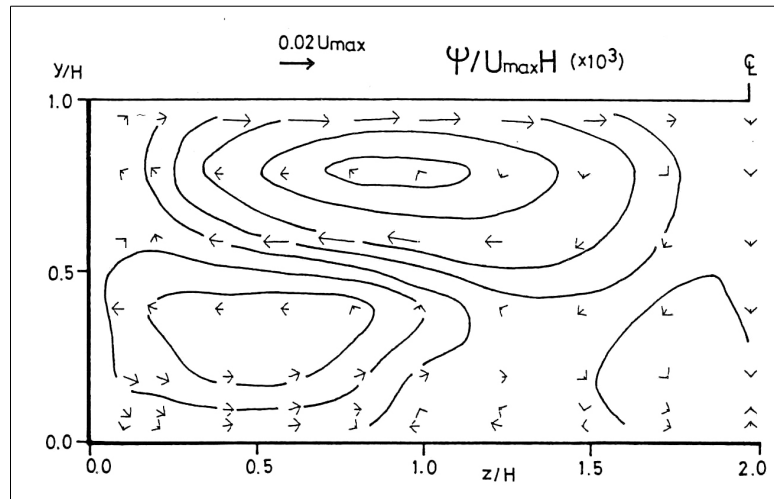


Figure 2.2: Isovells of streamwise velocity and vectors of secondary circulations in the left half of a rectangular channel of $AR = 3.94$, (Tominaga et al., 1989)

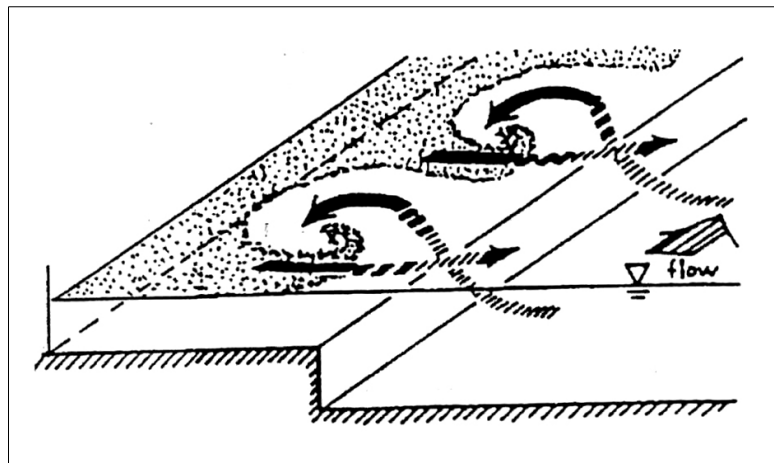
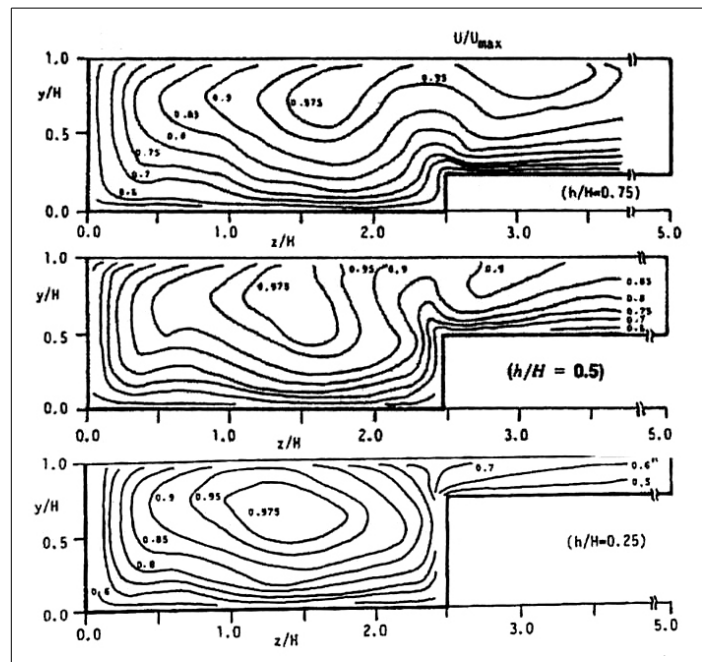
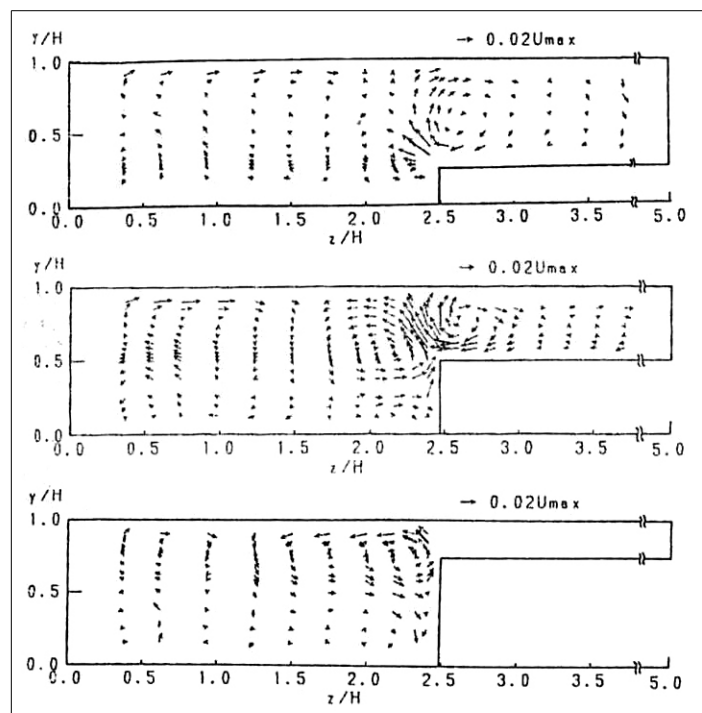


Figure 2.3: Schematic of vertically orientated vortices at the floodplain edge, (Fukuoka and Fujita, 1989)

2.5 The Research Gap



(a)



(b)

Figure 2.4: (a) Contours of streamwise velocity and (b) velocity vectors of secondary circulations from Tominaga and Nezu (1991)

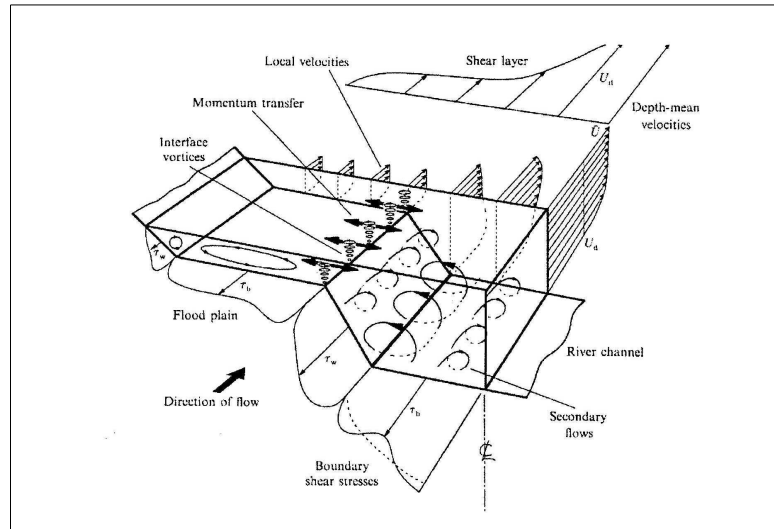


Figure 2.5: Schematic of flow in a straight, compound channel from Shiono and Knight (1991)

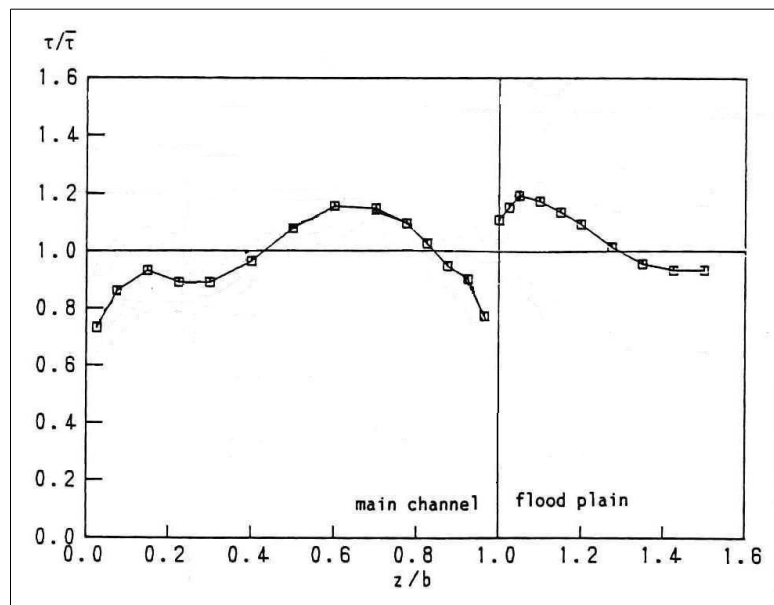


Figure 2.6: Distribution of Boundary Shear Stress in a compound channel with $D_r = 0.5$, adapted from Tominaga and Nezu (1991)

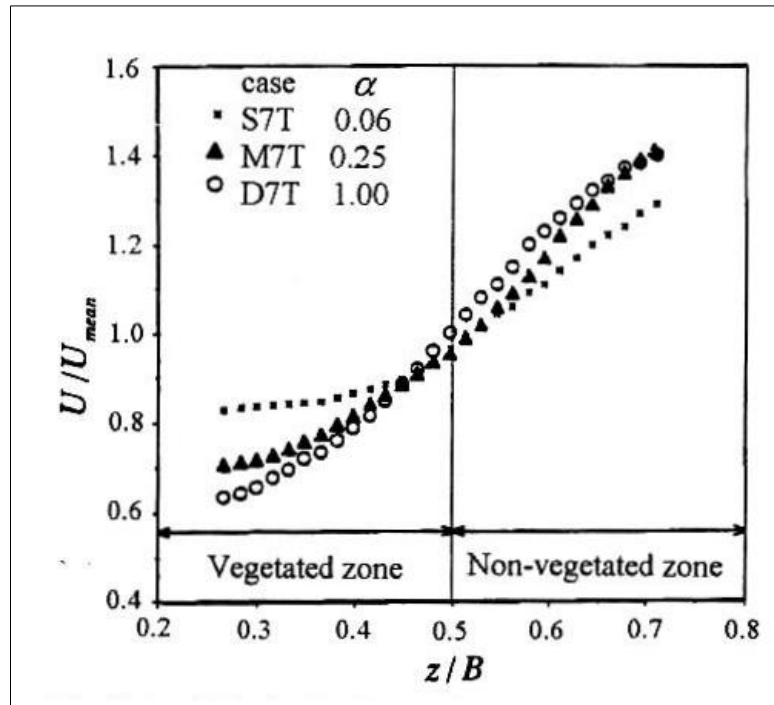


Figure 2.7: Spanwise variation of mean streamwise velocity across a partially vegetated channel, from Nezu and Onitsuka (2001). z/B is the spanwise position and α is the vegetation density.

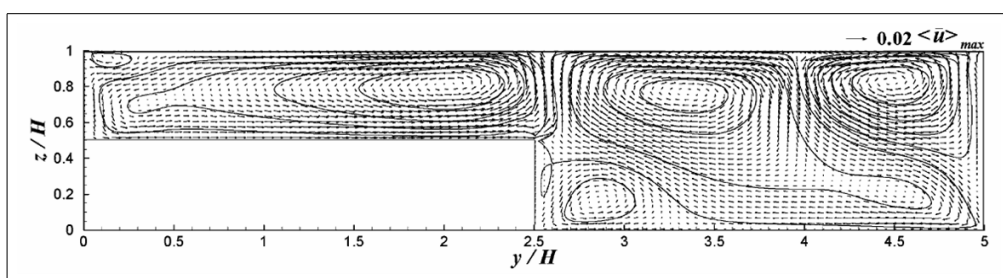


Figure 2.8: Secondary currents in a rectangular, compound channel with vegetated floodplain ($D_r = 0.5$, Vegetation density = 0.25m^{-1}), Kang and Choi (2006)

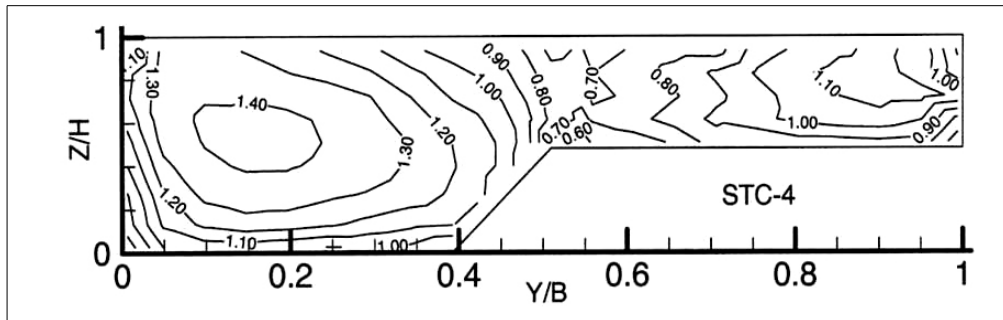


Figure 2.9: Contours of mean streamwise velocity, normalised with U_m , in a trapezoidal channel with one line of emergent blocks at the main channel/floodplain interface, Sun (2006)

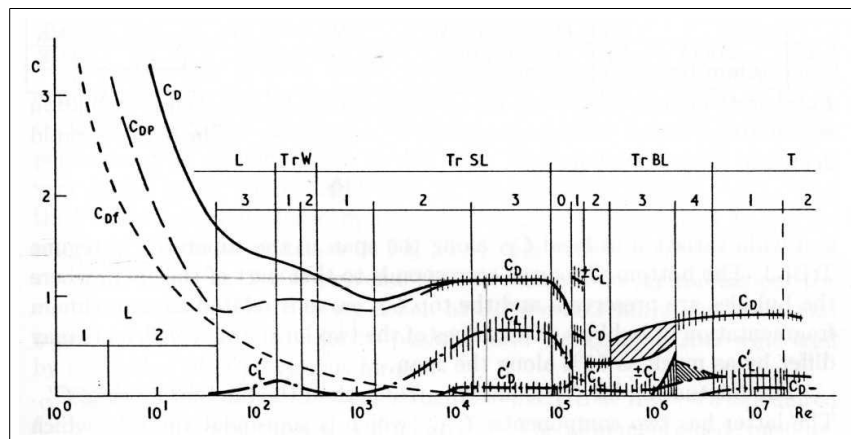


Figure 2.10: Variation of Drag Coefficient C_D with Reynolds number Re for a 2D circular cylinder in a uniform freestream with low turbulence, Zdravkovich (1997)

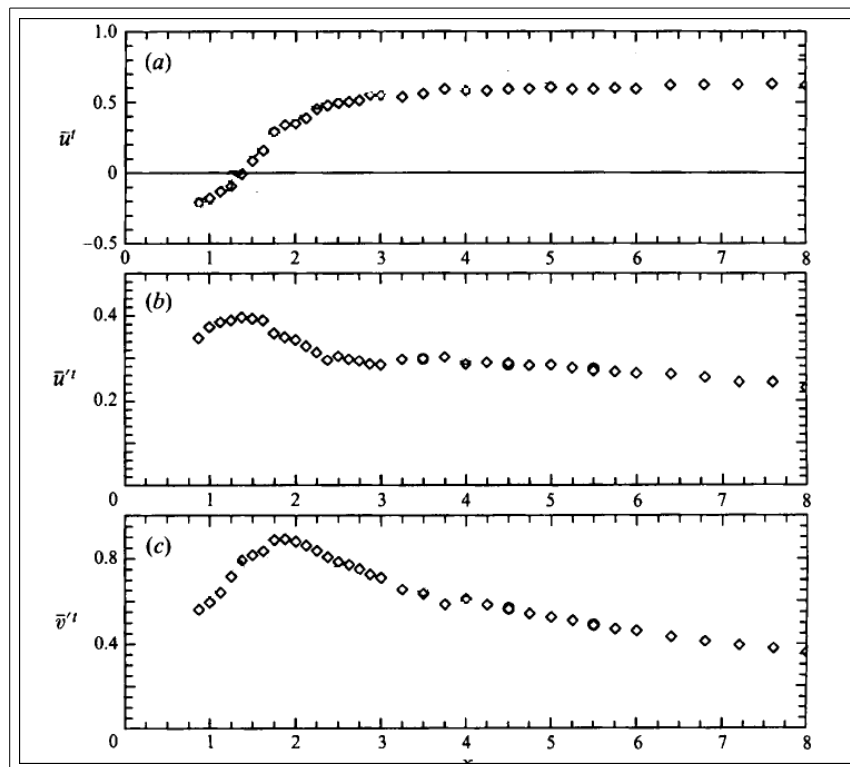


Figure 2.11: Streamwise variation of (a) Mean streamwise velocity, (b) streamwise turbulent intensity and (c) spanwise turbulent intensity on the centreline of the wake of a square 2D block, where all variables are normalised with U_m . Adapted from Lyn et al. (1995)

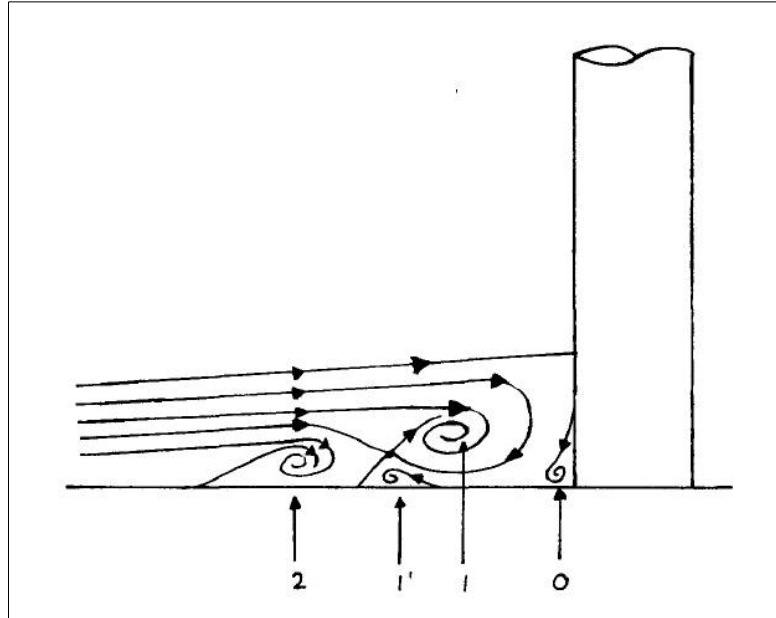


Figure 2.12: Spanwise orientated vortices upstream of a surface mounted circular cylinder, (Baker, 1980)

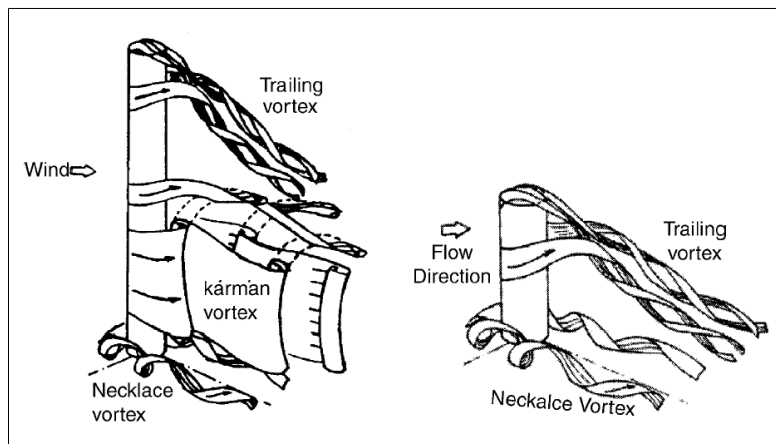


Figure 2.13: Flow fields around submerged circular cylinders, (Kawamura et al., 1984)

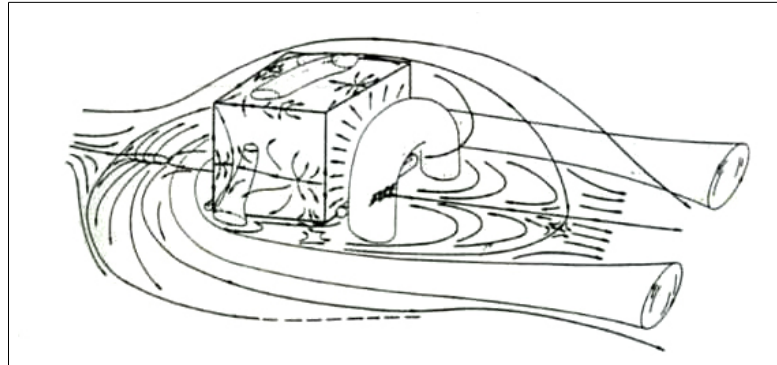


Figure 2.14: Schematic of flow around a surface mounted cube, (Martinuzzi and Tropea, 1993)

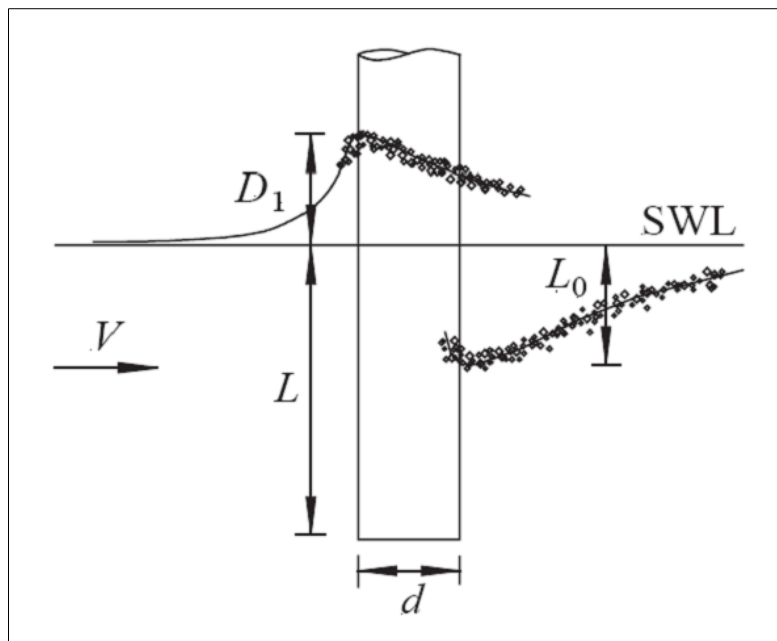


Figure 2.15: Schematic of flow around a surface piercing circular cylinder, (Chaplin and Teigen, 2003)

CHAPTER 3

Methodology

3.1 Physical Experiments

In order to test the hypothesis that the placement of a bluff body at the floodplain edge will influence the flow pattern around it and to provide data with which to verify the performance of the computational model, a series of physical experiments were performed in the flumes in the Loughborough University and Kansai University laboratories. This section will give details of how these experiments were carried out and an explanation of the experimental set-ups used.

In all sections, the following coordinate system will be applied; the origin for the streamwise axis is set at the centre of the furthest upstream block, for the spanwise axis at the block centre and for the vertical axis at the block base and all distances are normalised using the block width.

3.1.1 Loughborough Experiments

3.1.1.1 Experimental Equipment & Set-Up

Flow Environment All of the experiments detailed here were performed in the large flume in the hydraulics laboratory at Loughborough University. Figure 3.1 shows a plan view of the flume and a simple schematic of its cross sectional geometry.

3.1 Physical Experiments

The flume is lined with slate, has a length (L_{ch}) of 8.6m, a width of 0.917m and is flat bottomed. At the upstream end of the flume (at the top of the photograph in Figure 3.1), there is a stilling tank and a bank of plastic tubing, designed to straighten the flow before it enters the flume. At the downstream end, an adjustable gate allows for control of the water depth. Into this flume, a wooden bed has been inserted to create a bed slope and on top of this, a wooden step has been placed to create a compound cross-section. The wooden surfaces are either varnished or finished with a waterproof coating and can be considered as hydraulically smooth. As shown in Figure 3.1, the step has a width (W_{fl}) of 0.370m and a height (H_{fl}) of 0.150m. Although it was attempted to achieve a bed slope of 1×10^{-3} , the inaccuracies involved in construction with wood meant that achieving this exact figure was impossible. After construction, a detailed channel survey was therefore carried out using a theodolite in order to accurately calculate the relevant bed slopes. The results of this survey are depicted in Figure 3.2. The results for the main channel bed and floodplain bed are shown separately. The average bed slope at the centre of the main channel over the entire length of the channel is calculated to be 1.389×10^{-3} , whilst that of the floodplain centre is 1.282×10^{-3} .

Depth and level measurements made whilst the flume was running were performed with a point gauge, mounted on a millimetre scaled measure. Flow measurement was achieved using a stopwatch and a weigh tank, which was integral to the flume set-up.

Acoustic Doppler Velocimetry The acoustic doppler velocimeter (ADV) was used to measure the instantaneous velocity of the flow. Capturing this information over time allows for the calculation of statistical data such as mean velocities, turbulent intensities and Reynolds stresses. Where data quality is good, the ADV signal can also be analysed to extract the dominant frequencies of the local turbulence and identify any periodicity in the turbulent field. The ADV is a simple and robust piece of equipment, the use of which does not entail the extensive health and safety precautions associated with its main alternative, the laser doppler velocimeter (LDV).

3.1 Physical Experiments

Short pulses of sound are emitted by a transmitting transducer and are reflected from small particles being carried by the flow. Four receiving transducers pick up these reflected pulses and by measuring the change in frequency from the original pulse, the velocity of the particles, and therefore of the flow can be calculated. There are a number of constraints associated with its use, not least the fact that the acoustic transducers (shown in Figure 3.3(a) as the blue areas) must be submerged in the water whilst measurement is taking place. The ADV model used in this case is the Nortek Vectrino, which has a single transmitting transducer in its centre and four receiving transducers. Each receiving transducer measures velocity parallel to its beam and simple trigonometry is used to convert these measurements into the three Cartesian directions. For this model, the measurement volume is located 50mm below the transmitting transducer head. This has the obvious implication that velocities in the top 50mm of the flow cannot be directly measured.

The ability of the ADV to accurately measure the streamwise, spanwise and vertical velocity components is crucially dependent on the probe head's correct alignment to the flow. Although it is acknowledged that even the small variations in the construction of the flume and the rails along which the ADV was mounted can contribute significantly to the misalignment of the probe, preparations were made to minimise and standardise the error. As a first step and whilst the compound channel section was still to be constructed, a test was performed to choose a standard yaw angle, i.e. rotation with respect to the vertical axis. The probe was mounted at a chainage of 4.06m from the inlet, at the spanwise and vertical central positions of a flow of depth 0.266m . Although fully developed flow conditions would be required to ensure that the spanwise mean velocity component at the channel centre is exactly zero, this position offered the closest reproduction of these conditions that could be achieved with the available flume set-up. The spanwise mean velocity was then measured for a range of yaw angles between -2° and $+2^\circ$, where a negative rotation is towards the left bank and a positive rotation is towards the right bank. Two sets of results were taken and the average of these is plotted in Figure 3.4.

3.1 Physical Experiments

Fitting a linear relation to this data suggested that a yaw angle of -0.22° was suitable for the alignment of the probe with the flow in the flume. In practical terms, the measurement of such a small angle was difficult but despite this, an attempt was made to measure and mark this yaw position on the ADV mounting. Although not as influential on the final results as the yaw angle, both the pitch and roll angles, i.e. rotation about the spanwise and streamwise axes respectively, were also both investigated. Since the orientation of the ADV mounting was fixed, these angles could not be changed so that an investigation of the type described above was impossible. Instead, the discrepancies between the orientation of the probe and the channel bed were measured using a plumb line, spirit level and micrometer. Doing this at the location at which the blocks were to be placed, resulted in a pitch angle correction of $+0.942^\circ$ and a roll angle correction of -0.286° . These were applied to the measured data through the processing software accompanying the ADV.

Despite these precautions, later comparison of the experimental results with numerical simulations revealed that further corrections to these angles were necessary. For each experiment, the final rotation angles applied to the data taken by the ADV were chosen in order to provide a realistic fit between the contours of the streamwise velocity, which are largely insensitive to the small changes in rotation angle and the secondary circulation pattern. The rotation angles chosen as a result of this process are shown in Table 3.1.

During measurement, the accuracy of the data retrieved with an ADV is maximised through the control of two factors; the signal-to-noise ratio (SNR) and the correlation score. Previous work comparing the performance of the Nortek Vectrino (Rusello *et al.*, 2006; Voulgaris and Trowbridge, 1998) to non-invasive velocimetry techniques such as PIV found a maximum error of 4% in the streamwise velocity measurement between the two systems, provided that appropriate minimum values of SNR and correlation were maintained for each measurement.

Monitoring of the signal-to-noise ratio allows the user to ensure that the strength of the signal received by the transducers in reflection from moving particles is suf-

3.1 Physical Experiments

Table 3.1: Rotation Angles ($^{\circ}$) applied to the velocity vectors measured with the ADV

Series	Case	Heading ($^{\circ}$)	Pitch ($^{\circ}$)
1	I	-1.5	1.0
1	II	2.5	1.0
1	III	0.5	1.0
2	I	-1.0	0.0
2	II	-0.75	+0.25

ficiently large in comparison with the background noise. Since the ADV measures not the velocity of the water itself but rather the velocity of small particles being conveyed by the water, the SNR may drop if the number of such particles is too low. However, the SNR is also dependent on the nominal velocity range setting, which will be discussed below. The SNR value is calculated using equation 3.1. In order to maintain the accuracy quoted by Rusello *et al.* (2006), a minimum value of 19.5 was applied to the collection of data here.

$$SNR = 20 \log \left(\frac{Amplitude_{Signal+Noise}}{Amplitude_{Noise}} \right) \quad (3.1)$$

The correlation score gives an indication of the correlation of successive measurements. Rusello *et al.* (2006) quote the recommended minimum value of correlation in order to maintain accuracy to be 70% and this figure has been applied here.

In order to maintain the SNR and correlation scores for each measurement point such that the accuracy of the collected data was maximised, the ADV settings were carefully chosen, as follows:

- Recording Period (T) - Sun (2006) successfully used the same ADV equipment to record velocities in the same flume. Having performed sensitivity tests at a single measurement station to ascertain the minimum recording

period necessary to achieve a constant mean velocity reading, a period of 2 minutes was chosen. In this study, where the flow around the bluff bodies may include periodic vortex shedding, it was also necessary to confirm that this recording period was significantly longer than the shedding period of the body. Based on the work of Lyn *et al.* (1995), who took detailed measurements of the wake behind a two-dimensional square bluff body, a Strouhal number of 0.13 was assumed to be the order of that expected. Based on this assumption and a resultant shedding period of the order of a second, the two minute recording period is sufficient.

- Nominal Velocity Range (*VR*) - The nominal velocity range should be set to cover all of the anticipated velocities that are to be measured and is used to set the time lag between acoustic pulses. A low velocity range is equivalent to a longer time lag. Rusello *et al.* (2006) state that the setting of an excessively low velocity range leads to the decorrelation of successive measurements. Alternatively, an excessively high velocity range introduces considerable noise into the measurement, which emanates from the ADV circuitry. Rusello *et al.* recommend that "selecting the lowest velocity range applicable to a flow is generally the best option".

In order to test which velocity range would be most appropriate in this scenario, the setting was tested at two locations: in the main channel, where the highest velocity might be expected and directly behind the block, where the lowest velocity is expected. The position in the main channel was set so that measuring volume was 38.5mm from the floodplain bed and that $x = -5.53$ and $y = -9.43$. The position behind the block was set at the same vertical position but such that $x = 1.3$ and $y = 0.04$. The remaining ADV parameters were set to the following values: $T = 2\text{min}$, $f_{sa} = 200\text{Hz}$, $HSV = 2.5\text{mm}$, $LT = 1.8\text{mm}$. Data was then gathered at the following velocity ranges in the two positions: $\pm 0.03\text{m/s}$, $\pm 0.1\text{m/s}$, $\pm 0.3\text{m/s}$, $\pm 1\text{m/s}$, $\pm 2.5\text{m/s}$ and $\pm 4\text{m/s}$.

Figure 3.5 shows the mean streamwise velocity, turbulent kinetic energy and $\overline{u'v'}$ Reynolds shear stress results plotted against the velocity ranges for the main channel and behind the block positions respectively. The results for the remaining Reynolds shear stresses were similar to those for $\overline{u'v'}$ and have been omitted for brevity. All of the data was filtered using the criterion stated above, where low quality data points were removed from the series.

From an examination of the plots for the mean streamwise velocity, it is clear that both in the main channel and behind the block, the results at the two lowest velocity ranges are significantly different from those at the higher values. Following the advice that the lowest suitable velocity range should be chosen, this would suggest that the $\pm 0.3\text{m/s}$ range is the correct choice. The results for the turbulent kinetic energy are similar so that the results at the lowest two ranges suggest that they should be ruled out. For the $\overline{u'v'}$ Reynolds shear stress component, the pattern of variation is different between the two positions. In the main channel, the Reynolds stress is nearly constant up to and including at the $\pm 1\text{m/s}$ range. Behind the block, the $\pm 0.1\text{m/s}$, $\pm 1\text{m/s}$ and $\pm 2.5\text{m/s}$ ranges seem to give a consistent result. This pattern is mimicked in the other two components of the Reynolds shear stress. Instead of choosing the $\pm 0.3\text{m/s}$ range therefore, the experiments were carried out using the $\pm 1\text{m/s}$ range.

When the experimental data was processed, there were a number of locations, mainly in the block wakes on the floodplain, where the chosen velocity range appeared to be too high, introducing a high level of noise into the data set. At these stations, after filtering the data with the usual limit, two bands of erroneous data points were left. An example of this is shown in Figure 3.6 for the measurement point at $x = 3.5$ and $y = 1.86$ in Series 1, Case I. In order to remove this noise from the data, the maximum value limit was adjusted for each measurement point in turn.

3.1 Physical Experiments

- Sampling Rate (f_{sa}) - Based on a review of other authors work and an examination of the dominant turbulent frequencies in compound open channel flow in the Loughborough flume, Sun (2006) concluded that nearly all of the turbulent intensity is captured by using a sampling frequency of 50Hz. Assuming a Strouhal number of 0.13, this would equate to at least 29 readings per shedding period for the experiments in question.

Taking these basic facts into account however, a test was performed to find the optimum sampling frequency for use in this scenario. Intuitively, the measurement station directly behind the bluff body is a location at which the collection of good quality data is challenging and it was therefore at this position that the test was performed. Setting all of the other parameters to the final values described in their respective sections ($T = 2min$, $VR = \pm 1m/s$, $HSV = 2.5mm$, $LT = 1.8mm$) a set of velocity data was measured at a range of different sampling rates: 25, 50, 75, 100 and 200Hz. The resulting data sets were filtered using linear interpolation and the resulting data sets are shown in Figure 3.7, where U_x , U_y and U_z are the velocities in the stream-wise, spanwise and vertical directions respectively.

A visual inspection of the results quickly reveals that the data gathered at the higher frequencies of 75, 100 and 200Hz was of a poorer quality than that gathered at the lower frequencies. Details of the results at 50Hz and 25Hz are shown in Table 3.2. Although the mean velocity results are very similar between these two frequencies, it is clear that the turbulent kinetic energy results are significantly higher for the 50Hz case. This is an indication that the higher sampling frequency allows the user to pick up more of the turbulence spectrum than the lower frequency. The choice of sampling frequency is therefore a compromise between the proportion of the turbulent spectrum included and the overall quality of the data. As such, the 50Hz sampling frequency was chosen.

3.1 Physical Experiments

Table 3.2: Velocity statistics at sampling frequencies of 25 and 50Hz

f_{sa} [Hz]	U [cm/s]	V [cm/s]	W [cm/s]	K [cm ² /s ²]	$\overline{u'v'}$ [cm ² /s ²]	$\overline{u'w'}$ [cm ² /s ²]	$\overline{v'w'}$ [cm ² /s ²]
50	-16.12	-3.72	0.68	623.97	51.08	-9.87	-25.44
25	-16.59	-4.46	0.87	386.52	-39.51	-17.41	-20.64

- Height of Sampling Volume (*HSV*) - The sampling volume in which the ADV measures is set to be a block of diameter 6mm. The user can choose to define the height of the sampling volume however. In this case, the value of 2.5mm, taken by Sun (2006), has been applied in all cases.
- Transmitting Length (*LT*) - The transmitting length was uniformly set to 1.8mm.

In post-processing, the quality of the data can be further optimised by filtering the data sets according to two further parameters:

- Acceleration - This parameter allows the user to exclude a data point on the basis of the scale of difference between it and its neighbours. A limiting value of 3 times the gravitational acceleration was chosen as a standard here.
- Velocity - A velocity limit can be imposed on the data set to exclude outlying data points. This limit is expressed as a multiple of the standard deviation of the data. A limit of 3 times the standard deviation was generally chosen. However, for some data series, where excessive noise in the data caused by the operation of the ADV was required to be excluded, this limit was varied.

Flow Development Having chosen the settings with which to proceed, a further preliminary test was performed before commencing the experiment proper. Using a single header tank for both floodplain and main channel and at 8.6m in length,

3.1 Physical Experiments

recent work by Bousmar *et al.* (2005) suggests that the Loughborough flume may be too short in which to establish fully developed compound channel flow. Fully developed compound channel flow is characterised by a velocity gradient between the floodplain and main channel. The distinctive pattern of both streamwise and vertically orientated vortices that has been repeatedly observed at the floodplain edge is intrinsically linked to this velocity gradient and as such, the degree of development at the block test location was of vital interest.

Where a single header tank is used for both main channel and floodplain and the flow is entering both sections at a uniform velocity, it has been claimed that a significant downstream length is required in which momentum is transferred from the floodplain to the main channel, thus establishing the appropriate velocity gradient. A test was therefore devised to check whether the insertion of a board across the floodplain inlet would increase the rate at which a fully developed flow was obtained by reducing the velocity of the flow on the floodplain at the inlet. Figure 3.8 shows both configurations: (a) with the board and (b) without it.

Having chosen the position of the block to be at $CH6.95m$, the gradient of the water surface was calculated at the centre of the floodplain over the distance $CH4.25m$ to $CH7.25m$. The 'with board' case was tested first of all and using the downstream gate as a control, a water surface gradient of 1.333×10^{-3} was achieved with a total flow rate of $0.109m^3/s$. This results in a 3.9% difference between the gradient of the floodplain bed and the water surface and the flow is therefore considered to be uniform. The relative depth of this set-up is 0.472. In practice, the accuracy of the water surface gradient measurement is limited because of the scale of the depth probe in relation to the size of the change in depth over the length of the channel and also because of the unsteady nature of the water surface. For the experiments themselves, the methodology with regards to flow uniformity will be discussed below. In this preliminary stage, the flow and gate settings were kept constant for both the 'with board' and 'without board' cases. The ADV was set up with the following settings: $T = 2min$, $f_{sa} = 200Hz$, $VR = \pm 1m/s$, $HSV = 7.0mm$, $LT = 1.8mm$. A traverse of measurement was then undertaken

at a depth of $0.01m$ from the floodplain bed at chainages $1.25m$, $3.25m$, $5.25m$ and $7.25m$ for both cases. Figure 3.9 shows a comparison of the development of the mean streamwise velocity over the length of the flume, where the floodplain data is displayed on the left of each graph and the main channel data on the right, delineated by the vertical dashed line. The velocity is shown normalised with the bulk mean velocity and the lateral position is expressed as a proportion of the total channel width.

For the 'with board' case, it is clear from the results at $CH1.25m$ that there is a reversal of the flow on the floodplain immediately downstream of the inlet. At the positions further downstream, a clear velocity gradient can be observed between the floodplain and the main channel such that at $CH7.25m$, the velocity on the floodplain is approximately 57% of that in the main channel.

For the 'without board' case, the velocity at the first chainage position is approximately uniform across the section. At the downstream positions, a velocity gradient is seen to develop such that the floodplain velocity is approximately 95% of the main channel velocity. Although the velocity gradient is smaller in comparison with the 'with board' case, it is also observed that a large dip in velocity occurs at the floodplain edge.

Based on the observations of Tominaga and Nezu (1991), amongst others, on compound channel flow at a relative depth of 0.5, the presence of the large dip in velocity at the floodplain edge in the 'without board' case would tend to suggest that this is the flow that is closer to the fully developed scenario, despite the smaller velocity gradient. Inspection of the mean spanwise velocity data for the 'with board' case suggests that even at the furthest downstream position, fluid is moving from the floodplain into the main channel. It is likely therefore that although the pace of change in the data is slowing, the artificially lowered floodplain velocity is increasing, whilst the heightened main channel velocity is slowing. There is certainly no evidence to suggest that the characteristic secondary currents associated with fully developed flow of this type have begun to establish themselves. In fact, the 'with board' case could be interpreted as an exacerbation of the

problem, rather than an improvement.

Based on these observations, the experiments have been performed without the board at the inlet. It is, however, acknowledged that the flow at the block position is not likely to be fully developed since the velocity gradient is low. For most of the cases detailed below therefore, an upstream cross-section of velocity data has been gathered for use as boundary conditions in the numerical model. It is hoped that having achieved a good calibration of the model with these experimental results, the modelling results for a fully developed flow can be usefully analysed.

3.1.1.2 Experimental Series - Set-Up Details

Series 1 - Multiple Small Aspect Ratio Blocks In actual fact, a first set of experiments were performed before all of the preliminary steps outlined above had been completed. These tests were designed to test the central hypothesis using the materials immediately available, before proceeding to more detailed measurements. In these tests, a series of 5 concrete blocks of width $0.06m$ and of low aspect ratio (1.67) were placed along the floodplain edge, with the first block centre placed at a chainage of $4.25m$ and the subsequent blocks placed at a centre-to-centre spacing of $12W_{bl}$. The flume inlet was set up without the board, but in this case, the floodplain section did not start until a chainage of $1.50m$. A sampling frequency of $200Hz$ and a sampling volume height of $7mm$ were used.

The spacing of $12W_{bl}$ is based on the work of Havel *et al.* (2001), who both collated the work of other researchers and performed experiments around submerged sharp-edged bodies in tandem, in an attempt to define the spacings at which transition from one flow regime to the next occurs. According to their work, this spacing is the minimum spacing at which the shedding processes of two tandem bodies are completely independent. Since vortex shedding is a dominant factor in determining the drag force created by the presence of a bluff body, the independence of the shedding mechanisms is an important factor.

The set-up of the flume at the inlet for this series of experiments can be seen in Figure 3.1(a), which was taken before the floodplain section was extended to

3.1 Physical Experiments

the inlet. The abrupt change in cross-sectional geometry occurring at the start of the floodplain section means that the nearly developed flow described in the previous section for the 'without board' case does not exist in this case. However, measurements have been taken around the fourth block in the five block series and it is assumed that the flow is sufficiently developed due to the influence of the upstream blocks for measurements to be useful. Uniform flow conditions were attained between $CH4.25m$ and $CH7.25m$, although the uncertainty arising from the unsteady movement of the water surface and the coarse scale of the depth probe remain problematic.

In total, three sets of experiments were carried out within this series, the details of which are shown, together with the details of all the experiments performed, in Table 3.3. If a parameter value is missing from Table 3.3, this implies that the data is inapplicable or unavailable. For the emergent cases, it is suffice to say that the block height was significantly larger than the water depth. In order to define a block aspect ratio for these cases therefore, the suitable measure is the floodplain depth divided by the block width (D_{fl}/W_{bl}) or the total water depth divided by the block width for the simple channel cases (D_{ch}/W_{bl}). For the submerged cases, the block aspect ratio is equal to the block height divided by the block width (H_{bl}/W_{bl}).

3.1 Physical Experiments

Series/Case	Multiple blocks						Single blocks					
	S1CI	S1CII	S1CIII	S2CI	S2CII	S2CIII	S4CI	S4CII	S4CIII	S4CIV		
<i>Location</i>	Loughborough	Loughborough	Loughborough	Loughborough	Loughborough	Loughborough	Kansai	Kansai	Kansai	Kansai		
<i>Shape</i>	Compound	Compound	Compound	Compound	Compound	Compound	Compound	Compound	Simple	Simple		
<i>Status</i>	Submerged	Emergent	Submerged	Emergent	Submerged	Emergent	Emergent	Submerged	Emergent	Submerged		
$Q(m^3/s)$	0.172	0.066	0.130	0.109	0.109	0.0308	0.0308	0.0302	0.021	0.020		
$D_{ch}(m)$	0.360	0.227	0.298	0.283	0.293	0.154	0.154	0.151	0.075	0.074		
Re_{ch}	573,083	394,900	545,918	488,503	467,549	261,278	261,278	260,880	263,435	263,612		
Re_{bl}	37,497	25,839	35,720	20,243	19,375	9,929	9,929	9,913	10,011	10,017		
Fr_{ch}	0.333	0.289	0.348	0.320	0.301	0.425	0.425	0.428	0.613	0.621		
Fr_{bl}	0.815	0.561	0.776	0.873	0.835	1.210	1.210	1.209	1.220	1.221		
$T_u(\%)$	-	-	-	7.58	8.33	-	-	-	-	-		
$B(\%)$	1.667	2.035	2.013	1.786	1.232	2.259	2.259	1.519	3.800	2.457		
$I_e(10^{-3})$	1.389	1.389	1.389	1.389	1.389	0.650	0.650	0.836	1.250	1.644		
AR_{bl}	1.667	1.283	1.667	3.500	2.500	3.795	3.795	2.500	3.960	2.500		
AR_{ch}	2.547	4.040	3.077	3.222	3.130	3.245	3.245	3.300	6.645	6.806		
D_r	0.583	0.339	0.497	0.470	0.488	0.468	0.468	0.459	-	-		
W_{fl}/W_{ch}	0.399	0.399	0.399	0.399	0.399	0.400	0.400	0.400	-	-		
H_{bl}/D_{fl}	0.476	1.000	0.676	1.000	0.664	1.000	1.000	0.682	-	-		
H_{bl}/D_{ch}	-	-	-	-	-	-	-	-	1.000	0.647		
s/W_{bl}	12	12	12	-	-	-	-	-	-	-		

Table 3.3: Experimental Conditions

Figure 3.10 shows the streamwise measurement positions, stations $S1 - S4$, and their positions relative to the fourth block, which is shaded in grey. Station 1 is located at $x = -3.5$, Station 2 is located at $x = 0.0$, Station 3 is located at $x = +3.5$ and Station 4 is located at $x = +6.0$. The channel was traversed with the ADV at each of these cross-sections at a vertical position of $0.03m$ above the floodplain bed, i.e. $z = +0.5$. In the spanwise direction, the lateral spacing of the measurement points was $0.83W_{bl}$ in the outer regions of the flow. Within a region centred on the block of width and length $3W_{bl}$, the spacing was reduced to $0.25W_{bl}$. This area is shown with the dotted outline in Figure 3.10(b).

Series 2 - Single Large Aspect Ratio Blocks The second series of experiments was designed to fulfil the central aim of collecting detailed flow data around a single bluff body at the floodplain edge and examining the structure of the wake. Two cases were pursued: Case I with an emergent block and Case II, with a submerged block. In both cases, a single square sectioned aluminium block of width $W_{bl} = 0.038m$ was placed at $CH6.95m$ exactly at the edge of the floodplain. Since practicality excluded the obtaining of exactly uniform flow in the flume, the same flow ($Q = 0.109m^3/s$) and downstream boundary conditions were applied for all tests as were set-up for the flow development tests described in Section 3.1.1.1. The pertinent flow details are shown in Table 3.3 for both cases. The water depth used to determine the channel Reynolds number and Froude number was measured at $CH4.25m$.

The choice of flow geometry was a compromise between the block aspect ratio and the relative depth. For wall mounted submerged circular blocks, Kawamura *et al.* (1984) reported that for block aspect ratios at or below 2, regular vortex shedding is largely suppressed. In order to study the flow around blocks in which some regular shedding might be expected, it was therefore decided to maintain the block aspect ratios above this figure. The larger the block aspect ratio however, the larger the relative depth. Knight and Shiono (1996) maintain that the interaction between main channel and floodplain is greatest at relative depths of between 0.1

3.1 Physical Experiments

and 0.3. Although the creation of such low values was impossible, the relative depth was minimised and as such, all subsequent values are less than 0.5.

In each case, two sets of measurements were made: firstly, a horizontal surface of data at a height of $1.0W_{bl}$ from the floodplain bed and secondly, a cross-section of data at $x = 2.7$. Remote from the block, a spanwise measurement spacing of $1.184W_{bl}$ was used, whereas in a region defined by $-1.145 < y < 1.224$ a spanwise measurement spacing of $0.237W_{bl}$ was applied. For the horizontal surface, 7 traverses were made in the wake. For the cross section in Case I, 8 traverses were performed. The measurement points are shown in Figures 3.11 to 3.14, where grey circles represent measured points and black circles are assumed, extrapolated or interpolated data points.

In addition to these measurements points, a cross-section of data was also gathered upstream of the block at $x = -5.5$ for each case. The data from this cross-section, taken at a point assumed to be upstream of the area of influence of the block, was gathered in order to be put to use as upstream boundary conditions for any numerical simulation of the experiments. Since it cannot be assumed that fully developed uniform flow conditions were achieved, the availability of these upstream conditions will allow for a sensitivity analysis to be performed with the model. Since for each case, the horizontal plane of data was measured on a different occasion to the downstream cross-section, the velocity profile at this upstream station was used as an additional check on the similarity of the flows. A full cross-section of data was gathered upstream on the occasion of measuring the data in the horizontal plane, whilst a single traverse of data at a depth of $z = 1.579$ was measured when the flow was set up for the cross-sectional measurements. For Case I, the maximum difference between the mean streamwise velocities was 2.8%, whilst the average was 1.2%. For Case II, the maximum difference between the mean streamwise velocities was 3.4%, whilst the average was 1.5%.

3.1.2 Kansai Experiments

A second set of physical experiments was carried out in the hydraulics laboratory at Kansai University. Having established with the ADV data that the structure of the bluff body wakes at the floodplain edge is altered from that in a simple channel, the measurements in Kansai were carried out with the aim of measuring the drag coefficient of equivalent blocks in simple and compound channels. To this end, three values were measured from which the drag coefficient is calculated indirectly, namely the velocity, free surface position and boundary shear stress. As the large water depth in the Loughborough flume made the measurement of the boundary shear stress excessively difficult, the calculation of drag coefficient for the cases measured there was not possible.

3.1.2.1 Experimental Equipment & Set-Up

Flow Environment The flume in the Kansai laboratory is shown in Figure 3.15, which shows a photograph of the flume taken looking downstream from near the inlet and a simple schematic of its cross sectional geometry.

Unlike the large flume in the Loughborough laboratory, the Kansai flume is mounted in a frame, lifting it to eye level and allowing the user to easily adjust the slope of the base of the channel via three jacks at the upstream, central and downstream positions respectively. The flume is constructed from glass and is $14m$ in length (L_{ch}) and $0.5m$ wide (W_{ch}). Water is supplied in a closed system, with a large tank elevated above the channel at the upstream end, from which water falls through a notched weir to a stilling tank below. At the downstream end, a weir plate is fitted to enable control of the downstream water level.

The bed slope of the flume is set by adjusting the jacks and was measured by raising the downstream weir, filling the flume with still water and measuring the depth of the water over the length of the flume. The slope of the flume was set as close as possible to 0.001, where Figure 3.16 shows the position of the water surface at the channel centreline plotted against streamwise position. Linear

3.1 Physical Experiments

regression of the measured data shows that the overall slope is 0.001 with a R-squared value of 0.9829.

For the measurements in the simple sections, the blocks were attached directly to the centre of the glass flume floor using silicon sealant. For the measurements in the compound sections, a floodplain section was constructed out of lengths of solid plastic with a depth of $0.022m$ mounted on two lengths of rectangular aluminium piping of depth $0.060m$, making the total floodplain height (H_{fl}) $0.082m$. This construction starts at a chainage of $3.25m$, directly upstream of which, a wooden ramp was inserted to minimise flow disruption. Since considerable difficulty was experienced in securing this ramp to the body of the flume, to prevent it from floating, a heavy steel plate was set on top of the ramp, as shown in Figure 3.17.

Although the disadvantages of this floodplain set-up are acknowledged, the entire length of the flume, in common with the Loughborough flume, is unlikely to be sufficient to establish fully developed flow. The judgement was therefore made to provide as much upstream length of floodplain as the available materials allowed for and to follow the procedure set up for the Loughborough experiments, to measure the cross-sectional velocity profile upstream of the block and use these results as the inlet conditions for the numerical model. Once verified, the model should allow us to make a comparison of the experimental results to those in a truly fully developed flow. The test section onto which the blocks were mounted was constructed from glass and is shown in Figure 3.17. Considerable effort was expended to ensure that the glass test section was sealed and that no level differences occurred at the meeting of the glass and plastic sections.

Depth and level measurements made whilst the flume was running were performed with a number of point gauges, which all included Vernier scales allowing for measurements with an accuracy of a tenth of a millimetre.

Electromagnetic Velocimeter The electromagnetic velocimeter (EMV) consists of a magnet mounted within a velocity probe. As the probe is inserted into the flow, the movement of the fluid displaces the magnetic field and the electric field

3.1 Physical Experiments

that is created as a result of this change is measured by pairs of electrodes as a voltage, which can then be converted into a flow velocity. The EMV used in these experiments measured two components of the velocity to an accuracy of $\pm 2\text{mm/s}$; streamwise and spanwise velocity, with a head of diameter 8mm . The measurements provided by the EMV are useful only in determining mean values of velocity and have not been analysed for information regarding the turbulent field in this case.

The EMV must be correctly rotated with respect to the flow to produce accurate results. The rotation of the EMV was set by performing a series of crude test measurements in the simple channel section upstream of the floodplain ramp at a chainage of 1.5m . Although this section is certainly too short in which to establish developed flow and therefore to claim that the secondary circulations at the channel centre will be zero, it was assumed that the secondary circulations would be small. The heading of the EMV was therefore rotated until a spanwise velocity of less than $1 \times 10^{-3}\text{m/s}$ was registered by the probe at the channel centre (width and height). Where this was not possible, the spanwise velocity reading was reduced to its minimum possible value and an appropriate rotation was applied to the results. All of the data was collected on the assumption that the velocity data may require to be rotated again by small amounts in post-processing.

The reliability of the results from the EMV reduces when the probe is placed within 1cm of a boundary such as the channel bed, walls or free surface. This means that measurements could be taken far closer to the free surface in comparison with the ADV and provided useful data on the secondary flow patterns in that region. Since no turbulence analysis is to be performed with this data, the amount and frequency of data collection was relaxed. A sampling frequency of 20Hz was used for 25s at each point. The data was filtered using a limit of 3 times the standard deviation and the measured voltages were converted to velocities using Equation 3.2.

$$\text{Velocity} = 0.2 * \text{Voltage} \quad (3.2)$$

Table 3.4: *Rotation Angles (°) applied to the velocity vectors measured with the EMV*

Case	Rotation Angle (°)
I	+0.26
II	+0.92
III	+0.20
IV	+0.75

Measurements of time-averaged streamwise and spanwise velocity were therefore collected using the EMV at a matrix of points throughout both the simple and compound channel set-ups. Having collected and filtered the data, it was also necessary to rotate the velocity vectors to account for the difficulties in positioning the EMV. For measurements in the simple channel cases, the rotation angle was chosen such that the magnitude of the spanwise velocity component at the channel centre at the upstream station was minimised. For the compound channel cases, it was assumed that the spanwise velocity was zero at the location of the maximum streamwise velocity and a rotation angle applied to ensure that this was the case. The resulting rotation angles are shown in Table 3.4.

Pitot-static Tube In order to measure velocities and boundary shear stress values at the bed and wall boundaries of the channel, a 4mm diameter Pitot-static tube was also used in these experiments. Although boundary shear stress is more usually measured using a Preston tube, the shape of which is especially designed for the purpose, the mechanism of both tubes in measuring the dynamic pressure within the log-law region close to solid boundaries is the same. As such, the streamwise velocity was found directly from the dynamic pressure measurement and the boundary shear stress was found using the standard equations for this calculation from Patel (1965), i.e. equations 3.3a to 3.3e. The equations define the boundary shear stress in terms of the physical properties of the fluid (ρ) and (μ), a representative distance that is usually the Pitot-static tube diameter (d_{pst}) and the dynamic

3.1 Physical Experiments

pressure (P_D) measured within the region of influence of the log-law.

$$a^* = \log_{10}^{(P_D d_{pst}^2)/(4\rho v^2)} \quad (3.3a)$$

$$b^* = \log_{10}^{(\tau_b d_{pst}^2)/(4\rho v^2)} \quad (3.3b)$$

$$b^* = 0.5a^* + 0.037, b^* < 1.5 \quad (3.3c)$$

$$b^* = 0.8287 - 0.1381a^* + 0.1437a^{*2} - 0.006a^{*3}, 1.5 < b^* < 3.5 \quad (3.3d)$$

$$a^* = b^* + 2\log_{10}^{1.95b^*+4.1}, 3.5 < b^* < 5.3 \quad (3.3e)$$

The Pitot-static tube was connected to a pressure transducer, which was calibrated before the measurements were taken, to establish a relationship between the measured dynamic pressure and the voltage recorded by the computer. A photograph of the calibration process is shown with the resulting graph in Figure 3.18. This was achieved by connecting only the total pressure tube to the transducer and submerging the tube in water. The other side of the transducer was left open to the atmosphere and the pressure difference was varied to the limits of measurability by adjusting the vertical position of the transducer. Equation 3.4 is the result of this process.

$$\text{Head} = 0.1002 * \text{Voltage} - 0.0023 \quad (3.4)$$

It is acknowledged that whilst the coefficient of the calibration equation for the pressure transducer is invariant, the constant can be very sensitive and should be carefully checked. Indeed, whilst the pressure transducer is in use, monitoring this constant provides a confirmation that the performance of the transducer and Pitot tube is consistent. Before and after each set of measurements were taken

3.1 Physical Experiments

in the moving fluid therefore, a background value was taken by placing the Pitot-static tube (with both tubes now connected to the transducer) in a container of still water. Thus, instead of using the intercept value from equation 3.4, the average of these readings was subtracted from the values of head obtained in the flume. The dynamic pressure was sampled at a frequency of $5Hz$ for 120s at each location, where the locations were chosen to correspond with the lateral and vertical positions at which velocities were measured with the EMV.

Ultrasonic Level Sensor In order to know the static pressure distribution throughout the measured cross-sections, it was also necessary to measure the profile of the water surface. This was achieved to high accuracy using an ultrasonic level sensor. Before each use, the sensor was calibrated using the set height cylinders supplied with the sensor equipment. These cylinders were placed on top of a $6cm$ box to ensure that the calibration limits encapsulated the likely position of the water surface. In the case of the compound channel, this stack was set on top of the floodplain section. The calibration process provided the relationship between the voltage signal produced by the sensor and the water surface position.

The level sensor consists of a small disc of $2cm$ diameter. As the sensor is brought closer to the water surface, the water surface area over which measurements are made reduces. However, where the water surface is highly angled, such as in the wake of the blocks, at positions too close to the surface the sensor can fail to produce any meaningful results. The vertical position of the sensor was therefore chosen to be as close to the water surface as possible to capture sufficient data. The water surface position was sampled at a frequency of $20Hz$ for 120s at each location. At positions of maximum deformation of the surface, this time was extended to 180s to ensure that sufficient reliable data were recovered.

The sensor was positioned so that the centre of the disc was directly over the measurement point of interest. These points were chosen to coincide with the EMV velocity measurement positions. The resulting data was generally filtered in a similar fashion to the data from the EMV, using a limit of 3 times the standard

deviation to exclude outliers. However, in cases where the deformation of the free surface affected the results and the sensor returned invalid results, these points were recorded with values at or around 5. For data series affected by this type of result, the usual filtering was preceded by the removal of all data points above a certain value threshold.

A sample of the results from the sensor is shown in Figure 3.19. These show the profile of the water surface upstream of the block in Series 4, Case IV, where the profile of the water surface should be close to symmetry. The original measured profile is shown with a dotted line, from which it is clear that there is a significant lateral gradient associated with the results. This is likely to be due to a small gradient between the rails on which the mounting for the meter sits. Applying a correction for this gives the results shown with the solid line. Since the results for Series 4, Case III showed a very similar trend, an average correction factor was calculated from these two cases and then applied to all results measured with this equipment.

3.1.2.2 Experimental Series - Set-Up Details

The experiments pursued in the Kansai flume were designed to collect the necessary data to calculate and compare the coefficients of drag for equivalent bluff bodies in simple and compound channel flows. Although not including turbulence data, the mean velocities, boundary shear stresses and water surface positions are also helpful in directly comparing the state of the wakes between the two channels and in verifying the results from the Loughborough experiments. The experimental set-up for this, Series 4, is detailed in Table 3.3. The block used in the Kansai flume was a solid cubic block of aluminium of width $W_{bl} = 0.019m$, which was placed at the edge of the floodplain at a chainage of $9.5m$.

For the measurements of velocity with the EMV, a spanwise sample spacing of $2W_{bl}$ was used where possible far from the block and $0.25W_{bl}$ in a zone defined by $-1.0 < y < 1.0$. The resultant measurement grids are shown in Figures 3.20 and 3.21, where the EMV measurements are shown with the grey circles and assumed,

3.1 Physical Experiments

extrapolated and interpolated points are shown in black. The white points show the points measured with the Pitot-static tube. The points on the water surface were measured in order to correspond to the points shown in these figures.

Three streamwise locations were chosen for measurement. For the compound channel cases, upstream of the block at $x = -5.53$ and downstream of the block at $x = +5.53$, the EMV was used to gather data in the manner described above. The water surface profile and boundary shear stress distribution were also measured at these positions. Finally, the boundary shear stress distribution at the block centre, i.e. $x = 0$, was added.

The aim was to choose an upstream measurement position at which the compound channel flow was as yet undisturbed by the presence of the block and was originally chosen with respect to the work of Lyn *et al.* (1995). Taking measurements in the 2D plane at the vertical centre of a square block mounted in a closed channel, they reported a measurable effect from the presence of the block on the streamwise velocity profile at a position of $x = -3$. According to the work of Baker (1980), the position of the upstream separation point for a wall mounted circular cylinder is a function of the cylinder Reynolds number, cylinder aspect ratio, freestream turbulence, the ratio of the cylinder width to the boundary layer thickness and the boundary layer form function.

Without an accurate picture of all of these variables for the experiments of Lyn *et al.* (1995), direct comparison was not attempted. However, the Reynolds numbers and block aspect ratios were similar enough that the assumption was made that a near doubling of the distance to the upstream section would be sufficient.

Performing the compound channel cases first, the results presented in section 4.1.2.1 show that the velocities measured using the EMV do not betray any influence from the block. However, examination of the boundary shear stress distribution shows that the values of τ_b do not reach a maximum at the floodplain edge as observed by Tominaga and Nezu (1991). Instead, the values are depressed in this area, which can be interpreted as the early upstream influence of the presence of the block in decelerating the flow in this area. Despite this, it has been assumed

that the measurements of velocity at this cross-section are undisturbed enough to be representative of the freestream conditions.

When setting up the first simple channel case, it was found that at $x = -5.53$, the flow was significantly affected by the presence of the block. The vectors of mean spanwise velocity V clearly showed the flow diverging and a significant region of deceleration in streamwise velocity U in front of the block. The upstream cross-section of measurements was therefore taken further upstream at $x = -11$. Even this far upstream, the effects of the presence of the block could be observed in the velocity and boundary shear stress distributions. However, the influence was judged to be reduced sufficiently to provide a reliable estimate of freestream conditions. The upstream section of data was therefore collected at $x = -11$ for both the simple channel cases. The measurement positions at $x = 0$ and $x = +5.53$ were maintained.

3.2 Numerical Modelling

3.2.1 Basic Concepts & Equations

In order to complement the experimental results, simulations are also undertaken with a numerical model developed at Loughborough University (Vyas, 2007). The model solves the continuity and Reynolds Averaged Navier Stokes (RANS) equations on a structured, co-located grid using a Cartesian coordinate system. The structured grid is constructed using a separate programme to the main model. Variations in channel geometry can be achieved using the masking concept, where parts of the grid are blanked out and boundary conditions are applied along their edges. As previously mentioned, the Reynolds averaging approach is only capable of reproducing the average behaviour of the flow but, as a result of this simplification, is relatively cheap to implement. The model therefore solves the equations of flow in the forms shown in Equations 3.5a to 3.5d, namely the continuity equation (Equation 3.5a) for the conservation of mass and the steady RANS equations

3.2 Numerical Modelling

(Equations 3.5b, 3.5c and 3.5d) for the conservation of momentum.

$$\frac{\partial U}{\partial x} + \frac{\partial V}{\partial y} + \frac{\partial W}{\partial z} = 0 \quad (3.5a)$$

$$\begin{aligned} U \frac{\partial}{\partial x}(\rho U) + V \frac{\partial}{\partial y}(\rho U) + W \frac{\partial}{\partial z}(\rho U) = -\frac{\partial P}{\partial x} + \\ \mu \frac{\partial^2 U}{\partial x^2} + \mu \frac{\partial^2 V}{\partial y^2} + \mu \frac{\partial^2 W}{\partial z^2} - \frac{\partial}{\partial x}(\rho \overline{u'u'}) - \frac{\partial}{\partial y}(\rho \overline{u'v'}) - \frac{\partial}{\partial z}(\rho \overline{u'w'}) + \rho g \sin \theta \end{aligned} \quad (3.5b)$$

$$\begin{aligned} U \frac{\partial}{\partial x}(\rho V) + V \frac{\partial}{\partial y}(\rho V) + W \frac{\partial}{\partial z}(\rho V) = -\frac{\partial P}{\partial y} + \\ \mu \frac{\partial^2 V}{\partial x^2} - \frac{\partial}{\partial x}(\rho \overline{u'v'}) - \frac{\partial}{\partial y}(\rho \overline{v'v'}) - \frac{\partial}{\partial z}(\rho \overline{v'w'}) \end{aligned} \quad (3.5c)$$

$$\begin{aligned} U \frac{\partial}{\partial x}(\rho W) + V \frac{\partial}{\partial y}(\rho W) + W \frac{\partial}{\partial z}(\rho W) = -\frac{\partial P}{\partial z} + \\ \mu \frac{\partial^2 W}{\partial x^2} - \frac{\partial}{\partial x}(\rho \overline{u'w'}) - \frac{\partial}{\partial y}(\rho \overline{v'w'}) - \frac{\partial}{\partial z}(\rho \overline{w'w'}) \end{aligned} \quad (3.5d)$$

where P is the static pressure, μ is the fluid viscosity, ρ is the fluid density, g is the gravitational acceleration and θ is the angle between the channel bed and the horizontal.

The momentum equations represent the balance between the convection of momentum and the sum of forces causing that convection. For flow in an open channel, these include the static pressure gradient, gravity, molecular and turbulent normal and shear stresses and for certain cases, surface tension, centrifugal and Coriolis forces. By assuming that the fluid is Newtonian in character and that the flow is incompressible, we can write the stresses caused by molecular motion in terms of the static pressure and the dynamic viscosity.

The equations are solved using a finite volume formulation, where the diffusion terms are discretised using a central differencing scheme and the convection terms are discretised using a blend of upwind and central differencing techniques (UDS and CDS). In order to calculate the pressure terms in a manner that also satisfies continuity, the well known Semi-Implicit Method for Pressure Linked Equations (SIMPLE, (Patankar and Spalding, 1972)) is used. After an initial pressure field is guessed, a Poisson equation for the pressure correction is solved with the momentum equations on each iteration so that the velocity and pressure fields develop simultaneously in the calculation. The linearised equations are solved using the strongly implicit procedure (SIP) method of Stone (1968).

For steady, laminar flow modelling, the procedure in the code is therefore:

- Set initial values of dependant variables at all nodes.
- Assemble momentum equations using these initial variable values to linearise the non-linear terms.
- Iterate to solve the linearised momentum equations using the SIP to find intermediary values of U , V and W .
- Calculate residual error in this solution.
- Assemble the pressure correction equation using these intermediary velocities.
- Iterate to solve for the pressure correction and update pressure and velocities.
- Calculate residual error in this solution.
- Re-assemble the momentum equations using the updated values and repeat the procedure.
- Print solution when error residual values fall below predetermined threshold.

3.2.2 Turbulence Modelling

3.2.2.1 The K- ϵ model

Since we are using Reynolds averaging, the momentum equations include terms that represent the time-averaged stresses caused by the turbulent motion. In order to solve the equations, we must introduce a model for these unknown correlations. To do this, we use the eddy viscosity concept (Boussinesq, 1887). Boussinesq (1887) created a model whereby the turbulent stresses are assumed to be directly proportional to the mean velocity gradients and therefore the mean strain rates. Equation 3.6 is called the Boussinesq Equation and describes this idea in index notation.

$$-\rho \overline{u'_i u'_j} = \mu_t \left(\frac{\partial U_i}{\partial x_j} + \frac{\partial U_j}{\partial x_i} \right) - \frac{2}{3} \rho K \delta_{ij} \quad (3.6)$$

where K is the turbulent kinetic energy, and δ_{ij} is the Kronecker delta. Inclusion of this term ensures that when $i = j$, i.e. for the normal stresses, the equation is always positive and equal to double the turbulent kinetic energy. The δ_{ij} term is absorbed into the pressure gradient term when the Boussinesq equation is substituted into the momentum equations. μ_t is the turbulent eddy viscosity and is a property of the flow, as opposed to μ , which is a property of the fluid. The model means that the action of the turbulence increases the effective viscosity of the fluid. If the Boussinesq model is used, the terms including the dynamic viscosity in the RANS equations are replaced by terms including the turbulent viscosity μ_t . The Boussinesq model allows us to predict the distribution of the turbulent stresses if we know the corresponding distribution of the turbulent eddy viscosity.

There are a number of different models available to predict the distribution of the eddy viscosity. The simplest methods involve attributing values of μ_t based on experimental measurements, trial and error or by relating μ_t to the mean strain rate. One of the most commonly used methods, the $k - \epsilon$ model however, attempts

to account for the transport of the turbulence properties within the flow field. It requires us to solve two transport equations - one for the turbulent intensity, represented by the turbulent kinetic energy K (Equation 3.7), and one for the turbulent length scale, represented by the turbulent kinetic energy dissipation rate ϵ (Equation 3.8). This model is based on the assumption that the dissipation rate is directly proportional to $\frac{K^{\frac{3}{2}}}{l}$, where l is the turbulent length scale. By solving these equations to calculate the distributions of K and ϵ , the eddy viscosity is then found using the Kolmogorov-Prandtl formula (Equation 3.9).

$$U \frac{\partial}{\partial x}(\rho K) + V \frac{\partial}{\partial y}(\rho K) + W \frac{\partial}{\partial z}(\rho K) = \frac{\partial}{\partial x} \left(\frac{\mu_t}{\sigma_K} \frac{\partial K}{\partial x} \right) + \frac{\partial}{\partial y} \left(\frac{\mu_t}{\sigma_K} \frac{\partial K}{\partial y} \right) + \frac{\partial}{\partial z} \left(\frac{\mu_t}{\sigma_K} \frac{\partial K}{\partial z} \right) + P_K - \rho \epsilon \quad (3.7)$$

$$U \frac{\partial}{\partial x}(\rho \epsilon) + V \frac{\partial}{\partial y}(\rho \epsilon) + W \frac{\partial}{\partial z}(\rho \epsilon) = \frac{\partial}{\partial x} \left(\frac{\mu_t}{\sigma_\epsilon} \frac{\partial \epsilon}{\partial x} \right) + \frac{\partial}{\partial y} \left(\frac{\mu_t}{\sigma_\epsilon} \frac{\partial \epsilon}{\partial y} \right) + \frac{\partial}{\partial z} \left(\frac{\mu_t}{\sigma_\epsilon} \frac{\partial \epsilon}{\partial z} \right) + \frac{\epsilon}{k} (C_{\epsilon 1} P_k - C_{\epsilon 2} \rho \epsilon) \quad (3.8)$$

$$\mu_t = \rho C_\mu \frac{k^2}{\epsilon} \quad (3.9)$$

The model is based on a series of empirical coefficients, simplifications and assumptions but for many applications can produce very useful results. The coefficient values set in the model used here are taken from Rodi (1993) and are as follows - $C_{\epsilon 1} = 1.44$, $C_{\epsilon 2} = 1.92$, $C_\mu = 0.09$, $\sigma_k = 1.0$, $\sigma_\epsilon = 1.3$. Although the $k - \epsilon$ model is very widely applicable, its assumption that the relationship between Reynolds stresses and the mean strain rate is the same in every direction limits its usefulness. As a first consideration, it is unable to model the behaviour of open channel flow in which the anisotropy of the turbulence is a governing parameter, as described in Section 2.2.

3.2.2.2 Higher Order Turbulence Closures

Vyas (2007) constructed the model with an original aim of reproducing the secondary circulations observed in uniform open channel flow. To this end, three models were built into the code in order to calculate the values of the Reynolds stress terms in the Navier Stokes equations in addition to the simple linear $k - \epsilon$ model. The original computer code included the following model options for the inclusion of the Reynolds stress terms: Launder and Ying (1973), Naot and Rodi (1982) and the non-linear $k - \epsilon$ model of Speziale (1987).

As mentioned previously, Reynolds stress modelling involves the solution of the full transport equations for the Reynolds stresses, which can be found in Launder *et al.* (1975). Algebraic stress modelling is a simplification of this system and forms the basis of the work by Launder and Ying (1973) and Naot and Rodi (1982). By assuming local equilibrium of turbulence, simplifications occur as firstly, the convection and diffusion terms are neglected and secondly, the production term is set equal to the dissipation. It is also assumed that the gradients in the lateral and vertical mean velocities (V and W) are significantly less than those in the streamwise velocity (U). In Launder and Ying (1973), these terms are neglected completely, whilst in Naot and Rodi (1982), they are modelled using an eddy viscosity term as opposed to being included explicitly. The result of these simplifications are algebraic expressions for the Reynolds stresses in terms of the mean velocity gradients, which can be substituted directly into the momentum equations. The derivation of the model of Speziale (1987) takes a different approach. Instead of bypassing it completely, the non-linear $k - \epsilon$ model is based upon a higher order approximation to Equation 3.6. Whereas the original approximation of the linear $k - \epsilon$ model only considers the linear mean velocity gradient terms, the model of Speziale (1987) is extended to also include the quadratic mean velocity gradients.

For the original purposes of the code, it was only necessary to model the Reynolds stress components that appear in the momentum equations in lateral and vertical gradient terms, namely $\overline{v'^2}$, $\overline{w'^2}$ and $\overline{v'w'}$. However, since the code

is now to be applied to the non-uniform flow around floodplain vegetation, it is necessary to include all of the Reynolds stress terms. Instead of simply extending one of the existing models, a new non-linear $k - \epsilon$ model was introduced.

Kimura and Hosoda (2003) based their model on the earlier work of Speziale (1987) but tuned their model to be particularly applicable to bluff body flows. At this point, it is important to note the deficiencies that computational models generally exhibit in predicting the mean flow about bluff bodies. For the flow around square sectioned bodies, it is well documented (Bosch and Rodi, 1998; Franke and Rodi, 1993; Kato and Launder, 1993; Ramesh *et al.*, 2005) that the standard $k - \epsilon$ model cannot satisfactorily reproduce the expected flow pattern due to its inability to distinguish between the normal Reynolds stresses, which are important in the production of turbulent kinetic energy in stagnation regions, i.e. at the upstream face of a bluff body. However it is true of all models thus far tested, including the more sophisticated LES, that the turbulent kinetic energy behind the body is consistently under-predicted. Having acknowledged this limitation, the model of Kimura and Hosoda (2003) performs relatively well in comparison with other approaches and as such has been chosen for inclusion here.

Extending the Boussinesq model to include non-linear terms means that Equation 3.6 becomes Equation 3.10.

$$\begin{aligned}
 -\overline{\rho u'_i u'_j} = & \mu_t S_{ij} + \frac{2}{3} \rho K \delta_{ij} + \\
 \frac{K}{\epsilon} \mu_t (& \alpha_1 (S_{il} \Omega_{lj} + \Omega_{il} S_{lj}) + \alpha_2 (S_{il} S_{lj} - \frac{1}{3} S_{km} S_{mk} \delta_{ij}) + \alpha_3 (\Omega_{il} \Omega_{lj} - \frac{1}{3} \Omega_{km} \Omega_{mk} \delta_{ij}))
 \end{aligned} \tag{3.10}$$

$$S_{ij} = \frac{\partial U_i}{\partial x_j} + \frac{\partial U_j}{\partial x_i} \tag{3.11}$$

$$\Omega_{ij} = \frac{\partial U_i}{\partial x_j} - \frac{\partial U_j}{\partial x_i} \tag{3.12}$$

3.2 Numerical Modelling

The model constants ($\alpha_1 - \alpha_3$) are set by the relationships described by Equations 3.13 to 3.15. The values of C_1 to C_3 are, in turn, tuned by comparison with experimental data from the flow around a 2D square block and a 3D submerged square block and are functions of a strain parameter (S) and a rotation parameter (Ω) as described in Equations 3.16 to 3.18. According to the constraints of realizability (Schumann, 1977), the constant C_μ in Equation 3.9 now also becomes a function of (S) and (Ω).

$$C_1 = -2\alpha_1 + \alpha_2 - \alpha_3 = \frac{0.4}{1 + 0.01M^2} \quad (3.13)$$

$$C_2 = 2(\alpha_2 + \alpha_3) = 0 \quad (3.14)$$

$$C_3 = 2\alpha_1 + \alpha_2 - \alpha_3 = \frac{-0.13}{1 + 0.01M^2} \quad (3.15)$$

$$M = \max(S, \Omega) \quad (3.16)$$

$$S = \frac{K}{\epsilon} \sqrt{\frac{1}{2} \left(\frac{\partial U_i}{\partial x_j} + \frac{\partial U_j}{\partial x_i} \right)^2} \quad (3.17)$$

$$\Omega = \frac{K}{\epsilon} \sqrt{\frac{1}{2} \left(\frac{\partial U_i}{\partial x_j} - \frac{\partial U_j}{\partial x_i} \right)^2} \quad (3.18)$$

$$C_\mu = \min\left(0.09, \frac{0.3}{1 + 0.09M^2}\right) \quad (3.19)$$

3.2.3 Boundary Conditions

Inlet & Outlet Values of streamwise velocity, turbulent kinetic energy and dissipation rate can be applied directly to the inlet boundary nodes. This allows for the application of periodic boundary conditions, which can be used to good effect to achieve fully developed flow conditions when grid size is limited.

At the outlet, Neumann boundary conditions are applied, i.e gradients are set to zero and values of velocity are extrapolated from the interior of the grid. These values of velocity must be corrected to ensure that the mass outflux is equal to the mass influx set at the inlet.

Wall Boundaries Instead of solving the equations right up to the solid boundaries, the standard 'law of the wall' approach is used. In an open channel flow, the vertical boundary layer extends from the bed to the free surface but the surface micro-roughness does not usually affect this entire layer. Instead, a distinct wall layer has also been defined, in which the surface micro-roughness is a governing parameter.

The flow behaviour in the wall layer is distinct from that in the rest of the boundary layer. As the velocity nearest the wall is low, the Reynolds number is small and the flow is likely to be dominated by viscous forces. Thus, nearest the wall a region exists that is often called the viscous sub-layer. The assumptions which allowed us to neglect the viscous dissipation terms in the RANS equations break down in this sub-layer, introducing the need for a model to bridge the gap.

Beyond the viscous sub-layer, an inertial sub-layer has also been identified. Experimental measurements in this zone have shown that the velocity profile can be approximated with a logarithmic function:

$$u^+ = \frac{1}{\kappa} \ln E n^+ \quad (3.20)$$

where u^+ is the dimensionless velocity, κ is the Von Kármán constant equal to 0.41, E is the roughness parameter associated with the thickness of the viscous sub-layer and n^+ is the dimensionless distance from the wall:

$$n^+ = \frac{\rho U_* n}{\mu} \quad (3.21)$$

Thus, as long as we ensure that the first node of the model grid is within the inertial sub-layer, we can set the velocity as a function of the shear velocity U_* . In the model in question, a value for the shear velocity is found using the latest iteration value of turbulent kinetic energy K , where:

$$U_* = C_\mu^{\frac{1}{4}} \sqrt{K} \quad (3.22)$$

The velocity u^+ is not directly applied at the node. Rather, the shear stress experienced by the flow at that point is calculated using a modified viscosity based upon U_* . Having found the dimensionless distance of the node from the wall using equations 3.21 and 3.22, the law of the wall is manipulated to find the modified viscosity at the node so that:

$$\mu_{mod} = \mu n^+ \frac{\kappa}{\ln(En^+)} \quad (3.23)$$

Large obstacles of the type to be analysed in this project can be referred to as macro-roughness elements. It is of interest to know how the flow field around such elements is affected by smaller scale, surface micro-roughness. In the model, this micro-roughness may be simulated through the roughness parameter E . By collating and comparing a large volume of experimental data on pipe roughness, Jayatilke (1969) developed a relationship between the parameter E and the parameter R_r , where:

$$R_r = y_r \sqrt{\frac{\tau_b \rho}{\mu}} \quad (3.24)$$

y_r is the mean height of the roughness and τ_b is the boundary shear stress. By plotting the data collected by Nikuradse (1932) in terms of these parameters, the distribution shown in Figure 3.22 was revealed.

At low roughness heights, E is equal to approximately 9.535 and the surface can be described as hydraulically smooth. As the roughness height increases, the flow enters a transition regime, for which a number of different relationships between E and R_r have been suggested. For high values of R_r , the flow can be described as fully rough and the following equation applies:

$$E = \frac{\beta}{R_r} \quad \beta \approx 30 \quad (3.25)$$

Symmetry Boundaries At symmetry boundaries, simple boundary conditions are applied to all variables such that the gradient of the variable at the boundary is equal to zero. In testing the model in its initial state, it was found that the provision that had been made to take account of the free surface to model open channel flow was not functioning correctly. The effects of the presence of the free surface in open channel flows is felt in the increased anisotropy of the turbulence and the limitation of the turbulent length scale. For most of the flow variables, this implies that the free surface can be treated as a symmetry boundary. As such, the velocities and the turbulent kinetic energy are treated with symmetry boundary conditions in any case. In order to modify the turbulent length scale, it is normal practice to prescribe the values of the turbulent dissipation rate at the surface cells. However, since this system produced unreliable results for open channel flow calculations, a simple symmetry boundary has been substituted. The drawbacks of this approach are acknowledged. However, since the purpose of the simulations is to identify the features of the flow that are caused by the floodplain edge position of bluff bodies, the most important feature of the model is its ability to reproduce the turbulent

field associated with this channel profile. This will be tested in Chapter 5 and account will be taken of the nature of the boundary conditions when analysing the model results.

3.3 Summary

This chapter has described the experimental methods and equipment used to collect and filter raw data from the laboratory and also the computational model created to enhance the data set. The experiments were designed to take advantage of the different equipment and flumes available in the Kansai and Loughborough laboratories. As displayed in Table 3.3, the geometry of experimental Series 2 and 4 in particular was designed in order to maintain the relative geometries of the blocks and channels and allow the results to be compared and the trends confirmed. This data is presented in Chapter 4. The structure of the computational model presents both opportunities and limitations on the usefulness of its results. These will be discussed further in Chapter 5, where the results of its testing and use are presented.

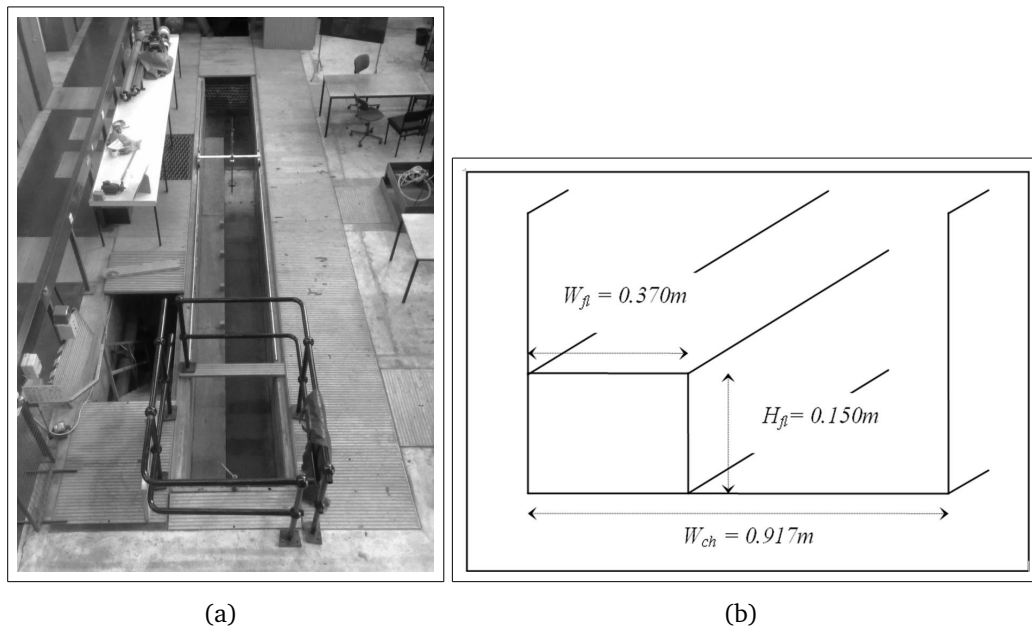
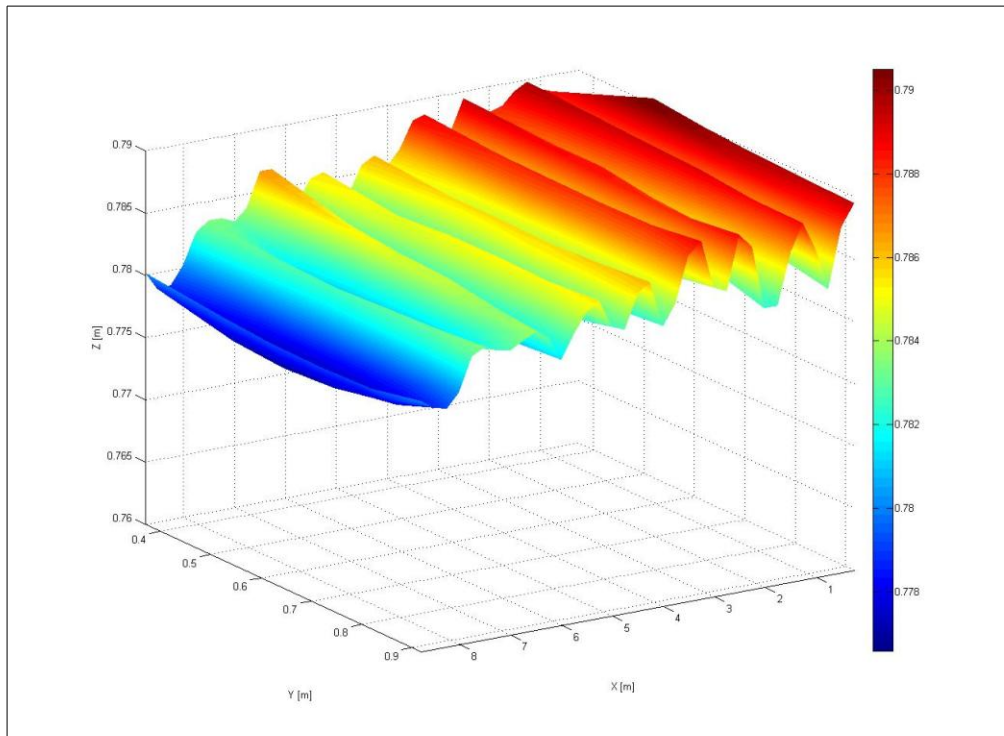
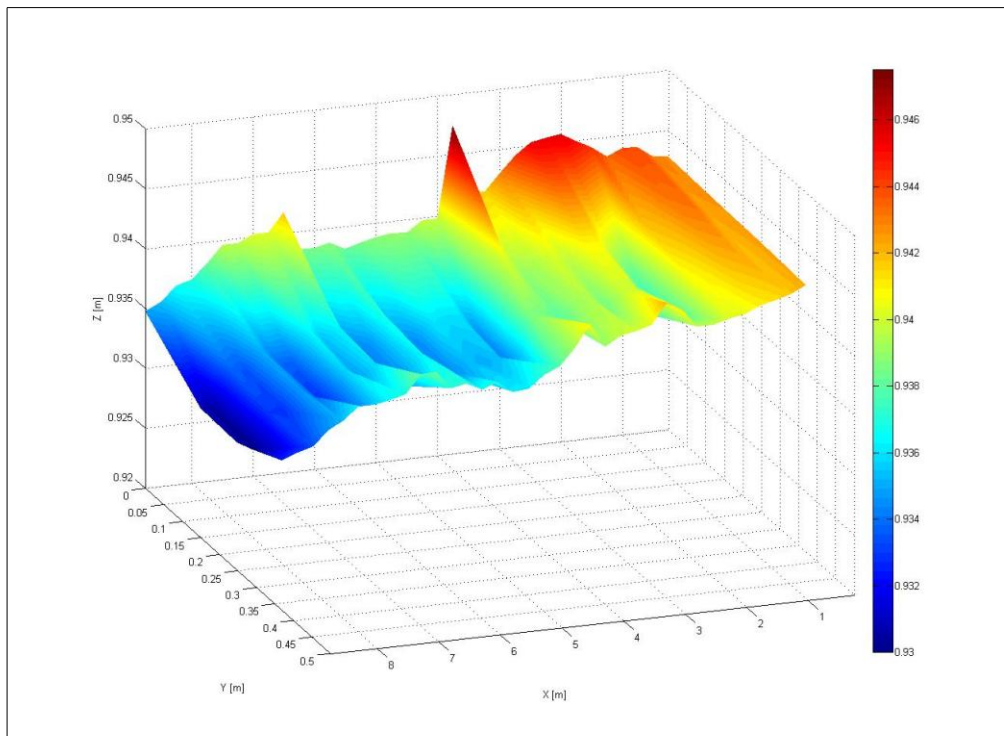


Figure 3.1: (a) Plan view of the Loughborough flume and (b) cross-section schematic



(a)



(b)

Figure 3.2: Channel survey results in Loughborough flume for (a) the main channel bed and (b) the floodplain bed

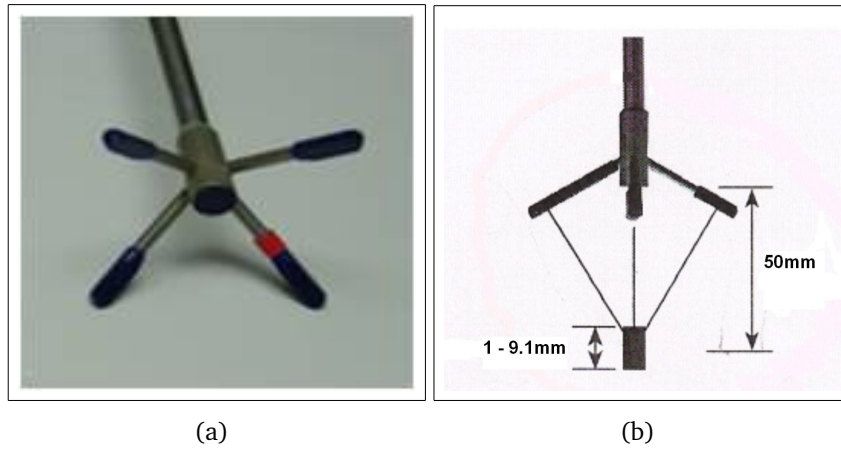


Figure 3.3: The ADV, (a) Acoustic transducers and (b) operational schematic

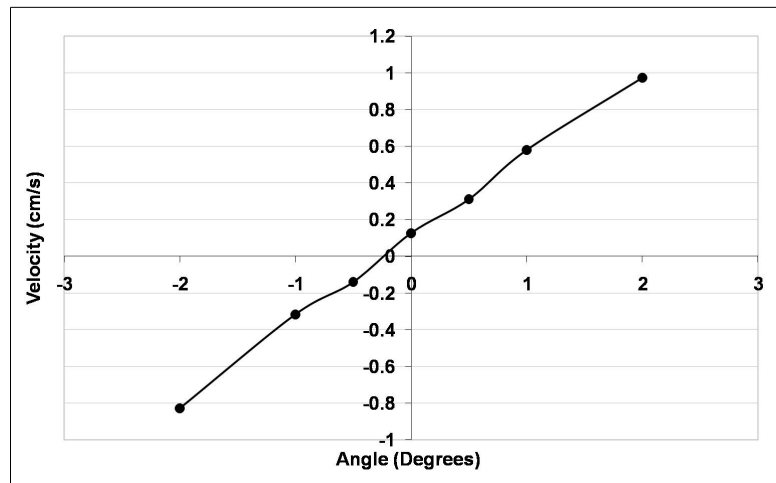


Figure 3.4: Mean spanwise velocity vs. Yaw angle in the simple open channel

3.3 Summary

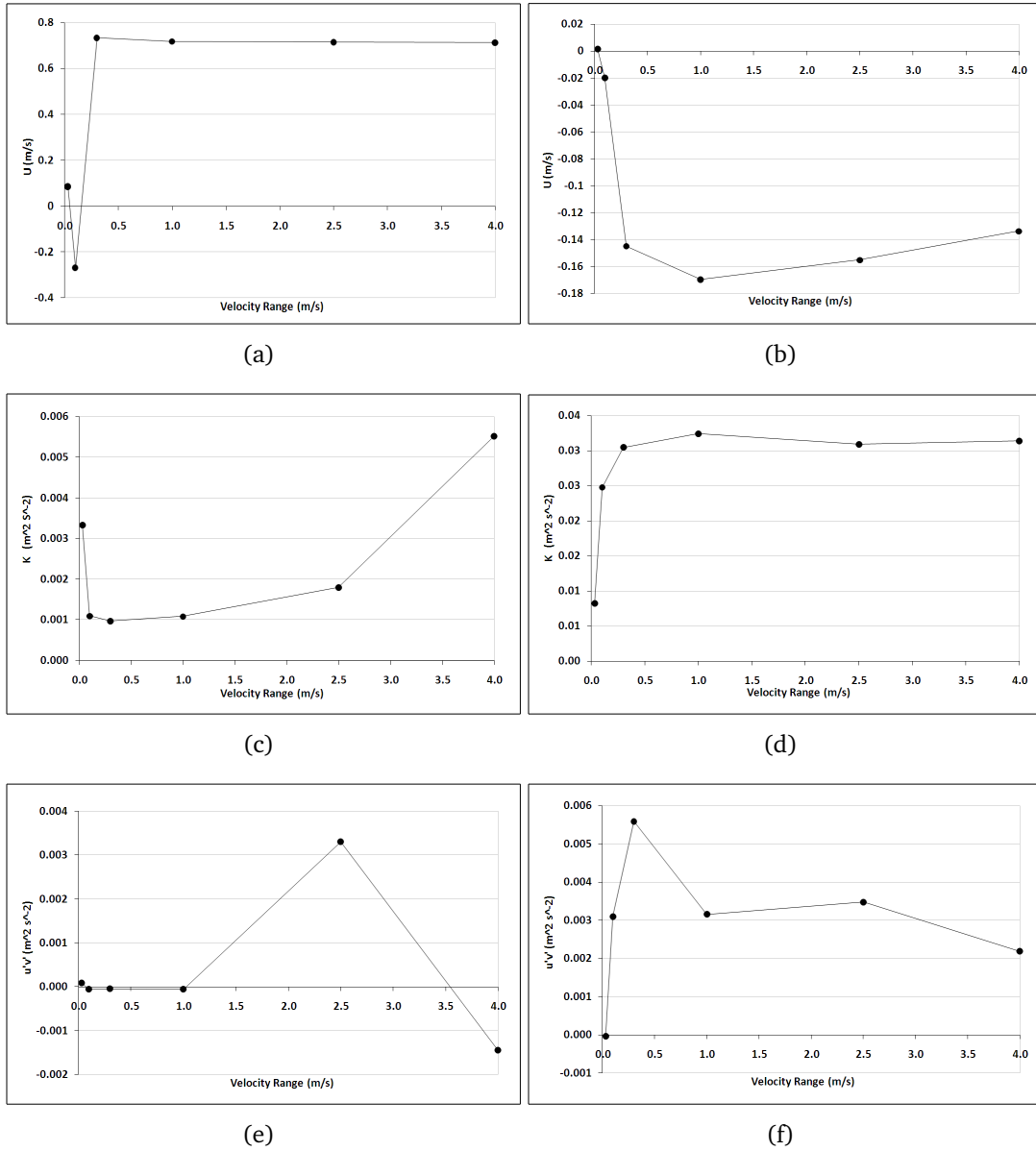


Figure 3.5: Flow statistics vs. Velocity Range for the main channel position (left column) and the position behind the block (right column)

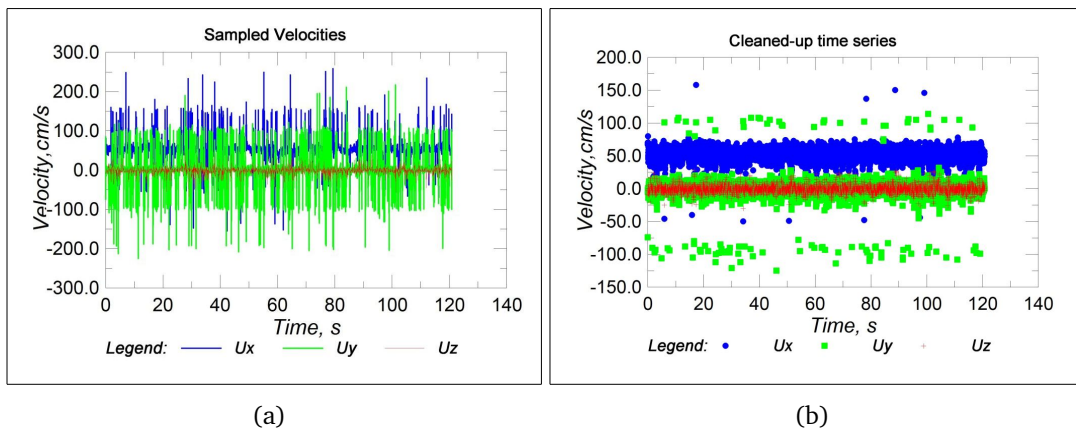


Figure 3.6: (a) Raw and (b) filtered data sets at $x = 3.5$ and $y = 1.86$ for the multiple, deep submerged, small AR case (S1C1)

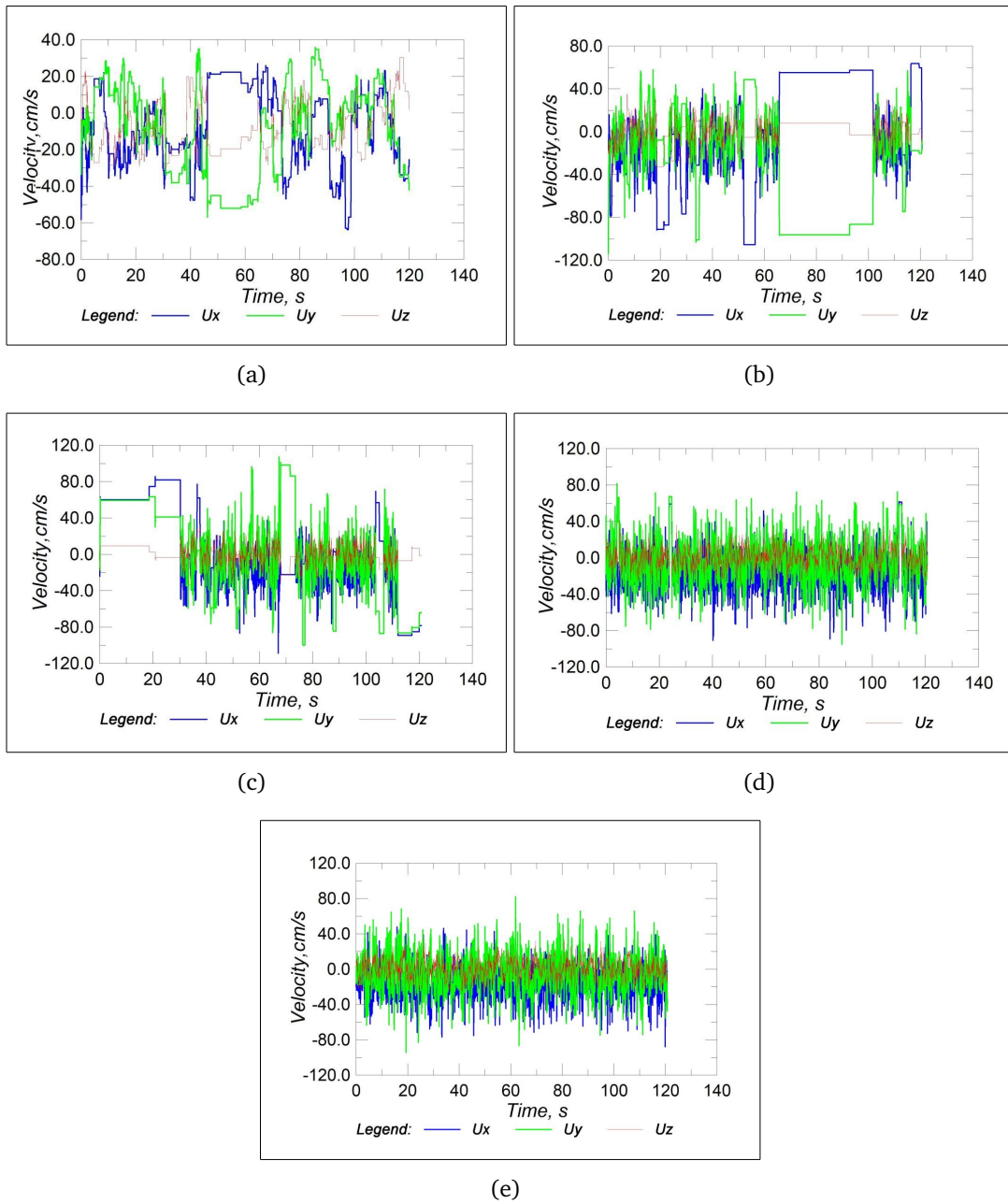
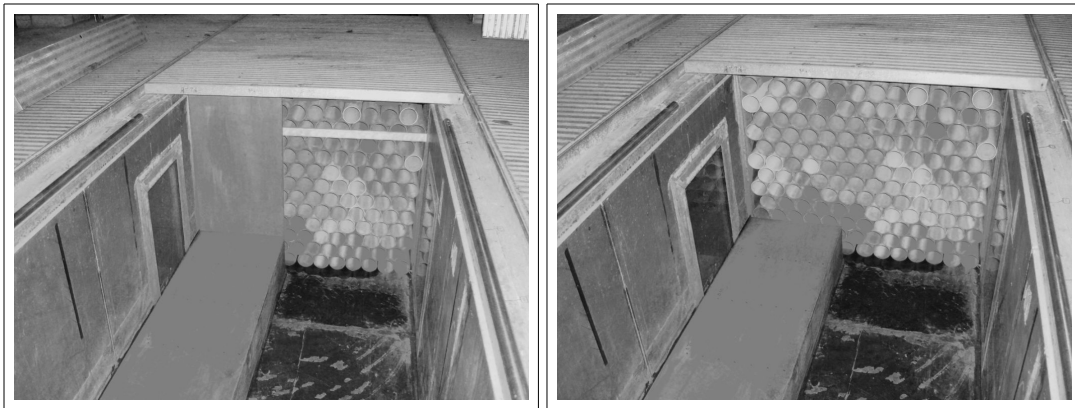


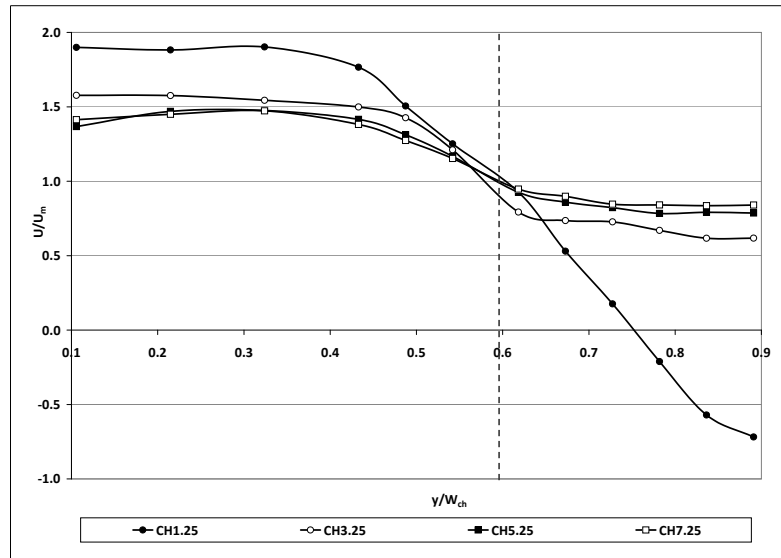
Figure 3.7: Data sets collected behind the block after filtering using linear interpolation at sampling frequencies of (a) 200, (b) 100, (c) 75, (d) 50 and (e) 25Hz



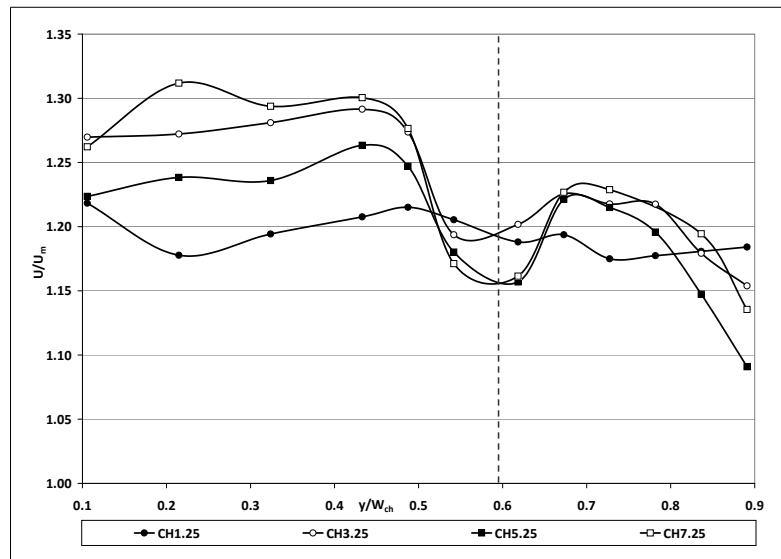
(a)

(b)

Figure 3.8: Arrangement at flume inlet (a) with board and (b) without board



(a)



(b)

Figure 3.9: Mean streamwise velocity at 0.01m from the floodplain bed for (a) the 'with board' case and (b) the 'without board' case

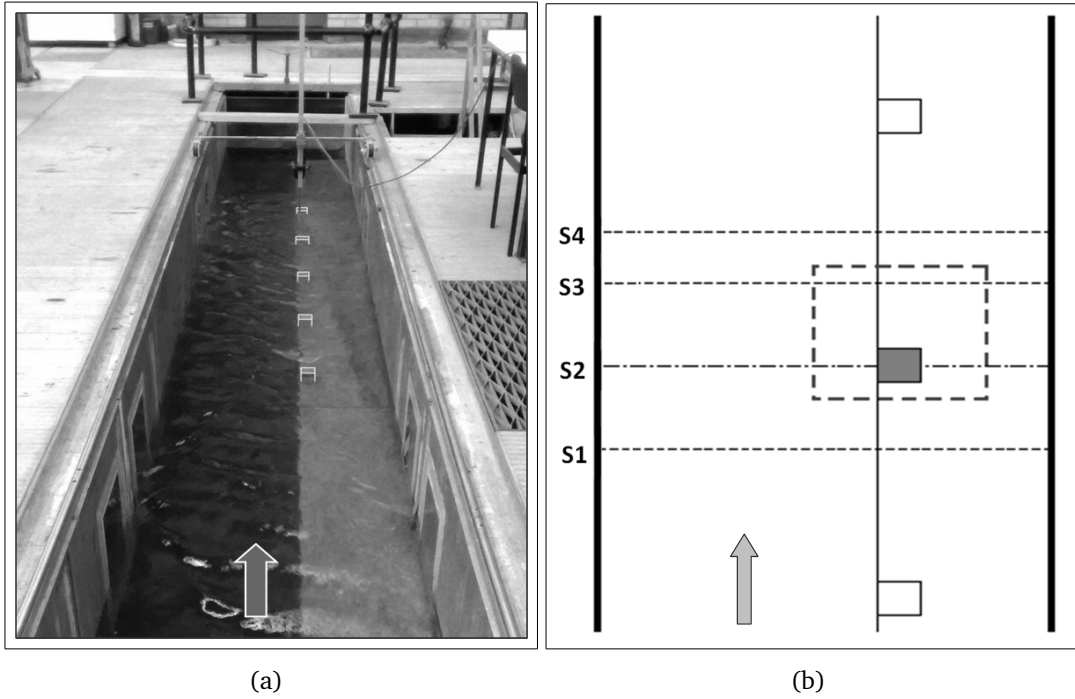


Figure 3.10: *Experimental Series 1 - Multiple, small blocks (a) experiment set-up and (b) measurement positions*

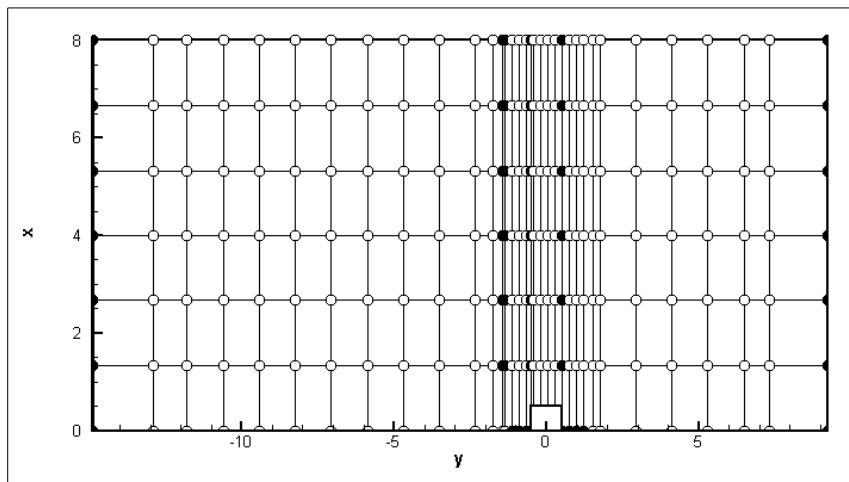


Figure 3.11: *Plan Measurement grid for single, large AR, emergent block (S2CI). White circles are measured points and black circles are assumed, extrapolated or interpolated points.*

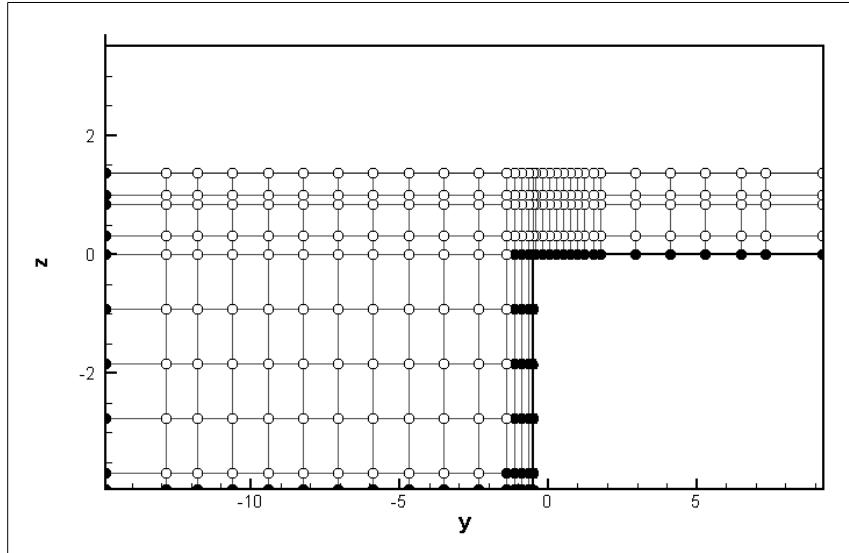


Figure 3.12: *Cross-section Measurement grid for single, large AR, emergent block (S2CI). White circles are measured points and black circles are assumed, extrapolated or interpolated points.*

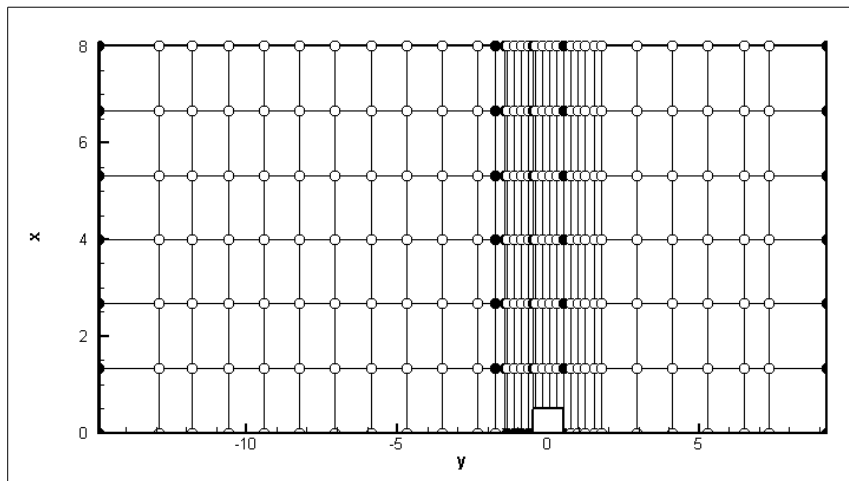


Figure 3.13: *Plan Measurement grid for single, large AR, submerged block (S2CII). White circles are measured points and black circles are assumed, extrapolated or interpolated points.*

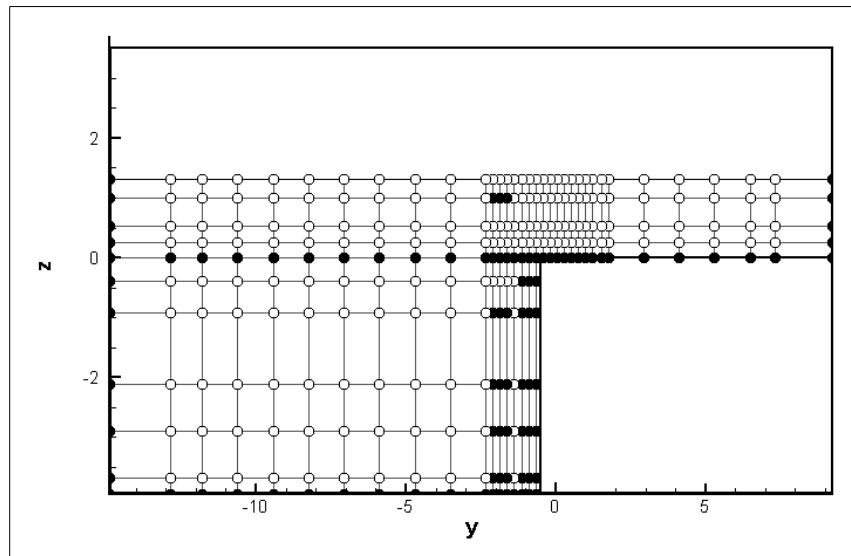


Figure 3.14: Cross-section Measurement grid for single, large AR, submerged block (S2CII). White circles are measured points and black circles are assumed, extrapolated or interpolated points.

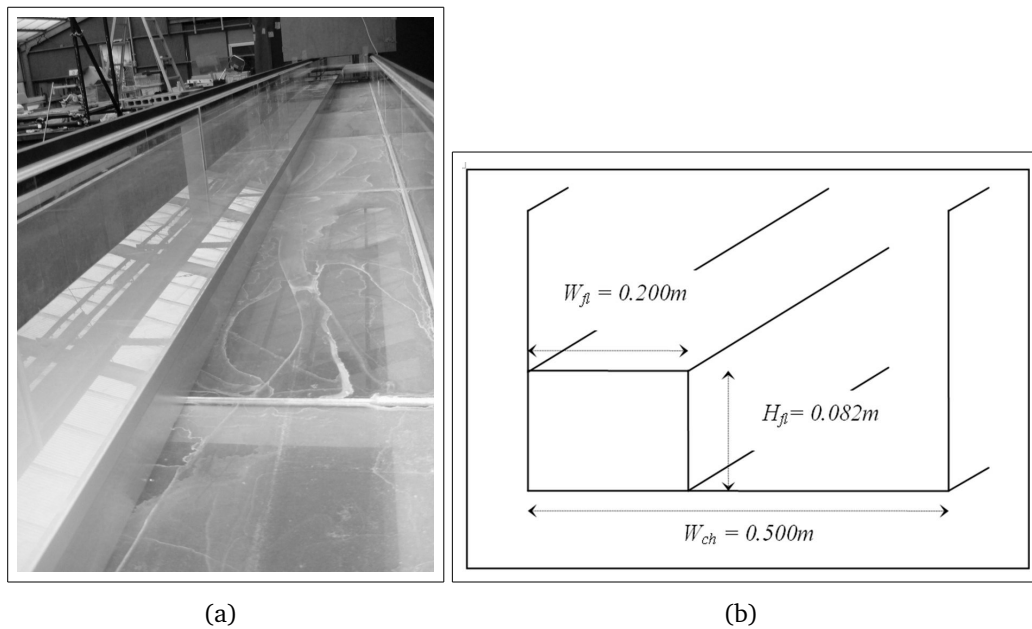


Figure 3.15: (a) Photograph of the Kansai flume and (b) cross-section schematic

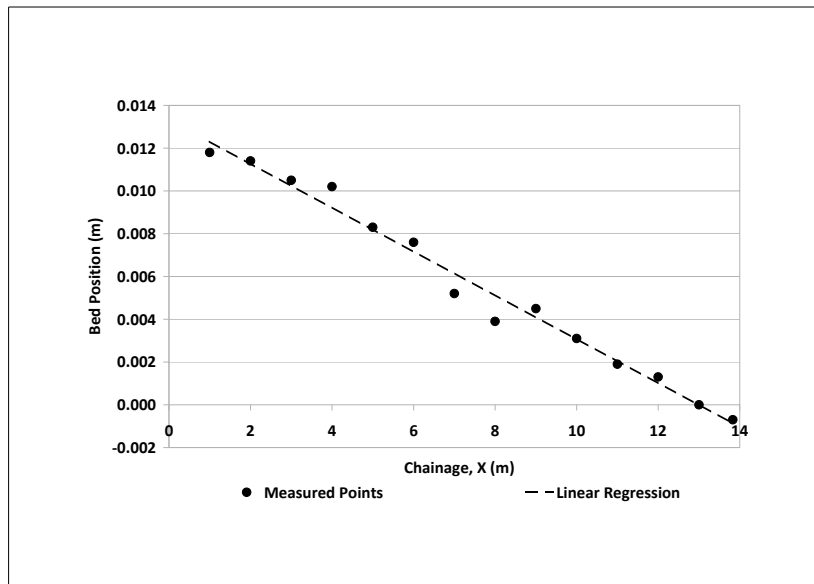


Figure 3.16: Centreline channel survey results for the main channel bed, Kansai flume

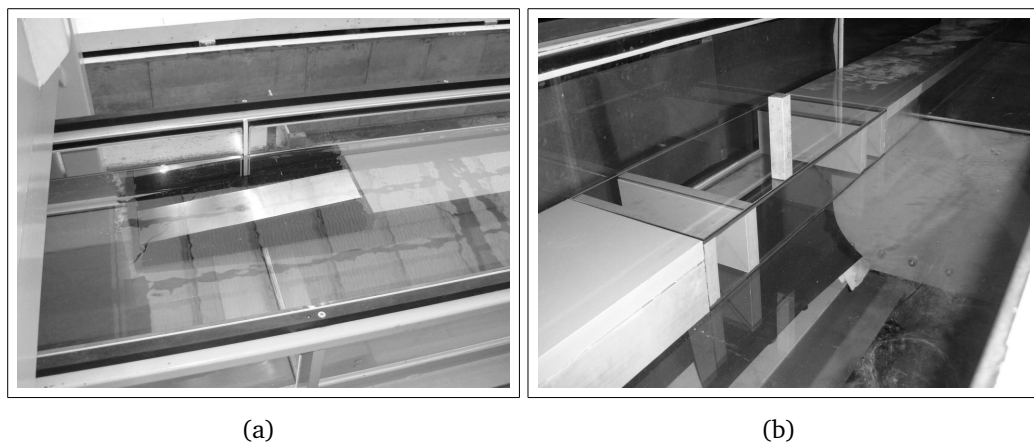
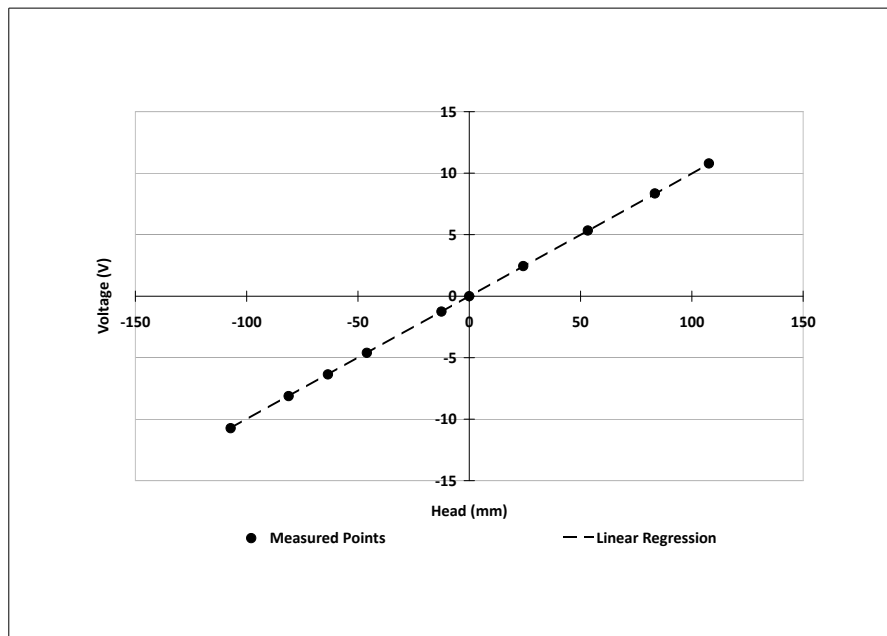


Figure 3.17: Kansai flume floodplain section - (a) upstream set-up, (b) glass test section



(a)



(b)

Figure 3.18: *Calibrating the Pitot-static tube - (a) calibration set-up, (b) calibration curve*

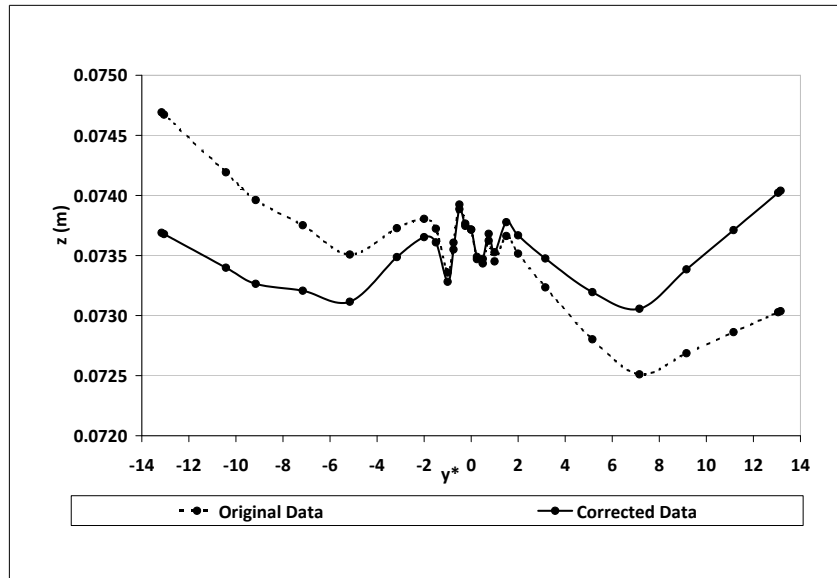


Figure 3.19: Water Surface measured with Ultrasonic Level Meter upstream of the single, large AR, submerged block in a simple channel (S4CIV)

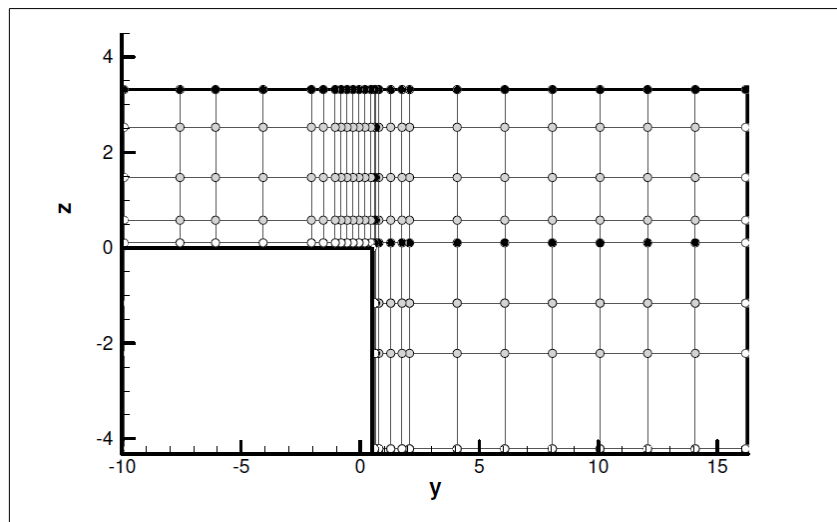


Figure 3.20: Measurement grid for the single, large aspect ratio blocks in the compound channel in the Kansai flume (S4CI&II)

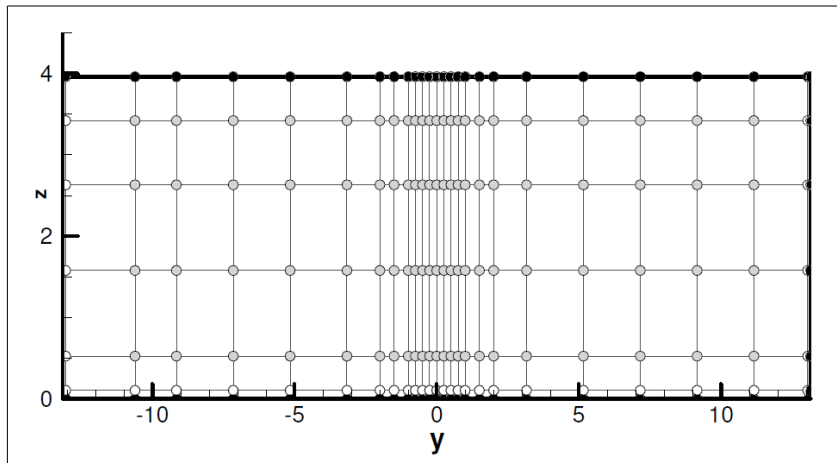


Figure 3.21: *Measurement grid for the single, large aspect ratio blocks in the simple channel in the Kansai flume (S4CIII&IV)*

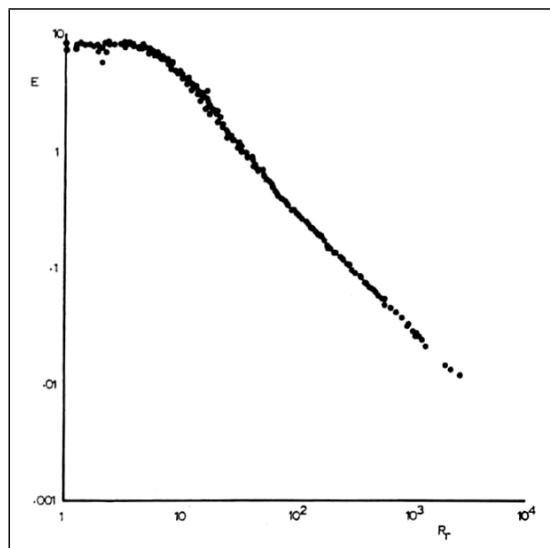


Figure 3.22: *$E(Rr)$ from the experimental data of (Nikuradse, 1932)*

CHAPTER 4

Experimental Results

This chapter will present the results from the physical experiments in the Kansai and Loughborough flumes. In order to present a coherent argument for each case, the results have been grouped together with respect to the status of the block. The results for the emergent blocks are described in Section 4.1 whilst the results for the submerged blocks are described in Section 4.2. As this system is to be adopted, the numbering of series and cases in this chapter is not sequential. Please refer to Table 3.3 for experimental conditions for each case.

In all of the subsequent figures, the following conventions are adhered to unless otherwise stated; all mean velocity values are non-dimensionalised using the bulk mean velocity (U_m), all turbulent stresses and the overall turbulent kinetic energy are normalised using the square of the mean shear stress (U_*^2). The spatial coordinates are consistent with the explanation provided in the introduction to Chapter 3.

4.1 Emergent Cases

4.1.1 Kansai - Single, large aspect ratio block in a simple channel (S4 CIII)

Series 4, Case III consists of an emergent block immersed in the centre of a simple open channel flow. As such, it will provide a baseline to which the more complex compound channel cases can be compared in order to understand the influence of the block location on its wake. Although no exact replica of this simple channel experiment exists in the literature, the results may be evaluated with respect to similar results to summarise the pertinent flow features.

4.1.1.1 Upstream Conditions

Figure 4.1 shows the contours of streamwise and spanwise velocity in the simple channel upstream of the emergent block ($x = -11$). In all figures for Series 4, the values of U are extrapolated from the highest measurement level to the surface and contours are plotted as such. Contours of spanwise velocity are not extrapolated to the free surface, since this process is not expected to produce realistic results and contours are shown up to the highest measurement level only. The contours of U show the expected pattern for open channel flow, where the maximum velocity is found beneath the free surface. The results of (Tominaga *et al.*, 1989) for fully developed open channel flow show that the velocity maximum is at a vertical position of approximately $Z/H_{ch} = 0.79$, where the channel aspect ratio was 3.94 and $Z/H_{ch} = 0.88$, where the channel aspect ratio was 8.00. In this case, where the channel aspect ratio is 6.65, the maximum velocity is at $z = 1.58$, an equivalent of $Z/H_{ch} = 0.40$, which is lower than the published results. It is also apparent that the maximum values of U do not occur exactly in the spanwise centre of the channel but that there is an area of deceleration here. It may be supposed that this slight deceleration is a consequence of the presence of the block in the downstream flow.

Although it was impossible to measure the vertical velocity component and therefore to plot the vectors of the secondary circulations, from examination of the contours of the spanwise velocity, we can see evidence that the expected circulations do occur. In the top left sector and the bottom right, the contours suggest clockwise circulations, whilst in the top right and bottom left sectors, the contours suggest anti-clockwise circulations. The maximum recorded strength of the spanwise velocity is equivalent to 1.86% of the bulk mean velocity, which is comparable to the result of (Tominaga *et al.*, 1989).

Figure 4.2 shows the normalised values of boundary shear stress for the section plotted against wetted perimeter. The values in this figure have been normalised using the average value for this section. The profile is fairly symmetrical but there is clearly a dip in the values at the channel centre. (Tominaga *et al.*, 1989) gives results for a fully developed, uniform flow in a simple open channel of aspect ratio 3.94. From their results on the bed, $\tau/\bar{\tau}$ reaches a maximum of approximately 1.28 at the channel centre. The results from this experiment show a maximum of 1.17 at an off centre position. The depression of the values at the channel centre is likely to be associated with the deceleration of the flow due to the presence of the block at this lateral position in the downstream flow, as shown in Figure 4.1. Tominaga *et al.* (1989) also noted a secondary peak on the channel bed associated with the bottom vortex, where $\tau/\bar{\tau} = 1.04$ at $y/W_{ch} = 0.115$. Such a peak is visible in these results on the left side of the channel, where $\tau/\bar{\tau} = 1.07$ at $y/W_{ch} = 0.152$. No such peak is observed on the right side. On the channel wall, Tominaga *et al.* (1989) described a peak of 1.04 at $z/H_{ch} = 0.667$. In these results, on the right wall, this peak is observed exactly in magnitude and position. On the left bank, the peak is smaller with a magnitude of 0.89.

Overall, the results show that the influence of the presence of the block transmits very far upstream of its position and that the approaching flow is three-dimensional in nature, negating the assumptions that may be made for uniform flows. However, there is evidence of the existence of the flow structures associated with rectangular open channel flow in which we are interested and as such, the

experiment provides a useful comparison to the compound channel case, which is presented in the next section. The slight asymmetries in the results at this section are likely to be a result of a small lateral gradient in the flume bed. Since this factor must be the same for all of the cases in this flume, it is hoped that this will not preclude useful conclusions being drawn from the comparison between simple and compound channel cases.

4.1.1.2 Wake Structure

The measurements downstream of the emergent block were taken at $x = +5.5$. The velocity contours are shown in Figure 4.3, where for this and all subsequent downstream figures, the position of the block is shown with light black lines in order to aid meaningful analysis of the results. The streamwise velocity contours at the downstream cross-section clearly show the deceleration behind the block and the acceleration of the flow around the wake. The contours show that the wake widens significantly towards the free surface, which is consistent with the findings of Kawamura *et al.* (2002), who worked with a surface piercing circular cylinder. They examined the vertical profile of the streamwise velocity at the channel centre in the wake and noted that the maximum velocity tended to occur at approximately one cylinder diameter under the free surface. Above this point, the velocity decreased sharply and usually with a linear profile.

Figure 4.4 shows the vertical profile of streamwise velocity at the block centreline, both upstream and downstream of the block. In this case, the streamwise velocity reaches a maximum at approximately $1.3W_{bl}$ below the free surface and then decreases sharply. Taking an average of both the upstream and downstream centreline profiles, the wake centreline velocity is calculated to be a factor of 0.785 of the approach velocity.

Kawamura *et al.* (2002) suggests that there should be two counter-rotating axial vortices just under the surface downstream of the block; clockwise on left, anti-clockwise on right. The contours of spanwise velocity measured here are not quite symmetrical, but show the flow moving toward the channel centre, expect for two

opposite peaks just under the free surface directly behind the block. The reversal of the flow direction occurs at approximately $1.0W_{bl}$ below the free surface. The reversed spanwise flow measured at the highest possible level ($0.579W_{bl}$ below the surface) suggests that these circulations are present in the current results.

Figure 4.5 shows a comparison of the distributions of the boundary shear stress at the upstream, central and downstream sections. To allow for meaningful comparison, the values have all been normalised using the average boundary shear stress for the entire control volume as defined by the up and downstream sections. At Station 3, i.e. at the block position, the bed shear stress values become very large in the vicinity of the block and are generally elevated from their upstream values throughout the cross section. Downstream of the block, the profile shows a clear dip, symmetrical about the centre of the channel associated with the block wake, whereas the peak value on the bed has increased to $\tau/\bar{\tau} = 1.318$ and the values outside of the wake zone have increased from their Station 3 values more generally.

Bearing in mind the asymmetry in both of the measured velocity profiles that has already been acknowledged, the boundary shear stress data is a good reflection of the changes in the near-bed streamwise velocity distribution that we might expect around an emergent block. As the flow separates from the front edges of the block, there is a nearly equal acceleration around the separated zones. Further downstream, after reattachment, the wake gradually widens out so that velocities outside of it increase further.

Figure 4.6 shows the difference between the upstream and downstream free surface positions, normalised with the block width for both Cases I & III. For the simple channel case, the free surface clearly shows two large troughs, bounding a large central peak. Following the work of Chaplin and Teigen (2003), we would expect there to be a dip in the water surface directly behind the block and indeed this is observed in this experiment, where the difference parameter is mostly negative. The large peak in the profile is directly correlated to the zone of deceleration in the channel centre described in Figure 4.3.

In summary, the results for Series 4, Case III show many of the features that we might expect for the flow around an emergent block from comparison with previous experiments in the record. With this example in mind, we may then proceed to analyse the compound channel cases with reference to it in order to identify any changes in the wake structures that come about by this positioning.

4.1.2 Kansai - Single, large aspect ratio block at the floodplain edge (S4 CI)

Series 4, Case I consists of an emergent block positioned at the edge of the floodplain of a compound open channel flow. The characteristics of the flow, as detailed in Table 3.3, were chosen as to minimise the difference in the relevant influencing flow parameters, i.e. Re/Fr , AR_{bl} and B , and to render the results comparable with those described in Section 4.1.1.

4.1.2.1 Upstream Conditions

Figure 4.7 shows the contours of streamwise and spanwise velocity at the upstream position. When comparing these results to those of Tominaga and Nezu (1991) shown in Figure 2.4 for the fully developed uniform flow case, it is clear that the same characteristic bulging of the streamwise velocity contours at the floodplain edge can be observed. The pattern of the spanwise velocities also suggests that the secondary circulations that tend to produce this exist, since there is a strong positive peak at the floodplain edge. The contours suggest two circulations emanating from the floodplain edge, one close to the floodplain wall and one on the floodplain itself. Although the vertical velocity components are not available, the circulations proposed here are shown, superimposed onto the contours of spanwise velocity in Figure 4.7. The maximum value of spanwise velocity is 4.67% of the bulk mean velocity and is therefore in the approximately correct range as compared to the results of Tominaga and Nezu (1991). Since the geometry of the channel, specifically the ratio of the widths of floodplain and main channel, is different to that

of Tominaga and Nezu (1991) and the flow in this case is not uniform, differences such as the vertical position of the maximum streamwise velocity do exist. In this case, the position of the maximum velocity appears to be lower than that reported previously. However, in general, the flow exhibits the essential features of compound channel flow, relevant to this investigation; a drop in streamwise velocity at the floodplain edge associated with the distribution of turbulent stresses, significant secondary circulations and a gradient of streamwise velocity between the floodplain and main channel.

Comparing the results to the $D_r = 0.5$ case of Tominaga and Nezu (1991) as shown in Figure 2.6, the values of boundary shear stress, shown in Figure 4.8, match well in the main channel. The maximum value in the main channel is $\tau/\bar{\tau} = 1.26$ at a position of $y/W_{mc} = 0.515$, compared to $\tau/\bar{\tau} = 1.15$ at a position of $y/W_{mc} = 0.6$ from Tominaga and Nezu (1991). The secondary peak is also present; in Tominaga and Nezu (1991), $\tau/\bar{\tau} = 0.93$ at a position of $y/W_{mc} = 0.155$ and here, $\tau/\bar{\tau} = 1.1$ at a position of $y/W_{mc} = 0.193$. In general, therefore, the values are slightly higher than those observed by Tominaga and Nezu (1991). On the floodplain bed, both profiles show a gradual increase towards the floodplain edge followed by a sharp decrease in its immediate vicinity. The position of the maximum value is clearly different between the two cases however, where it is further from the floodplain edge in these measurements. This result suggests that whilst the velocity contours do not betray any obvious influence transmitting upstream from the block at this streamwise location, the reduction of streamwise velocity values has to a small extent, in fact, already begun.

Despite this small deviation from the ideal freestream conditions, the measured profile of boundary shear stress broadly confirms that the desired flow structure demonstrated through the velocity measurements does indeed exist at this upstream position. As such, the results from the downstream section and the resultant calculation of drag coefficient can be usefully compared with the results from the simple channel to interrogate the differences in wake structure that the floodplain edge position initiates.

4.1.2.2 Wake Structure

Figure 4.9 shows the contours of streamwise and spanwise velocity downstream of the emergent block at the edge of the compound channel floodplain. At this position in the wake, the streamwise velocity contours directly behind the block show a high degree of lateral symmetry. This symmetrical dip sits within a gradient, whereby the main channel velocities are larger than those on the floodplain. At the measurement point closest to the floodplain bed at $z = 0.589$, the main channel peak velocity is a factor of 1.25 larger than that on the floodplain. At the measurement point closest to the free surface at $z = 3.314$, this has reduced to a factor of 1.07. Under the influence of the altered secondary circulations, the maximum velocity in the channel has moved upward and toward the floodplain from its upstream position.

The contours of spanwise velocity show the flow converging over the majority of the height of the block and evidence of flow reversal near the free surface, in common with the pattern of spanwise velocity observed for the simple channel case. Although at this level of detail, it is impossible to compare and contrast the size of the circulations at the free surface between these two cases, clues may be taken from the remaining data to surmise the likely changes in the character of the flow structure.

Figure 4.10 shows the changes in the vertical profile of streamwise velocity at the downstream block centreline that occur when the block is transferred to the floodplain edge of a compound channel. In comparison with the same plot for the simple channel case, it is clear that the distribution is quite different. Here, the maximum streamwise velocity is found $3.2W_{bl}$ below the free surface with a linear decrease above this point. The average wake centreline velocity is a factor of 0.719 of the approach velocity. Since the wake velocities are clearly less well recovered in the compound channel case, it might be assumed that the recirculation zone is simply longer and that the structural differences are accounted for purely by the different relative position in the wake at which the measurement section falls.

However, Kawamura *et al.* (2002) record a structurally similar wake at various streamwise positions behind their circular cylinder ($x = 1.0, 2.5, 4.5$) so that nowhere in the development of the axial vorticity at the free surface does the vertical profile of U resemble that measured in this case. This suggests that the near-linear decrease in streamwise velocity over the height of the block that is observed here is due to a different process, unconnected to the influence of the free surface.

Figure 4.11 shows the profiles of boundary shear stress normalised with the control volume mean value at the three streamwise measurement stations. At both Stations 3 and 5, the values on the main channel right bank and on the majority of the main channel bed are little changed in magnitude from their upstream counterparts. There are, however, changes to the shape of the profile in these areas, notably including the disappearance of the shoulder on the main channel bed associated with the corner vortex there. This is consistent with the radical changes to the pattern of secondary circulations that occur between the up- and downstream sections. The influence of the block on the streamwise velocity distribution at the bed and therefore the magnitudes of the boundary shear stress begins to appear in a very significant way on the main channel bed at a spanwise position of $y = 4.18$ and continues across the floodplain bed as we might expect, where the boundary shear stress values are elevated at the downstream positions.

Turning to the profile of the downstream water surface as shown in Figure 4.6, it can now be compared to the simple channel case. In the compound channel case, the average downstream water level is again less than upstream and a similar pattern of a distinct peak bounded by two troughs can be seen in the profile. However, the average difference parameter over the cross section and its maximum range is clearly significantly less than that in the simple case.

The smaller average gradient in pressure indicates that the pressure field in the compound channel case is more recovered than that in the simple channel case at this point. The smaller range of values may be a result of the lower channel Froude number of the compound channel flow, due to the greater depth in the

main channel. A detailed comparison of the streamwise velocity profiles at each measured depth suggests that the wake widening associated with the free surface vortices occurs within a narrower vertical band than in the simple channel case. However, at the free surface, the evidence suggests that the wake is wider in the compound channel case since it can also be observed that the lowest points in the water surface in the compound channel case are spread more widely than in the simple channel case. For the simple channel, they are separated by approximately $6W_{bl}$, whilst in the compound channel case, this increases to $12W_{bl}$. This would suggest that the free surface vortices have a smaller vertical scale but larger horizontal scale in the compound channel case.

These results show marked differences in the flow structures between the compound channel case and its simple channel counterpart. Overall, the results indicate that the recovery of the streamwise velocities in the compound channel wake is slower but that the recovery of the pressure field is more advanced. The balance between these two factors and their influence on the overall drag will be explored in the next section.

4.1.2.3 Emergent Block in Simple & Compound Channels - Comparison of Drag Coefficients

For each of the cases in Series 4, data was collected with the aim of calculating a drag coefficient for the flow based on an indirect momentum balance method. The drag force induced by the presence of the block is calculated using Equation 4.1 for the control volume bounded by the channel walls, surface and the up and downstream measurement sections. The value is converted to a drag coefficient with Equation 4.2. The subscripts u and d refer to the upstream and downstream sections respectively, L in this instance is the length of the control volume and p is the perimeter position.

$$f_d = \int_0^A \rho U_d (U_u - U_d) dA + \int_0^A (P_u - P_d) dA - \int_0^p \tau_b L dp + \rho g \sin \theta AL \quad (4.1)$$

Case	Simple Channel	Compound Channel
U_a	0.56	0.46
Re_{bl}	10,011	9,929
Fr_{bl}	1.22	1.21
Fr_{ch}	0.61	0.43
$B(\%)$	3.8	2.3
C_D	1.99	7.05

Table 4.1: Flow Parameters and Drag Coefficients for Single, Emergent Blocks in Simple and Compound Channels

$$C_D = \frac{f_d}{\frac{1}{2}\rho U_a^2 W_{bl} H_{bl}} \quad (4.2)$$

Whilst the accuracy of the electromagnetic velocimeter is quantifiable (see Section 3.1.2.1), the accuracy of the other equipment used to collect the data necessary to use this equation, namely the ultrasonic level meter and the Pitot tube, is not as easy to estimate. As a check on the consistency of the combined data therefore, the time averaged integrated discharge at the upstream and downstream sections is compared. For the simple channel case, the difference is 3%, whilst for the compound channel case, it is 1.6%.

The values of drag coefficient for these two cases are shown in Table 4.1, together with a reminder of the pertinent flow parameters.

Since no exact comparative results are available from other experiments, it is very difficult to validate these results directly. However, a comparison with some previous quantitative and qualitative data provides one means by which to sense check them. Lyn *et al.* (1995) reported the 2D drag coefficient for a square sectioned block to be 2.1. However, the experiments of Chaplin and Teigen (2003)

and others imply that the end effects would tend to suppress the vortex shedding mechanism locally. As the vortex shedding process contributes strongly to the overall drag force exerted by the body, we would expect the overall drag coefficient for a 3D square sectioned block to be less than 2.1. On this basis, the figure calculated here for the simple channel case appears to be reasonable.

For the value calculated for the compound channel, the very great discrepancy between it and the value in the simple channel is a result of the changes in the wake behaviour observed in the velocity distributions described in the preceding sections, where the recovery of the velocities in the wake of the block in the compound channel is significantly delayed. Whilst the other terms in Equation 4.1 vary by a small amount between the simple and compound channel cases, the momentum term changes very significantly.

Whilst the Reynolds number of the oncoming flow in both cases is sufficiently similar to be discounted as an influencing parameter, the nature of the changes to the channel Froude number appear to be responsible for the reduction in the deformation of the free surface between the simple and compound channel cases. The results described in the preceding section suggest that influence of the axial vortices associated with the deformation of the free surface is much reduced in the compound channel case so that the contribution to the overall drag coefficient from these structures is lessened. Despite this change in the extremity of the deformation, the overall recovery of the total pressure field and its consequent contribution to the drag coefficient changes only slightly between the simple and compound channel cases. Whilst the contribution of the axial vortices induced by the deformation of the free surface reduces therefore, this is more than compensated for by an increase in the form drag.

The reduced blockage ratio may also contribute to the increase in drag coefficient as overall, a smaller blockage ratio should result in less entrainment into the wake from the mean flow and a slower recovery. However, the degree of overall difference is small and the effects of the blockage on the wake structure must be complicated as a result of the non-central position of the block in the compound

channel and the wider geometrical effects. Likewise, although not listed here as it could not be calculated from the experimental results, the influence of the change in freestream turbulence between the simple and compound channel cases must be bound up with the complexities of the geometry.

In summary therefore, the large increase in drag coefficient calculated here for the block in the compound channel comes about as a result of a large change in the momentum term in Equation 4.1, which, in turn, is a consequence of the slower recovery rate of the velocity. The details of how the geometrical effects may combine to slow the recovery of the velocity in the compound channel case are explored in the next section.

4.1.3 Loughborough - Single, large aspect ratio block at the floodplain edge (S2 CI)

Series 2, Case I is the case of the single emergent block located at the floodplain edge of the compound channel in the Loughborough flume. From Table 3.3 it is clear that the values of AR_{bl} are very similar to those for the cases above. The value of B is even smaller than those used in the Kansai flume experiments so that its influence should be small. However, when considering the comparability of the results, it must be noted that the Re/Fr ratio is considerably larger in this case. Although the flow around square blocks is much less sensitive to changes in the Reynolds number than the equivalent flow around a circular cylinder, the drop in Froude number that contributes to the change in this ratio may mean that the balance between the mechanisms of flow separation and deformation of the free surface may be different to the previous cases. Broadly speaking however, the results in both flumes should be comparable with care.

4.1.3.1 Upstream Conditions

The difference in the upstream set-up of the flumes in Series 2 and Series 4 is described in Sections 3.1.1.1 and 3.1.2.1. Figure 4.12 shows the contours of stream-

wise mean velocity, the vectors of secondary circulation and the contours of turbulent kinetic energy upstream of the single emergent block in the Loughborough flume. Please note that as the ADV was impossible to use close to the water surface in this case, extrapolation of values to the free surface position at $z = 3.5$ has not been attempted for the following figures. Extrapolation has however been used close to the floodplain bed, where measurements were missed.

The contours of mean streamwise velocity again show the characteristic bulging at the floodplain edge associated with the secondary currents of compound channel flow. This corresponds to a strong peak in the vectors of secondary circulation and in the contours of turbulent kinetic energy at this location. As such, the flow behaviour at the floodplain edge matches the pattern of that which we might expect from the results of Tominaga and Nezu (1991). When comparing the magnitudes of mean streamwise velocity between Figures 2.4 and 4.12, the matter is complicated by the difference in normalisation factor; U_{max} is used by Tominaga and Nezu (1991), while U_m is used here. Since the velocities in the uppermost part of the channel could not be measured, it is impossible to definitively state a vertical position for the maximum streamwise velocity. However, the highest measured velocity is located in the main channel at approximately $Z/H_{ch} = 0.77$, which is reasonable with reference to the results of Tominaga and Nezu (1991) as shown in Figure 2.4. Conversion of the normalisation factor in this case shows that the magnitudes also match very closely. The maximum secondary circulation value is 4.75% of the bulk mean velocity, which is again in the correct range compared to previous results. The magnitude of the values of K/U_*^2 is, in general, lower than those quoted by the previous authors. Tominaga and Nezu (1991) give values in the range of 0 – 4, whereas these results are in the range 0 – 2. This is likely to be due to inaccuracy in the calculation of the mean shear velocity in this case, since an accurate measurement of the free surface and therefore the energy slope was very difficult.

The turbulent intensity at the block centreline at the upstream cross-section was examined in particular in order to provide a comparative freestream turbulent

intensity with the experiments around blocks described in Chapter 2. Lyn *et al.* (1995) define freestream turbulent intensity as $\overline{u'}/U_m$. Calculating this value at the two measurement points at the upstream block centreline gives 7.30% and 7.85% at $z = 1.58$ and $z = 1.79$ respectively. These values are considerably higher than, for example, the 2% value quoted by Lyn *et al.* (1995).

4.1.3.2 Wake Structure - Mean Flow

Figure 4.13 shows the contours of normalised streamwise velocity around the emergent block at a vertical position where $z = 1.1$ and at the measured downstream cross-section at $x = 2.7$. From both plots, it is clear that the structure of the near wake is skewed significantly to the floodplain side of the block centreline throughout the flow depth. The absolute minimum velocity measured was $U = -0.35$ at a position of $(x, y) = (1.3, 0.28)$. Further downstream, outside the recirculation zone, the minimum velocity point moves back towards the main channel so that it is at the central position by a streamwise position of $x = 4.00$. At $x = 5.33$, the profile of U resembles that described in Section 4.1.2.2, where a symmetrical dip sits within a wider overall lateral gradient. Finally, in the lowest portions of the measured wake, the contours show that the wake is widening out into the main channel. This is not accompanied by a similar phenomenon on the floodplain side. These results clearly elucidate that the floodplain edge location has implications not only for the wave making resistance at the free surface, as described in Section 4.1.2.2, but also for the pattern of flow separation about the main shaft of the block.

Although the recirculation zone is no longer symmetrical about the block axis, an estimation of the reattachment length at the block centreline is useful to compare the wake size with that from previous experiments. Using the data collected at $z = 1.1$, the limiting 0 contour is located at the centreline at $x = 2.06$. For the purposes of comparison, the recovery of the streamwise velocity in the case of Lyn *et al.* (1995), which is shown in Figure 2.11, gave a recirculation zone ending at approximately $x = 1.4$. It must be noted that the end effects at the free surface

would act to suppress the vortex shedding and result in a longer recirculation zone near the free surface than that measured by Lyn *et al.* (1995), even in the simple channel case. However, at this height in the wake, this near doubling of the length of the recirculation zone is another hint that the floodplain edge positioning is having a measurable effect on the flow separation process.

In order to meaningfully analyse the streamwise contour pattern, Figure 4.14 shows the contours of mean spanwise and vertical velocity in plan at $z = 1.1$. From the spanwise contours, it can be observed that at the block streamwise centreline, the contours of spanwise velocity are nearly symmetrical, which would suggest similarity between the flow separating from the two leading edges of the block, at least at this vertical position. Despite this initial symmetry in the flow, the distribution of the spanwise velocity begins to show a significant degree of asymmetry in the wake zone behind the block. In the near wake, the maximum values of spanwise velocity are staggered across the wake width. On the floodplain side, the peak value is -0.309 and occurs at $x = 1.3$, whereas on the main channel side, the peak value is approximately 15% smaller at $+0.264$ and occurs at $x = 2.7$. This imbalance suggests that whilst the initial flow separation may be equal, the differing flow conditions on each side of the block affect the development of the recirculation zones and therefore the growth mechanism of the vortices to be shed into the downstream flow. Further downstream in the wake, where the peak values of V on both sides of the block are gradually reducing, the values on the floodplain side can be seen to diminish more quickly than those on the main channel side. A slower decay of the secondary circulations associated with the wake is consistent with the widening of the wake into the main channel that is observed.

Although more detailed measurement would be required to confirm it conclusively, the near equality of the peak spanwise velocities at the streamwise block centreline suggests that the mean position of the separation streamlines on both sides of the block is very similar. We may therefore surmise that the frequency of shedding of vortices on the two sides should be similar. The imbalance in the wake structure must then be a consequence of an imbalance in the size and energy

of the vortices being shed. On the floodplain side, where the geometry resembles the simple case more closely, the vortices are larger and more energetic than those shed from the main channel side, where the separation process is affected by the floodplain edge position and the structure of the separation zone is not simple. Thus, the more efficient creation of vertically orientated vorticity on the floodplain side ensures that the minimum streamwise velocity occurs there.

Once shed however, the process of decay of the vortices is also affected by the floodplain edge positioning. Although calculation of the fluctuating strain rate and vorticity are not possible, an examination of the mean vorticity sheds some light on the process involved in the dissipation of energy. The mean vortex stretching term in the mean vertical vorticity equation $\Omega_z \frac{\partial W}{\partial z}$ was calculated at the only position where enough data was available to do so, i.e. at the intersection of the plan and cross-sectional measurement planes at $(x, z) = (2.7, 1.0)$. This is shown in Figure 4.15. Although the profile is complex in character, it demonstrates that the vortex stretching term peaks at a larger magnitude in the main channel. If this behaviour persists throughout the wake, it would mean that energy transfer from the mean flow to the eddies was greater on the main channel side of the block, delaying the recovery of the mean streamwise velocity.

The contours of mean vertical velocity shown in Figure 4.14 give an indication of a mechanism by which the recirculation zone and vortex shedding process is altered from that which is expected for a simple block. Whilst the spanwise velocities at the streamwise centreline are symmetrical in magnitude, the vertical velocity on the main channel side is 40% greater than that on the floodplain side. In the near wake, this difference increases to 50%. This means that the downflow associated with the rapidly changing pressure field around the block is significantly affected by the floodplain edge position, where the downward flow is limited on the floodplain side by the presence of the floodplain bed but that on the main channel side is not.

As the pressure field recovers behind the block, a positive peak in the vertical velocity profile develops although the position of this peak varies throughout the

length of the wake. This implies that axial vorticity develops in the wake, a consequence of the placement of the block onto the channel bed. Such vorticity was not recognised in the results of the work of Kawamura *et al.* (2002), which have been used elsewhere in this study to provide comparative results, since the block on which they performed experiments was towed through a deep water tank.

The nature of the development of this axial vorticity is not, however, symmetrical. At $x = 2.7$, the peak in W is firmly located on the floodplain side of the block centre at $y = +0.28$. Further downstream, it moves gradually towards the block centreline, reaching its absolute maximum at $x = 4.0$. This correlates well with the measurements of the free surface for the emergent block in the compound channel in the Kansai flume, since a close inspection of Figure 4.6 suggests that the maximum water level is reached on the floodplain side of the block centreline. Finally, at the furthest downstream measurement point at $x = 8.0$, the peak moves to the main channel side at $y = -0.43$.

In order to gain an impression of how the secondary circulations combine to create mean axial vorticity in the wake, the vectors at $x = 2.7$ are plotted in Figure 4.16, showing the detail around the block location. It is of note that the maximum magnitude of the measured vectors is 45% of the bulk mean velocity, which is an order of magnitude larger than the turbulence-induced secondary circulations at the upstream position. At the higher vertical positions, the difference in the pattern of the vertical component is in obvious agreement with that described above. Outside of the zone plotted here, there is evidence of a strong upflow against the floodplain wall, which feeds into the block wake structure. Far from the block in the main channel, the secondary flow vectors appear to be little changed from their upstream pattern.

In order to further elucidate this pattern of secondary circulations, an estimation of the axial vorticity Ω_x is made. Reliable estimations of the mean velocity gradients being required, it was deemed inappropriate to calculate Ω_x at locations where extrapolation had been used to find velocities. As opposed to a contour plot of the entire section therefore, Figure 4.17(a) plots the axial vorticity values at two

vertical levels at $x = 2.7$: $z = 0.84$ and $z = 1.0$. As expected, there are two large peaks in vorticity in the block wake, representing the angular momentum shown in Figure 4.16. At both levels however, it is also clear that the peak on the main channel side is considerably larger than that on the floodplain side. At $z = 0.84$, the main channel peak is 32% larger than that on the floodplain side. At $z = 1.0$, this has decreased to 25%.

The two measurement planes coincide at $(x, z) = (2.7, 1.0)$ and it is therefore possible to calculate all of the mean velocity gradients at these points and ultimately, the magnitude of the production terms in the mean axial vorticity equation. These values are plotted for the area within $-1.5 < y < 1.5$ in Figure 4.17(b) together with P_{Ω_x} , the sum of these contributions. It is clear from this plot that the transverse and vertical contributions are largely cancelled out by one another so that the vortex stretching component is the greatest contributor to the production of axial vorticity. The distribution of this component shows that due to the changes induced in the separation zone on the main channel side of the block by the unequal distribution of vertical momentum, the vortex stretching mechanism tends to be stronger on this side.

These results show that the difference in the distribution of vertical momentum due to the differing water depths on the two sides of the block has significant implications for the turbulent structures that form around it. Whilst the separated zone on the floodplain side of the block forms in a way close to that which we might expect for a block in a simple flow, that on the main channel side does not. This results in a striking imbalance in the vertically orientated vortices that are shed from the shaft of the block, where those on the main channel side are less energetic than those on the floodplain side. It also creates asymmetrical axial vorticity in the wake zone, so that the secondary flows on the main channel side are stronger than those on the floodplain side and act to change the secondary flow pattern in the main channel, particularly at the floodplain wall.

Downstream of the base region very near to the block, the differing intensities of vertical vortex stretching because of the different flow depths either side of the

block appear to contribute to different rates of decay, such that flow recovery is slower on the main channel side.

4.1.3.3 Wake Structure - Turbulence Statistics

The data collected from the ADV also allows for the presentation and analysis of the turbulent field. In this section, results will be presented that combine both the periodical component of the turbulence due to regular structures such as von Karman type eddies with the truly random component. Although the results have not been disaggregated, the differences between the measured profiles and those recorded in the literature for blocks in simple channels are worth investigation.

Lyn *et al.* (1995) described the pattern of the streamwise and spanwise normal Reynolds stresses for the 2D case in which vortex shedding is the dominant process, at a streamwise location where $x = 1$. The profile of $\overline{u'^2}$ shows that a maximum value is attained in the shear layer region, which for their experiment was found at approximately $y = \pm 0.7$. At the block centreline, the magnitude drops to 65% of this maximum value. The profile of $\overline{v'^2}$ is more nuanced, but shows its maximum value at the block centreline. The difference in the distribution of the periodic component of the normal turbulent stresses is an important factor in the final structure of the wake.

Lyn *et al.* (1995) set up their experiment so as to create 2D conditions at the vertically central position of a square block mounted in a wind tunnel. Having satisfied themselves that the flow at this position was sufficiently close to the 2D condition, they based their calculation of the total fluctuating kinetic energy on the streamwise and spanwise components alone; the vertical components were assumed to be negligible and were not measured. The total turbulent kinetic energy K for this case, including the vertical component, is plotted in Figure 4.18, where it is normalised using the bulk mean velocity. At the centreline, the peak turbulent kinetic energy is located at approximately $x = 3.4$, where a value of 0.184 is reached. This peak is significantly smaller and later than that observed in the 2D

case of Lyn *et al.* (1995), which correlates well with the observation in the previous section that this case exhibits a significantly longer recirculation region.

The streamwise variation in K is also plotted at $y = \pm 0.5$. This shows that the lateral distribution of turbulence also deviates from the symmetrical 2D case considerably, such that the peak in turbulent kinetic energy on the floodplain side of the block is considerably larger than that on the main channel side. This can be explained via an examination of the individual normal fluctuating stresses. For this case, Figure 4.19 shows the plots of the streamwise normal Reynolds stress $\overline{u'^2}$, where part (a) shows the plan profile and part (b) shows detail of the downstream cross-section at the block location. Although the flow around the block in this case is highly 3D, the two distinct peaks in $\overline{u'^2}$ identified in Lyn *et al.* (1995) are clearly observable in these results, where at $x = 1.3$, the peak values are found at $y = -0.67$ and $y = +0.75$ respectively. Unlike the results of Lyn *et al.* (1995) however, the two peak values are clearly unequal throughout the length of the wake, where the absolute peak value on the floodplain side of the block is 9.2% greater than that on the main channel side. The spanwise normal Reynolds stresses $\overline{v'^2}$ is shown in Figure 4.20. In the near wake zone, there are two distinct peaks in the profile, where the peak on the floodplain side is 19.5% larger than that on the main channel side. From the results of Lyn *et al.* (1995), we might not expect a pattern of two peaks in the spanwise component. However, the recirculation length in this case, it must be remembered, is considerably larger than that in the purely 2D case so that the measurements are not being taken at equivalent points in the wake. Indeed, further downstream in this case, a single peak in $\overline{v'^2}$ does emerge. This is located not at the block centreline but toward the floodplain side of the block, where it gradually reduces. Thus the patterns of the streamwise and spanwise Reynolds stress components in the plan dataset show agreement with the measurements of mean velocity, namely that the vortex shedding phenomenon is being altered such that at equivalent depth, the vortices shed on the floodplain side of the block are more energetic than those shed on the main channel side.

The limitations of the analogy with the 2D case can be understood by observation of the cross-sectional data in both Figures 4.19 and 4.20. Both profiles show that the tendency of the larger Reynolds stresses to lie on the floodplain side of the block persists throughout the measured depth. This is consistent with the observation that the minimum streamwise velocity is located on the floodplain side throughout this measurement set. However, neither profile is vertically uniform. The cross-sectional detail of the streamwise component shows that the double peaked profile exists at all measurement points. Likewise, the single peak in the spanwise component can also be observed throughout the depth. Although positions near to the free surface or very close to the bed could not be measured, this indicates that the vortex shedding regime is indeed present over a substantial portion of the shaft of the block.

However, it is also true that the magnitudes of the streamwise component tend to increase with increasing vertical position, whilst the magnitudes of the spanwise components show the opposite tendency. Perhaps of more pertinence to this case in particular, is the variation in the asymmetry over the depth. As we might expect, the difference between the two peaks in $\overline{u^2}$ is higher near the floodplain bed than near the free surface. The position of the peak in $\overline{v^2}$ is further towards the floodplain side near the floodplain bed than near the free surface. Since the velocity gradient between the floodplain and main channel flow is at its greatest near to the floodplain bed, it is consistent that the discrepancy between the energy of the vortices being shed from the two sides of the block is greatest there also.

To complete this description, it is necessary to examine the vertical normal Reynolds stress, which is plotted in Figure 4.21. The magnitude of the vertical component is considerably less than the spanwise and streamwise components so that the vertically orientated vortices, as we might expect, contain the largest proportion of the total fluctuating energy. The vertical component, i.e. the turbulence associated with the axial and lateral vorticity, also however reaches its maximum on the floodplain side of the block, a pattern that is consistent throughout most of

the measured depth. This must be associated with the greater lateral vorticity that the presence of the floodplain bed on that side of the block initiates.

In order to further analyse the sources and distribution of the turbulent kinetic energy in the wake, the Reynolds shear stress data at the intersection points between the measured planes was combined with the mean strain rates, thus enabling the calculation of the production term in the turbulent kinetic energy conservation equation, P_K , using Equation 4.3.

$$P_K = -\overline{u'_i u'_j} \left(\frac{\partial U_i}{\partial x_j} \right) \quad (4.3)$$

Figure 4.22 shows the components of and overall turbulent kinetic energy production in this location. As suggested by the normal turbulent stresses, the greatest contribution to the production of turbulent energy is the component in the horizontal plane, i.e. that associated with the shed vortices. The axial contribution is relatively modest but crucially, it is the transverse contribution that ensures that the overall production term is significantly greater on the floodplain side of the block. This distribution of P_K would suggest that the imbalance in the distribution of fluctuating energy that we observe is due to the large difference in the production term, rather than any significant transport of K by the mean flow.

The distribution of the turbulent shear stresses is key to the production of turbulent kinetic energy. In the horizontal plane, as might be expected, the two peaks in $-\overline{u'v'}$, plotted in Figure 4.23, are unequal with the larger value occurring consistently in the shear layer on the floodplain side of the block. This is consistent with the greater shear associated with the larger spanwise gradient in U , which must exist on the floodplain side of the wake, where the minimum wake velocity lies. The spanwise positions of the peaks at $x = 1.3$ are approximately in line with the results for the 2D case of Lyn *et al.* (1995), who noted the peak to appear at approximately $y = 0.75$ at $x = 1.0$. As the positions of these peaks provide a reliable estimate of the position of the shear layers, this serves to confirm that in the very

near wake at least, there is no largescale change in the width of the wake to the symmetrical, 2D case. Although not shown, this pattern persists throughout the measured depth at the measured cross section. In the transverse plane, the same pattern of the absolute maximum appearing on the floodplain side of the block is apparent throughout the majority of the wake and throughout the depth at the measured cross-section. This turbulent component is dependant on shear in the transverse plane so that the differences in the distribution of vertical momentum across the wake due to the floodplain edge location must be a controlling influence.

Finally, the cross-sectional component $-\overline{v'w'}$ shows a complex distribution, particularly in the near wake where the axial vorticity emanating from the separated regions is establishing itself. Further downstream, the larger vorticity on the main channel side identified in the contours and vectors of V and W ensures that the shear force in the cross-sectional plane and the consequent turbulent shear stress also peaks on this side.

4.1.3.4 Summary

The results described above for the single, large aspect ratio, emergent block at the floodplain edge clearly show significant differences from those that we might expect to see in a simple, symmetrical channel set-up. Although these results suggest that the separation angle from the upstream leading edges of the block shaft is similar on both sides, the nature of the wake as measured here requires that significant differences must develop within the lateral separation zones. Changes in the expected development of the separation zone on the main channel side in particular, cause asymmetry in the wake structure from its inception. Whilst the increased blockage due to the non-central position of the floodplain edge in the channel may be contributing to this asymmetry, changes in the main channel separation zone due to the sudden increase in water depth are also important.

The results suggest that the vertically orientated vortices remain the most energetic wake structures overall, which goes to explain why the disruption of the

shedding process results in a significant change in the wake structure; the distribution of the fluctuating energy is skewed to the floodplain side from the outset, since the eddies shed from that side of the block tend to be larger and more dominant than those shed from the main channel side. Due to this difference in behaviour, the minimum wake velocity occurs skewed towards the floodplain side of the block centre.

Further downstream in the wake, where the shed vorticity must dissipate, the vortex stretching process appears to be more exaggerated in the deeper main channel flow, so that the vorticity on this side is dissipated more slowly and the rate of the recovery of the wake is reduced compared to that on the floodplain. Whilst the initial separation pattern ensures that the actual magnitude of U at the measured depth remains higher on the main channel side than on the floodplain side, the difference in recovery rate eventually leads to a reversal of this trend and the widening of the wake into the main channel.

In addition to the changes induced in the energetic horizontal vortex structures, the floodplain edge geometry also has a significant impact on the transverse and axial vorticity associated with the recovering flow. In particular, the vertical momentum created as the flow passes around the block on the main channel side is considerably greater than that on the floodplain side. As the flow begins to recover, the vertical momentum in the main channel decays more slowly. This slower rate of change means that less energy is associated with the transverse shear in the main channel. The persisting vertical momentum in the main channel, which causes significant changes to the secondary circulations, contributes to the greater axial vorticity found there.

Thus, the results from the Loughborough flume for a single, large aspect ratio block tend to suggest the pattern implied by the Kansai results, namely that the deeper main channel flow on one side of the block alters the characteristics of the wake in such a way to slow the recovery of the flow in the wake and increase the overall drag coefficient of the block.

4.1.4 Loughborough - Multiple, small blocks at the floodplain edge (S1 CII)

In order to provide some context to the single block experiments and to provide a starting point into an investigation of the effects of changes in block and channel geometry on the processes described above, the multiple block arrangement of this case is very useful. The important differences between this case and those preceding it are as follows: a much lower block aspect ratio such that no area of regular vortex shedding may be expected, a significantly lower relative depth in the compound channel and finally, the arrangement of multiple blocks along the floodplain edge. It is hoped that by also considering this data, it may be possible to see what features of the flow as described above are enhanced or diminished as a result of these changes. The vertical measurement position in this case is at $z = 0.5$. From these changes, we might expect that the deformation of the free surface would have a greater relative impact on the dynamics of the wake, that there may be stronger shear between the floodplain and main channel flow and that each block would be affected by the influence of its predecessors.

The amount of measured data for this case is much less than the previous cases. However, it is sufficient to highlight some important similarities and differences in the flow structure from that observed for the single large aspect ratio blocks. Figure 4.24 plots all of the measured mean velocities, from which it is immediately clear that the relative wake width is considerably greater, especially on the floodplain side of the block. The overall spanwise gradient of U from the floodplain into the main channel is also much greater than previously, where at Station 3 ($x = +3.5$) the peak velocity in the main channel is a factor of 1.46 larger than that on the floodplain. The greater velocity gradient between the floodplain and main channel flow must develop as the result of a combination of factors; firstly, the smaller relative depth of the floodplain flow and secondly, the effects of the multiple block arrangement in gradually decelerating the floodplain flow. This suggests that the blocks exist in a stronger shear layer than that in the previous experiments. A final

feature that is not observed in the single, large aspect ratio experimental results is the existence of two maxima in the streamwise velocity profile in the main channel, at approximately $y = -2.5$ and $y = -6.5$.

The spanwise and vertical mean velocities are plotted as vectors in Figure 4.24(b). At the upstream station, $S1$, the axial vorticity from the preceding block can be observed. As with the single, large aspect ratio block case, the recovering wake flow tends to form two axial circulations, rotating such that there is a resultant upflow at or near the block centreline. The vectors at the upstream position suggest that there may be an anti-clockwise circulation in the main channel and a clockwise circulation on the floodplain near the block, forming this vorticity. The vortices meet not at the block centre however, but at the main channel edge.

As the flow passes the block, the characteristic imbalance in the vertical velocities across it appears, where at this vertical position, there is upflow on the floodplain side and some downflow on the main channel side. At the third and fourth stations, the vectors show that the two axial circulations at the blocks have been firmly reestablished. This pattern of flow has parallels with that observed in Series 2, Case I, where two zones of axial vorticity are also observed and of these, the main channel circulation is dominant. A difference again lies however, in the spanwise positions of these circulations since in this case, the maximum vertical velocity and the zero spanwise velocity are pushed to the main channel edge of the block thus suggesting that the position of the circulations is shifted into the main channel in comparison to those measured in Series 2. The vectors also suggest that the dominance of the main channel circulation is enhanced in this case.

From these measurements, it is again clear that the floodplain edge positioning of the block has significant implications for the pattern of flow separation and reattachment in the wakes. Due to the differences in block aspect ratio, it is to be expected that the contribution of the vertically orientated vorticity to the wake energy will be considerably less than in the large aspect ratio cases. However, the sudden increase in depth on the main channel side of the block is impacting strongly on the distribution of vertical momentum, such that, just as previously,

the axial vorticity on the main channel side is more significant than that on the floodplain side, on this occasion emphatically so. No doubt due to the smaller relative depth, this effect is even stronger here than in the large aspect ratio case. It seems likely, therefore, that the secondary circulations induced as the flow passes around the obstacle at the floodplain edge, are responsible for the double peak observed in the streamwise velocity profile.

Figure 4.25 shows both the overall mean turbulent kinetic energy and the three individual components of the normal turbulent stress. There is a large peak in the turbulent kinetic energy located directly at the main channel edge of the block in this case, accompanied by a shoulder in the profile on the floodplain side. From the plots of the individual normal turbulent stresses, it can be seen that each component follows the general pattern established previously so that the streamwise component peaks in both of the shear layers, whilst the other components peak once near the centreline. However, for this block geometry, the maximum value of all three components is found at $y = -0.5$, i.e. exactly at the floodplain edge position. The distribution of the turbulent Reynolds stresses is wholly consistent with this pattern, as shown in Figure 4.26. For every component, the distribution is skewed so that large negative values are found at the floodplain edge position.

The changes observed in the distribution of the turbulence parameters are indicative of the sensitivity of the turbulent field to changes in the geometric parameters of the block and channel and also of the impact of setting the blocks in series. The lower relative depth of flow on the floodplain and the smaller block aspect ratio mean that the axial vorticity is more significant in contributing to the overall wake turbulence than would be the case in the previous series. The lower relative depth must also act to accentuate the degree of difference in the distribution of vertical momentum around the block so that the difference in the turbulent energy associated with the two axial vortices is proportionally greater and the position of the vortices appears to move toward the main channel. However, since it is the case that as the flow passes successive blocks at the floodplain edge, the floodplain flow will be decelerated whilst the main channel flow far from the block is not, the

degree of asymmetry in the turbulent structure of the wake must also be a consequence of the multiple block arrangement and the large difference in the peaks of $\overline{u'v'}$ that develops. The small block aspect ratio and relative depth then ensure that the other components peak in the same location. In order to explore the variation of these features with the changing geometry and arrangement of blocks, would require many physical experiments to be performed. The numerical model will therefore be used to investigate these variations, where its ability to usefully reproduce the experimental results is explored in Chapter 5.

4.2 Submerged Cases

This section includes a similar presentation of the results of measurements around submerged blocks as Section 4.1 provides for emergent blocks. In these cases, the measured values must be viewed with consideration of the different flow structures that we might expect from this flow type, since the submergence of the block will involve flow separation not only from the block sides but also from the block top and consequent downflow in the wake.

4.2.1 Kansai - Single, large aspect ratio block in simple channel (S4 CIV)

4.2.1.1 Upstream Conditions

For this experiment in the simple rectangular channel, the contours of streamwise and spanwise mean velocity and the distribution of boundary shear stress at the upstream section ($x = -11$), as shown in Figures 4.27 and 4.28, closely resemble those presented in Section 4.1.1.1. The influence of the block can be observed through both the distortion of the velocity field and the drop in boundary shear stress at the channel centre. The contours of streamwise velocity show a very similar pattern to that shown in Figure 4.1, where the maximum velocity is to be found at a low vertical level in the channel and there is a clear asymmetry in the distribution of the velocity, with the values in the upper right quadrant being significantly depressed in comparison with those in the left quadrant.

The contours of spanwise velocity also show a similar picture, where the contours suggest a clockwise circulation in the top left corner of the channel and an anti-clockwise circulation in the top right. In common with Case III, there is stronger evidence of the counter-rotating vortices that we would expect in the lower corners of the channel on the right than on the left. At the channel centre, where the flow is decelerating in front of the block, there is a complex pattern of spanwise velocities. Overall, the maximum spanwise velocity in the measured zone

is 1.36% of the bulk mean velocity, which is slightly smaller than that measured in Case III.

The profile of boundary shear stress measured at this location is shown in Figure 4.28, again where values have been normalised using the section mean value. In this case, the maximum value is $\tau/\bar{\tau} = 1.15$, which is very similar to that measured in Case III. The depression at the channel centre associated with the presence of the block in the downstream flow is again apparent. Although no distinct secondary peaks are observed in the measurements, the shape of the profile on the left of the channel suggests that there may be one, again at approximately $y/W_{ch} = 0.115$. On the right channel wall, a peak of $\tau/\bar{\tau} = 0.914$ occurs at $z = 0.49$. On the left channel wall, a peak of $\tau/\bar{\tau} = 0.975$ occurs at $z = 0.52$. Both values are therefore slightly lower both in magnitude and position than those observed by Tominaga *et al.* (1989).

From these results, it is clear that the flow is very similar to that observed in Case III for the emergent block in so much as it is not fully developed and uniform but rather 3D in nature, although exhibiting many of the features of the developed flow case.

4.2.1.2 Wake Structure

Figure 4.29 shows the mean velocity contours in the wake of the submerged block at $x = +5.5$. The depression of mean streamwise velocity in the upper right quadrant is again noticeable and has an effect on the symmetry of the flow around the block. However, otherwise the contours show the flow pattern that we might expect. The flow accelerates around a central wake in the lower part of the channel, in which there are two peaks at the block edges and a central dip. The vertical profile of the wake according to the contours of mean streamwise velocity is such that it is narrower at the top and widens out towards the bottom. In this respect, it is similar to the modelled results of Fröhlich and Rodi (2004) for a submerged circular block.

Figure 4.30 shows the vertical profile of the mean streamwise velocity at the block centreline upstream and downstream of the block for the simple channel case. The top of the block is located on this vertical scale where $z = 2.5$. For this, the simple channel case, in the zone behind the block, the profile agrees with the results of Fröhlich and Rodi (2004). They observed that the recirculation zone is shorter near the top of the cylinder and longer at the bottom, which correlates with the greater recovery of the flow near the top of the block measured here. This profile means that the mean value throughout the depth at this location in the wake is a factor of 0.94 of that at the upstream position. The contours of spanwise velocity are consistent with the presence of two counter-rotating vortices in the wake, where there is a clockwise circulation on the left side and an anti-clockwise circulation on the right. This is consistent with previously published results including Fröhlich and Rodi (2004) and Martinuzzi and Tropea (1993), who identified the vorticity as emanating from the separated region around the block.

The profiles of boundary shear stress at the three streamwise locations are shown in Figure 4.31. The profiles are generally similar to those observed for the emergent block, however the profile at the downstream location in particular shows that the wake for the submerged case is considerably wider and the minimum bed shear stress value at the centre of the wake is smaller. As the bed shear stress profile is a reflection of the near bed velocities, this observation is consistent with the suppression of the vortex shedding as described by Fröhlich and Rodi (2004), which implies a wider wake width and a lesser minimum wake velocity. Finally, Figure 4.32 gives a comparison of the deformation of the free surface for the submerged simple and compound channel cases. In this simple case, the profile is similar to that for the emergent case (Figure 4.6) in that there is a central peak bounded by two large troughs, which delineate the wake zone. Since the wake in the submerged case tends to be wider than that in the emergent case, the greater blockage caused by the larger separated zone causes the overall deformation of

the free surface to be larger, although the relative deformation from the minimum point on the surface to the peak of the central trough is approximately similar.

4.2.2 Kansai - Single, large aspect ratio block at the floodplain edge (S4 CII)

In line with the methodology for the emergent block cases in the Kansai flume, Case II was set-up in order to minimise the differences in Re/Fr , AR_{bl} and B with Case IV. This data can be examined in Table 3.3.

4.2.2.1 Upstream Conditions

As we might expect, the contours of mean streamwise and spanwise velocity at the upstream position in this case, as shown in Figure 4.33, are very similar to those observed for the emergent compound channel case (Figure 4.7). The maximum magnitude of the spanwise velocity is slightly smaller at 3.61% of the bulk mean velocity but still similar to that observed by Tominaga and Nezu (1991). The accompanying profile of boundary shear stress (Figure 4.34) is, again, very similar to that measured in the emergent block case (Figure 4.8). Here, the maximum value in the main channel is $\tau/\bar{\tau} = 1.24$ at a position of $y/W_{mc} = 0.497$, compared to $\tau/\bar{\tau} = 1.26$ at a position of $y/W_{mc} = 0.515$ from Case I. The secondary peak is again present, where $\tau/\bar{\tau} = 1.13$ at $y/W_{mc} = 0.193$. The spanwise area over which the effect of the block can be seen in the boundary shear stress profile is reduced in this case in comparison to Case I but the same pattern is evident on the floodplain bed, where the boundary shear stress increases from the floodplain wall towards the floodplain edge zone until it is depressed in the zone directly upstream of the block location.

4.2.2.2 Wake Structure

The data measured at the downstream position for the submerged block on the floodplain edge shows quite different flow behaviour to that observed in the cor-

responding simple channel case. From the contours of streamwise mean velocity, shown in Figure 4.35, although the deceleration behind the block associated with the wake can be observed, it is clear that the central dip evident in the simple channel case has disappeared. The contours also appear to bulge significantly towards the main channel. The contours of spanwise velocity show no evidence of the circulating flow that was observed in the simple channel case since there is no change in direction near the block base. Instead, the flow toward the centre directly behind the block is characterised by larger velocity magnitudes on the floodplain side. In the zone above the block however, the dominance is reversed so that the orientation of the zero contour is significantly deviated from the vertical in both directions.

The vertical profile of the mean streamwise velocity at the block centreline, as shown in Figure 4.36, shows more clearly that the wake behind the block in the compound channel is significantly less well recovered than that in the simple channel. As a result of this, the depth-averaged value at this location in the wake is a factor of 0.8 of that at the upstream position. However, it is not only the magnitudes of the velocity at the centreline that have changed, but also the shape of the profile since the degree of difference between the recovery at the top and the bottom of the block has reduced.

The results for the boundary shear stress throughout the measurement zone are shown in Figure 4.37. It is obvious that at the downstream position, the distribution of bed shear stress in the wake can clearly be seen to be skewed toward the main channel, which is consistent with the velocity measurement results.

The skew of the flow above the block towards the floodplain side of the wake is clear in the profile of the downstream water surface for the compound channel case, which is shown in Figure 4.32. The position of the maximum water level is displaced by approximately one block width towards the floodplain side, which is consistent with the distribution of spanwise velocities in this location. Overall, the positioning of the block at the floodplain edge position tends to produce a much smaller deformation of the free surface outside of the wake zone. However, the

much larger central peak is an indication that the relative deceleration in the wake is significantly larger, which corresponds well with the mean streamwise velocity profile as described in Figure 4.36.

Unlike the emergent cases, where the wake structure over the majority of the height of the block is dominated by the balance of the flow separating from the sides and the resultant vortex shedding oscillation, the wake behind the submerged blocks is controlled by a combination of this process and the effect of the flow over the top surface. For this case in the compound channel, the velocity contours suggest the presence of these two features since the wake is skewed in one direction near the block base and in the other near the block top. One may speculate that the process of axial vortex formation on the main channel side of the block is disrupted by a complex interaction of the separating flow with the floodplain edge. Separation on this side of the block being thus inhibited, it may be postulated that the recirculation region on the floodplain side grows to be more dominant.

The freestream flow approaching the top of the block is complex due to the secondary currents associated with floodplain edge of the compound channel (Tomimaga and Nezu, 1991) and must therefore also cause the separation pattern on the top of the block to be altered. The flow, having separated at the leading edge, would be expected to re-attach onto the top surface, before again separating at the trailing edge. The point of reattachment, however is likely to vary across the width of the block top in this case. The higher freestream turbulence level or lower freestream velocity on the main channel side may lead to earlier reattachment, skewing the separation streamline and consequently also the flow over it.

4.2.2.3 Submerged blocks in simple & compound channels - Comparison of Drag Coefficients

As in the emergent block cases, the drag coefficients for the submerged blocks in simple and compound channel set-ups are shown below in Table 4.2. In this case, the difference in time averaged integrated discharge at the upstream and

4.2 Submerged Cases

Case	Simple Channel	Compound Channel
Re_{bl}	10,764	9,006
Fr_{bl}	1.31	1.10
Fr_{ch}	0.62	0.42
$B(\%)$	2.4	1.5
C_D	3.55	3.35

Table 4.2: *Flow Parameters and Drag Coefficients for Single, Submerged Blocks in Simple and Compound Channels*

downstream sections for the simple channel case is 2.6%, whilst for the compound channel case, it is 0.3%.

The values of C_D calculated here for both cases are striking for their relatively large magnitudes. Even accounting for the larger drag coefficient that we might expect for a square block, the value for the block in the simple channel is clearly significantly larger than the value predicted by Fröhlich and Rodi (2004) for the case described in Section 2.4.3, $C_D = 0.88$. This may suggest that there is a discrepancy in the results for the simple channel case, causing the drag coefficient to be over-estimated. Even accounting for such a discrepancy, the results clearly demonstrate that the difference between the values measured in the simple and compound channels is far smaller in comparison to that for the emergent cases.

The influence of the important flow parameters shown in Table 4.2 must of course be considered. The assumptions to be drawn from the figures in Table 4.2 must be largely similar to those for the emergent blocks. Again, the difference in the Reynolds number of the approaching flow is unlikely to be large enough to significantly affect the structure of the wakes and here, even more so, the overall magnitudes and the degree of difference between the blockage ratios is very small. Unlike the emergent cases however, the reduction in the channel Froude number would in this case have a minimal effect on the vortex shedding process, where it

exists around the submerged blocks. The smaller Froude number may, however, partially account for the smaller overall deformation of the free surface in the compound channel case.

The influence of the compound channel geometry and the changing upstream distribution of turbulent kinetic energy have been shown to have a clear effect on the recovery of the pressure and velocity fields. Their part in the alteration of the drag coefficient will be examined in the next section.

4.2.3 Loughborough - Single, large aspect ratio block at the floodplain edge (S2 CII)

Series 2, Case II is the case of a submerged block at the floodplain edge in the Loughborough flume. As with the emergent cases, efforts were made to make comparisons possible such that the aspect ratio of the block is identical to that used in Series 4 and the blockage ratio is very similar to that in Series 4, Case II. Re/Fr is again larger in this case than that achieved in the Kansai experiments but it is hoped that the difference is not so large as to disbar comparison of the results.

4.2.3.1 Upstream Conditions

Figure 4.38 details the upstream conditions for this experiment, showing the contours of mean streamwise velocity and turbulent kinetic energy and the vectors of the secondary circulations. Again, due to the inability of the ADV to measure in the upper portion of the flow, data is shown only for vertical positions where measurement was possible and the figures do not extend to the free surface.

The results are very similar to those observed in the emergent case, where bulging of the streamwise velocity contours at the floodplain edge position can be seen, together with a peak in the turbulent kinetic energy at this position. The highest measured streamwise velocity in this case occurs at $Z/H_{ch} = 0.77$, which is identical to the emergent case and therefore compares favourably with the results of Tominaga and Nezu (1991). The maximum secondary circulation is 5.80% of

the bulk mean velocity, which is slightly higher than that measured in the emergent case but nevertheless, reasonable when compared to previously published results. The values of K are also again slightly lower than that which we might expect from Tominaga and Nezu (1991), being in the range of 0–1.5. Using the definition from Lyn *et al.* (1995) for freestream turbulent intensity of $\overline{u'}/U_m$, the values available at the upstream centreline for the block are 9.71%, 7.81% and 7.45% at $z = 0.26$, $z = 1.58$ and $z = 2.00$ respectively. With the requisite spanwise gradient in mean streamwise velocity, significant secondary circulations and this elevated turbulent energy level, the following results from the wake of the block should give a good indication of the effects of this positioning on the wake structure.

4.2.3.2 Wake Structure - Mean Flow

Figure 4.39 shows the contours of normalised streamwise velocity around the emergent block at a vertical position where $z = 1.0$ and at the downstream cross-section at $x = 2.7$. The plan data confirms that the skew of the wake into the main channel is occurring throughout the length of the wake. In the recirculation zone, the absolute minimum streamwise velocity is $U = -0.253$ and occurs at $(x, y) = (1.3, -0.20)$, although overall within the recirculation zone, the symmetry of the wake is much greater than that of the emergent case. After reattachment, the skew into the main channel becomes progressively more accentuated until at $x = 4.0$, the minimum velocity is situated at the main channel edge of the block. The cross-section of data shows the nascent skew in development and although data was not captured near the top of the block, like the results in the Kansai flume, the trend is for the effect to lessen as the vertical position increases. Although there are no results with which to directly compare, since the results from the Kansai flume suggest that the recirculation zone is larger for the compound channel case, it is worth noting that at $z = 1.0$ in this case, at the block centreline the recirculation zone ends just beyond $x = 2.0$.

Figure 4.40 shows the contours of mean spanwise and vertical velocity in plan. Since the position of the wake according to the contours of streamwise velocity cor-

responds well with the previous results from the Kansai flume, at the measurement depth of the plan results, we might expect to and do indeed see larger spanwise mean velocity values on the floodplain side of the block centreline in the wake. However, these results reveal that this feature occurs throughout the length of the wake. Unlike the emergent case, where there was no evidence of a significant difference in size of the separation zones on either side of the block, in this case, there is a small discrepancy in the spanwise velocities at the block streamwise centre position, where the higher main channel values would suggest that the separation zone on the main channel side may be slightly larger. As is clear from the contours of streamwise velocity, the imbalance in the wake positioning tends to grow significantly in the downstream direction. This is reiterated in the spanwise velocity results since the imbalance between the peak values on either side of the wake also increases.

Just as with the emergent case, the vertical velocity profile shows that the downflow associated with the separating flow around the shaft of the block is greater in the main channel than on the floodplain. However, the structure of the wake in this case being complicated by the flow over the top of the block, the wake distribution of vertical momentum is more complex. Although it is difficult to make out from the figures, the results indicate that the flow coming over the top of the block is angled towards the main channel, which supports the theory discussed in Section 4.2.2.2 that the reattachment and separation pattern on the top of the block will be angled because of the floodplain edge positioning.

In the near wake, a small but strong circulation can be identified in Figure 4.40(b) on the main channel side, which is completely lacking on the floodplain side. This is rotating in an opposite sense to the axial vorticity that we see more centrally due to the flow over the top of the block. Although this feature quickly diminishes, its effects are felt downstream, as can be clearly seen in the plot of the secondary velocity vectors at $x = 2.7$, shown in Figure 4.41. This shows that the axial vorticity on the main channel side is hindered from forming as it does on the floodplain side by a strong upflow from the main channel. The upflow noted at the

floodplain wall in the main channel is also present in the secondary flow vectors in the emergent case (Figure 4.16). In that case, a commonality of direction means that it reinforces the axial vorticity contribution on the main channel side of the wake. In this submerged case, where the direction of rotation of the prevailing vorticity is opposite, it has the reverse effect and diminishes the main channel vortex in comparison with that on the floodplain side.

Estimations of the vorticity components were again made at $(x, z) = (2.7, 1.0)$ and are plotted in Figure 4.42. At this location, the results show that whilst the vertical vorticity of the average flow remains that largest component overall, its dominance over the other components is slightly reduced from that of the emergent case and its profile is symmetrical. The profiles for the axial component and crucially, for the transverse component are heavily skewed towards maxima on the main channel side.

These results show that, perhaps even more so than in the emergent case, the floodplain edge positioning of the submerged block has considerable implications for the formation of the wake and the subsequent flow pattern in the channel more widely. Not only is the separation and reattachment of the flow around the block shaft affected, particularly by the uneven vertical momentum distribution on either side of the block, but the pattern of reattachment on the top of the block is also skewed. These effects combine to create an axial vorticity pattern in which the vortex structure on the main channel side is disrupted and comes to be dominated by the structure on the floodplain side. Moving downstream, this effect is accentuated as the wake drifts into the main channel.

4.2.3.3 Wake Structure - Turbulence Statistics

The key features of the turbulent field that are contributing to the wake structure described above are revealed through the following data. Figure 4.43 shows the total turbulent energy distribution, at $y = -0.5, 0, 0.5$. In comparison with the peak values measured in the emergent case, which are shown in Figure 4.18, the total energy of the turbulent field is reduced in this case. This is consistent with

the suppression of vortex shedding by the flow over the top of the block that has been observed in experiments in simple channels. The pattern of distribution of the turbulence across the wake is, however, very similar to that observed for the emergent block, where larger values are found on the floodplain.

Figures 4.44, 4.45 and 4.46 show the streamwise, spanwise and vertical normal Reynolds stress components for both the plan measurement plane and the detail of the contours in the block wake for the cross-sectional measurement plane.

From the measurements of the streamwise component, the familiar double peak in $\overline{u'u'}$ in the shear layers surrounding the wake can be seen and just like the emergent case, the larger peak is to be found on the floodplain. In line with the drift in the streamwise velocity contours into the main channel, the positions of the peaks in $\overline{u'u'}$ can also be seen to move toward the main channel in the downstream direction. The cross-sectional profile shows a similar trend to the emergent case in that the degree of asymmetry across the block reduces as the vertical position moves away from the floodplain bed.

The distribution of the spanwise component at the plan measurement level is also highly similar to that in the emergent case, with a single peak developing on the floodplain side of the block centreline. Moving downstream, this also moves gradually towards the main channel. This pattern of normal Reynolds stresses is consistent with the information gleaned from the mean velocity contours, namely that the separating flow from the shaft is disrupted on the main channel side, leading to more powerful and therefore, higher energy circulations on the floodplain side of both vertical and axial orientations.

The relative contribution of the vertical component $\overline{w'w'}$ to the overall turbulent kinetic energy in the wake is much larger in this case than in the emergent case. The peak magnitude of the component is associated with the region just after reattachment, where the mean vertical velocity component is also at a maximum. Confirming the observations from the mean vertical velocity profile that the altered shape of the recirculation zone and the angling of the flow separating from the top

of the block result in a downflow at this location that is skewed toward the main channel, the peak in $\overline{w'w'}$ is located on the floodplain side.

As may be expected from the previous results, the plot of the Reynolds shear stress in the horizontal plane shown in Figure 4.47(a) shows higher values on the floodplain side of the block. In comparison with the emergent case, both the absolute magnitudes and the degree of difference between them across the wake are lessened. With dampened vortex shedding due to the flow over the top of the block, the overall drop in magnitude is to be expected as the minimum wake velocity will not be as extreme in this case. The higher floodplain values persist partially due to the higher blockage on the floodplain side, which ensures that the peak velocity outside of the wake is higher, leading to a higher strain rate. As the flow passes downward over the recirculation zone, a large positive peak appears in the profile of $-\overline{u'w'}$ shown in Figure 4.47(b). Finally, the distribution of $-\overline{v'w'}$ shown in Figure 4.47(c) shows the opposite trend to that identified in the emergent case so that higher values are found on the floodplain side. This distribution is a result of the dominance of the axial circulation on the floodplain identified in the contours of mean velocity and confirms that these structures are balanced in an opposite sense to their equivalents in the emergent case.

4.2.3.4 Summary

The flow around a single large aspect ratio submerged block at the floodplain edge exhibits significant differences from that around a similar block in a simple channel. Like its emergent counterpart, the floodplain edge positioning is again influential in disrupting the characteristics of the separated flow on the main channel side of the block shaft such that the vorticity formation associated with this separation zone does not proceed as would otherwise be expected and together with the influence of the asymmetric blockage, results in more turbulent kinetic energy being associated with the floodplain side of the wake. Unlike its emergent counterpart, due to the more complex shape of the recirculation zone, including the influence of the flow separating from the top of the block, this does not result in a skew

of the wake to the floodplain side. The channel geometry heavily influences the distribution of vertical momentum such that a small but powerful axial rotation develops on the main channel side of the block in the separation zone. Rotating in an opposite sense to the axial vorticity that we expect in the wake of a submerged block, this feature has an important role in changing the nature of the wake on this side, as the wake gradually becomes skewed into the main channel.

The flow over the top of the block, which would normally be expected to separate from the leading edge and reattach at a uniform streamwise position on the top surface is also clearly affected by the floodplain edge position such that reattachment and the subsequent separation from the rear edge are likely to be skewed. The results certainly indicate that where this flow passes over the recirculation zone, it is angled toward the main channel and thus has an asymmetrical influence on the subsequent wake development.

Whilst the vortex shedding process is much reduced in extent and influence, the greatest turbulent kinetic energy is still associated with the turbulent structures in the horizontal plane. In both this and the axial plane, the uneven pattern of separation leads to a dominance by the floodplain structures. The imbalance originating in the separation zones is emphasised by the differences in magnitude of the vortex stretching terms in the wake so that behind the block, the wake appears to gradually drift into the main channel.

The results from the Kansai and Loughborough experiments suggest that the floodplain edge positioning acts to slow the overall recovery of the streamwise velocities in the wake, in much a similar way to the emergent cases.

4.2.4 Loughborough - Multiple, small blocks at the floodplain edge (S1 CI & III)

In Series 1, two submerged cases with multiple small blocks were tested with different degrees of submergence. This data complements that collected for the single block with data for a set of in-line blocks. Not only that however, but the change in

the degree of submergence reveals some interesting flow characteristics, giving an insight into the influence of this factor. The aspect ratio of the block in both cases is 1.67 but the relative depth varies such that in Case III, it is similar to that of the single large aspect ratio block of the previous section, whilst in Case I, it is much greater.

This section details the data collected in both the deep submergence case and the shallow submergence case. Figure 4.48 shows the mean velocity data for the former case while Figure 4.49 shows it for the latter. For both cases, the overall spanwise gradient of U is considerably larger than that measured for the single block case. This does not appear to qualitatively change the distribution of the mean velocities.

In the deep submergence case, the results for the distribution of the streamwise velocity downstream of the block are similar to those observed for the single large aspect ratio block, namely that the wake can be observed to move into the main channel in the downstream direction. The upstream profile, itself measured in the wake of the third block, shows a wake from the previous block that is largely indistinguishable from the floodplain flow. This suggests that the wake is well recovered at this point. The vectors of the secondary circulations at this station still show evidence of axial circulations however and just as with the single large aspect ratio block, the vectors suggest that the vortex structure on the floodplain side is heavily dominant over that on the main channel side. Moving downstream past the fourth block, the vectors show that this pattern is augmented so that the process described for the single, large aspect ratio block may be assumed to be also present for these small blocks and to be enhanced by the arrangement of the blocks in a line at the floodplain edge.

In the shallow submergence case, the streamwise velocity distribution shows exactly the opposite tendency to the deep submergence case so that the minimum streamwise velocity is consistently found on the floodplain side of the block centreline. In this respect, the flow resembles the emergent case much more closely than the deep submergence case, suggesting that the relative influence of the flow

coming over the top of the block in determining the wake structure is very large. The vectors of secondary circulations for this case suggest that the axial vorticity associated with the wakes is also more akin to that of the emergent case so that there is an upflow near the block centre and a tendency for the main channel axial vortex structure to dominate. Despite these similarities, the characteristic double peak in the main channel distribution of streamwise velocity of the emergent case is however, conspicuously absent here and the shape of the wake suggested by the streamwise velocity profiles is also different. Whilst in the emergent case, the wake widens out on the floodplain side, in the shallow submergence case, this widening is less remarkable.

The total turbulent kinetic energy and the normal turbulent shear stress contributions are shown in Figures 4.50 and 4.51. For the deep submergence case, despite the similar distribution of mean velocities with the single, large aspect ratio block case, the peak value of turbulent energy is generally at or near the block centreline at all of the measurement stations. An examination of the individual normal turbulent stress components reveals that this is the result of a change in the relative contributions and distributions of these. Since the aspect ratio of the blocks is much reduced in this case, we must expect that the relative influence of turbulent structures emanating from separation around the block shaft will be lessened. Thus, the relative magnitude of $\overline{u'u'}$ is smaller and its influence on the final turbulent energy distribution is reduced. Although $\overline{u'u'}$ and $\overline{v'v'}$ follow the pattern established for the single large aspect ratio block and peak on the floodplain, $\overline{w'w'}$ does not.

For the shallow submergence case, the K profile moves closer to that observed for the emergent block in this series with the overall maximum occurring near to the main channel edge of the block, where both $\overline{u'u'}$ and $\overline{w'w'}$ peak. Thus it is again clear that the degree of submergence is highly influential in determining the final relative significance of the turbulent structures in each plane and the development of the wake in the downstream direction.

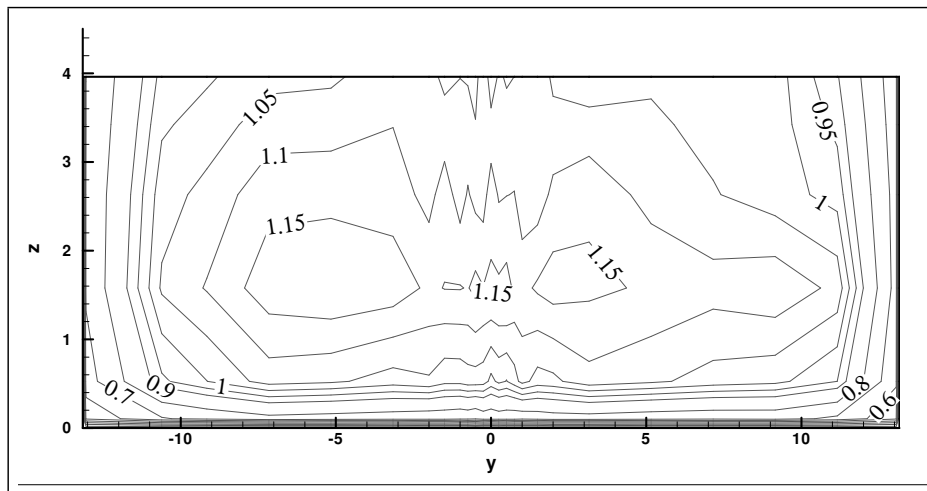
The turbulent shear stresses are plotted in Figures 4.52 and 4.53 in the horizontal, transverse and cross-sectional planes respectively. For the deep submergence case, the turbulent shear stress distributions are very similar to those described for the single, large aspect ratio submerged block since the larger peak of $-\overline{u'v'}$ is found on the floodplain side, despite the tendency of the minimum streamwise velocity to lie near the main channel. The skewed downward flow over the top of the recirculation zone also again results in a large positive peak in $-\overline{u'w'}$ on the floodplain side. For the shallow submergence case, similarities with the emergent case prevail for both $-\overline{u'w'}$ and $-\overline{v'w'}$, where the values at the main channel interface are disproportionately large and reflect an axial flow structure highly dependent on the nature of separation around the block shaft. Only the profile of $-\overline{u'v'}$ is significantly different, since its imbalance is reversed.

Whilst the results for the deep submergence case in this section confirm many of the observations made for the single, large aspect ratio block and suggest that these features are accentuated by the smaller aspect ratio and the in-line arrangement, the results for the shallow submergence case reveal that the degree of submergence has a powerful influence on the final wake structure and the influence of the floodplain edge positioning thereon. Whilst it has been observed for the former cases that the floodplain edge positioning and the resulting skew in the flow passing over the top of the block results in significantly stronger axial vorticity on the floodplain and the gradual movement of the wake into the main channel, for the shallow submerged case, many of the effects associated with the emergent blocks are observed. The relative influence of these features on the drag created by the blocks will be examined with the numerical model in Chapter 5.

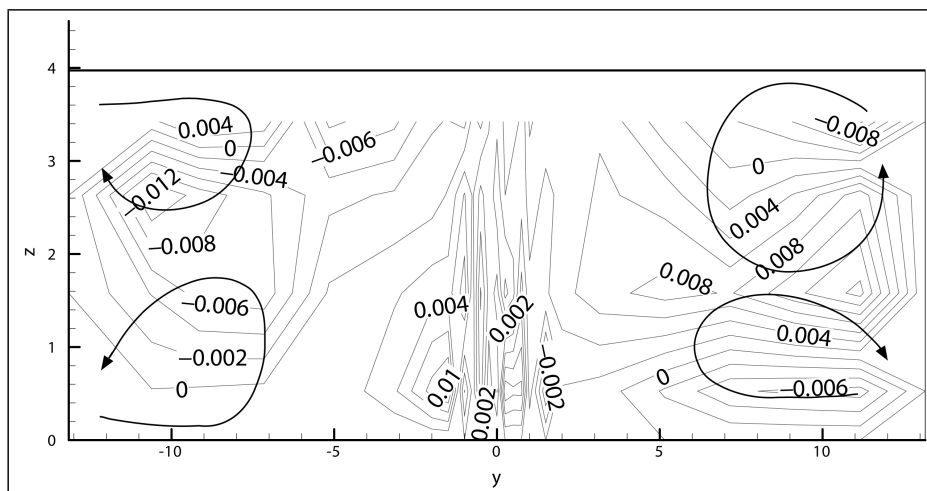
4.3 Summary

This chapter has presented the results gleaned from physical experiments in straight channels in the Kansai and Loughborough laboratories. The experiments in the Kansai flume demonstrated directly the differences in wake structure induced by

the placement of blocks at the floodplain edge of a compound channel, whilst those from the Loughborough flume added detail to the mechanisms causing these differences and provided a contrasting set of results for blocks of varied aspect ratio and arrangement. The results in general reveal significant differences in the wake structures behind cylindrical obstacles induced by their positioning at the edge of the floodplain of a compound channel and a tangible impact on the drag force produced by these blocks in comparison to their counterparts in simple channels.



(a)



(b)

Figure 4.1: Mean (a) streamwise velocity contours (U) and (b) spanwise velocity contours (V) upstream of the large aspect ratio, emergent block in the simple channel (S4CIII)

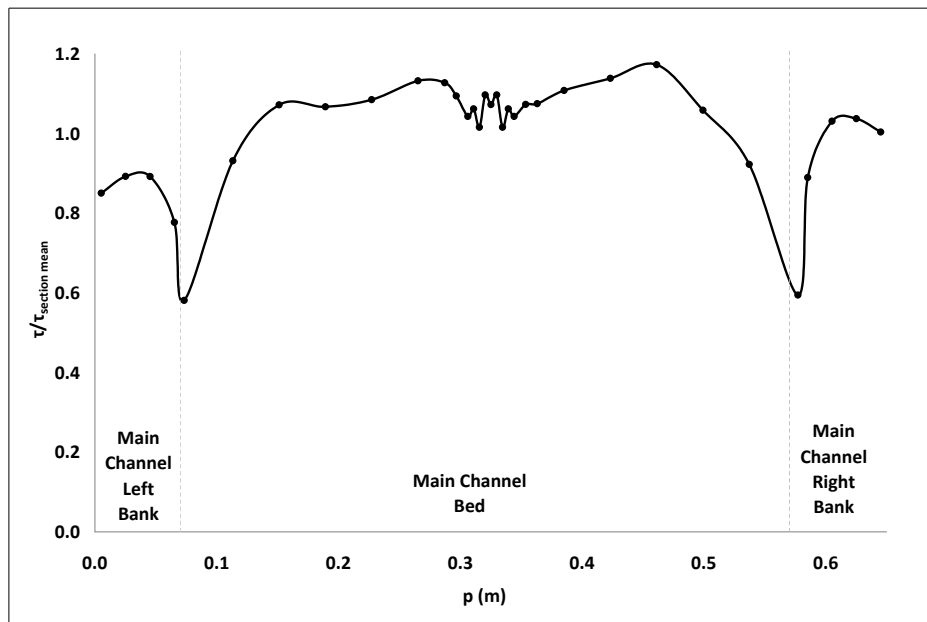
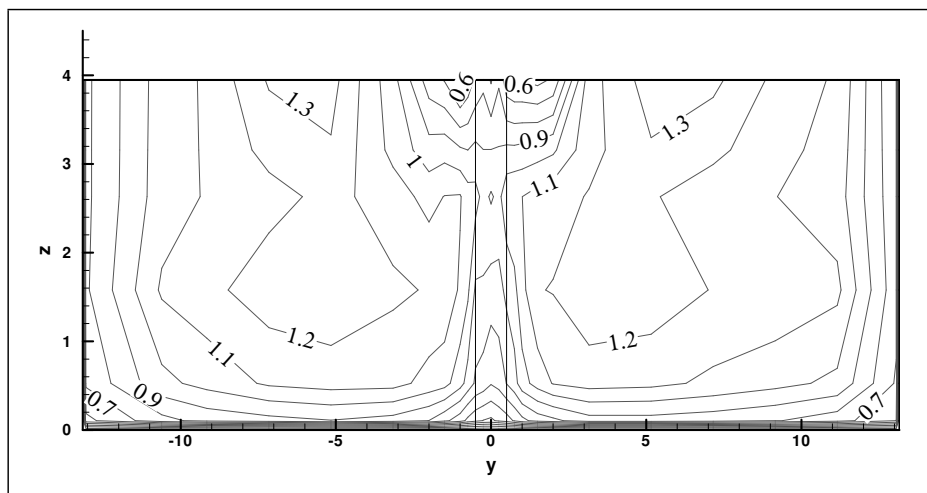
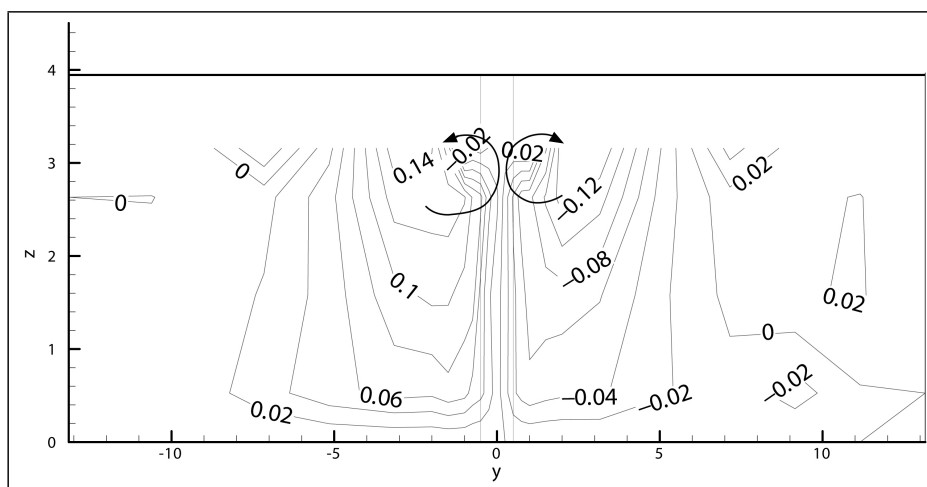


Figure 4.2: Distribution of boundary shear stress upstream of the large aspect ratio, emergent block in the simple channel (S4CIII)



(a)



(b)

Figure 4.3: Mean (a) streamwise velocity contours (U) and (b) spanwise velocity contours (V) downstream of the large aspect ratio, emergent block in the simple channel (S4CIII)

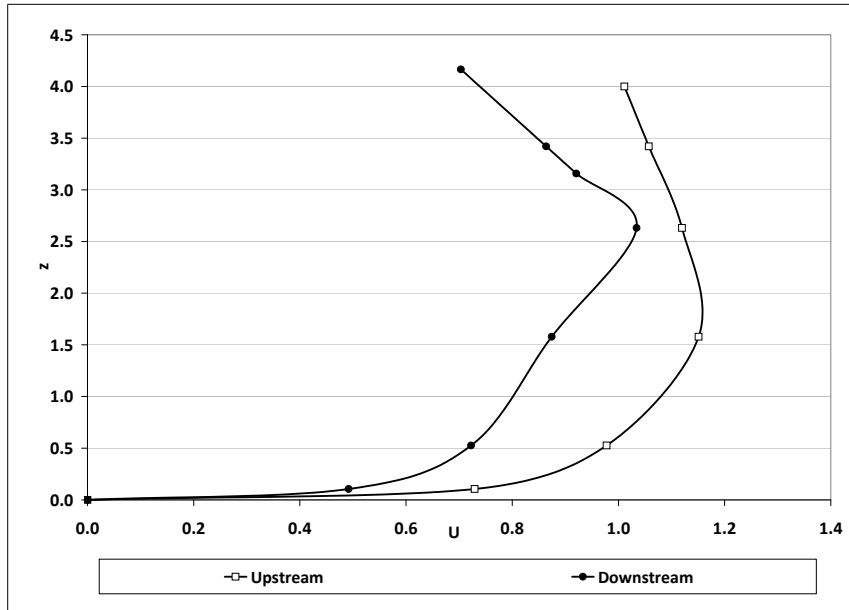


Figure 4.4: Vertical distribution of streamwise velocity U at the block centreline upstream and downstream of the large aspect ratio, emergent block in the simple channel (S4CIII)

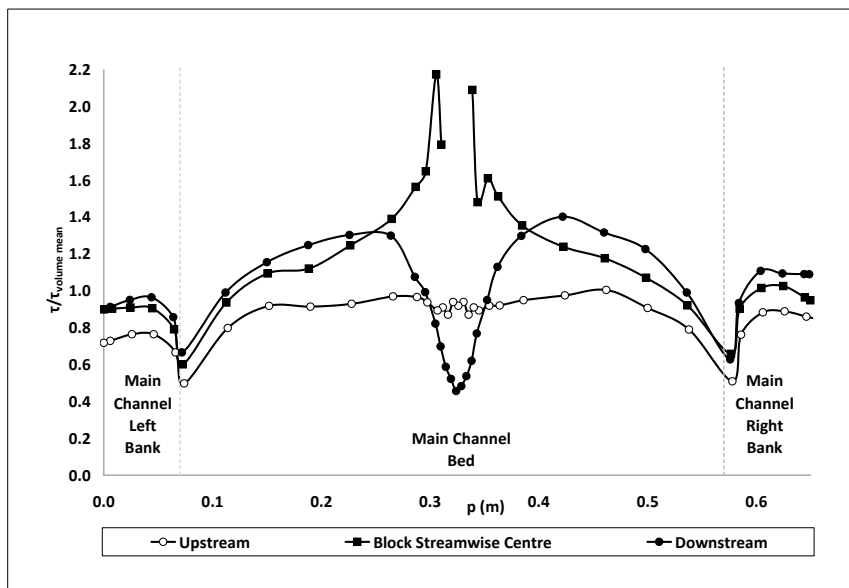


Figure 4.5: Distribution of boundary shear stress at all sections for the large aspect ratio, emergent block in the simple channel (S4CIII)

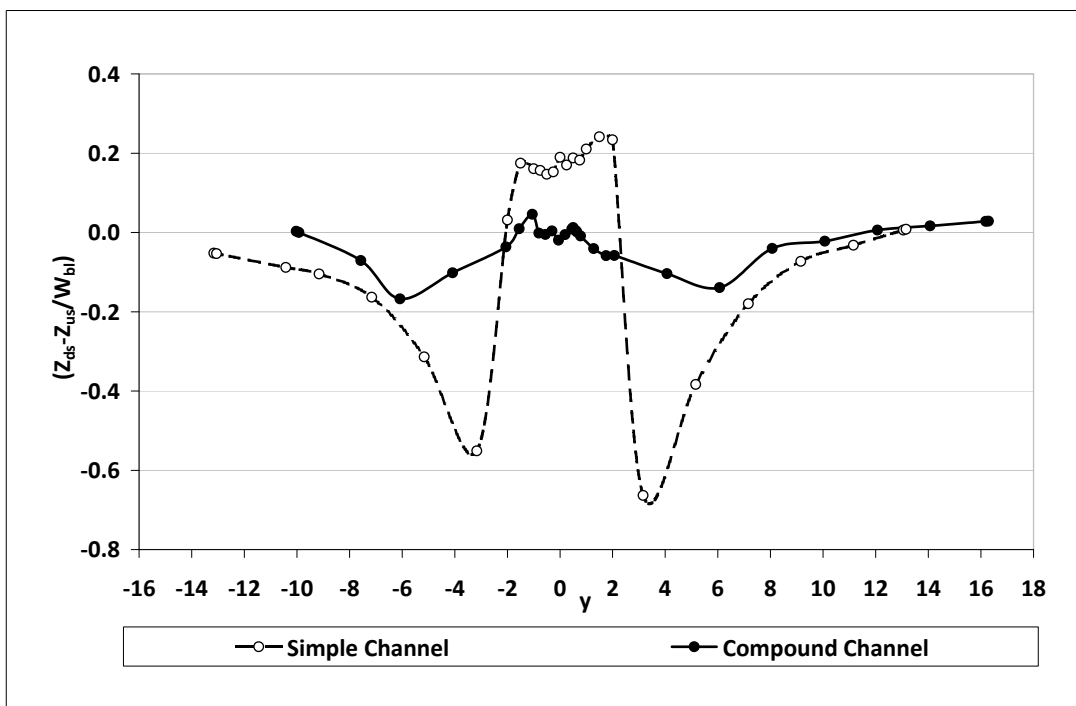
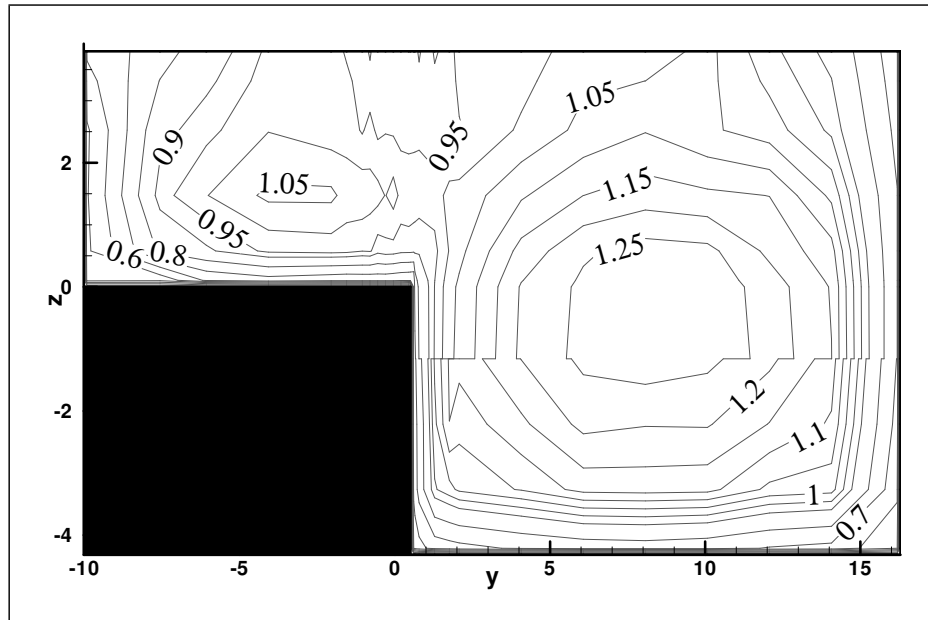
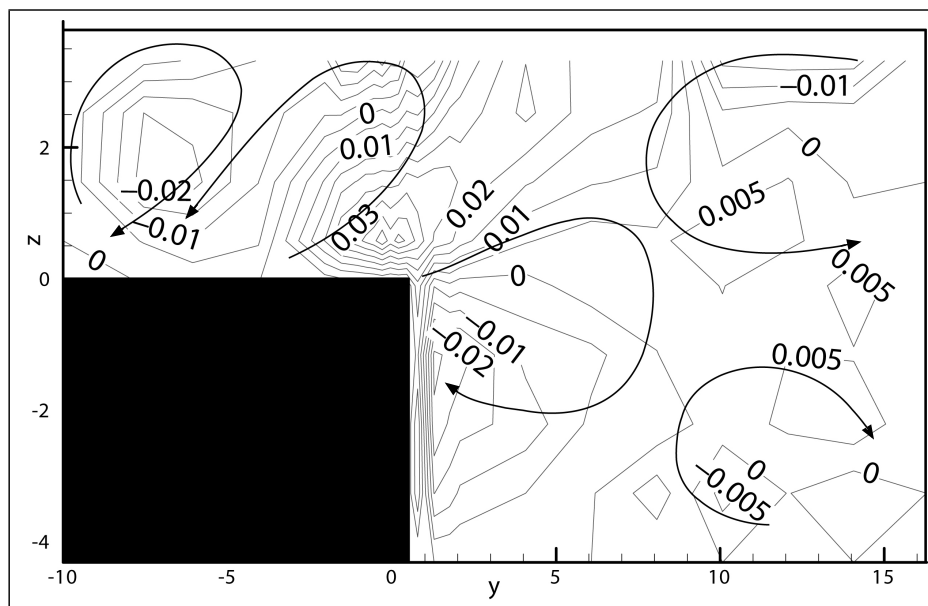


Figure 4.6: Difference between downstream water level and average upstream water level, normalised with block width for large aspect ratio, emergent blocks in both simple and compound channels (S4CIII, S4CI)



(a)



(b)

Figure 4.7: Mean (a) streamwise velocity contours (U) and (b) spanwise velocity contours (V) upstream of the large aspect ratio, emergent block in the compound channel (S4CI)

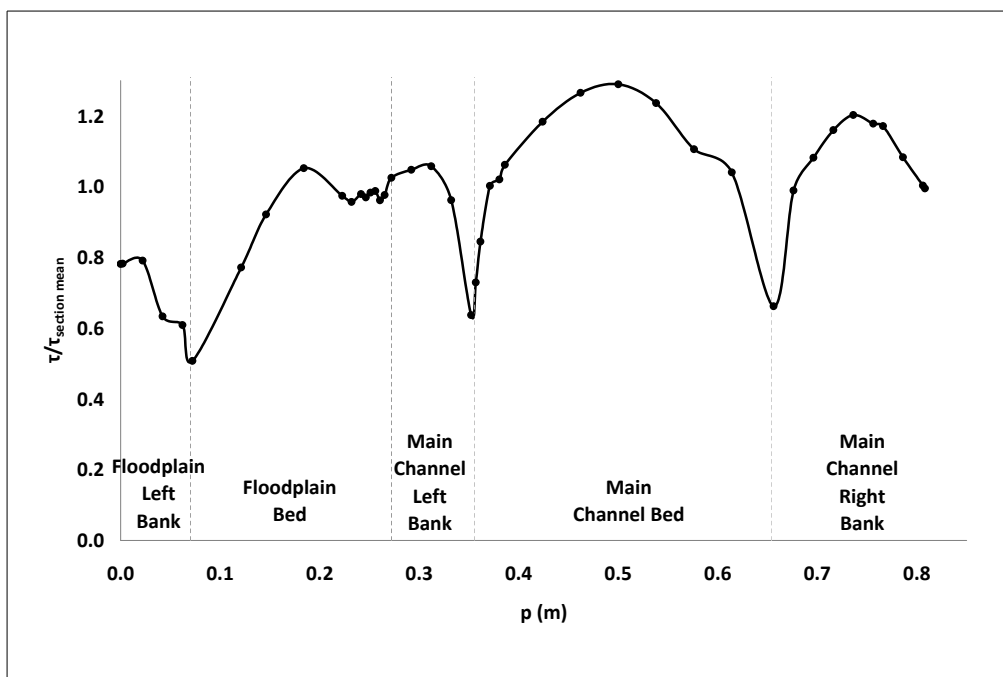
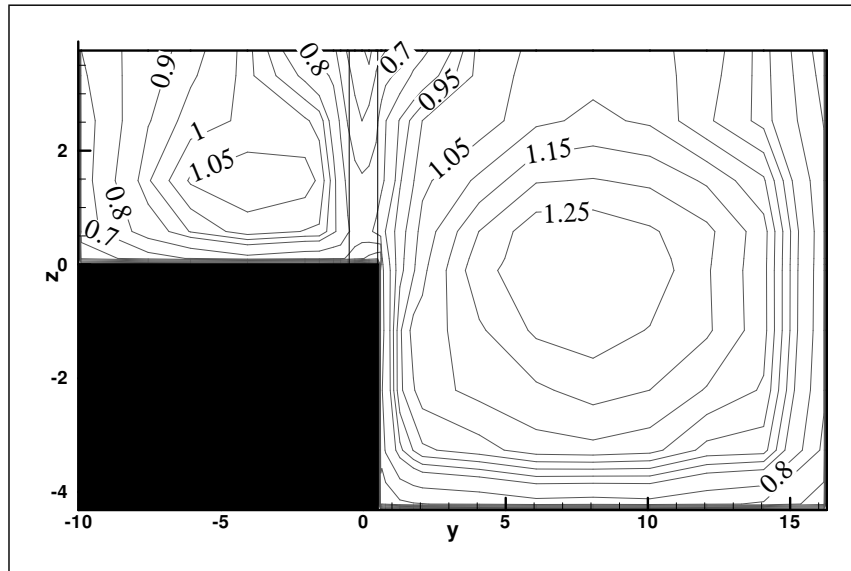
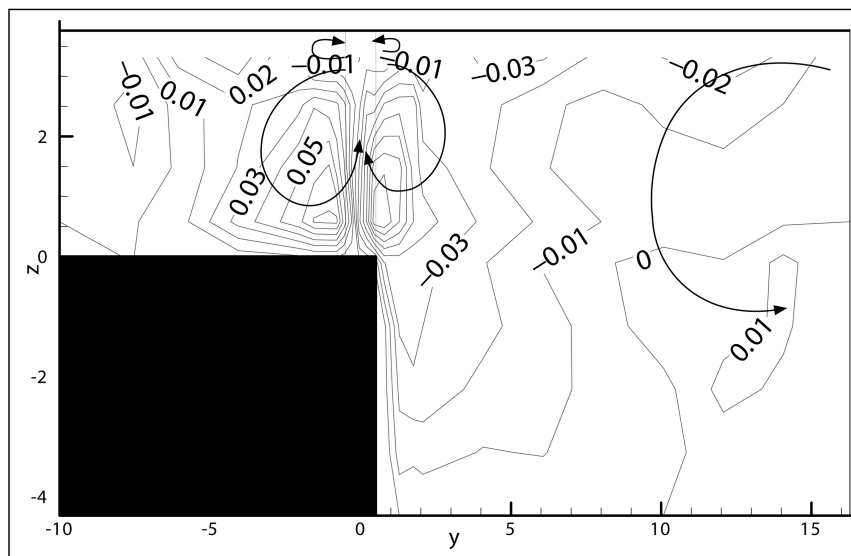


Figure 4.8: *Distribution of boundary shear stress upstream of the large aspect ratio, emergent block in the compound channel (S4CI)*



(a)



(b)

Figure 4.9: Mean (a) streamwise velocity contours (U) and (b) spanwise velocity contours (V) downstream of the large aspect ratio, emergent block in the compound channel (S4CI)

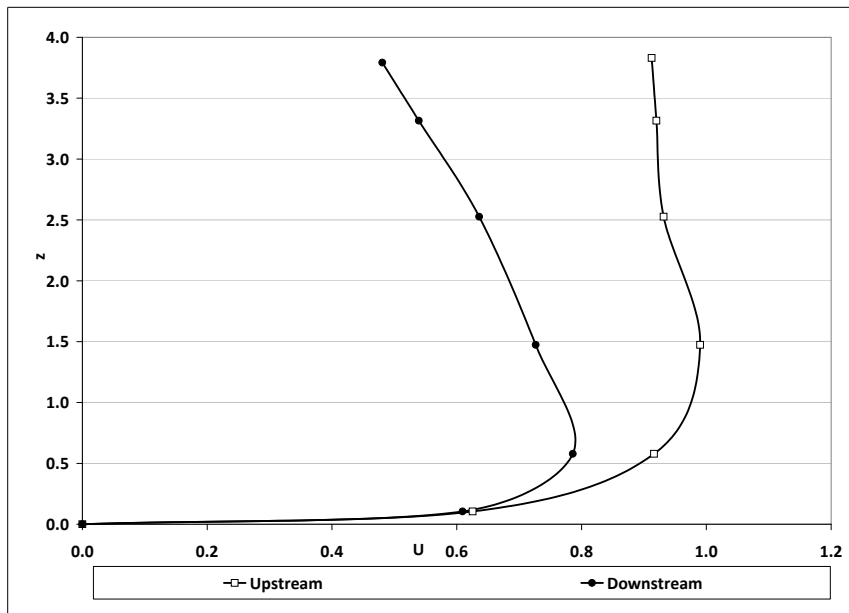


Figure 4.10: Vertical distribution of streamwise velocity U at the block centreline upstream and downstream of the large aspect ratio, emergent block in the compound channel (S4CI)

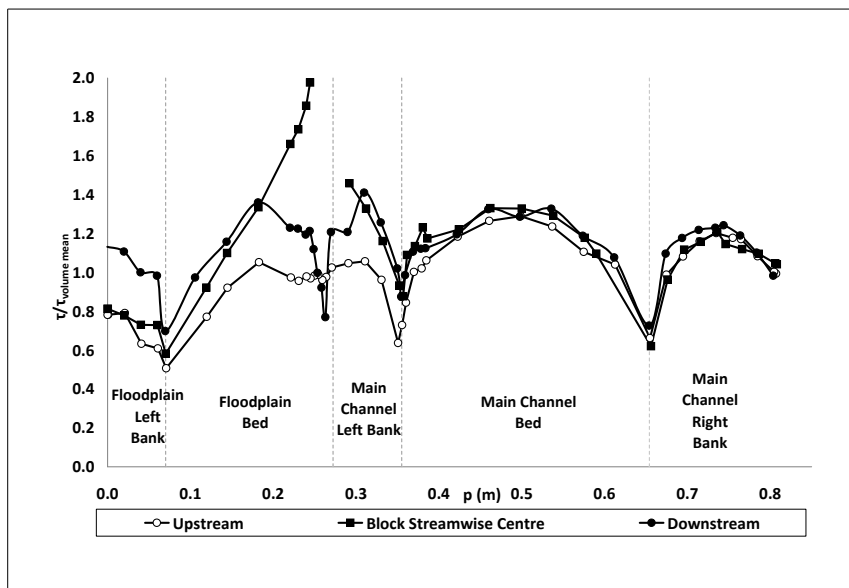
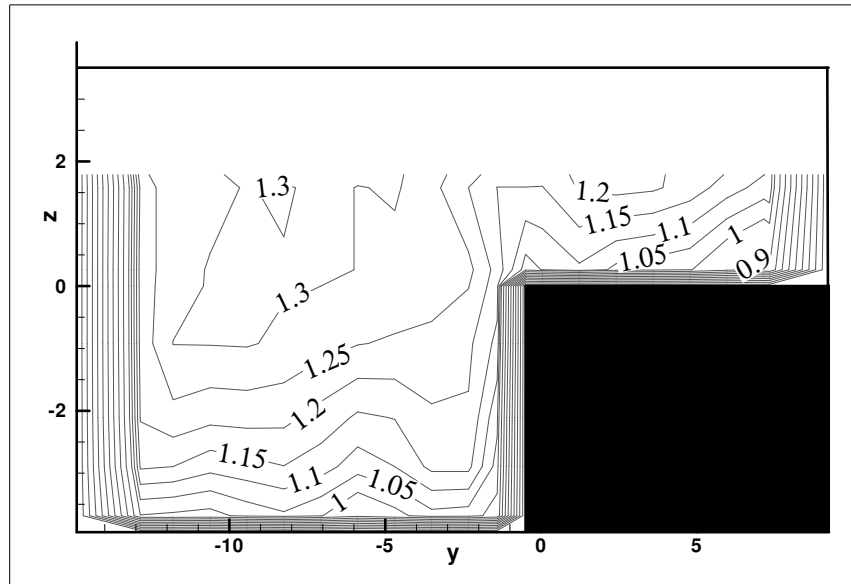
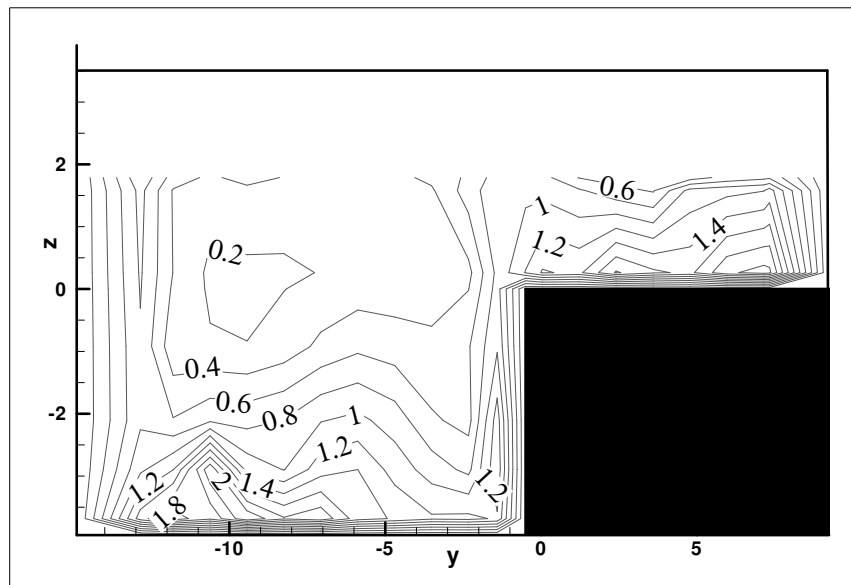


Figure 4.11: Distribution of boundary shear stress at all sections for the large aspect ratio, emergent block in the compound channel (S4CI)

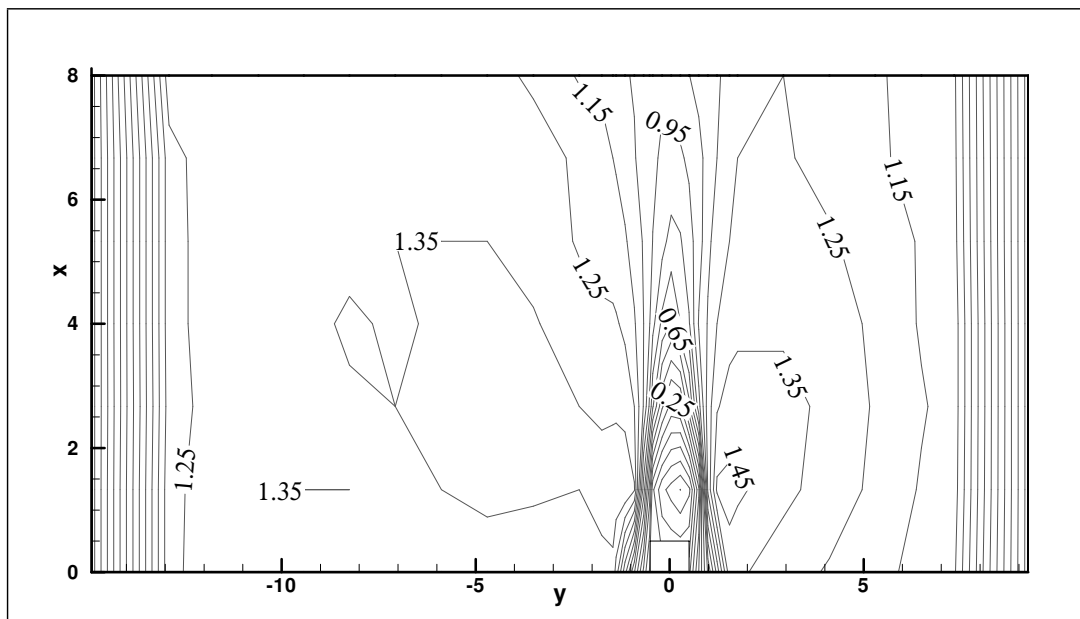


(a)

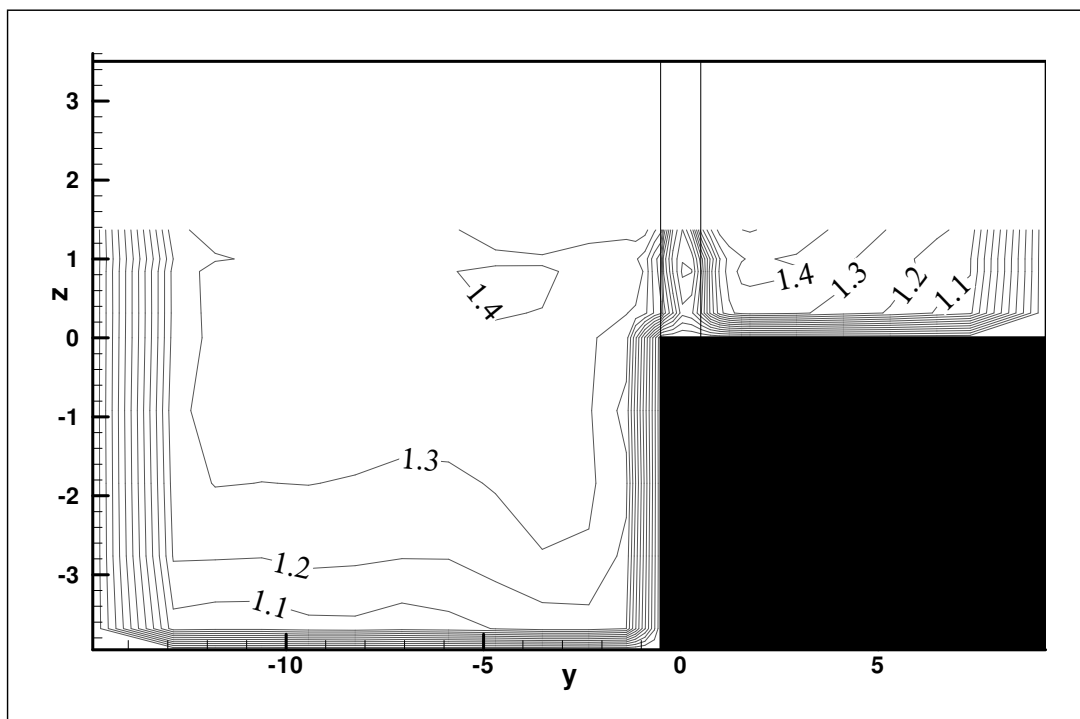


(b)

Figure 4.12: (a) Mean streamwise velocity contours (U) and (b) mean turbulent kinetic energy contours (K) upstream of the large aspect ratio, emergent block in the compound channel (S2CI)

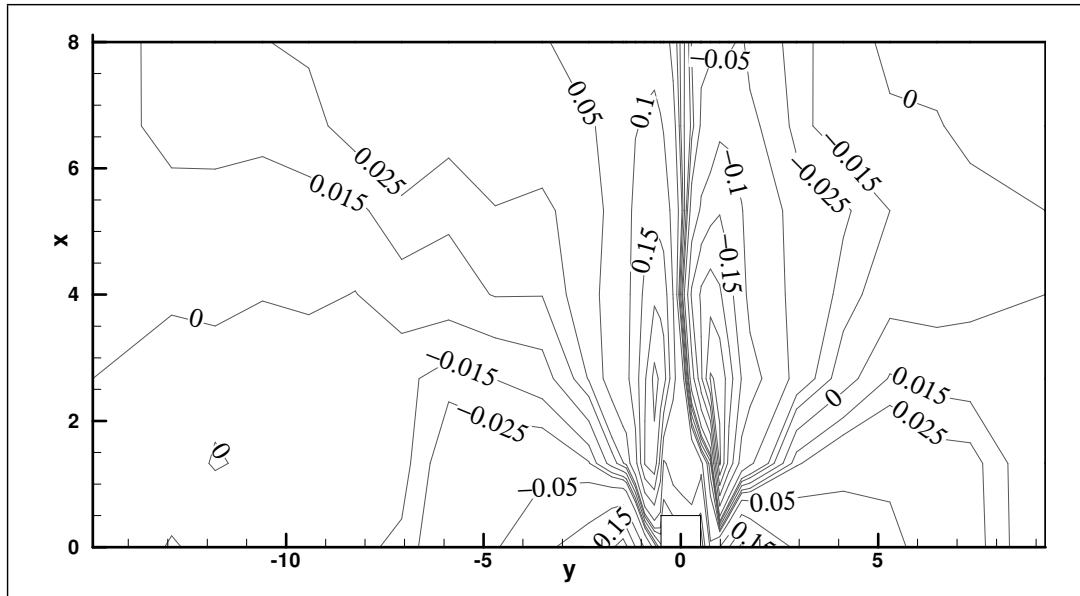


(a)

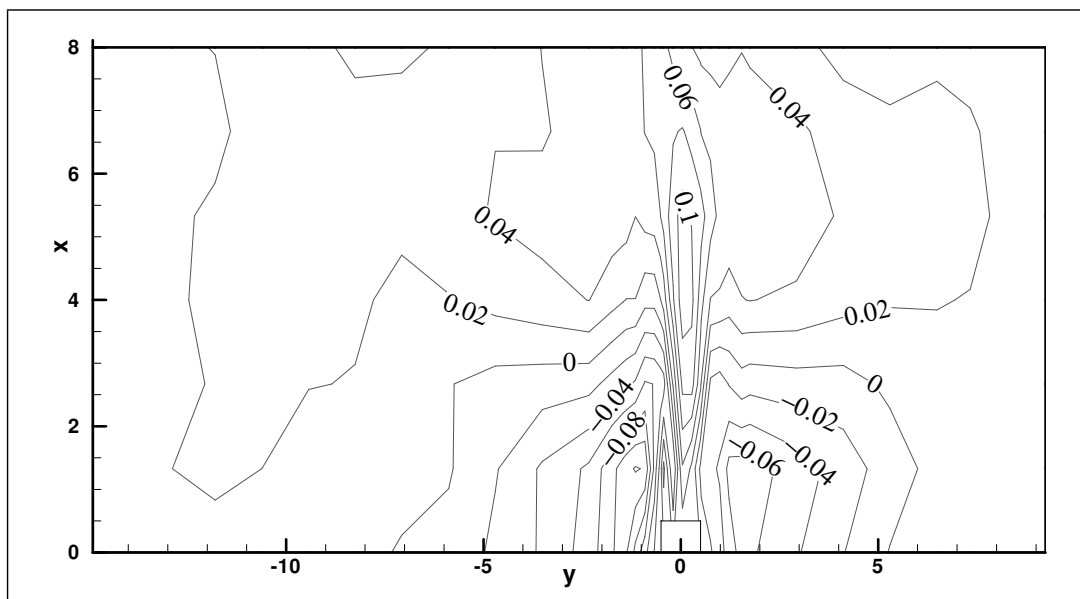


(b)

Figure 4.13: Mean streamwise velocity contours (U) (a) around ($z = 1$) and (b) downstream ($x = 2.7$) of the large aspect ratio, emergent block in the compound channel (S2CI)



(a)



(b)

Figure 4.14: Mean (a) spanwise velocity contours (V) and (b) vertical velocity contours (W) around ($z = 1$) the large aspect ratio, emergent block in the compound channel (S2CI)

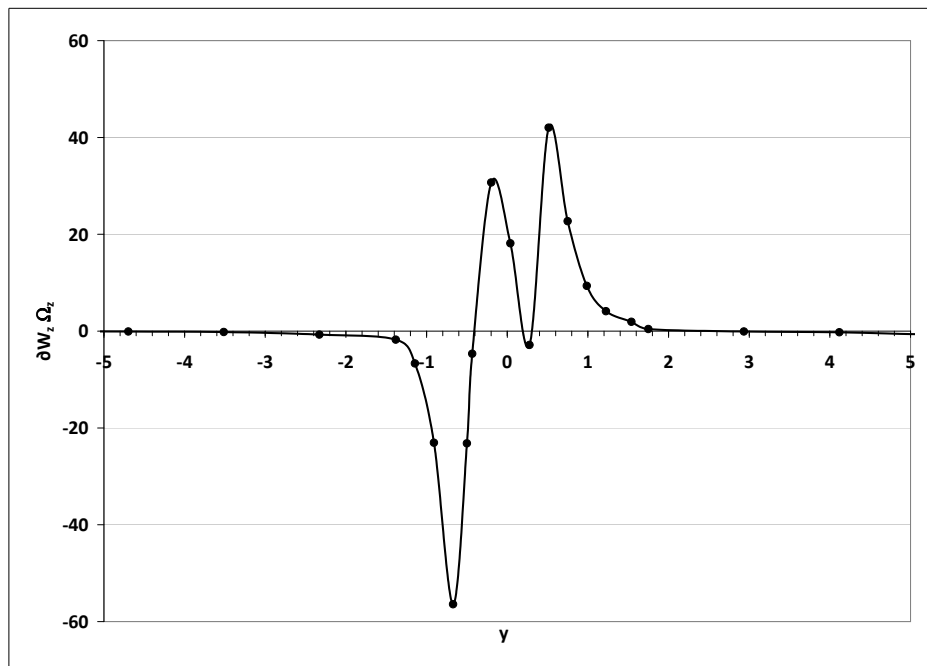


Figure 4.15: Vortex stretching of vertical vortices downstream ($x, z = 2.7, 1.0$) of the large aspect ratio, emergent block in the compound channel (S2CI)

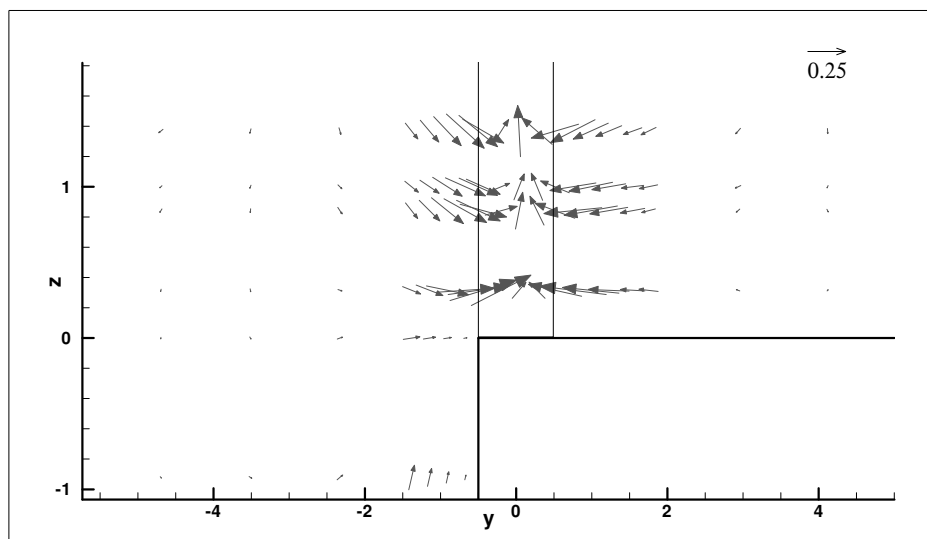
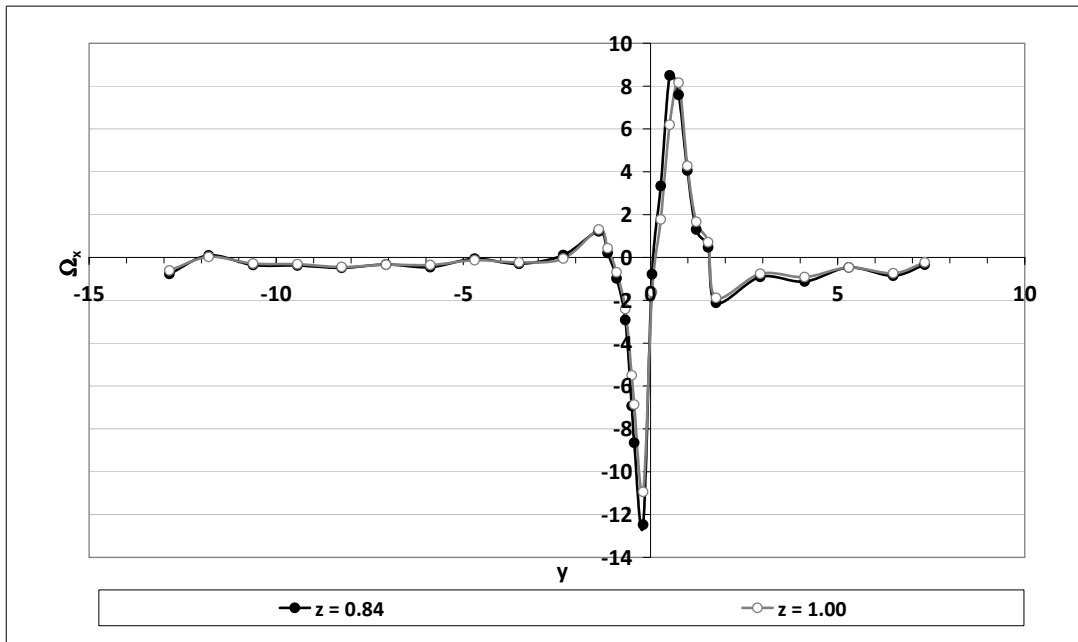
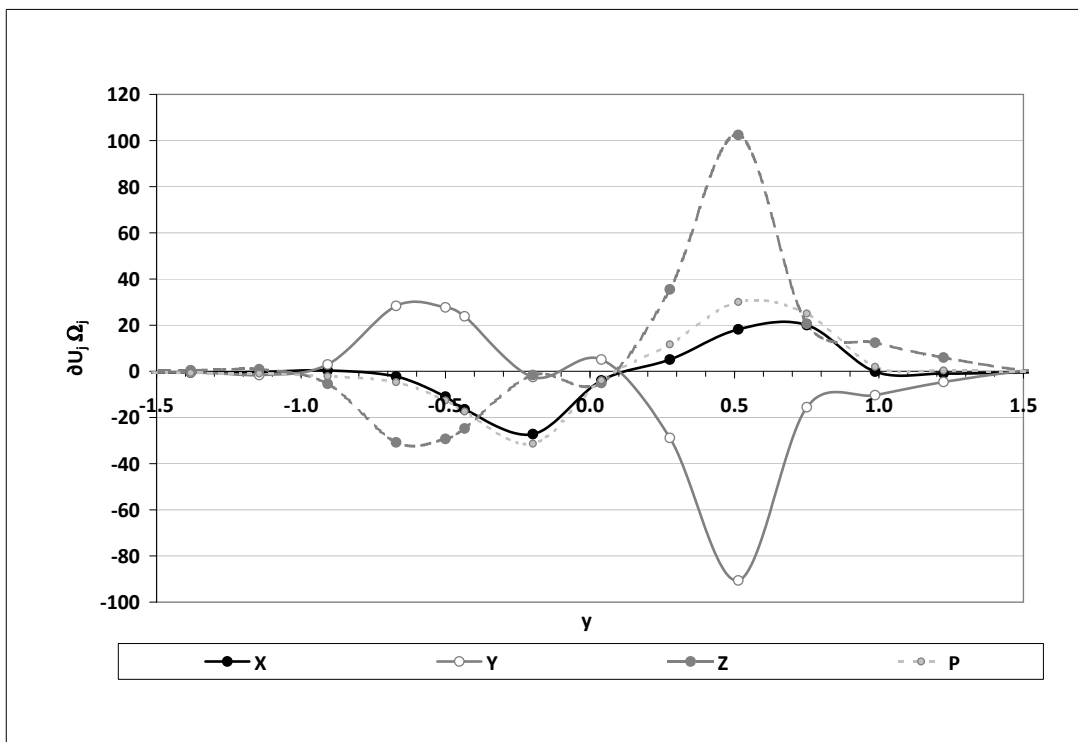


Figure 4.16: Vectors of secondary circulations downstream ($x = 2.7$) of the large aspect ratio, emergent block in the compound channel (S2CI)



(a)



(b)

Figure 4.17: (a) Axial vorticity and (b) contributions to axial vorticity production downstream ($x = 2.7$) of the large aspect ratio, emergent block in the compound channel (S2CI)

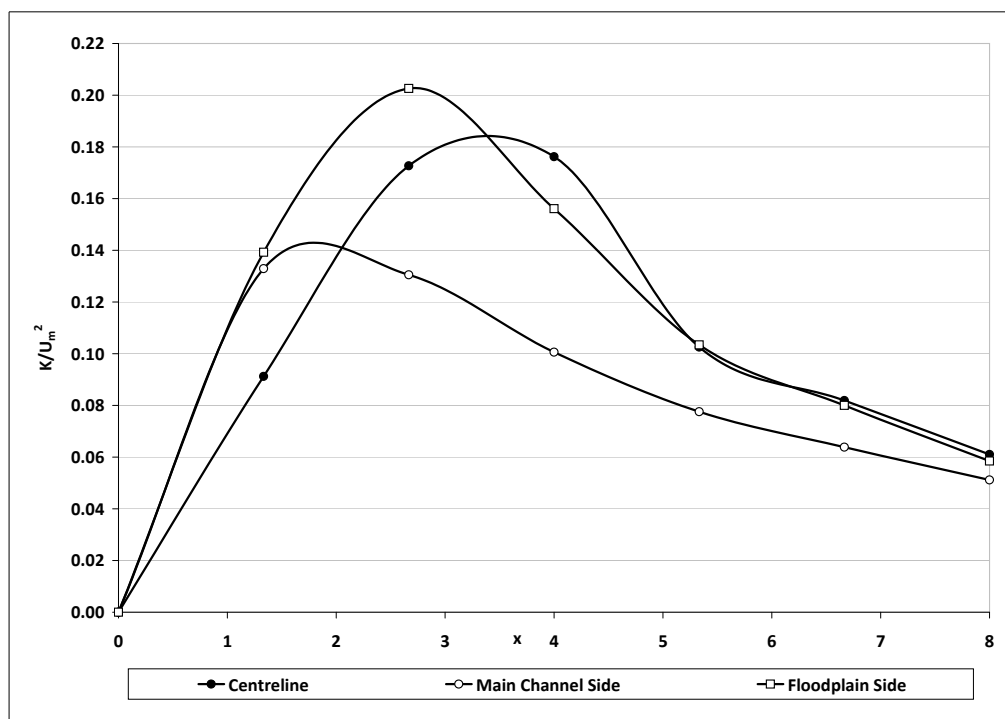
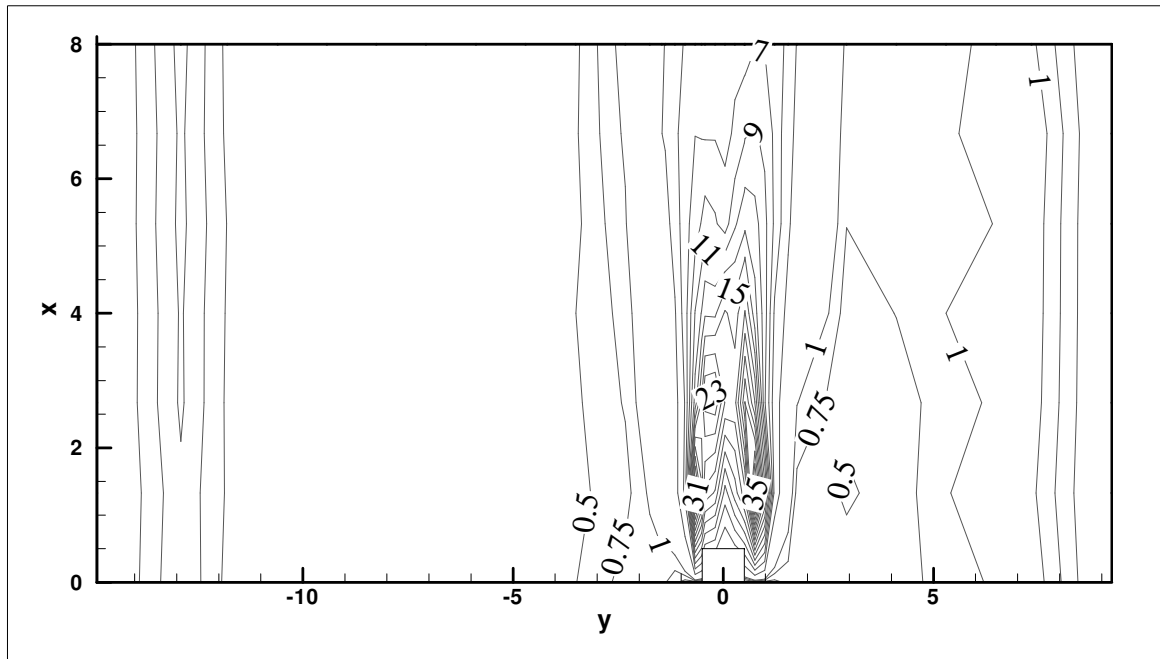
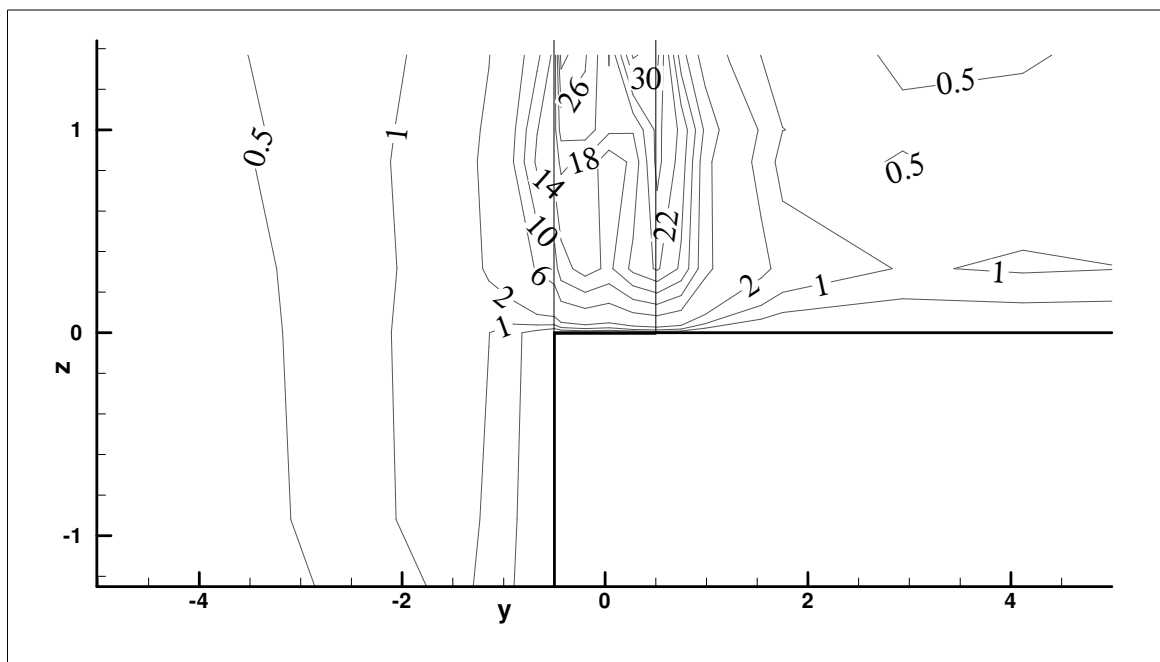


Figure 4.18: Normalised mean turbulent kinetic energy (K/U_m^2) in the wake of the large aspect ratio, emergent block in the compound channel (S2CI)

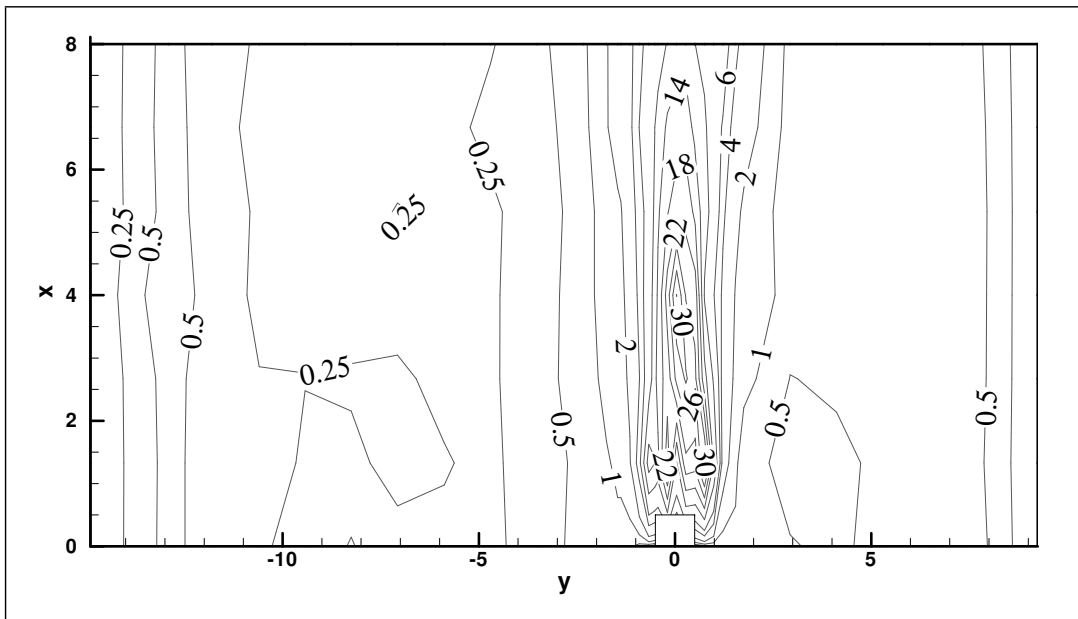


(a)

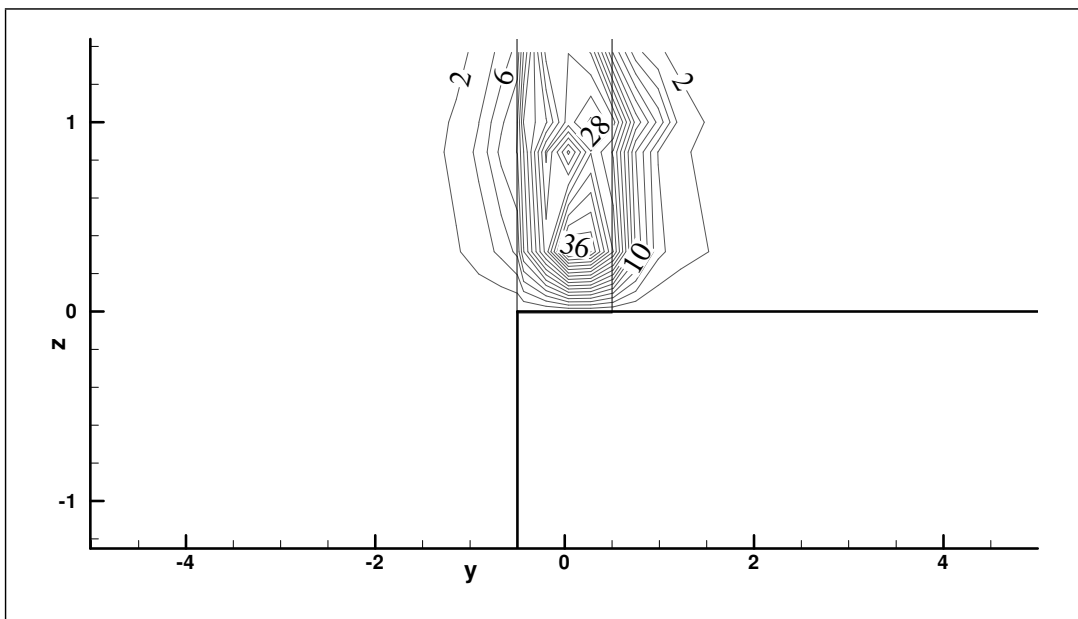


(b)

Figure 4.19: Mean streamwise normal Reynolds stress contours $\overline{u'u'}$ (a) around ($z = 1$) and (b) downstream ($x = 2.7$) of the large aspect ratio, emergent block in the compound channel (S2CI)

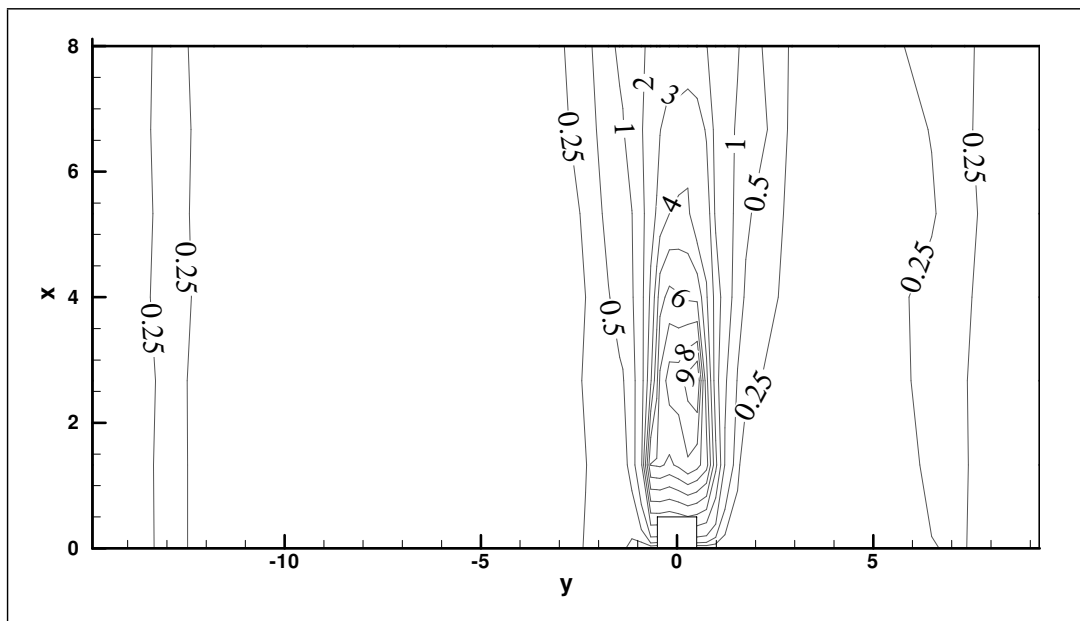


(a)

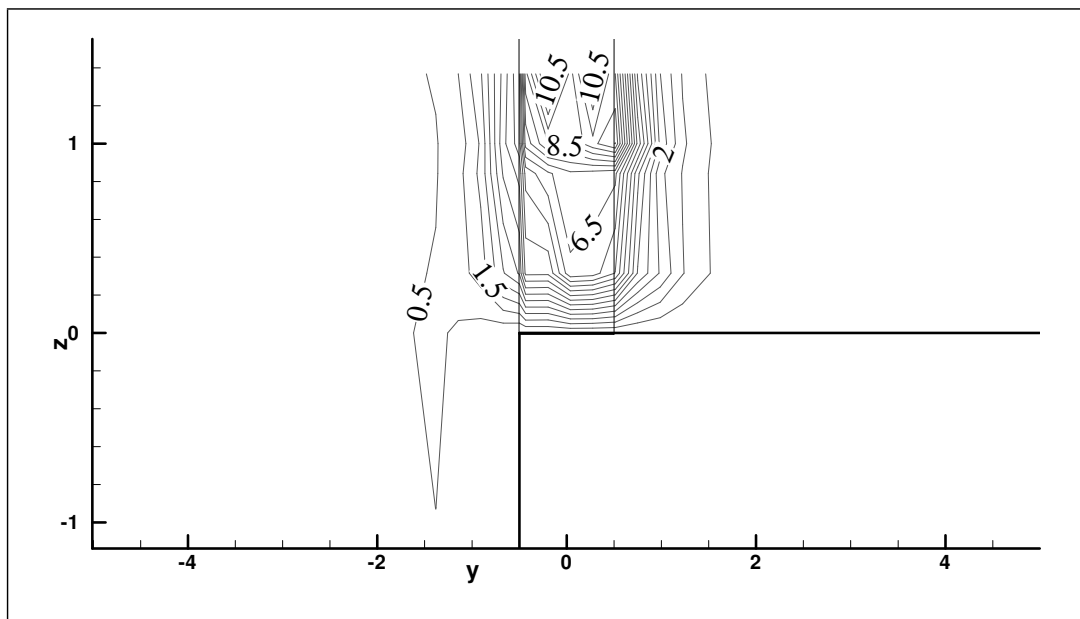


(b)

Figure 4.20: Mean spanwise normal Reynolds stress contours $\overline{(v'v')}$ (a) around ($z = 1$) and (b) downstream ($x = 2.7$) of the large aspect ratio, emergent block in the compound channel (S2CI)

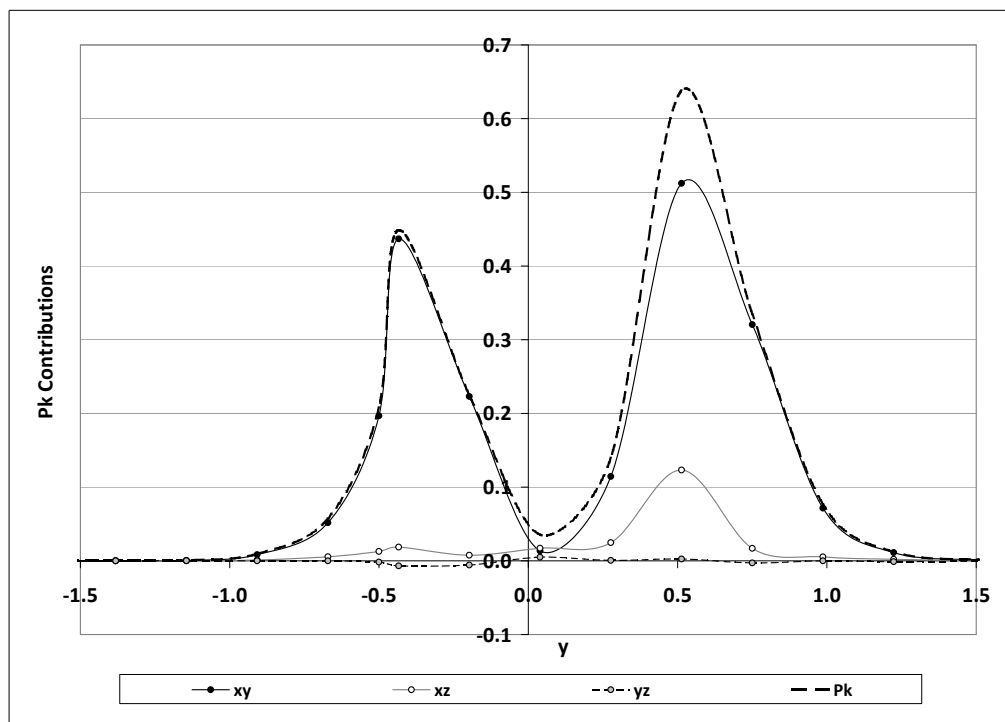


(a)



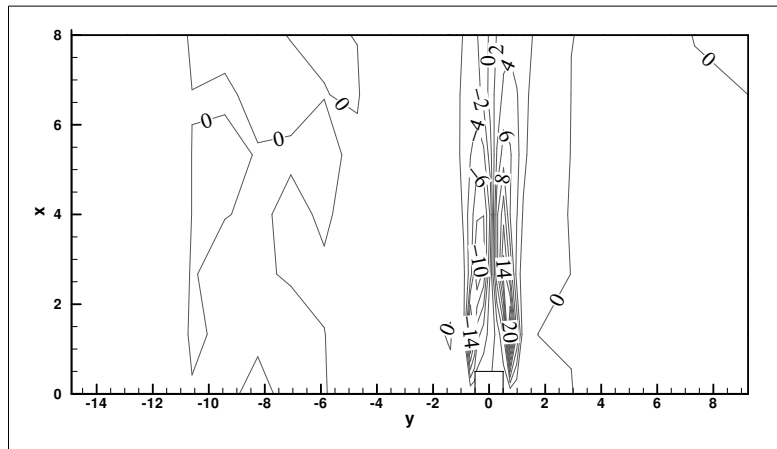
(b)

Figure 4.21: Mean vertical normal Reynolds stress contours ($\overline{w'w'}$) (a) around ($z = 1$) and (b) downstream ($x = 2.7$) of the large aspect ratio, emergent block in the compound channel (S2CI)

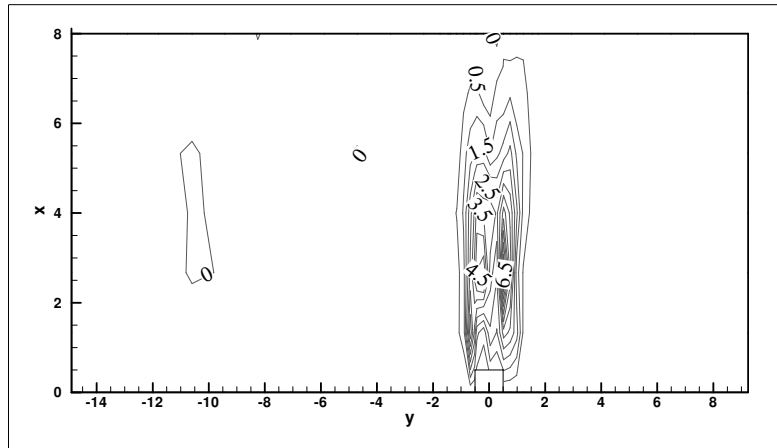


(a)

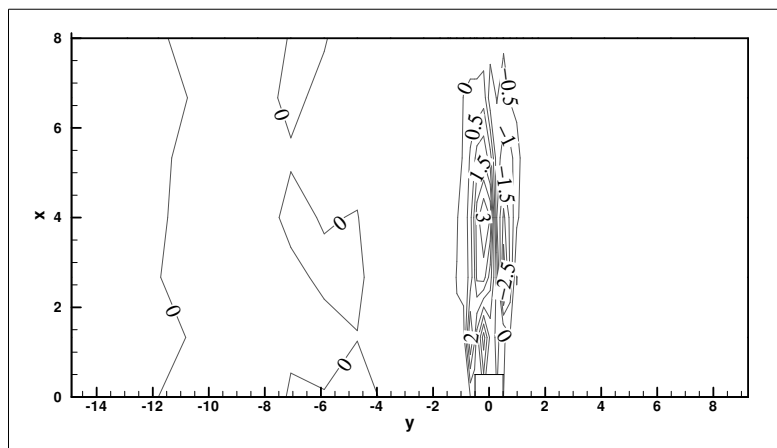
Figure 4.22: Components of and total turbulent kinetic energy production at $(x, z = 2.7, 1.0)$ for the large aspect ratio, emergent block in the compound channel (S2CI)



(a)

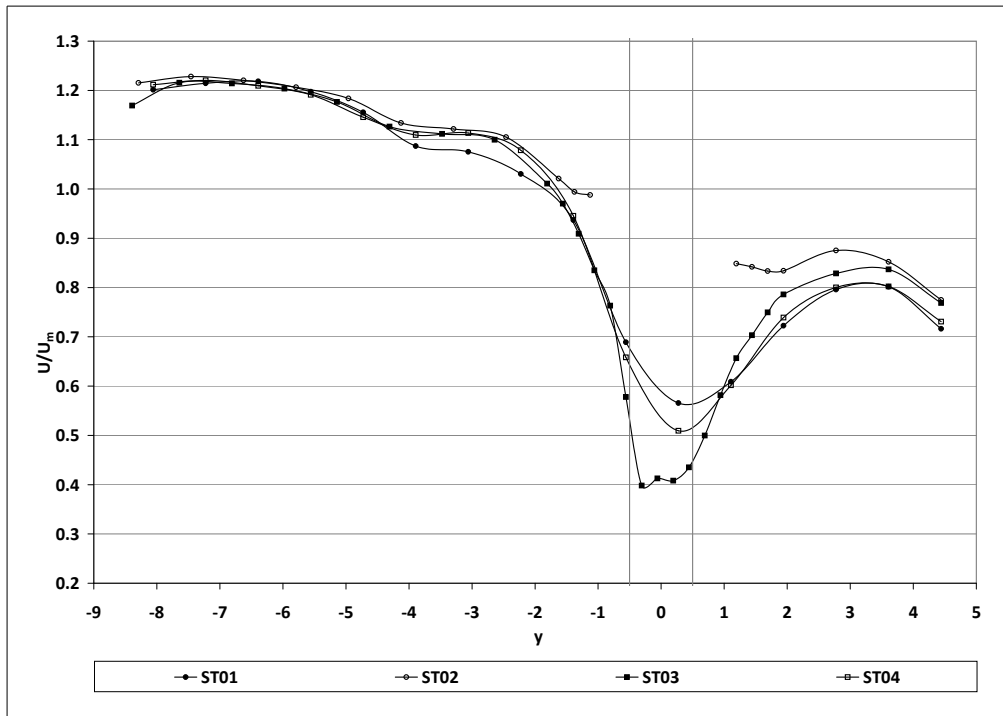


(b)

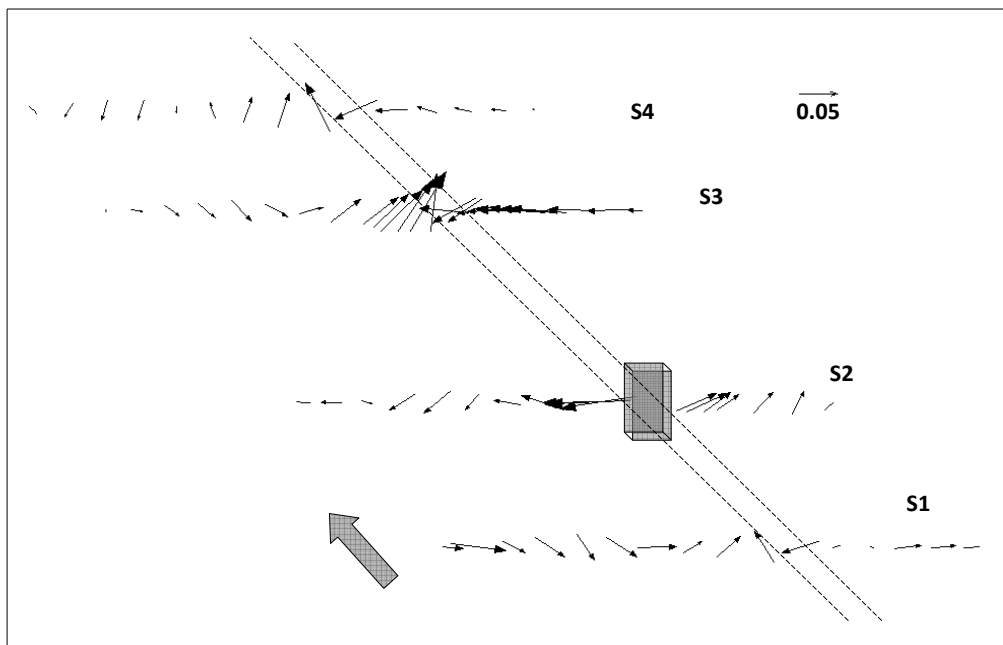


(c)

Figure 4.23: Mean Reynolds shear stress contours ($-\overline{u'v'}$, $-\overline{u'w'}$, $-\overline{v'w'}$) around ($z = 1.0$) the large aspect ratio, emergent block in the compound channel (S2CI)



(a)



(b)

Figure 4.24: Mean velocity components around small, emergent block in the multiple block arrangement in the compound channel (S1CII) (a) U and (b) Vectors of V and W

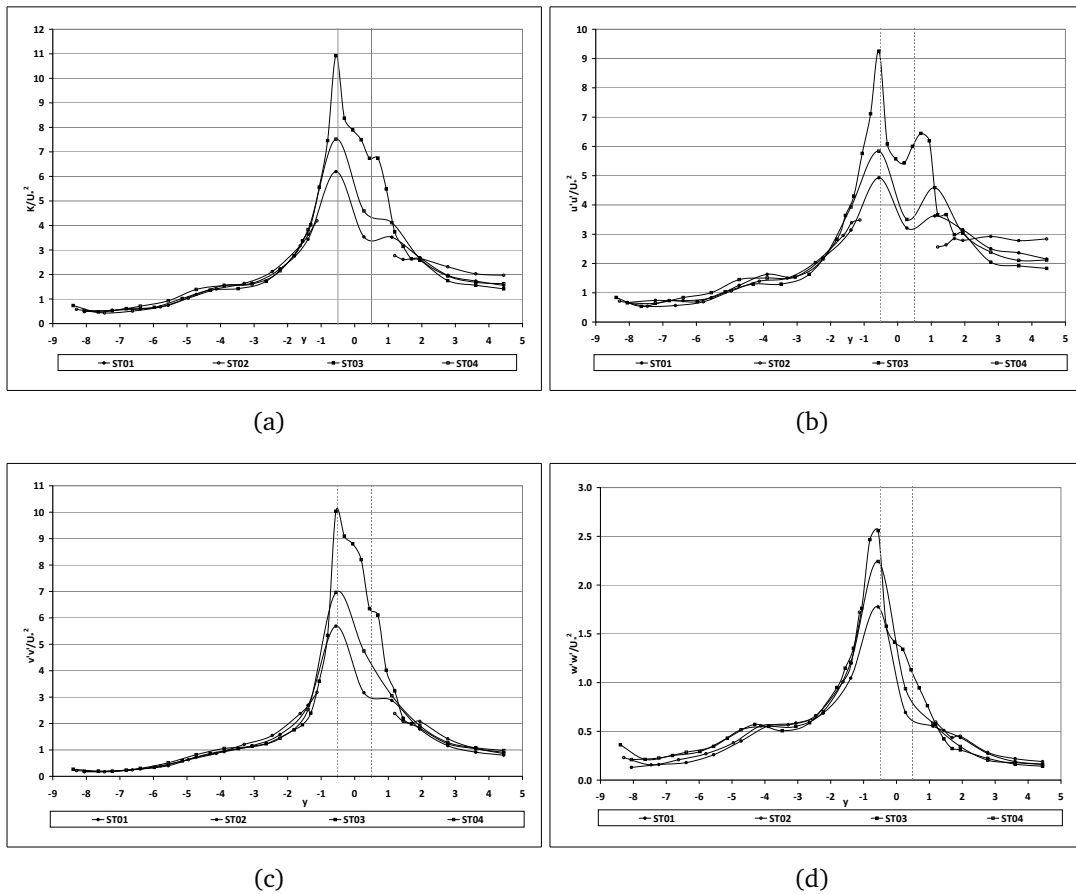
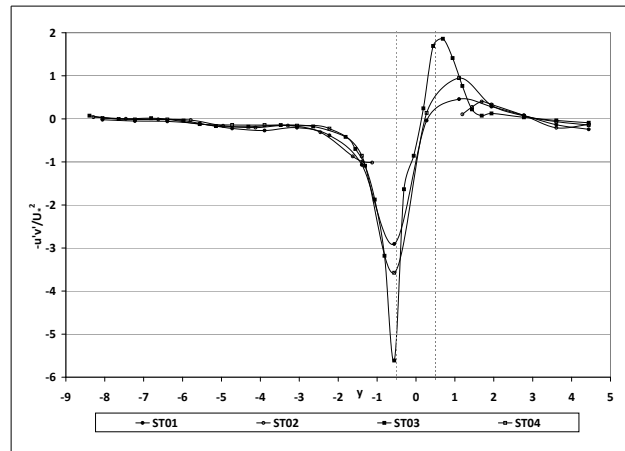
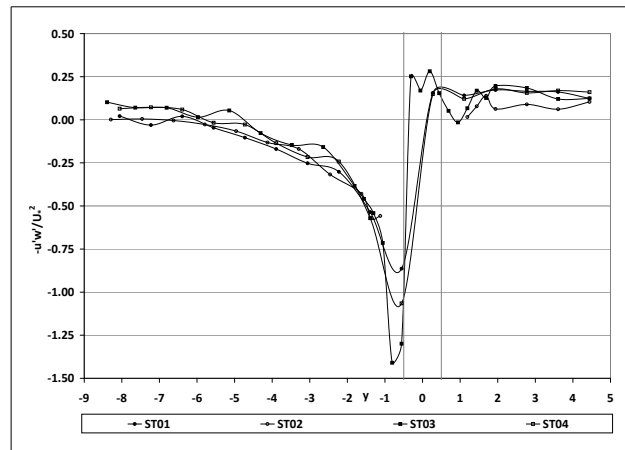


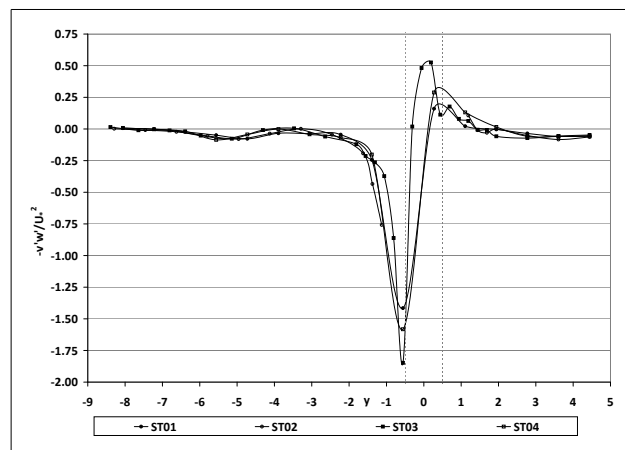
Figure 4.25: *Turbulent kinetic energy and normal turbulent stresses around small, emergent block in the multiple block arrangement in the compound channel (S1CII) (a) K , (b) $\overline{u'u'}$, (c) $\overline{v'v'}$ and (d) $\overline{w'w'}$*



(a)

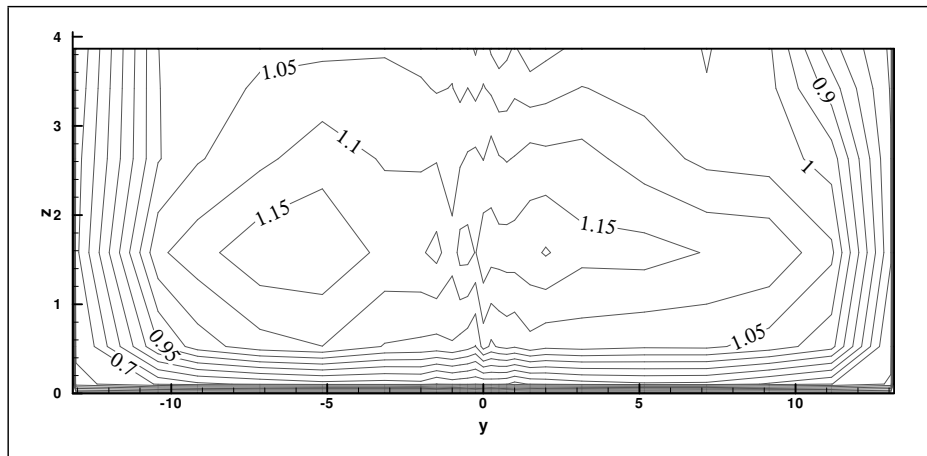


(b)

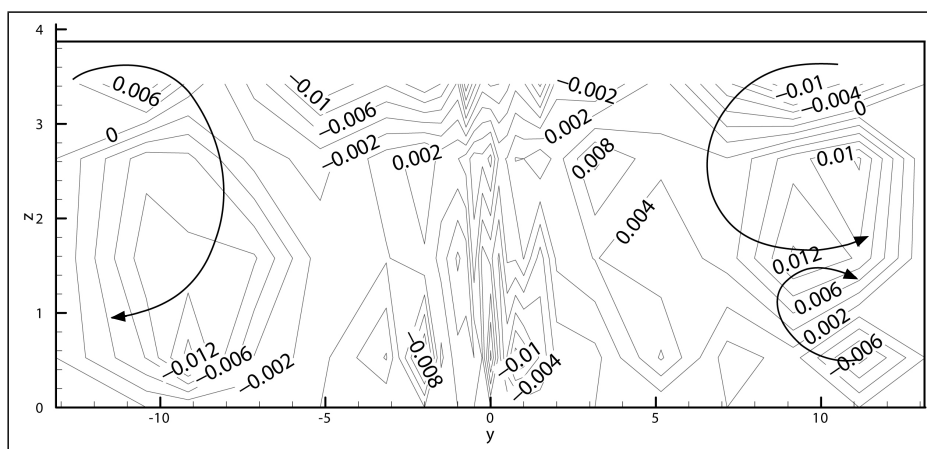


(c)

Figure 4.26: Turbulent shear stresses around small, emergent block in the multiple block arrangement in the compound channel (S1CII) (a) $-\overline{u'v'}$, (b) $-\overline{u'w'}$ and (c) $-\overline{v'w'}$



(a)



(b)

Figure 4.27: Mean (a) streamwise velocity contours (U) and (b) spanwise velocity contours (V) upstream of the large aspect ratio, submerged block in the simple channel (S4CIV)

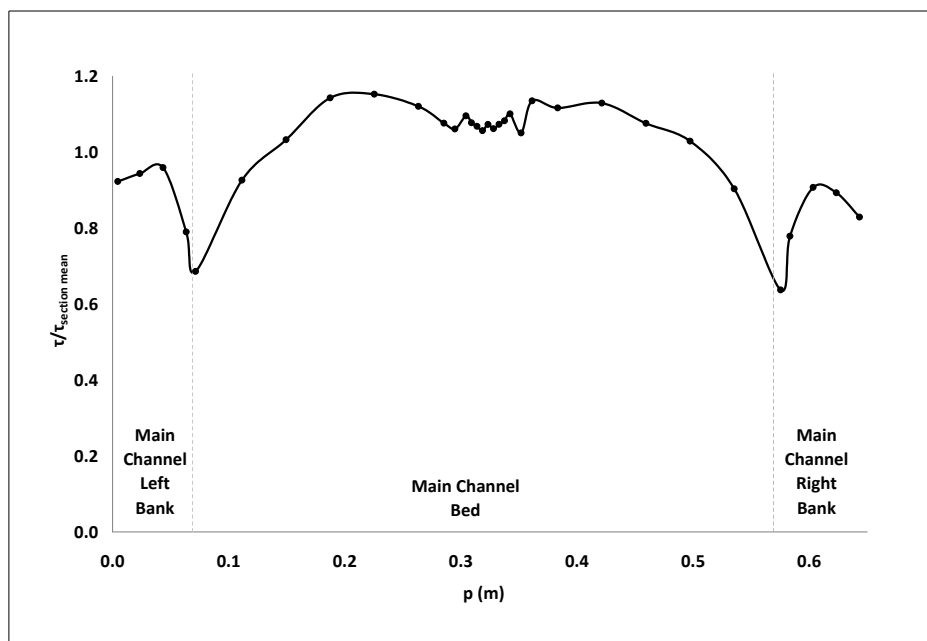
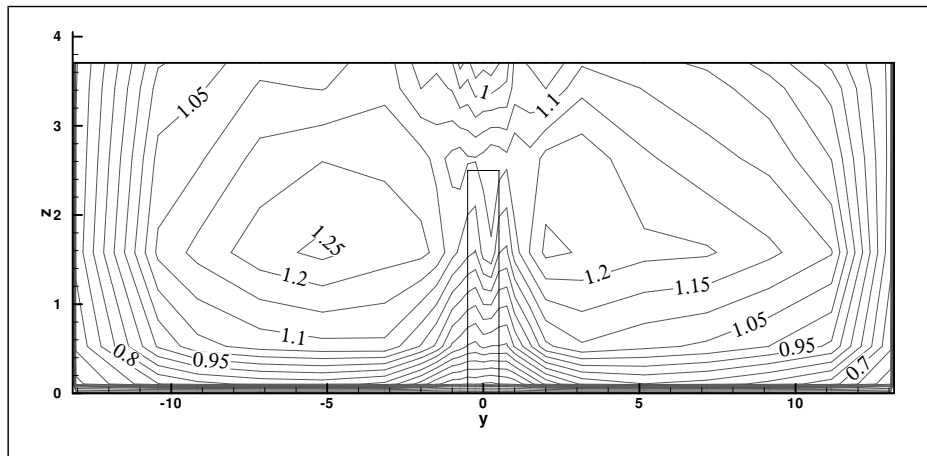
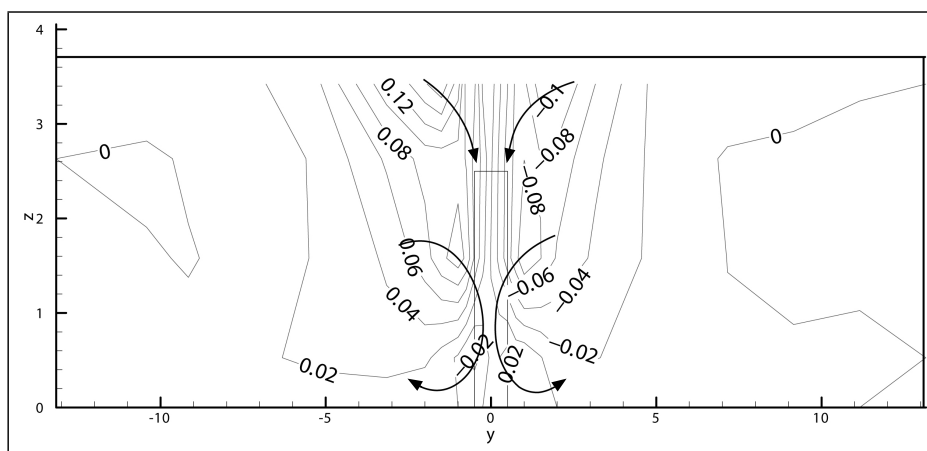


Figure 4.28: Distribution of boundary shear stress at the upstream section for the large aspect ratio, submerged block in the simple channel (S4CIV)



(a)



(b)

Figure 4.29: Mean (a) streamwise velocity contours (U) and (b) spanwise velocity contours (V) downstream of the large aspect ratio, submerged block in the simple channel (S4CIV)

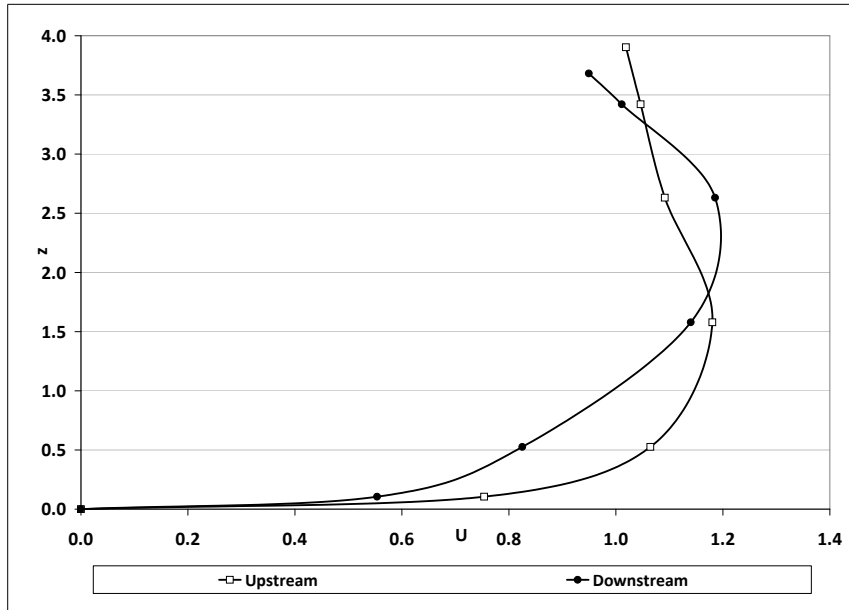


Figure 4.30: Vertical distribution of streamwise velocity U at the block centreline upstream and downstream of the large aspect ratio, submerged block in the simple channel (S4CIV)

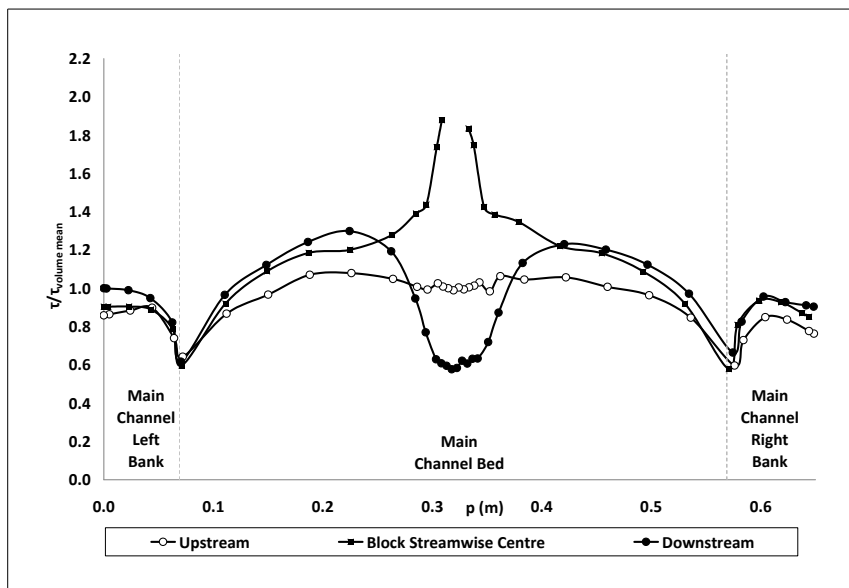


Figure 4.31: Distribution of boundary shear stress at all sections for the large aspect ratio, submerged block in the simple channel (S4CIV)

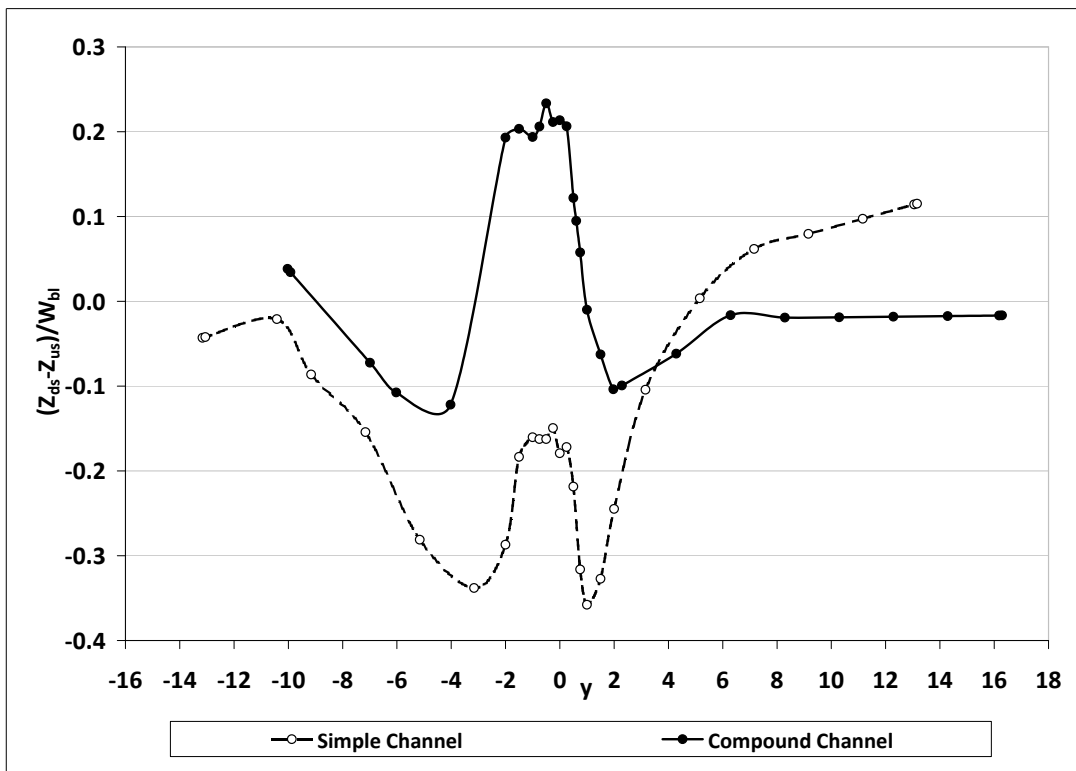
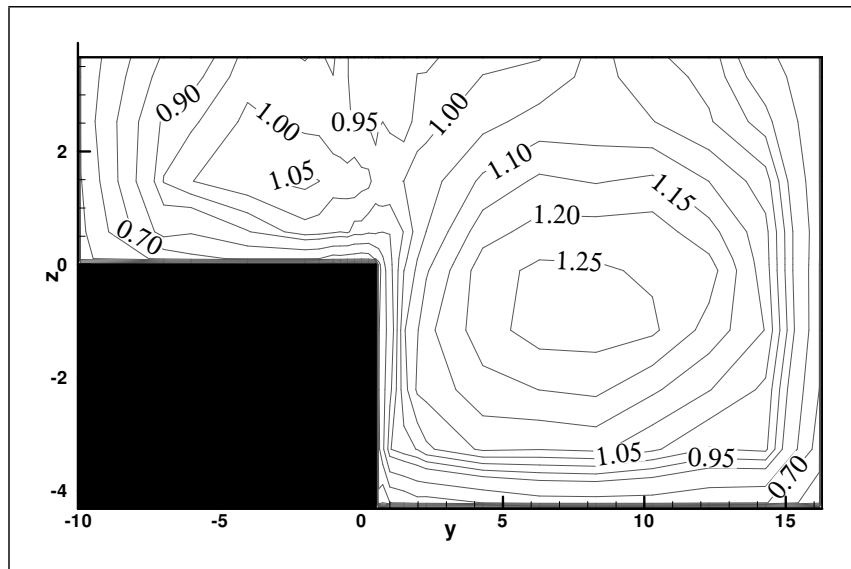
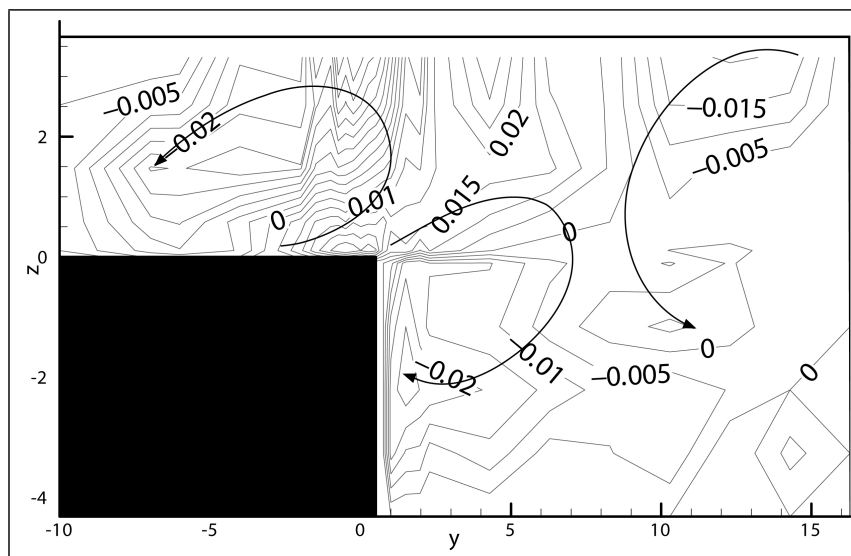


Figure 4.32: Difference between downstream water level and average upstream water level, normalised with block width, for the large aspect ratio, submerged blocks in the simple and compound channel (S4CIV,S4CII)



(a)



(b)

Figure 4.33: Mean (a) streamwise velocity contours (U) and (b) spanwise velocity contours (V) upstream of the large aspect ratio, submerged block in the compound channel (S4CII)

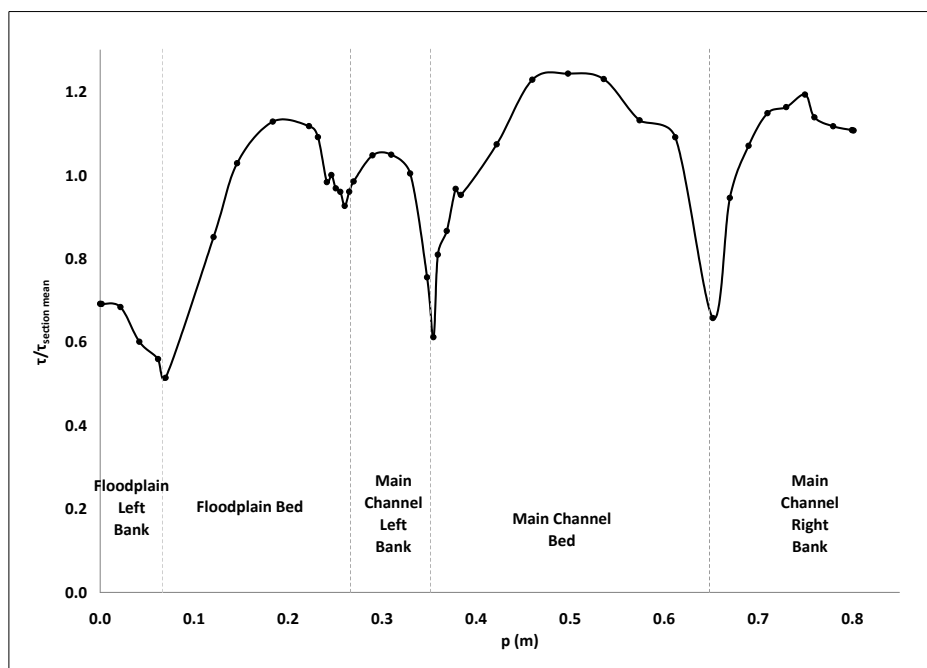
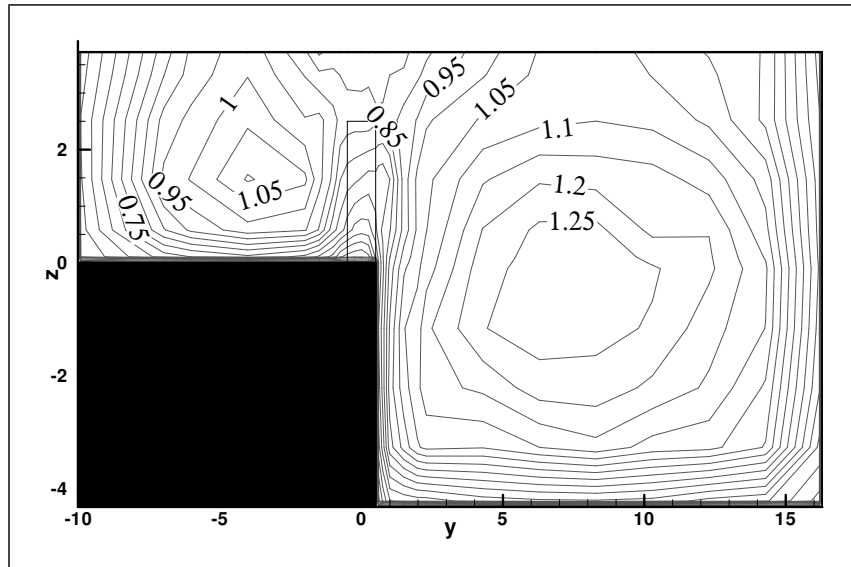
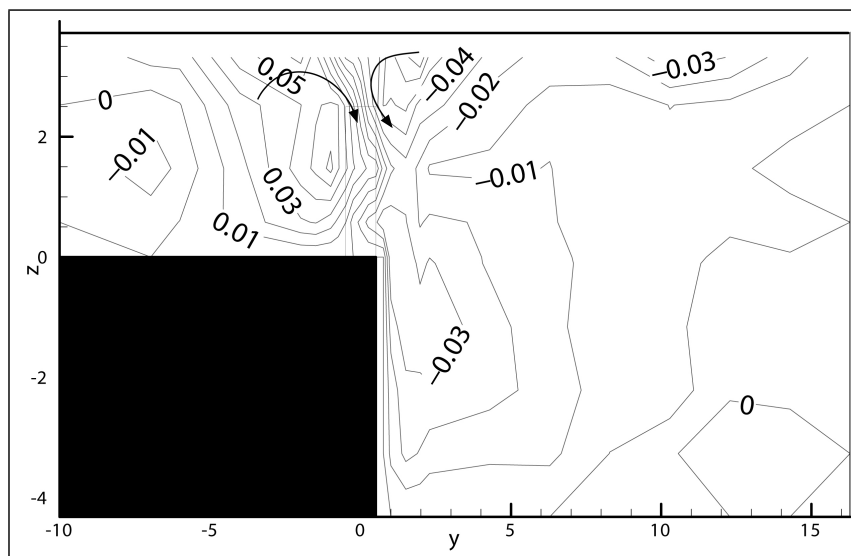


Figure 4.34: *Distribution of boundary shear stress upstream of the large aspect ratio, submerged block in the compound channel (S4CII)*



(a)



(b)

Figure 4.35: Mean (a) streamwise velocity contours (U) and (b) spanwise velocity contours (V) downstream of the large aspect ratio, submerged block in the compound channel (S4CII)

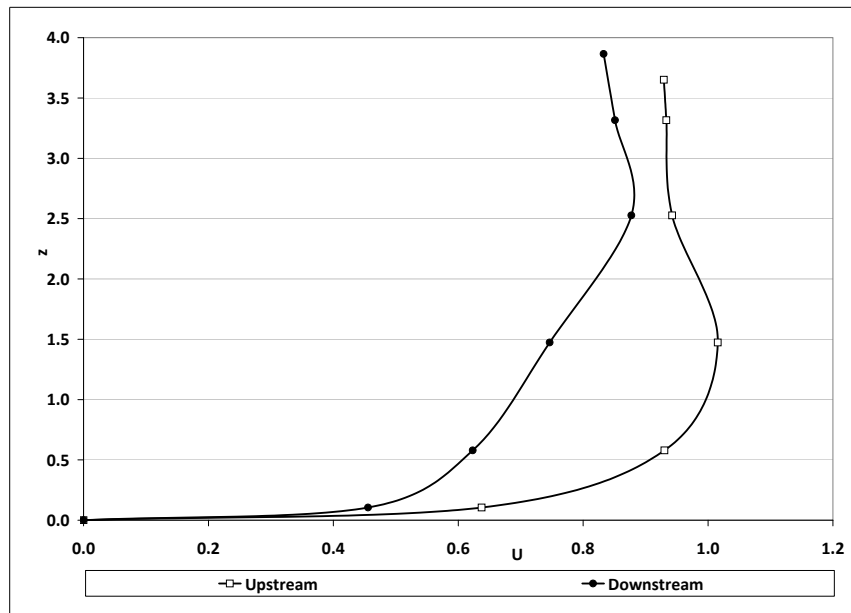


Figure 4.36: Vertical distribution of streamwise velocity U at the block centreline upstream and downstream of the large aspect ratio, submerged block in the compound channel (S4CII)

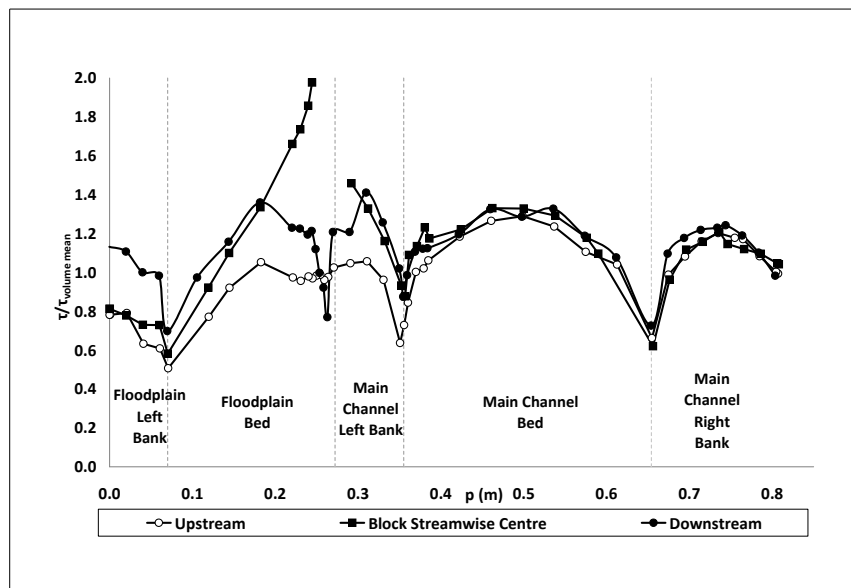
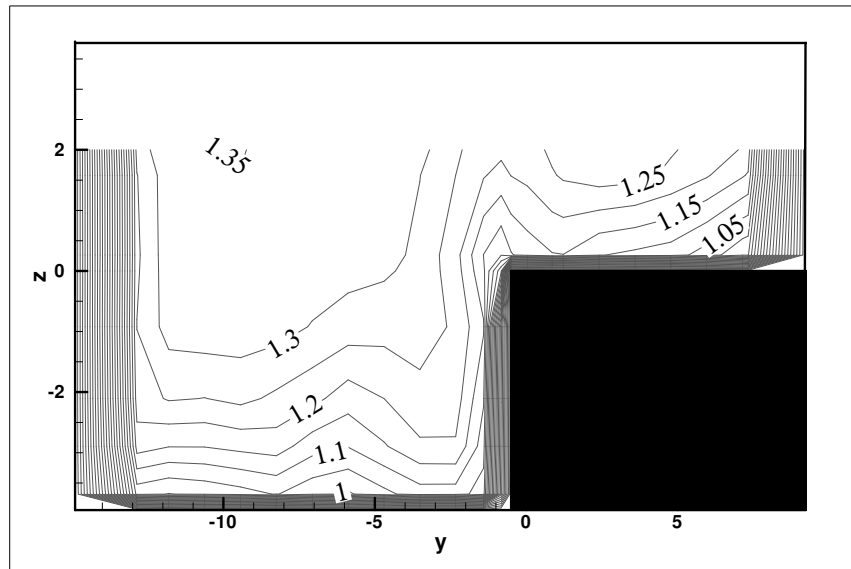
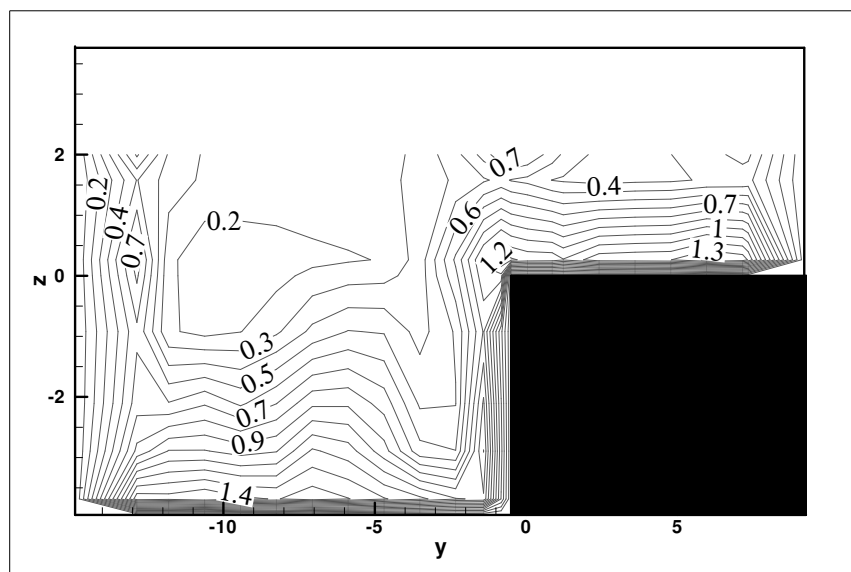


Figure 4.37: Distribution of boundary shear stress at all sections for the large aspect ratio, submerged block in the compound channel (S4CII)

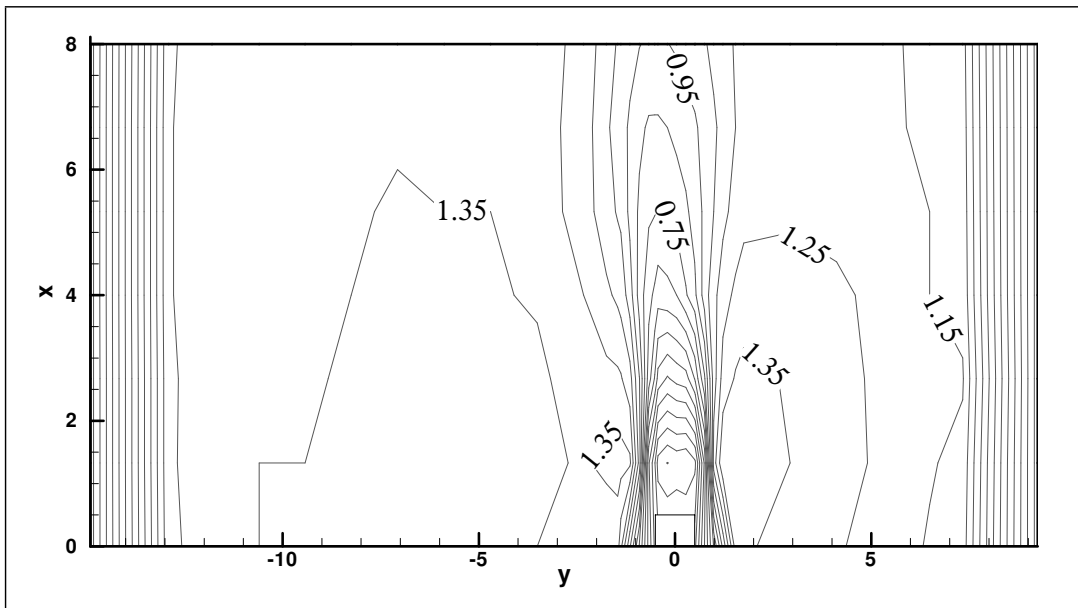


(a)

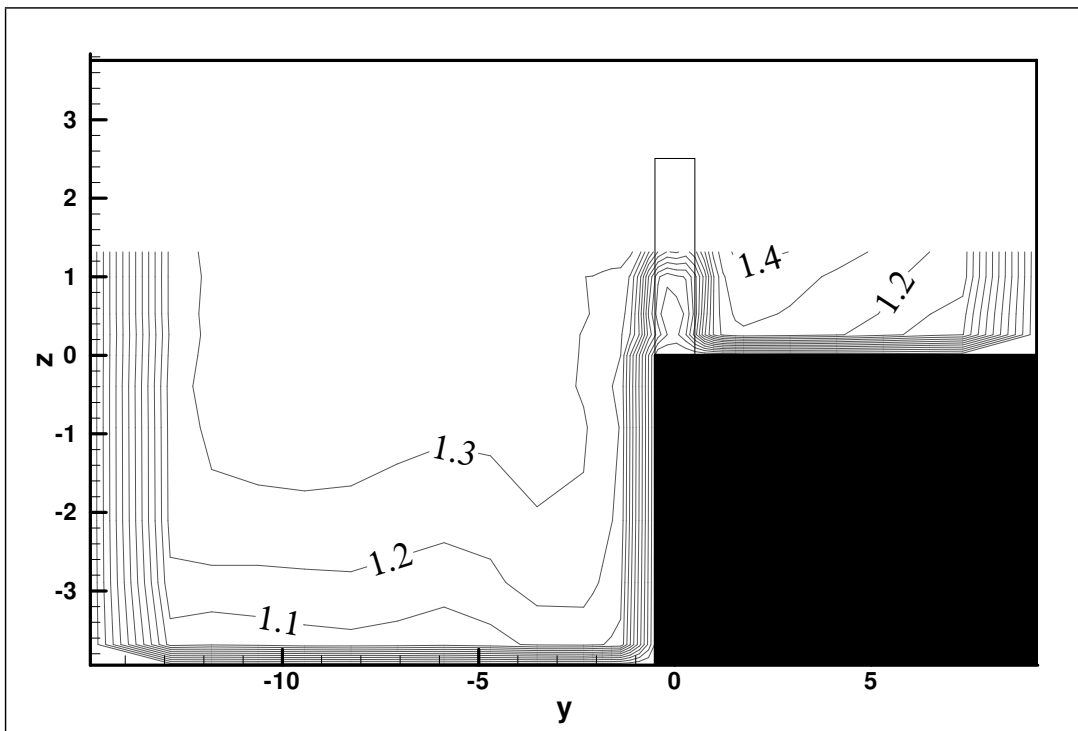


(b)

Figure 4.38: (a) Mean streamwise velocity contours (U) and (b) mean turbulent kinetic energy contours (K) upstream of the large aspect ratio, submerged block in the compound channel (S2CII)

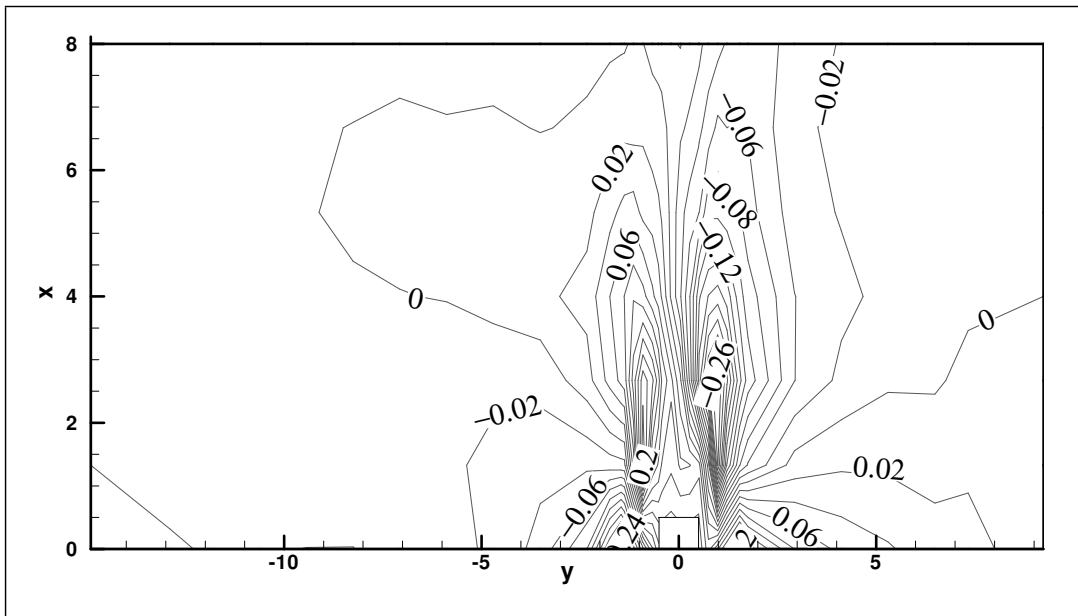


(a)

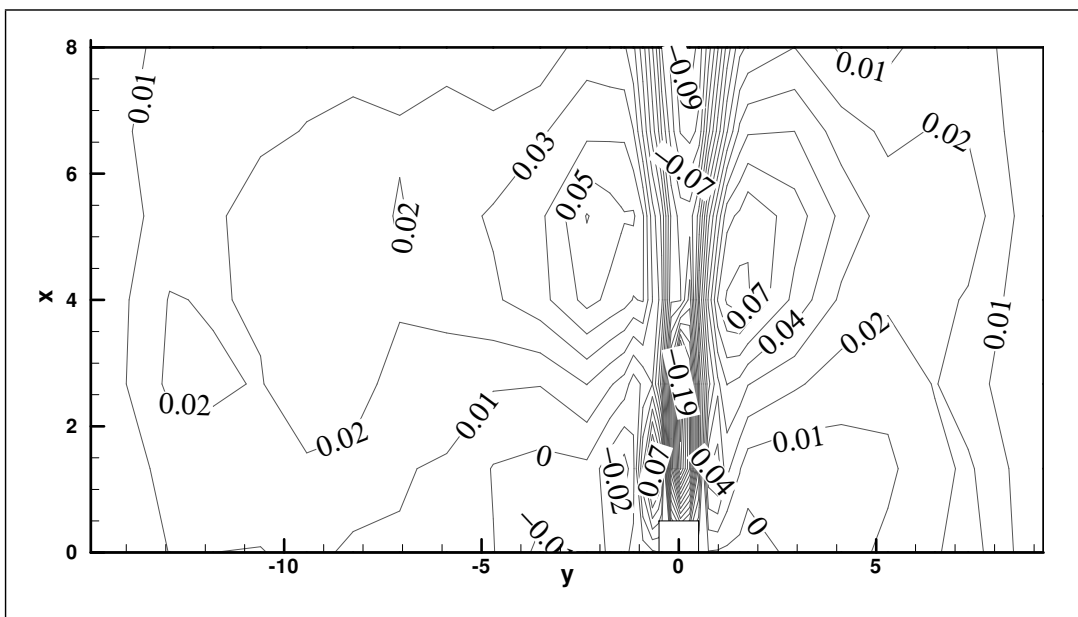


(b)

Figure 4.39: Mean streamwise velocity contours (U) (a) around ($z = 1$) and (b) downstream ($x = 2.7$) of the large aspect ratio, submerged block in the compound channel (S2CII)



(a)



(b)

Figure 4.40: Mean (a) spanwise velocity contours (V) and (b) vertical velocity contours (W) around ($z = 1.0$) the large aspect ratio, submerged block in the compound channel (S2CII)

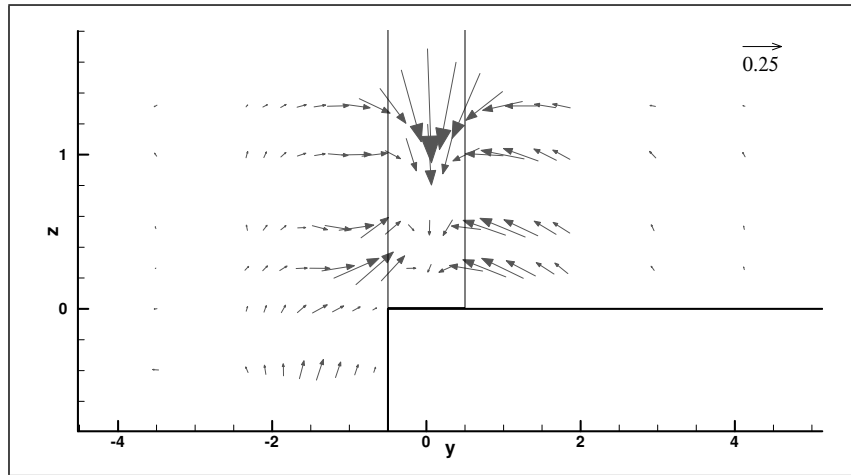


Figure 4.41: Vectors of secondary circulations downstream ($x = 2.7$) of the large aspect ratio, submerged block in the compound channel (S2CII)

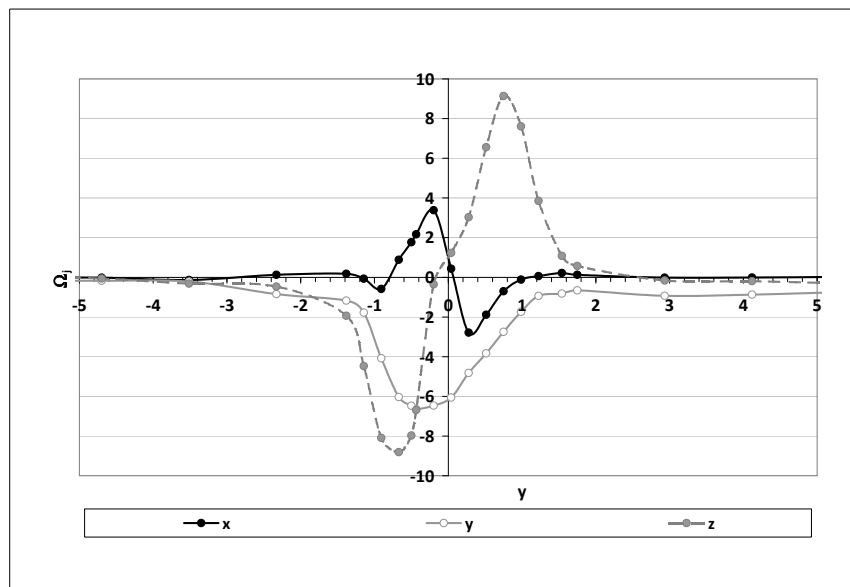


Figure 4.42: Mean vorticity components downstream ($x, z = 2.7, 1.0$) of the large aspect ratio, submerged block in the compound channel (S2CII)

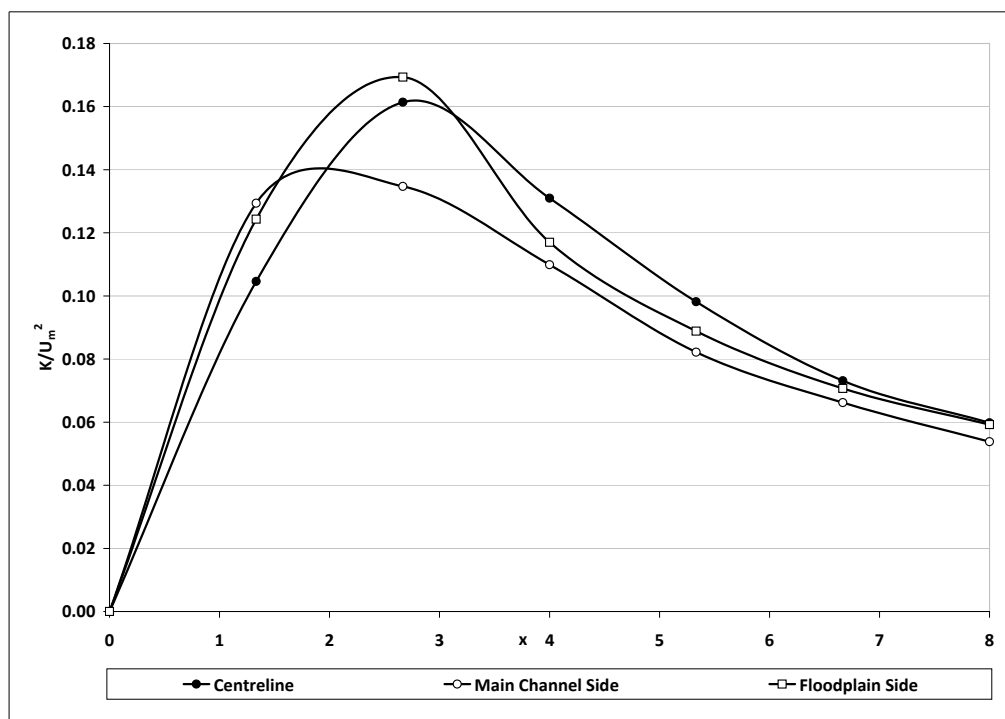
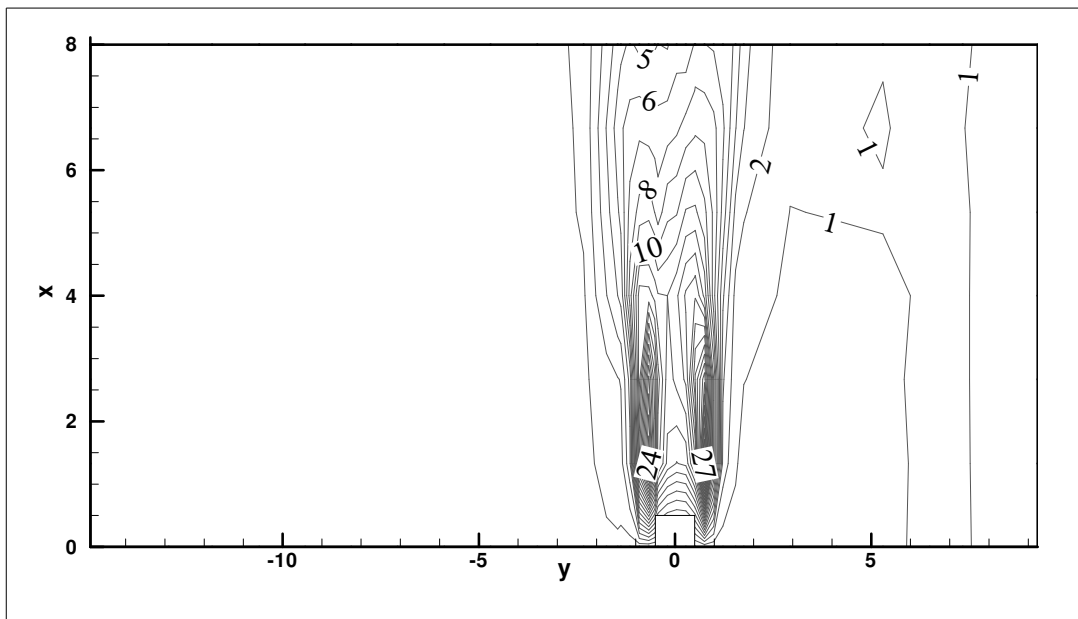
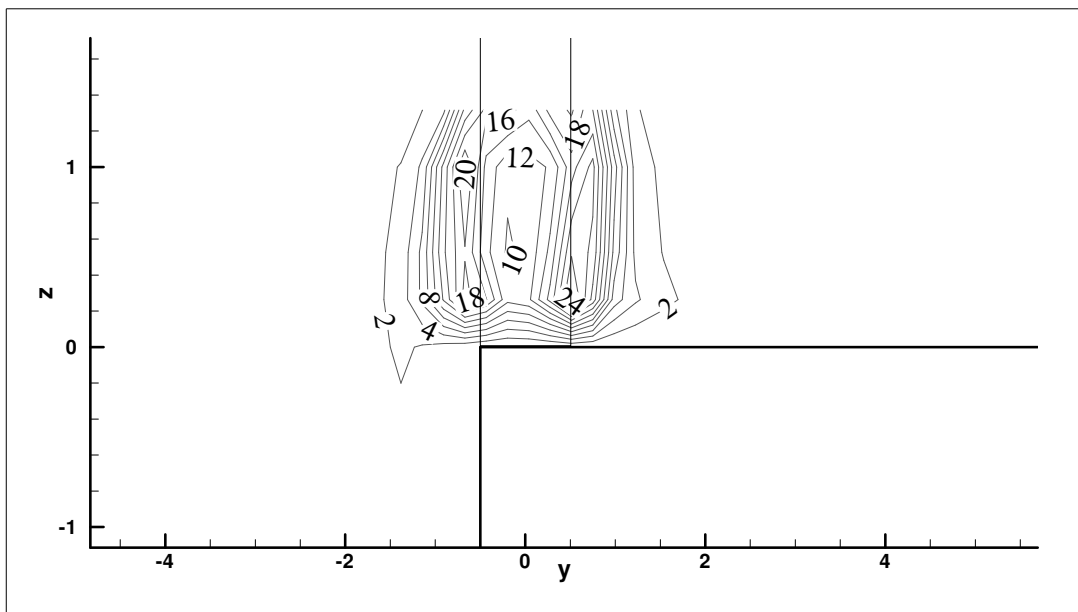


Figure 4.43: Normalised mean turbulent kinetic energy (K/U_m^2) in the wake of the large aspect ratio, submerged block in the compound channel (S2CII)

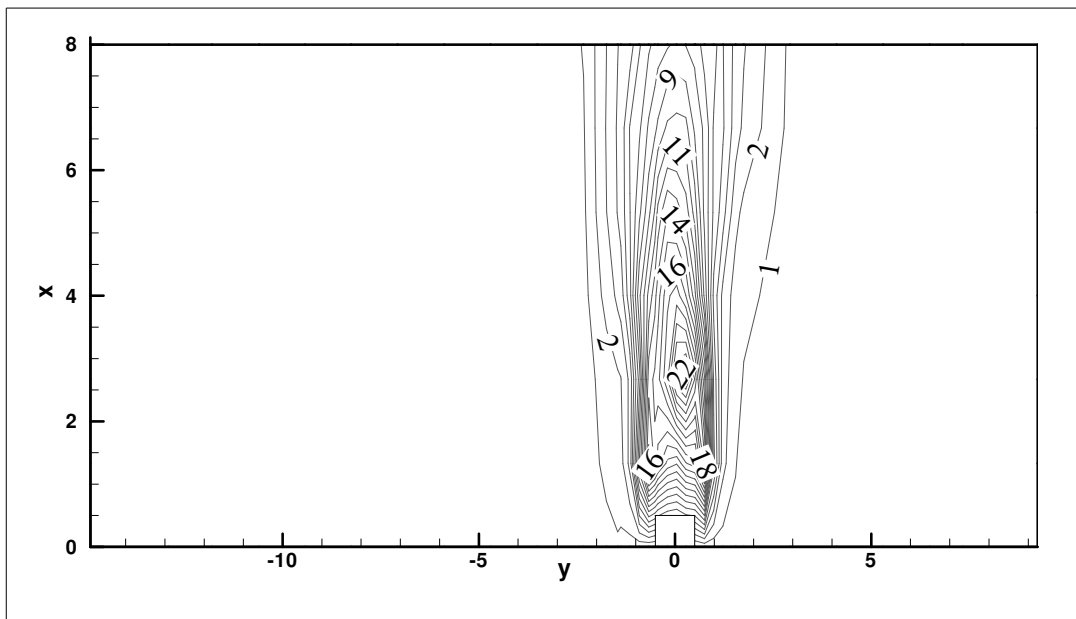


(a)

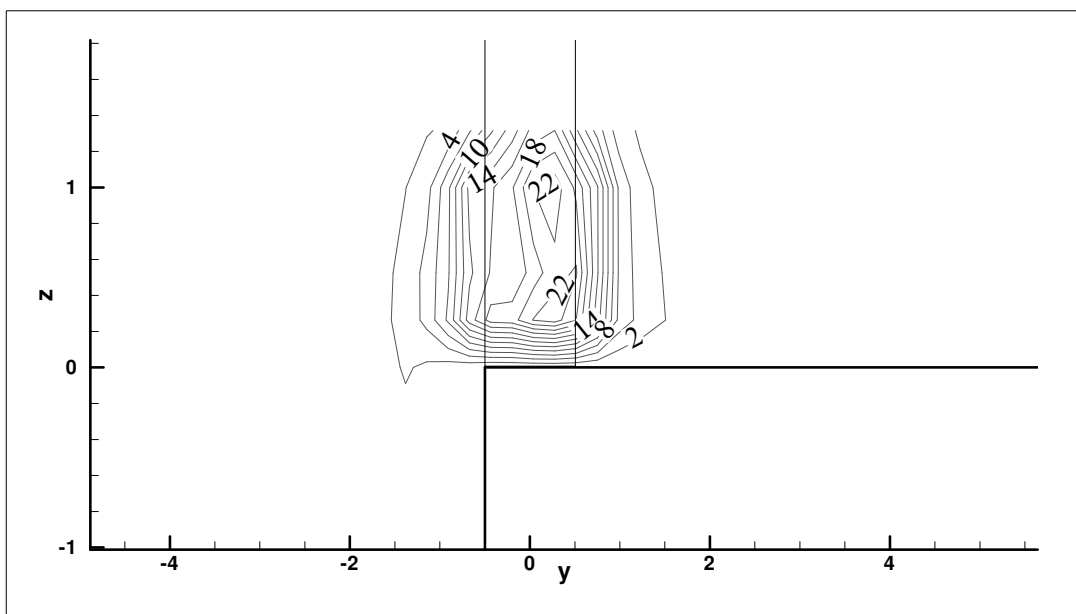


(b)

Figure 4.44: Mean streamwise normal Reynolds stress contours $\overline{u'u'}$ (a) around ($z = 1$) and (b) downstream ($x = 2.7$) of the large aspect ratio, submerged block in the compound channel (S2CII)

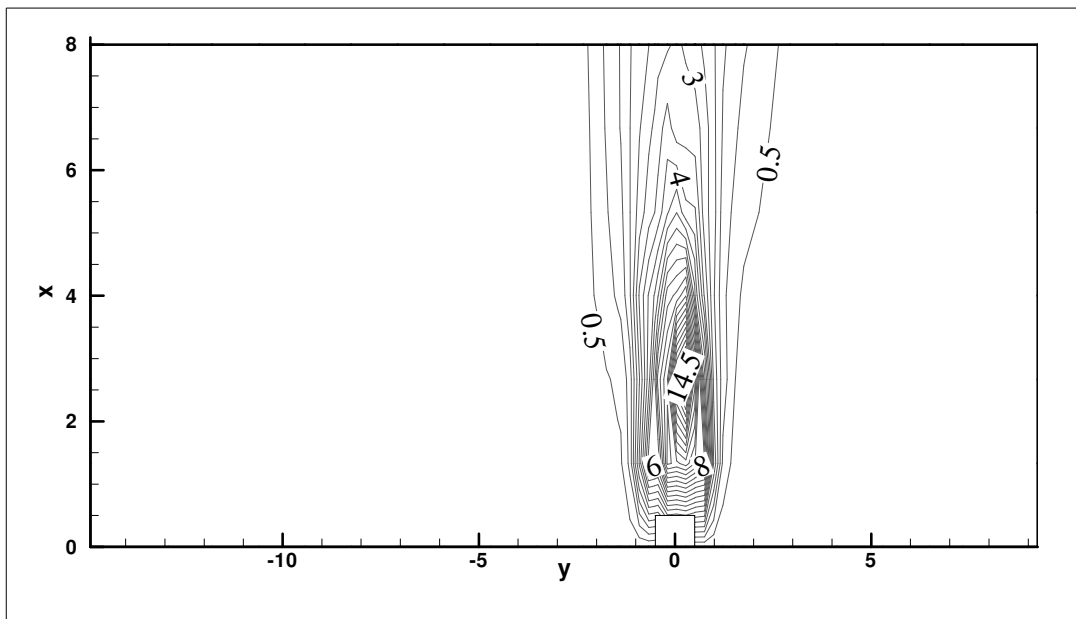


(a)

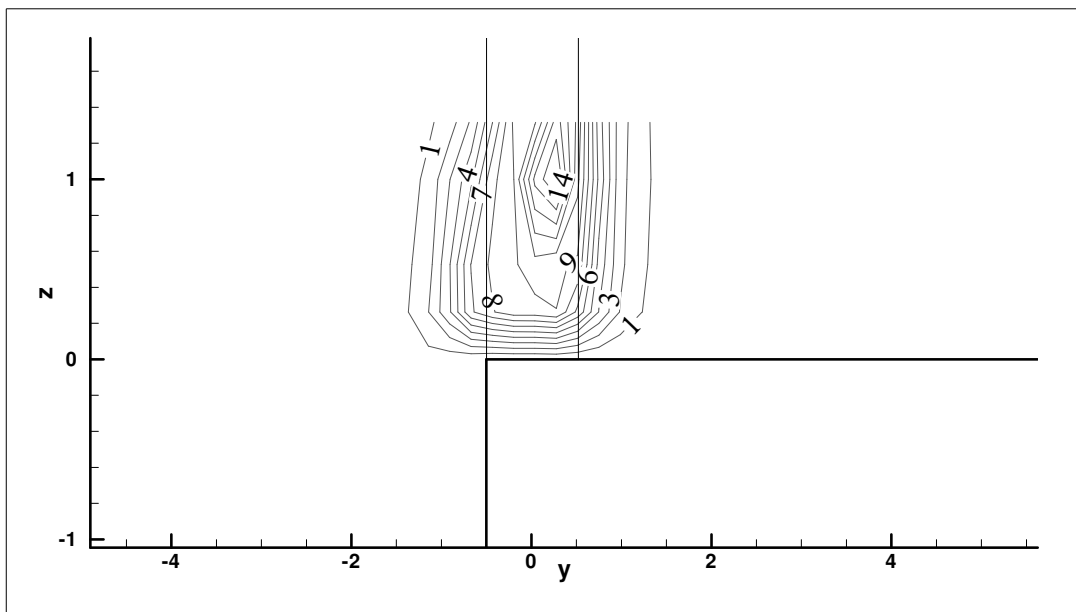


(b)

Figure 4.45: Mean spanwise normal Reynolds stress contours $\overline{(v'v')}$ (a) around ($z = 1$) and (b) downstream ($x = 2.7$) of the large aspect ratio, submerged block in the compound channel (S2CII)

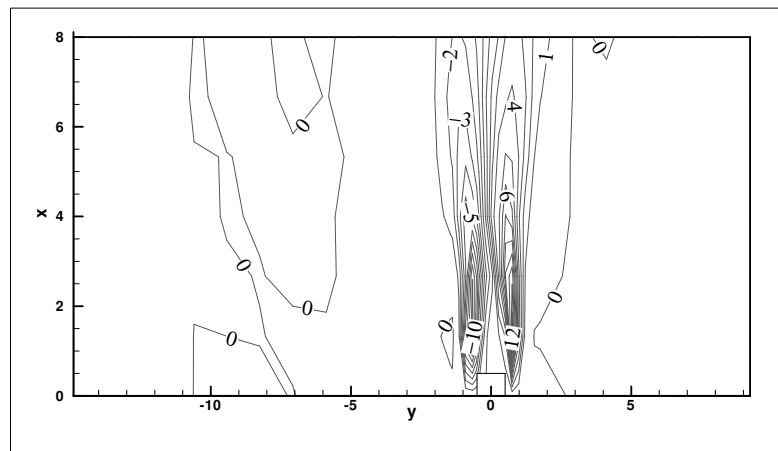


(a)

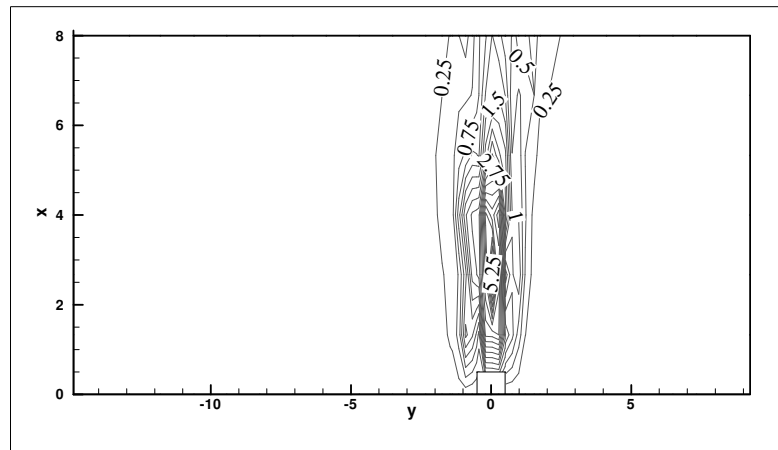


(b)

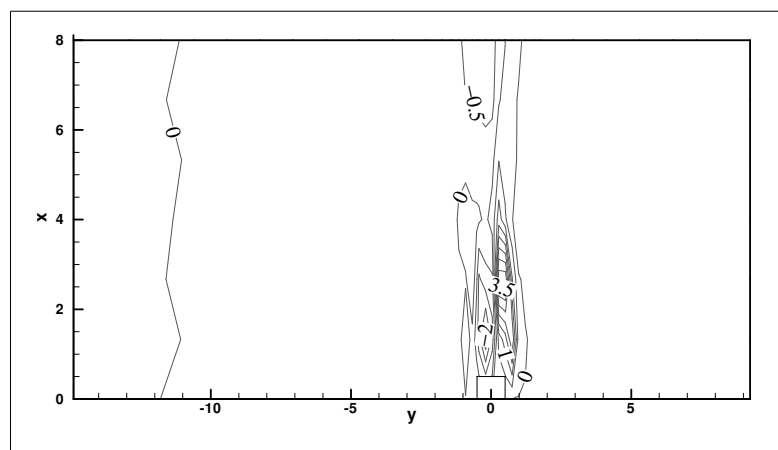
Figure 4.46: Mean vertical normal Reynolds stress contours $\overline{(w'w')}$ (a) around ($z = 1$) and (b) downstream ($x = 2.7$) of the large aspect ratio, submerged block in the compound channel (S2CII)



(a)

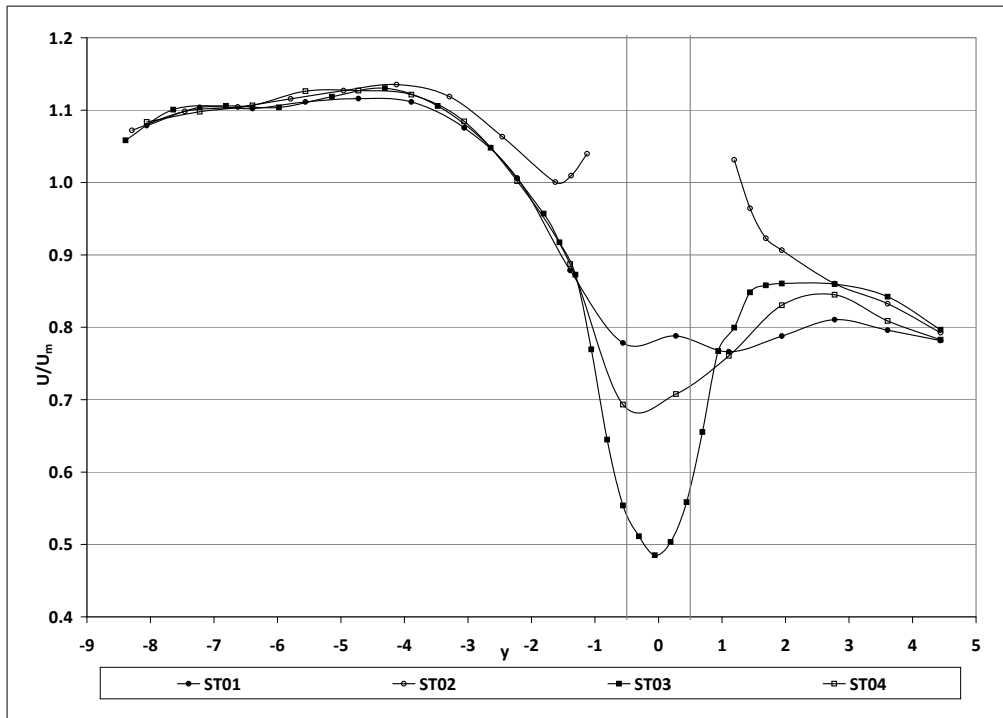


(b)

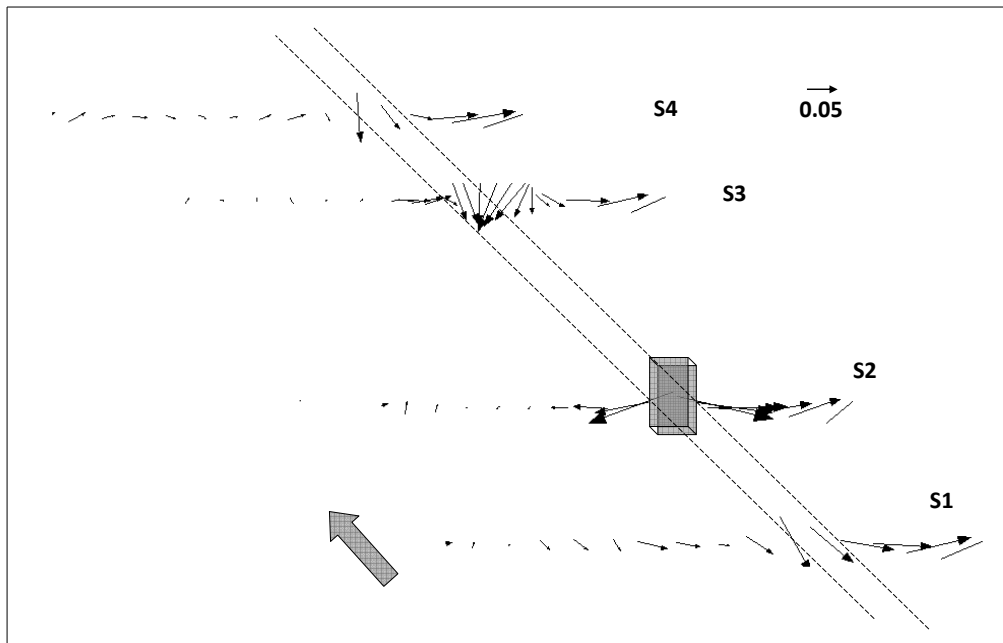


(c)

Figure 4.47: Mean Reynolds shear stress contours ($-\overline{u'v'}$, $-\overline{u'w'}$, $-\overline{v'w'}$) around ($z = 1.0$) the large aspect ratio, submerged block in the compound channel (S2CII)

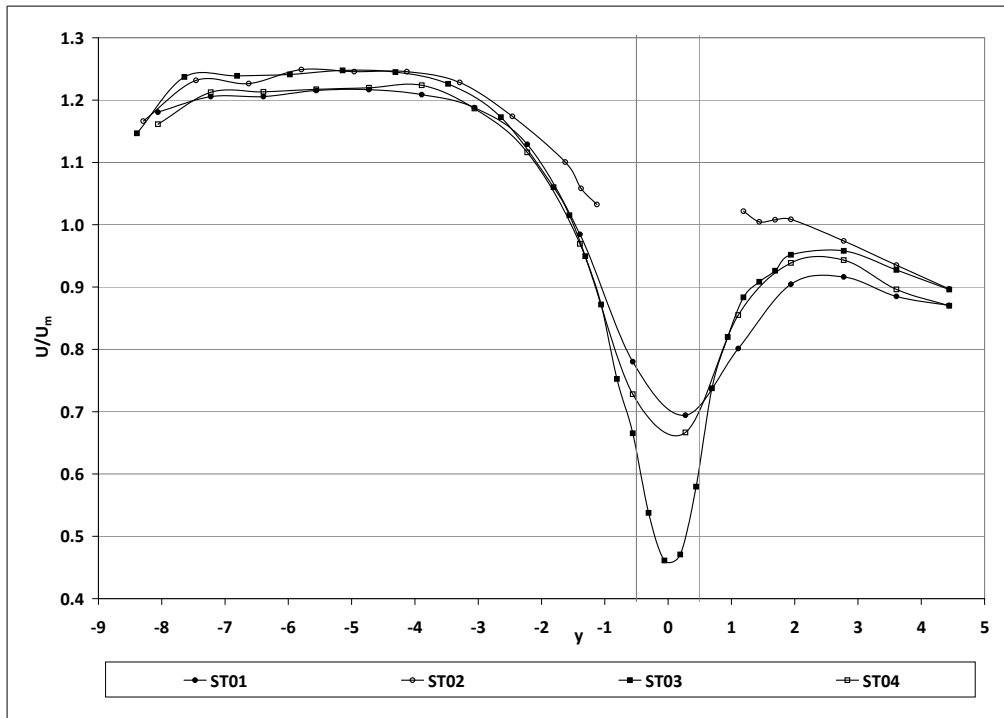


(a)

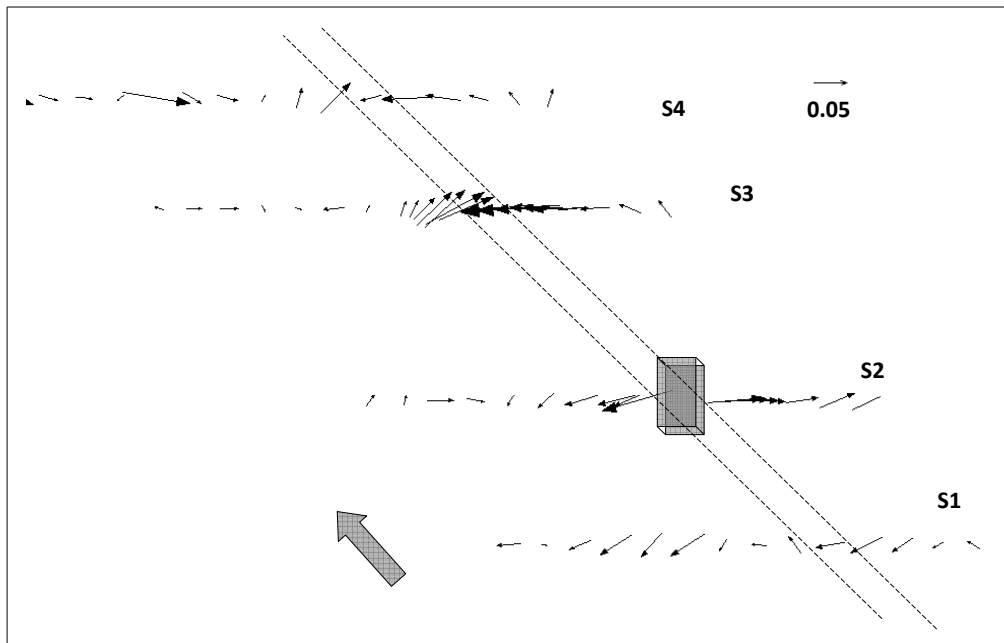


(b)

Figure 4.48: Mean velocity components around small, deep submerged block in the multiple block arrangement in the compound channel (S1CI) (a) U and (b) Vectors of V and W



(a)



(b)

Figure 4.49: Mean velocity components around small, shallow submerged block in the multiple block arrangement in the compound channel (S1CIII) (a) U and (b) Vectors of V and W

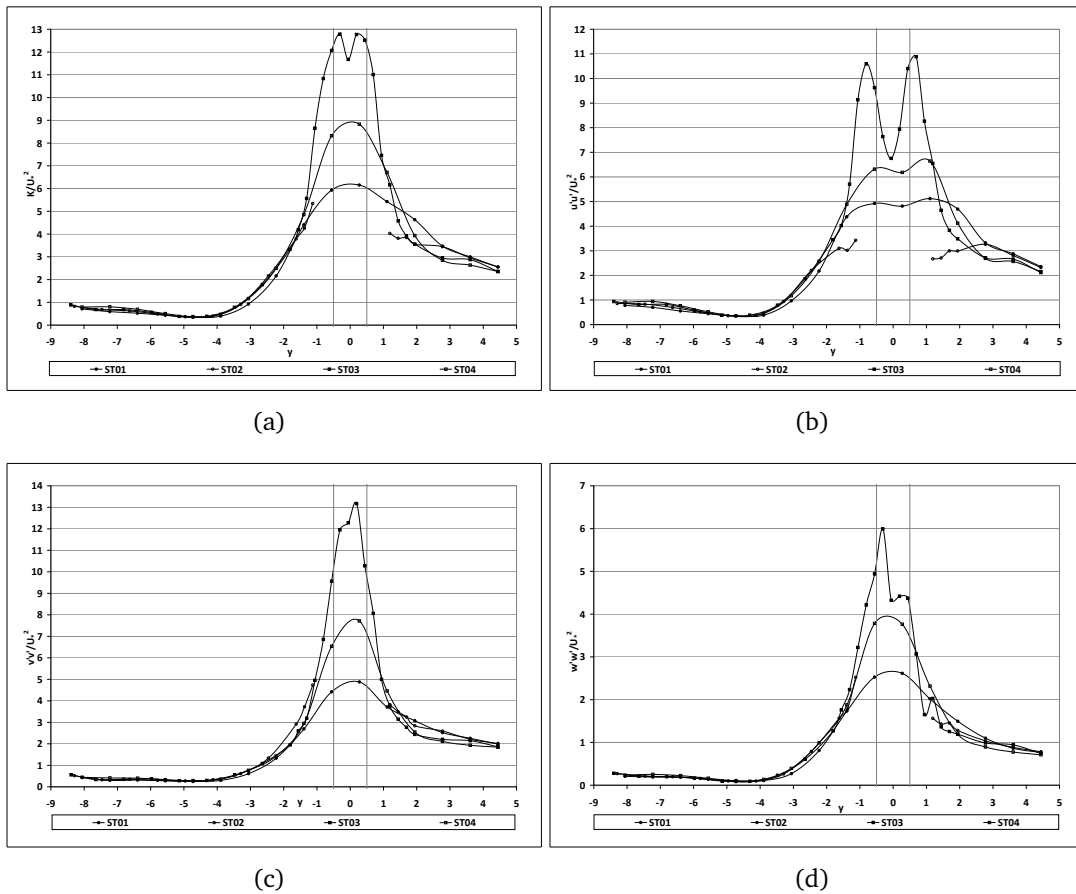


Figure 4.50: Turbulent kinetic energy and normal turbulent stresses around small, deep submerged block in the multiple block arrangement in the compound channel (S1C1) (a) K , (b) $\overline{u'u'}$, (c) $\overline{v'v'}$ and (d) $\overline{w'w'}$

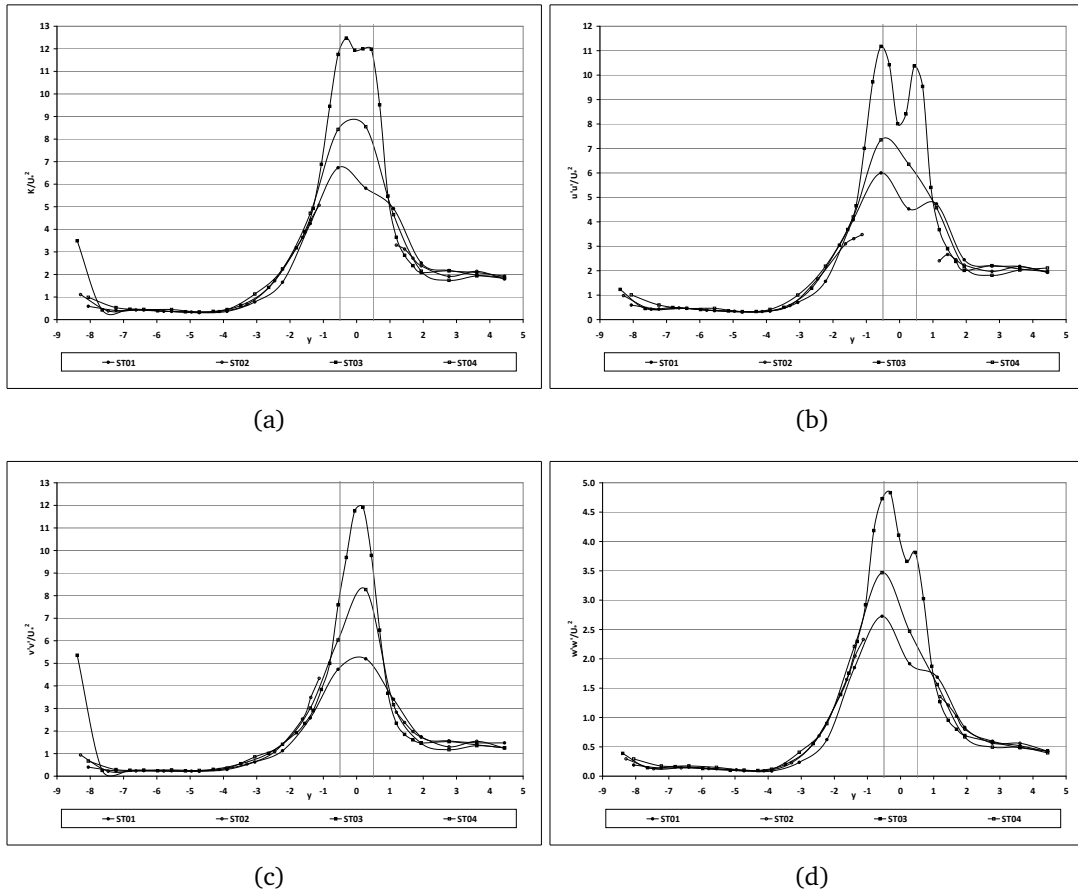
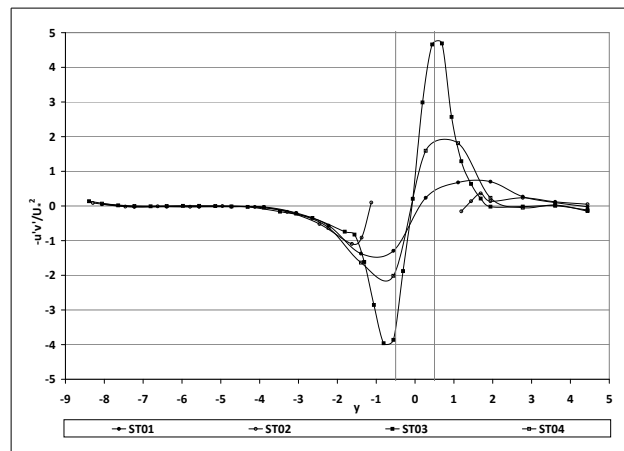
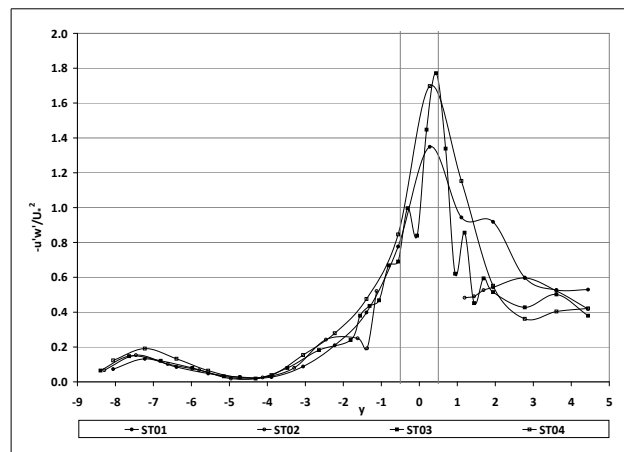


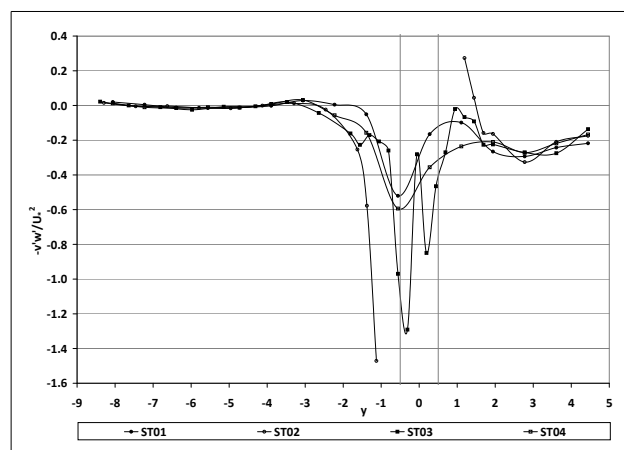
Figure 4.51: Turbulent kinetic energy and normal turbulent stresses around small, shallow submerged block in the multiple block arrangement in the compound channel (S1CIII) (a) K , (b) $\overline{u'u'}$, (c) $\overline{v'v'}$ and (d) $\overline{w'w'}$



(a)

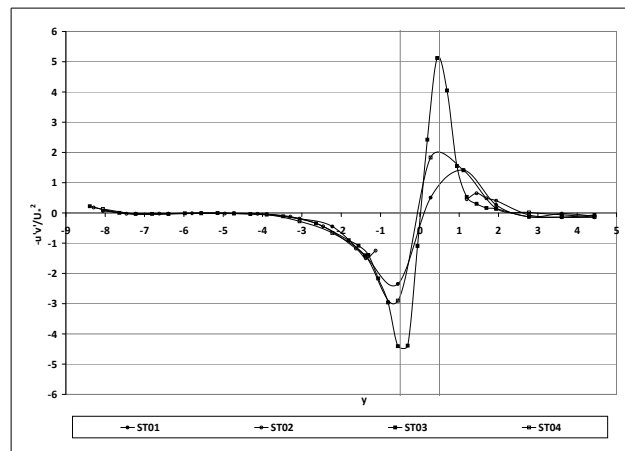


(b)

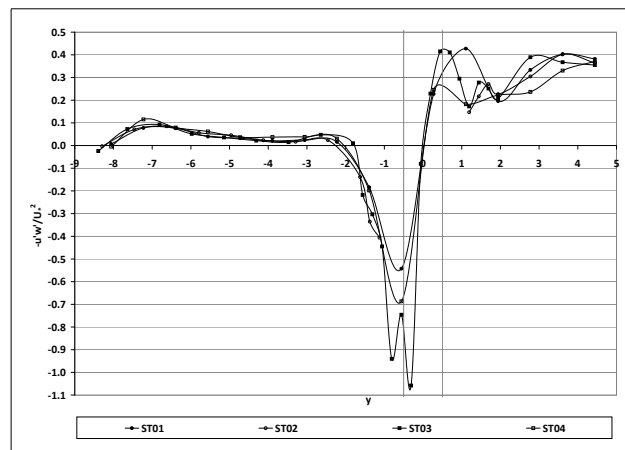


(c)

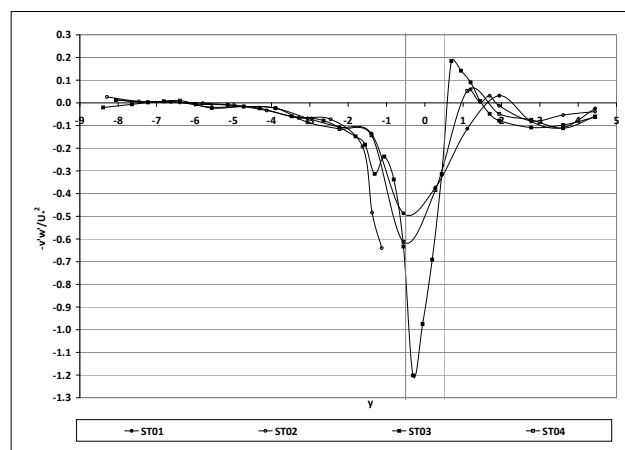
Figure 4.52: Turbulent shear stresses around small, deep submerged block in the multiple block arrangement in the compound channel (S1C1) (a) $-\overline{u'v'}$, (b) $-\overline{u'w'}$ and (c) $-\overline{v'w'}$



(a)



(b)



(c)

Figure 4.53: Turbulent shear stresses around small, shallow submerged block in the multiple block arrangement in the compound channel (S1CIII) (a) $-\overline{u'v'}$, (b) $-\overline{u'w'}$ and (c) $-\overline{v'w'}$

CHAPTER 5

Computational Modelling

5.1 Model Testing - Simple Scenarios

The structure and algorithm for the computational model was described in Chapter 3. In its original form, the code was tested by its author (Vyas, 2007). However, since a new turbulence closure was added to the code for this project, it was first necessary to test its application to simple flow cases and compare the results to those obtained with the existing turbulence closure mechanisms.

Square Duct Flow The first test case considered was that of a simple square duct flow with a Reynolds number of 5×10^4 . This corresponds to the Reynolds number chosen for model testing by Vyas (2007). Setting the upstream boundary condition to a uniform velocity value, the linear $k - \epsilon$ model was used initially. At the conclusion of the first simulation, the resulting downstream profile was applied as the upstream boundary condition to the next simulation. In this way, fully developed flow was achieved using the more efficient linear $k - \epsilon$ model. The grid for this simulation is shown in Figure 5.1. The grid, and all subsequent grids used in this work, are designed in order to minimise the simulation times associated with them. To this end, smaller cell sizes were created near boundaries and larger cell sizes were used far from boundaries. In this case, in the streamwise direction, the

grid cells are equally spaced with 72 cells covering a length of 5, giving a cell length of 0.0695. In the lateral and vertical directions, the cell distributions are identical, with a total of 80 cells in each direction and an equal width and height of 1. The minimum cell size is 0.00894 and the expansion factor, namely the factor by which cell size increases from one cell to its neighbour, is 1.034. Cells are smallest at the boundaries, increase in size towards the quarter-width point and then reduce in size again to the centre of the channel. The vertical and lateral boundaries are set to be wall boundaries, functioning as described in Section 3.2.3 and the outlet boundary is set up using the Neumann boundary condition described in Section 3.2.3.

The distribution of mean streamwise velocity, the turbulent kinetic energy and the vectors of the secondary circulations produced by the $k - \epsilon$ model are shown in Figure 5.2. The maximum magnitude of the secondary circulations was found to be approximately $0.5 \times 10^{-6} U_m$. It is clear from this result that, as expected, the $k - \epsilon$ model fails to reproduce the secondary circulations associated with the anisotropy of the lateral and vertical normal Reynolds stress components. Figure 5.2(b) shows the distribution of the turbulent kinetic energy (K), which, as expected, shows higher values near the channel walls.

Using these results as upstream boundary conditions, a simulation was then performed using the Speziale (1987) model. The performance of this model for this scenario was tested by Vyas (2007), allowing us to directly compare our results. Figure 5.3 gives the results for this simulation and the secondary circulations can be clearly seen in the plot in (c). The maximum secondary circulation value as a proportion of the bulk mean velocity is 0.926%. In comparison to the experimental data described in Section 2.2.1, this value is low and this is reflected in the weak bulging of the contours of streamwise velocity that can be observed in Figure 5.3(a). These results also match those of Vyas (2007), who noted that of the three models originally included in the code, the model of Speziale (1987) tended to produce the least change in the streamwise velocity contours. The contours of

turbulent kinetic energy are largely unchanged from the results of the linear $k - \epsilon$ model.

Figure 5.4 shows the results from the same simulation performed with the turbulence closure scheme of Kimura and Hosoda (2003), which will henceforth be called the *K&H* scheme. The streamwise velocity contours are changed from the results of the linear $k - \epsilon$ model and although the pattern of the secondary circulations is broadly similar to the previous results, in this case, the maximum magnitude of the secondary circulations is 2.49% of the bulk mean velocity. This value is exactly within the 1 – 4% range of experimental values described in Section 2.2.1. The contours of turbulent kinetic energy show that the model of Kimura and Hosoda (2003) is predicting significantly larger peak values than the previous two models. From this test, we can therefore conclude that the *K&H* turbulence closure performs favourably for square duct flow.

Compound Channel Flow The second test case was that of compound duct flow. This test was important to ensure that the model was capable of reproducing the characteristic velocity profile of the compound channel in which we are interested. The grid from the square duct case was modified for this purpose. Symmetry boundaries were substituted for wall boundaries on the top and right of the cross-section and the bottom left hand quadrant was removed from the calculation domain using the masking concept described in Section 3.2.1. The resulting grid is shown in Figure 5.5, where the plan view of the grid is taken in the bottom half of the channel, showing the masked region.

A similar approach was adopted to the simulation as in the square duct case. However, for the compound channel case, a bed slope of 0.0005 and a higher Reynolds number of 1.163×10^6 was adopted. This higher Reynolds number was used in order to confirm the applicability of the model over the range of Reynolds numbers of interest. The results from the simulations with the linear $k - \epsilon$ model are shown in Figure 5.6.

The results from the $k - \epsilon$ model show that the masked boundaries are operating correctly but of course, the results do not have any of the features of compound channel flow as described in Section 2.2.3. Using the $K\&H$ model, the results in Figure 5.7 were then created. The contours of streamwise velocity have moved from the $k - \epsilon$ results to show a slight bulge at the floodplain edge and the pattern of secondary circulations causing this phenomenon can be clearly seen by comparing the vector plots between the two cases. The maximum strength of the secondary flow as a proportion of the bulk mean velocity is now 1.67%. The contours of turbulent kinetic energy show that the values at the floodplain edge area have increased in relation to the values in the remainder of the channel as compared to the results from the $k - \epsilon$ model.

When comparing these results with previous experimental data, it is clear that the strength of the secondary circulations is smaller than we might expect. Tomimaga and Nezu (1991), for example, quote a maximum secondary flow of 4.45% of the bulk mean velocity, where the Reynolds number is 5.45×10^4 , whilst an average value of 4.71% was recorded in the experiments described in Chapter 4, where the Reynolds numbers were between 2.6×10^5 and 4.8×10^5 . However, having chosen the algebraic stress model of Naot and Rodi (1982) as the best performer of the original three options, Vyas (2007) produced a broadly similar result of 2% for his simulation of a compound duct flow with $Re = 1 \times 10^5$. The bulging of the streamwise velocity contours in the modelled results is also mild in comparison with that observed in the experimental data. This must partially be due to the weaker secondary circulations but is also a consequence of the way in which the free surface is modelled. Since a symmetry boundary is used for all dependent variables, this boundary does not make allowance of the limitation that the free surface places on the turbulent length scale in the vertical direction. The neglect of this phenomenon may also act to suppress the deformation of the streamwise velocity contours.

In general, however, the model successfully represents the lateral gradient in streamwise velocity between the floodplain and main channel and the pattern of secondary flow vectors induced by the distribution of the normal turbulent stress

components in the spanwise and vertical directions. The next section will compare results from the model with some of the experimental data presented in the previous chapter to investigate what features of the flow the model can successfully represent.

5.2 Model Testing - Experimental Scenarios

5.2.1 Emergent Cases

5.2.1.1 Emergent, Low Aspect Ratio In-line Blocks (S1CII)

Since the model is limited to steady flow modelling only, it is inherently better suited to the modelling of flows without a periodic component, i.e. we would expect the model results to match the experimental results more closely for cases without strong vortex shedding phenomena. As such, the in-line emergent low aspect ratio experimental case (Series 1, Case II) was chosen as the first case with which to test the model. This is the final case for which both the linear $k - \epsilon$ and non-linear $K\&H$ closure schemes have been used. The grid for this simulation encompassed the length of the flume and since no detailed information was available on inlet conditions from the experiments, the streamwise velocity at the inlet was set to a uniform value matching that of the bulk mean velocity. The turbulent kinetic energy and turbulence dissipation rate were also set to uniform values at the model inlet, using Equations 5.1 and 5.2 and assuming a freestream turbulent intensity of 2%. All wall and masked boundaries were set up in the same way as described for the models of simple flows, as was the outlet boundary. A symmetry boundary condition was again applied at the free surface.

$$K = 1.5(UT_i)^2 \quad (5.1)$$

$$\epsilon = \frac{C_\mu^{0.75} K^{1.5}}{0.07R} \quad (5.2)$$

5.2 Model Testing - Experimental Scenarios

Figure 5.8 shows the mean velocity components and the turbulent kinetic energy from both the experiment and the models at Station 3, which lies a distance of $3.5W_{bl}$ downstream of the centre of the fourth block as described in Section 3.1.1.2. The comparison is performed at a vertical position of $z = +0.5$. In order to provide context to the comparison of the measured and modelled results, error bars have been added to the plots of streamwise mean velocity in all of the subsequent cases. These error bars show the 4% error reported by Rusello *et al.* (2006) in their comparison of the performance of the Nortek Vectrino ADV with non-intrusive velocity measurement techniques. In this case, the plot of mean streamwise velocity shows that the modelling results display higher values far from the block in both the main channel and on the floodplain, greatly exceeding the error bar thresholds. This feature may be linked to the tendency of the model, as described in Section 5.1, to underestimate the secondary circulations and turbulent kinetic energy associated with the anisotropic distribution of the normal turbulent stresses in the compound channel and the inability of the model to fully reflect the changes induced in the velocity distribution by the free surface.

Inside the wake, the larger relative drop in streamwise velocity predicted by the models suggests that the modelled flow is recovering more slowly to the freestream conditions than we might expect. Whilst outside of the wake, the two turbulence closures produces very similar distributions of the mean streamwise velocity, it is clear that the $k - \epsilon$ model is predicting a faster recovery of streamwise velocity within the wake. This is accompanied by a slightly larger prediction of the total turbulent kinetic energy at this streamwise location. This behaviour is directly opposite to that noted by Bosch and Rodi (1998) for the 2D square block case, where the linear turbulent closure tended to over-produce turbulent kinetic energy in the stagnation region upstream of the block and over-predict the length of the recirculation zone behind it.

Concentrating on the prediction of the turbulent kinetic energy by the non-linear model, it is clear that, in common with many modelled flows, the model gives a lower result than the measured profile. Despite this, the shape of the profile

5.2 Model Testing - Experimental Scenarios

matches the experimental data well and reproduces the imbalance in the peaks, which is characteristic of this flow. The original testing of the *K&H* scheme for the 2D flow of Lyn *et al.* (1995) showed that the model reproduced the total fluctuating energy well. However, it achieved this through a combination of over-predicting the contribution from the regular shedding and under-predicting the contribution from the truly random turbulence. In this case, where regular shedding is likely to be minimal due to the low block aspect ratio, the larger influence of the under-prediction of the turbulence means that the model is more likely to under-estimate the total fluctuating energy and therefore predict the longer recovery zone that is observed in these results. This may be true to such an extent that the normal pattern of turbulence and wake recovery prediction by the linear and non-linear models at this location is reversed.

However, whilst the $k - \epsilon$ fails to do so, the *K&H* model successfully, although weakly, reproduces the double bump in the profile in the main channel, a consequence of an improvement in the prediction of the secondary circulations. This is particularly true of the vertical component, where implementation of the non-linear closure improves both the magnitude and the distribution.

An examination of the model results around the fourth block shows the formation and augmentation of the axial vorticity that was identified in the experiments around the single, large aspect ratio blocks described in Chapter 4. Figure 5.9 shows the mean streamwise velocity contours and the secondary flow vectors at Stations 2 and 3, i.e. at the streamwise block centre and $3.5W_{bl}$ downstream. The plots of the secondary flow vectors concentrate on the area around the block whilst the contours of streamwise velocity are shown for the whole section.

At the streamwise centre, a large anti-clockwise circulation can be observed in the main channel, which has been set up by the flow past the upstream blocks in the series. The presence of this circulation goes to explain the distortions in the contours of streamwise velocity at this position. However, the plot of secondary circulations also shows a small but powerful anti-clockwise circulation appearing right on the block edge on the main channel side. From an examination of the

results in plan, it is clear that this circulation is strongest on the upstream half of the block side wall for all cases and within the series of blocks, is strongest at the first block and gradually decreases in strength in the downstream direction. However, it is still clearly strong enough to have a significant impact on the structure of the wake for the fourth block, since the pattern of secondary circulations for the downstream position shows that the symmetrical axial vorticity pattern that we might otherwise expect behind a block in a simple stream has become significantly distorted, with a dominant main channel vortex and little or no vorticity on the floodplain side.

These simulated results show that the model is a useful tool for analysing this flow type and lead to the conclusion that the results from the *K&H* turbulence closure are more useful in simulating this kind of flow than those from the linear turbulence closure. Taking into account its limitations, particularly in reference to the prediction of turbulent energy, it may therefore be put to use to examine the effects of changes in channel geometry and freestream flow parameters on wake structures.

5.2.1.2 Single, Emergent, Large Aspect Ratio Block at the Floodplain Edge (S2CI)

The experimental case of Series 2, Case I, where a single large aspect ratio square block was placed at the edge of the flume in the laboratory in Loughborough, was modelled on a $150 \times 125 \times 100$ grid encompassing a length of flume from $x = -5.5$ to $x = 12.5$. The inlet of the model area therefore coincided with the inlet section measured during the experiment and inlet conditions were thus set using the variables measured in the experiment. This method should provide a more accurate set of inlet conditions than the uniform inlet used in the previous section. All other boundaries were set using the same methods as the previous section.

Taking into consideration the experiments and simulations to be found in the literature record, it is clear that vortex shedding processes may be present for this case, although the experimental results show that the regular vortex shedding that

5.2 Model Testing - Experimental Scenarios

we might normally expect is disrupted here. It is however true that the best numerical modelling results for cases where shedding processes are significant are to be achieved by long-time averaging of the results of unsteady flow modelling using the ensemble-averaged Navier Stokes equations. In this approach, the shedding process is simulated directly, whilst the truly random component of the turbulence is modelled. Unfortunately, this option was not available for this project and the following results are from a steady flow simulation, where both regular fluctuations and turbulent contributions are modelled using the *K&H* model.

Figures 5.10, 5.11 and 5.12 show a detailed comparison of the experimental and modelled results at $x = 1.3$, $x = 4.00$ and $x = 6.67$. The plots of mean streamwise velocity show that the model can produce accurate results in the near wake, where at $x = 1.3$ (5.10) the model predicts not only the minimum value on the floodplain side of the block centreline but also predicts the values of streamwise velocity exceedingly well. Only on the floodplain are magnitudes under-predicted to an extent significantly greater than the scope of the ADV error. Further downstream at $x = 4.00$ (5.11), the plot of streamwise velocity is starting to show that the model is again predicting a slower recovery than the experimental results. However, the width and shape of the wake are well predicted, as is the shape of the profile outwith the wake zone. At $x = 6.67$ (5.12), the gap between the modelled and experimental results is widening. This behaviour correlates well with that observed by the model's authors (Kimura and Hosoda, 2003), who, when modelling flow around a 2D square block, found that the streamwise velocity recovery was predicted very well in the region where $x < 4$ after which the modelled results recovery slowed in comparison to the experimental results.

The varying performance of the model in predicting the distribution of the streamwise velocity component is summarised in Figure 5.13. For each of the points that were measured at $z = 1$ in the experiment described in Section 3.1.1.2, a percentage difference was found between the measured and modelled values of U . The value plotted in this figure has been found by taking an average of these values at each streamwise measurement position.

5.2 Model Testing - Experimental Scenarios

For this, the emergent case, it is clear that whilst the modelled results at $x = 1.3$ have been shown to match the measured results generally very well, the discrepancy in values in the wake on the floodplain side of the block contributes to a large average difference. Between $x = 2.25$ and $x = 6$, the difference is less than 5% after which, it grows steadily. From this information, it may be concluded that any force balance calculation to find a drag coefficient from the modelled results should be performed with a downstream station located between $x = 2.25$ and $x = 6$.

At $x = 1.3$, the spanwise and vertical velocities are predicted to reasonable accuracy outside of the wake in the wider channel. Within the wake, the values are less well predicted; the spanwise values are in the correct range but show a different pattern, whilst the vertical velocities show the right pattern but the values are over-predicted. At $x = 4.00$, this pattern for the vertical velocities is repeated. The spanwise velocity plot shows that the model correctly predicts the peak on the floodplain side to be larger than that on the main channel side. However, the degree of difference of these two peaks is larger and this correlates well with the tendency of the model to show the distribution of vertical velocity to be offset from the experimental results and the minimum streamwise velocity to be positioned further toward the main channel. At $x = 6.67$, the spanwise velocity profiles match well on the main channel side, but the model again over-predicts the peak on the floodplain side. The vertical velocities measured in the experiment have diminished considerably at this streamwise position. The modelled results, although reasonable in trend, continue to be over-predicted in magnitude.

An examination of the prediction of the turbulent kinetic energy instantly shows that the model is significantly under-predicting the measured turbulent kinetic energy in the block's wake. This is exaggerated in comparison with the previous case, presumably because of the presence of unsteadiness in the form of regular velocity fluctuations in the experimental results that are failing to be represented in the steady simulation. Despite this, both profiles show higher peaks on the floodplain side of the block centreline, which suggests that this imbalance exists not only in

the regular vortex structures but also in the truly random component of the turbulence.

The results suggest that the distribution of energy between the mean flow and the turbulent fluctuations is mispredicted such that the magnitudes of the secondary circulations associated with the wake are too large and the magnitude of the turbulent kinetic energy is too small. However, overall, these results show that the model is capable of reproducing the structure and size of the wake behind the block at the floodplain edge with reasonable enough accuracy to draw useful engineering conclusions from subsequent runs using different geometries and numbers of blocks. Combining the results for both simulations for emergent blocks allows us considerable confidence in the capability of the model.

5.2.2 Submerged Cases

5.2.2.1 Submerged, Low Aspect Ratio, In-line Blocks (S1CI)

The model validation process is now extended to the submerged block cases, where the flow structures, as detailed in Chapters 2 and 4, are quite different to those around emergent blocks. Of the two in-line low aspect ratio experiments performed (Series 1, Cases I & III), the case with deeper block submergence (Case I) has been simulated using the model. The grid for this simulation differed from that used for the emergent case (Case II) only in the vertical scale, where it was slightly modified to ensure a fine enough grid resolution at the top of the block and to take account of the change in total water depth. All of the model boundaries were set in the same way as described in Section 5.2.1.1, where the inlet values were adjusted to reflect the different bulk mean velocity.

Figure 5.14 shows the measured and modelled results downstream of the fourth block at Station 3, as described in Section 3.1.1.2. It is immediately clear that the results for this submerged case are less successful than those shown above for the emergent block case. Some of the discrepancies between the experimental and modelled data here are due to similar reasons as those mentioned above, namely

5.2 Model Testing - Experimental Scenarios

that the K&H turbulence closure has a tendency to underestimate the random component of the turbulent field. This means that again, the simulated streamwise velocity values in the block wake are less well recovered than the experimental data, whilst the values outside of the wake zone are over-predicted.

However, in addition to these phenomena, it is clear that the pattern of secondary circulations in the block wake is being predicted to be significantly more complex than that observed in the experimental data. The result of this complexity is that the distribution of the streamwise velocity at this position is also made more complex than its measured counterpart. This is clarified in Figure 5.15, which shows both the contours of streamwise velocity and vectors of secondary flow, upstream of the block at Station 1 and downstream at Station 3.

The vectors of secondary flow at both the upstream and downstream stations show that the flow is dominated by a large anti-clockwise circulation on the floodplain. The presence of such a circulation is consistent with the measurements in all of the experiments for submerged blocks performed as part of this project (Figures 4.48 and 4.49). For the single block cases, the evidence suggests that the formation of axial vorticity that might normally be expected from both sides of the block is disrupted on the main channel side for blocks at the floodplain edge. The model results for this multiple in-line block case not only support this theory but also suggest that this phenomenon is consolidated for each block in turn.

The comparison plot of spanwise velocity in Figure 5.14 shows that although there is an inappropriate positive peak at the block centreline, the prediction is generally good. The differences between the profiles on the floodplain indicate that the model's prediction of the width of the circulation there is perhaps slightly too small, causing the bump in the prediction of streamwise velocity on the floodplain. The large peaks and troughs in the prediction of the vertical velocity mean that this component is less well predicted and an examination of the vectors predicted at Station 3 in Figure 5.15 shows the complex wake circulations that are causing this.

5.2 Model Testing - Experimental Scenarios

Having taken into account the tendency of the model to under-predict the turbulent kinetic energy, the results in Figure 5.14 show that the model is predicting a significant difference between the peaks on either side of the block. An examination of the individual normal Reynolds stress components shows that this is due to a discrepancy between the measured and modelled profiles of the vertical component, where the measured data shows a large peak on the main channel side (Figure 4.50) and the modelled data does not. This phenomenon fits in well with the difficulties experienced in predicting the distribution of the mean vertical velocity component. Overall however, the model appears to successfully reproduce the width and shape of the peak in turbulent kinetic energy associated with the wake.

Despite the problems encountered in predicting the details of the secondary currents in the wake zone, an examination of the contours of streamwise velocity for the entire section show an overall tendency for the wake to bulge out into the main channel. Although not as noticeable at the height of the measurements used to produce Figure 5.14, this behaviour is very consistent with the results presented in Sections 4.2.2 and 4.2.3.2 and may allow us confidence in the model's ability to predict the bulk features of the flow.

5.2.2.2 Submerged, Single, Large Aspect Ratio Block at the Floodplain Edge (S2CII)

The final test simulation was designed to reproduce the experimental flow around the single large aspect ratio submerged block at the floodplain edge. An identical technique was used as described in Section 5.2.1.2, where a length of flume from $-5.5 < x < 12.5$ was modelled using a $150 \times 125 \times 116$ grid. The grid therefore differed from that used for the emergent case only in the vertical direction. Figures 5.16, 5.17 and 5.18 again show a detailed comparison of the experimental and modelled results at $x = 1.3$, $x = 4.00$ and $x = 6.67$.

Some tendencies of the model can be recognised from the previous results for other cases, namely that the streamwise velocity profile behind the block is ex-

5.2 Model Testing - Experimental Scenarios

cellently represented in the near wake at $x = 1.3$, where only the values on the floodplain are significantly outwith the error bounds of the measured data but that the modelled values recover more slowly than those in the experiment so that the gap between measured and modelled values grows larger at $x = 4.00$ and $x = 6.67$ respectively. At $x = 4.00$, despite the difference in the magnitude, the model successfully shows the tendency of the wake to be skewed toward the main channel side of the block. At $x = 6.67$, both the shape and the magnitude of the streamwise velocity profile are failing. The shape of the profiles outside of the wake zone are reasonably well reproduced in all locations. Reference to Figure 5.13 confirms that by the average difference parameter for the streamwise velocity component, the model's performance is best at $x = 1.3$. However, after peaking at the next station, the trend, by this measure, is for the performance of the model to improve in the downstream direction.

The results for the spanwise and vertical velocity components show a similar trend to that noted in the previous section. Overall, the magnitudes of the secondary circulations are in the correct range but the profiles tend to be overly complex in the wake region. Of the two components, the vertical velocity is less well represented, particularly in the later stages of the wake. As in the single emergent block case, the model tends to over-predict the magnitudes of the vertical velocity at the downstream positions.

The under-prediction of the turbulent kinetic energy is also still apparent in these results, although the gap has narrowed from that observed in the emergent case. In this case, we would expect the influence of the vortex-shedding phenomenon to be much reduced, which is consistent with a reduction in the large discrepancy between the modelled and measured results. However, the tendency of the model to under-predict the random component of the fluctuating velocity field means that a gap still exists. The trend in the results for the turbulent kinetic energy are, as may be expected from the mean velocity profiles, best reproduced at $x = 1.3$. Further downstream, the similarity decreases. These results suggest that the model is less capable of producing accurate results for this more complex

submerged case, where flow separation is occurring both at the sides and at the top surface of the block.

5.2.3 Model Testing - Summary

The results set out in the preceding sections show that the performance of the model in reproducing the experimental data is mixed. In all cases, a similar pattern emerges when the measured and modelled results are compared such that the recovery of the mean streamwise velocity in the wake is excessively slow and the total turbulent kinetic energy in the wake is under-predicted. The under-prediction of turbulent kinetic energy for the individual cases is likely to emanate from slightly different sources. For the multiple, emergent block and both of the submerged cases, the under-prediction is likely due to the tendency, noted by Kimura and Hosoda (2003), for the K&H turbulence closure to under-predict the random component of the total turbulence in bluff body wakes. For the single, emergent block, where a more significant amount of vortex shedding would be expected to be present, the under-prediction is likely to emanate from the steady nature of the simulation. In order to properly account for the regular fluctuations in the velocities induced by the vortex shedding mechanism, previous authors (Bosch and Rodi, 1998; Kimura and Hosoda, 2003) have recommended that for such cases, the best results are obtained via long-time averaging of the results of an unsteady simulation. Both of these factors are also impacting on the rate of recovery of the mean streamwise velocity.

This suggests that the accuracy of the results for single, emergent case may be improved upon should an unsteady modelling technique be applied. The more intrinsic failures of the K&H turbulence closure however, are similar in nature to all of the other turbulence closures currently available and are less easily overcome. More complex, and ergo expensive, modelling methods such as Large Eddy Simulation (LES) have been found (Rodi, 1997) to give improved results for the modelling of flow around bluff bodies but even these exhibit significant differences from mea-

sured results. It is clear that incorporating all of the complex flow features of bluff body flows is extremely difficult to achieve cheaply.

The next section uses the model to create simulations of flows around blocks of different aspect ratio and distribution for comparison of the wake structures and resultant drag coefficients. Although the results of these simulations are of course, subject to the inaccuracies summarised here and the resultant values of drag coefficient may not form a continuum with those calculated from the experimental results, the results have shown that the model is capable of reproducing many of the bulk features of the wakes that impact on the drag coefficients, as observed in the experiments, including the sometimes highly asymmetric distributions of secondary circulations and total turbulent kinetic energy. As such, the model results described below should allow for meaningful analysis of the changes to these structures that come about as the block aspect ratio and distribution change.

5.3 Model Results - Emergent Cases

Using the computational model, it is possible to test the effects on the wake structure and drag coefficient of both variation of the block geometry and the arrangement of blocks at the floodplain edge. The following sections describe the modelled results for two series; in the first, the aspect ratio of a single block at the floodplain edge is varied whilst in the second, high aspect ratio blocks are arranged in a line along the floodplain edge.

5.3.1 Variation of Block Aspect Ratio (AR)

In order to identify the source of the differences in wake behaviour observed in the experimental results between the single, high aspect ratio cases and the multiple, low aspect ratio cases, it is first necessary to look at how the structure of the wake changes with the changing aspect ratio for a single block. To this end, the computational model was used to simulate the flow around a single block at the edge of

the floodplain for a number of values of AR . The channel geometry familiar from the single block experiments in the Loughborough flume was applied here (see Figure 3.1) and the width of the block was varied in order to change AR . This, of course, implies that the total width of the floodplain was kept constant so that the proportion of the floodplain width covered by the block decreases as AR rises.

The size of grid on which the simulations were performed was maintained for each block such that the upstream boundary was located $5.5W_{bl}$ upstream of the block centreline and the downstream boundary was located $12.5W_{bl}$ downstream of the block centreline. The expansion factors used for each grid were varied to take account of the changing value of W_{bl} but were always between the bounds of $0.9 \leq Ex, Ey, Ez \leq 1.1$. Inlet conditions for all of the simulations were identical, having been created by running the model a number of times to simulate flow in the empty channel, each time applying the downstream profile from the previous simulation as the upstream conditions for the next. The inlet conditions for each of these runs therefore represent fully developed uniform flow conditions in the empty channel. Figure 5.19 shows both the contours of streamwise velocity and the vectors of the secondary circulations that constituted the inlet boundary condition to all of the simulations in this series.

A summary of the governing parameters of each of the simulated flows is given in Table 5.1. Using an identical technique to that described for the experimental results, namely the indirect momentum balance method, a value of C_D was calculated for each case and these values are also shown.

Whilst the approach velocity at the upstream block centreline is identical for all cases, the changing block width accounts for the range of block Reynolds numbers. Although the value varies from 1.4×10^4 to 7.2×10^4 , this difference is unlikely to be influential in changing the structure of the wake and the resultant drag coefficient, as the square section shape ensures that the location of separation is fixed. As these simulations were all performed for the same compound channel geometry, the channel Froude number of the flow is the same for each case. The increase in

5.3 Model Results - Emergent Cases

Aspect Ratio	1	2	3	5
Re_{bl}	72,059	36,030	24,002	14,412
Fr_{bl}	0.47	0.66	0.81	1.05
$T_u(\%)$	4.8	4.8	4.8	4.8
$B(\%)$	8.7	4.3	2.9	1.7
C_D	2.96	3.80	3.81	3.73

Table 5.1: Flow Parameters for Emergent Cases

the block Froude number over the range of AR is accompanied by an increase in C_D , so that Fr_{bl} may be a contributing factor to the changing C_D .

There is a significant change in the overall blockage ratio B over the series of simulations. We might expect that a higher blockage ratio would decrease the curvature of the separation streamlines, causing the wake structures to form closer to the block and the pressure difference across the block to rise. However, (Lyn *et al.*, 1995) also states that as the flow recovers, a higher blockage ratio implies higher spanwise velocity gradients and therefore higher rates of entrainment. In this series, this latter effect, when combined with the influence of the other parameters, seems to be dominant.

The effects of freestream turbulence on the flow around bluff bodies was investigated by Bearman and Morel (1984), who concluded that whilst the turbulent length scale was unimportant, a high freestream turbulent intensity had two important effects. In the near-block region, high freestream turbulence increases entrainment into the separated shear layers so that the separated streamline tends to curve inward toward the body of the block. In more extreme cases, this leads to reattachment onto the side of the block. Depending on which of these processes occurs, the base pressure can increase or decrease. As the flow recovers, the free shear layers are also affected by freestream turbulence such that the normal component of the turbulence acts to reduce the coherence of any periodic structures such as

shed vortices, increasing the rate of recovery. The depth-averaged freestream turbulence level at the block centreline at the model inlet is the same for all the cases here. By the norms stated by Bearman and Morel (1984), the value of 4.8% would be considered as a medium level of freestream turbulence. However, the difference in the freestream turbulence intensity across the flow approaching the blocks at the floodplain edge may be a contributing factor to the resulting asymmetry of the separation characteristics and the wake recovery. Together with the final governing parameter, the geometry, the effects of the freestream turbulence distribution must be considered by examining the detailed model results for each case.

By far the most influential parameter in this case therefore is the changing geometry. This of course incorporates the changing AR , which will affect the size and structure of the wake no matter what its position. Previous experimental evidence (Spezeczy and Bearman, 1992) for a square sectioned block placed between two solid surfaces suggests that when AR is very low, vortex shedding processes are suppressed, leading to a smaller maximum pressure/velocity difference across the block, faster wake recovery and therefore a smaller value of C_D . As AR surpasses 2.5 and rises towards 5, the vortex shedding process gradually grows in strength and C_D increases.

Overall, the trend for these experiments is also generally for C_D to rise as the aspect ratio of the block rises. However, the results suggest that this process is being affected in a more complex way by the floodplain edge positioning, as C_D is virtually identical for the $AR = 2$ and $AR = 3$ cases.

A closer examination of the model results shows the different processes at work over the spectrum of values of AR . The recovery of the mean streamwise velocity component at the block centreline is plotted in Figure 5.20. The depth average streamwise velocity component at all downstream stations is plotted in this figure as a factor of the depth average streamwise velocity component at the model inlet. A comparison of the recovery profiles of the $AR = 2$ and $AR = 3$ cases shows that the structure of the wakes is quite different. In the $AR = 2$ case, the wake is characterised by a long, weak recirculation zone and a faster recovery. In the $AR =$

3 case, there is a much greater maximum velocity difference across the block at the centreline and a slower recovery. In this respect, the centreline recovery profiles are what we might expect from the results of Spezzzzy and Bearman (1992), as the vortex shedding process is established. However, the resultant values of C_D go against the trend that these centreline plots might otherwise suggest.

Whilst Figure 5.20 is a useful overall tool in identifying the trend in the wake structure over the range of AR , it masks some of the complexity of the wakes introduced by their asymmetrical floodplain edge positioning and does not reflect the changes induced by that positioning. It is therefore necessary to examine the changing flow pattern around and downstream of the blocks, to isolate how the floodplain edge positioning is contributing to this phenomenon. Figure 5.21 provides a means to compare the contours of mean streamwise velocity at the same streamwise position in each wake ($x = 4$), whilst Figure 5.22 does the same for the vectors of secondary flow. From these plots, a clear pattern of change across the range of AR becomes apparent.

For all of the blocks, the model predicts that on the floodplain bed, where the interaction between the main channel and floodplain flows is at its maximum, the wake is firmly skewed toward the main channel. For the lower values of AR , the wake position at the free surface is skewed in the opposite direction and the wake is significantly tilted over the height of the block as a result. At the higher values of AR , the height over which a tilt in the wake is visible becomes confined to the region close to the floodplain bed. The plots of the vectors of secondary circulations show the axial vorticity associated with these wake patterns, where there is a consistent pattern of dominance of the main channel circulation over that on the floodplain and a tilt in the axis between them.

To illustrate how this change in the influence of the floodplain edge positioning impacts on the characteristics of the wake affecting the drag coefficient, Figure 5.23 shows a plan view of the contours of streamwise velocity for the $AR = 1$ and $AR = 5$ cases. The plot represents the wake for each case at a vertical position where $Z/D_{fp} = 0.28$.

At $AR = 1$, at this height, reattachment can be seen to occur on both sides of the block, although much sooner on the main channel side. For the low aspect ratio cases, this pattern of very early reattachment on the main channel side of the block can be identified over a significant proportion of their height. This is demonstrated in Figure 5.24, which shows the streamwise velocity contours and secondary circulations at the streamwise block centre for $AR = 1$. At $Z/D_{fp} = 0.28$, the flow on the main channel side can then be seen to separate again at the rear of the block. On the floodplain side, the higher blockage caused by the large width of the block in relation to the width of the floodplain also acts to promote reattachment but overall, the re-separation pattern of the flow causes the wake to be skewed to the main channel side of the block centreline. In this respect, it mirrors the behaviour of the experimental data for the low aspect ratio, in-line blocks presented in Chapter 4, Section 4.1.4. Further downstream, the recovery of the flow on the main channel side is delayed under the influence of the persistent strong axial circulations on that side.

At $AR = 5$, the plan view is reminiscent of the experimental results plotted for the single, large aspect ratio block in the Loughborough flume (Chapter 4, Section 4.1.3.2, Figure 4.13). For these higher AR cases, it has already been demonstrated that the region of very early reattachment on the main channel side of the block and the associated tilting portion of the wake is confined to a vertical band near the floodplain bed. At the vertical position shown in this figure therefore, the separation pattern shows, like the experimental results, the minimum wake velocity on the floodplain side of the block centreline. This is related to a change in the reattachment characteristics such that whilst reattachment still tends to occur on the main channel side of the block, its influence is much reduced. On the floodplain side in contrast, the much reduced blockage means that reattachment may not happen at all, leading to much stronger vortex shedding processes on this side. Further downstream in the wake, it is still true that the recovery of the wake on the main channel side is delayed in comparison to that on the floodplain.

Overall therefore, the changing balance between the nature of the regions of separation due to the geometrical effects of the compound channel alters the variation of C_D with AR that we might otherwise expect. For all cases however, the reduction in the rate of recovery on the main channel side acts to increase the value of the drag coefficient.

5.3.2 Multiple blocks

Having successfully simulated the flow around multiple, low aspect ratio blocks at the floodplain edge in testing the model's performance against the experimental results in Section 5.2.1.1, the model was also used to simulate the flow around a series of high aspect ratio blocks. The geometry of the channel was again set to match that of the Loughborough flume and the relative spacing of the blocks, with aspect ratio 3.5, was set to be the same as the experimental case, namely such that $s/W_{bl} = 12$. At the upstream boundary of the model, which is located $5.5W_{bl}$ upstream of the first block, the inlet conditions are the same as those used in the AR series, namely representing fully developed uniform flow conditions in the empty channel (see Figure 5.19). The downstream boundary is located $6.5W_{bl}$ downstream of the last block. The expansion factors for the grid were maintained such that $0.9 \leq Ex, Ey, Ez \leq 1.1$.

The results from this simulation allow the comparison of the wake structures between different blocks in the series. As a first means to compare these, Figure 5.25 provides a comparison of the recovery rates for the first four blocks. In this figure, the depth averaged mean streamwise velocity at the block centreline is normalised using the depth averaged mean streamwise velocity at this lateral location at the model inlet. In order to compare recovery profiles, the results are plotted relative to each block's streamwise centre position, i.e. $x' = x_{cc} + x$.

Figure 5.25(a) shows a distinct change in behaviour between the wake from the first block and the others. This must largely be due to the reduced approach velocities that affect the later blocks so that whilst the depth averaged velocity

5.3 Model Results - Emergent Cases

Block	1	4
Re_{bl}	20.474	10,100
Fr_{bl}	0.88	0.44
$T_u(\%)$	4.9	7.7
C_D	2.22	1.65

Table 5.2: Flow Parameters for Blocks 1 and 4 in Multiple, Emergent, High AR Block Case

upstream of the first block at the model inlet is $\bar{U} = 1.01U_m$, for the subsequent blocks, the upstream depth averaged velocity only ever recovers to approximately $\bar{U} = 0.50U_m$. It is clear that for the subsequent blocks, the minimum wake velocity is higher than that for the first block and the recirculation length is also shorter. After reattachment, the recovery rate of the wakes are broadly very similar, until approximately $x' = 6.5$, where that of the downstream blocks falls below that of the first block. Given the drop in approach velocity experienced by the downstream blocks, it is necessary to take into account the effects on the governing parameters (Re, Fr, B, T_u) of the changing flow, where these values are compared in Table 5.2 for the first and fourth blocks. The blockage ratio is identical for both blocks and is therefore omitted.

In Figure 5.25(b), the results for the first block are plotted together with the recovery profile predicted by Equation 2.5 of Petryk (1969), for single lines of blocks, which is based on 2D idealised flow theory. The figure clearly shows that the 3D effects of the real flow at the floodplain edge result in a significant deviation between Petryk's prediction and the model results.

Relating Table 5.2 to Figure 5.25, the lower Reynolds number associated with the fourth block is certainly influential in creating the less powerful recirculation region of the fourth block. The lower Froude number of the fourth block would be expected to ensure less damping of vortex shedding processes by the deformation of the free surface and therefore, a faster recovery overall. The similarity of the recovery rates until $x' = 6.5$ effectively rules this out as a significant factor in

our consideration. The increase in freestream turbulence intensity in the approach to the fourth block might be likely to lead to earlier reattachment of the separated shear layers and accelerated recovery through increased entrainment into the wake. However, the organised nature of the turbulence upstream of the fourth block means that simple assumptions based on observations of the effects of truly random freestream turbulence are of limited applicability.

It must also be true that the structure of the wake inherited from the upstream block influences the formation of that of the downstream block. Although at this spacing, we are not expecting the shedding processes from the downstream blocks to be directly linked to those of the upstream blocks, the sustained imbalance in the approach velocity and freestream turbulence across the front face of the downstream block and the persistence of secondary circulations from the vorticity emanating from the upstream block might be reasonably be expected to affect the development of the separation zones on the downstream block. In addition to and in spite of the changes in the wake induced by the general changes to the approaching flow, an examination of the details of the wakes of the first and fourth blocks reveals how the features specifically related to the compound channel floodplain edge setting are changed by the in-line arrangement.

Figure 5.26 shows the contours of mean streamwise velocity at $x' = 5.5$ for the first and fourth blocks, where the overall profiles of the wakes are very similar; near the floodplain bed, the wake tilts into the floodplain and is associated with a strong upflow at the floodplain edge from the main channel into the floodplain. Indeed, at $x' = 3.5$ for both blocks, the maximum magnitude of the vertical velocity is a very similar proportion of the approach velocity; for the first block $W_{max}/U_A = 0.44$, whilst for the fourth block $W_{max}/U_A = 0.38$. At the higher elevations, the wake is consistently skewed toward the main channel side of the block centreline.

As the fourth block is located within the wake from the third block however, the plot also shows that at the fourth block the wake is of a substantially increased width. In addition, as the axial vorticity emanating from the separated regions at

the block sides (namely a clockwise circulation on the floodplain and an anticlockwise circulation in the main channel) is progressively reinforced, the wake tends to widen particularly near the free surface and combined with a general deceleration of the flow on the floodplain, this gradually alters the distribution of the mean streamwise velocity in the whole channel.

The changing pattern of U results in a distribution of turbulent kinetic energy in which larger values are consistently found on the main channel side. Figure 5.27 illustrates both the contours of mean streamwise velocity and of turbulent kinetic energy around the fourth block at a representative elevation of $z = 2.0$. It is clear from this figure not only that the main channel peak in turbulent kinetic energy is larger but also, crucially, that its decay is slower. The associated tendency of the wake to drift out into the main channel can be clearly seen in the contours of U .

In common with the results described for the single block cases, Figure 5.27 shows therefore that the tendency for the wake recovery on the main channel side to be slower is preserved for the in-line case. In general therefore, although the drag coefficients of the downstream blocks are reduced in comparison to that of the first block (Table 5.2), the features of the wakes that are brought about by the compound channel floodplain edge location persist so that in comparison to a set of in-line blocks in a simple channel, the blocks at the floodplain edge are still likely to cause increased amounts of drag.

5.4 Model Results - Submerged Cases

The test series for the variation of block aspect ratio and for placing blocks in line at the edge of the floodplain were also carried out for submerged blocks. In all cases, the flow conditions mimicked those of the experiments performed in the Loughborough flume and the positions of the inlet and outlet boundaries and of the multiple blocks in relation to one another are the same as those used for the emergent blocks. The inlet conditions for each simulation were again set to by running the model a number of times to simulate flow in the empty channel,

5.4 Model Results - Submerged Cases

Aspect Ratio	1.5	3.5	4.5	5.5
Re_{bl}	32,973	14,116	10,991	9,012
Fr_{bl}	0.66	1.01	1.15	1.27
$T_u(\%)$	4.9	4.9	4.9	4.9
$B(\%)$	2.8	1.2	0.9	0.8
C_D	2.20	2.67	2.52	2.48

Table 5.3: Flow Parameters for Submerged Cases

each time applying the downstream profile from the previous simulation as the upstream conditions for the next. Whilst the total flow depth is slightly larger for the submerged cases to reflect the experimental conditions, this small variation does not produce a significant difference in the flow structure and Figure 5.19 is still a useful guide to the inlet conditions for the simulations.

5.4.1 Variation of Block Aspect Ratio

For the submerged blocks, the governing flow parameters and resulting drag coefficients are shown in Table 5.3.

For the submerged cases therefore, it is clear that the drag coefficients calculated for the blocks are generally less than those of the emergent blocks. The range of values again reflects the changing nature of the wake. As for the emergent blocks, low aspect ratios ensure that no vortex shedding processes can be established. In submerged cases, the low aspect ratio ensures that the flow coming over the top of the block becomes the dominant feature. This accounts for the small value of C_D for the $AR = 1.5$ case in relation to the other cases and agrees with the results of Kawamura *et al.* (1984), who described the vortex shedding processes as being completely suppressed for $AR < 2$. However, for this series, a maximum value of C_D is reached at $AR = 3.5$, implying that another mechanism is acting to reduce the drag coefficient for the highest aspect ratio cases, where we might

otherwise expect to see the vortex shedding processes the least affected. The cause of this drop in C_D at the highest values of AR can be seen in Figure 5.28, however, to arise not from large changes to the absolute minimum velocity achieved in the base region, but rather from faster recovery rates for the higher AR cases.

Considering each of the influencing parameters detailed in Table 5.3 in turn, it is possible to estimate their influence on the changing results over the AR range. Some parameters are likely to have very little effect. For example, the variation in Reynolds number is again due to the changing block width rather than any change in approach velocity. As was the case for the emergent blocks, this range of Re_{bl} is unlikely to wield a large influence on the development of the wake structures. Also, in comparison with the emergent cases, the range of blockage ratios is much smaller for the submerged blocks. All of the values are less than 3% and the variation is limited to 2% so that it is unlikely that the overall change in blockage ratio is an important factor here either.

Whilst the sharp drop in C_D at the lowest value of AR can be well accounted for by the suppression of vortex shedding, the gradual decrease in C_D with AR for the higher values could be partially attributed to the changing block Froude number of the flow. We might expect the rising Froude number to increase the influence of the free surface deformation and thereby suppress the vortex shedding process. This would, however, cause a change in the behaviour of the base region that is not observable in Figure 5.28.

It is therefore more likely that the changes in wake behaviour are due to a combination of the asymmetrical distribution of the freestream turbulence and the geometric effects of the compound channel. Figures 5.29 and 5.30 provide a means by which these influences can be examined. The experimental results for the submerged blocks presented in Chapter 4 showed that the wake has a tendency to be skewed in its alignment in a complex way, under the influence of the asymmetrical separation and reattachment patterns on both the block sides and the block top surface. From the contours of streamwise velocity plotted in Figure 5.29, it is clear that these features are most apparent at low values of AR ; at $AR = 1.5$, the bulge

of the wake into the main channel can still be identified, whilst at $AR = 3.5$ and $AR = 4.5$, the contours appear to be much more symmetrical in structure.

Whilst the comparison of the model results with the experimental data in Section 5.2.2 reveals that the model tends to predict an overly complex pattern of secondary circulations in the wake of the submerged block, the results shown in Figure 5.30 do show the tendency for the influence of the characteristic upflow from the main channel into the wake at the floodplain edge to diminish as AR rises. We may conclude that for low values of AR , the disruption of the formation of the axial vorticity on the main channel side is more severe, so that the dominance of the axial circulation on the floodplain side would be greater for these cases. It is also the case that the difference in reattachment position on the top of the block is likely to be larger for the low AR values so that the angle of the flow coming over the top of these blocks is greater.

In the experimental results in Chapter 4, it was shown that the combination of the skewed flow over the top of the block, uneven lateral separation and the greater vortex stretching associated with the deeper main channel flow resulted in a slower recovery of the wake velocities, particularly on the main channel side. The modelled results in this section suggest that these effects are greatest at lower block aspect ratios so that the influence of the floodplain edge positioning in increasing the drag coefficient wanes as the aspect ratio increases.

5.4.2 Multiple Blocks

The final simulation performed examines the flow around multiple, submerged, high aspect ratio blocks at the floodplain edge. The geometry of the channel was set to match that of the Loughborough flume and the relative spacing of the blocks, with aspect ratio 2.5, was set to be such that $s/W_{bl} = 12$. In an identical manner to the equivalent emergent case, the upstream boundary of the model is located $5.5W_{bl}$ upstream of the first block and the inlet conditions are the same as those used in the AR series, namely representing fully developed uniform flow conditions

5.4 Model Results - Submerged Cases

Block	1	4
Re_{bl}	19,942	14,828
Fr_{bl}	0.86	0.64
$T_u(\%)$	4.9	28.8
C_D	0.28	0.65

Table 5.4: Flow Parameters for Cylinders 1 and 4 in Multiple, Submerged, High AR Block Case

in the empty channel. The downstream boundary is located $6.5W_{bl}$ downstream of the last block. The expansion factors for the grid were maintained such that $0.9 \leq Ex, Ey, Ez \leq 1.1$.

Figure 5.31 shows the depth averaged mean streamwise velocity at the block centreline, normalised using the depth averaged mean streamwise velocity at this lateral location at the model inlet. The results are plotted relative to each block's streamwise centre position, i.e. $x' = x_{cc} + x$. Unlike the emergent case, where a clear difference in wake behaviour was immediately noticeable in the centreline wake recovery plot, for this, the submerged case, the various wake recovery profiles appear to be very similar. The downstream block profiles are only distinguished by a slightly slower recovery rate.

Perhaps partially explaining this similarity, Table 5.4 shows that the Reynolds number of the approaching flow varies only a little, despite the initial deceleration experienced by the flow at the block centreline downstream of the first block. The difference in the Froude number of the approaching flow is also limited. Only the change in the freestream turbulence level, which is very large, may therefore be considered as a significant factor in the development of the downstream wakes.

The cross-sectional profiles shown in Figure 5.32 downstream of the first and the fourth blocks in the series reveal the gradual changes being experienced by the blocks as the flow develops. Whilst the tilting of the wake into the main channel remains a consistent feature and the skew of the flow over the top of the blocks is

likely therefore to be consistent, the acceleration of the flow in the main channel and the deceleration of that on the floodplain is marked. On the floodplain, this deceleration is partially attributable to the strong anticlockwise circulation, which gradually causes a bulge of low velocities to appear. Meanwhile, the circulation on the main channel side is limited in scope and fails to make any very significant impact on the distribution of velocities in the main channel.

In general therefore, the results suggest that the phenomena described for the single, high aspect ratio block at the floodplain edge are accentuated by the placement of such blocks in an in-line arrangement. The increasing impact of the floodplain circulation on the overall channel dynamics may explain the slowing wake recovery rate observed in Figure 5.31 but the model results suggest that the drag coefficients associated with the inline blocks will be similarly affected to the single block case.

5.5 Summary

This chapter has summarised the performance of the numerical model with respect to both simple, open channel flow cases and more complex cases involving the separating flow around cylindrical obstacles. Comparison of the simulated results with the experimental data collected and presented in Chapter 4 shows the opportunities and limitations of the model and taking these into account, the model has been applied to the simulation of a number of different scenarios including the variation of block aspect ratio and the number of blocks in place at the floodplain edge. The results of these simulations have revealed the fundamental features of wakes at the floodplain edge and how these features are variously affected by the chosen parameters.

Figure 5.33 summarises the values of C_D calculated for the numerically modelled cases discussed in this chapter, together with the 2D value for the square block in the simple channel, as calculated by Lyn *et al.* (1995). Whilst the range of Re covered in this figure is not very wide, the plot immediately confirms that there

Case	C_D	n_v
Single Emergent Block, AR=1	2.96	0.094
Single Emergent Block, AR=2	3.80	0.059
Single Emergent Block, AR=3	3.81	0.038
Single Emergent Block, AR=5	3.73	0.021
Multiple Emergent Block (4 of 5), AR=3.5	1.65	0.001

Table 5.5: Equivalent Manning's Coefficient Values for Blocks representing Vegetation

is no appreciable trend in C_D with relation to Re . Rather, the clear split between emergent and submerged bodies becomes obvious, as do the effects of the block geometry and the location of the block, as single bluff bodies or in multiple block arrangements.

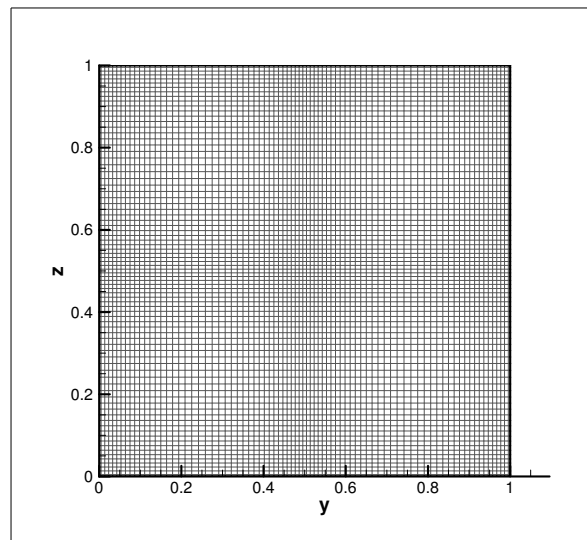
As described in Section 2.3.1, engineering practice commonly utilises Manning's 'n' as a mechanism by which the retardation of flow by roughness of all kinds is accounted for. Equation 5.3, in which (h) is the height of the block and (n_b) is the Manning's coefficient of the surface (for these cases equal to the value for hydraulically smooth surfaces), has been derived for emergent vegetation to give the total Manning's coefficient caused by both surface and vegetal roughness (Komatsu, 2009). By subtracting the Manning's coefficient for the surface from the total value found from this equation, the equivalent Manning's coefficient for the vegetation, here represented by the blocks, can be found. These values are shown in Table 5.5.

$$n = \frac{h^{\frac{1}{6}}}{U_m(\rho g)^{\frac{1}{2}}} \left(\frac{1}{2} \rho A C_D U_a^2 + \frac{\rho g U_m^2}{h^{\frac{1}{3}}} n_b^2 \right) \quad (5.3)$$

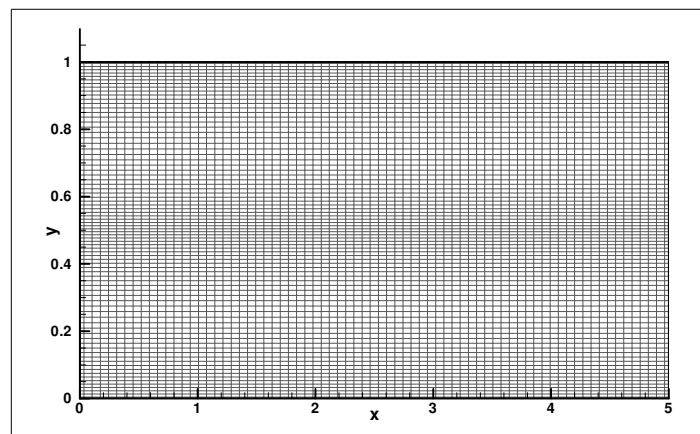
Table 5.5 shows that the contribution to the overall Manning's coefficient calculated by this method in the single block cases is very large. For the multiple

block case, the contribution is much smaller. This variance in the contribution to the Manning's coefficient would suggest that the sensitivity of different scenarios modelled using the Manning's coefficient approach will also vary widely. In a situation in which a whole river system were being modelled for example, these results suggest that the change induced in the overall Manning's coefficient by the floodplain edge location of a row of trees would be small. The value of the overall Manning's coefficient for such a model would therefore be better chosen on the basis of broader criteria. For situations in which a single reach were being modelled in more detail, to predict local flood levels for a new development or to model the seasonal variation in the rating at a gauging station for example, the floodplain edge location of vegetation could be very significant in choosing an appropriate overall Manning's coefficient.

The large drop in the Manning's coefficient associated with the multiple block arrangement also suggests that a closer examination of the dynamics of that arrangement, including a variation of the spacing of the blocks, would yield interesting results. This and other suggestions for future research are discussed in the next section, where all of the experimental and computational results will also be summarised.



(a)



(b)

Figure 5.1: *Square Duct Simulation - Grid Profile (a) Cross Section (b) Plan Section*

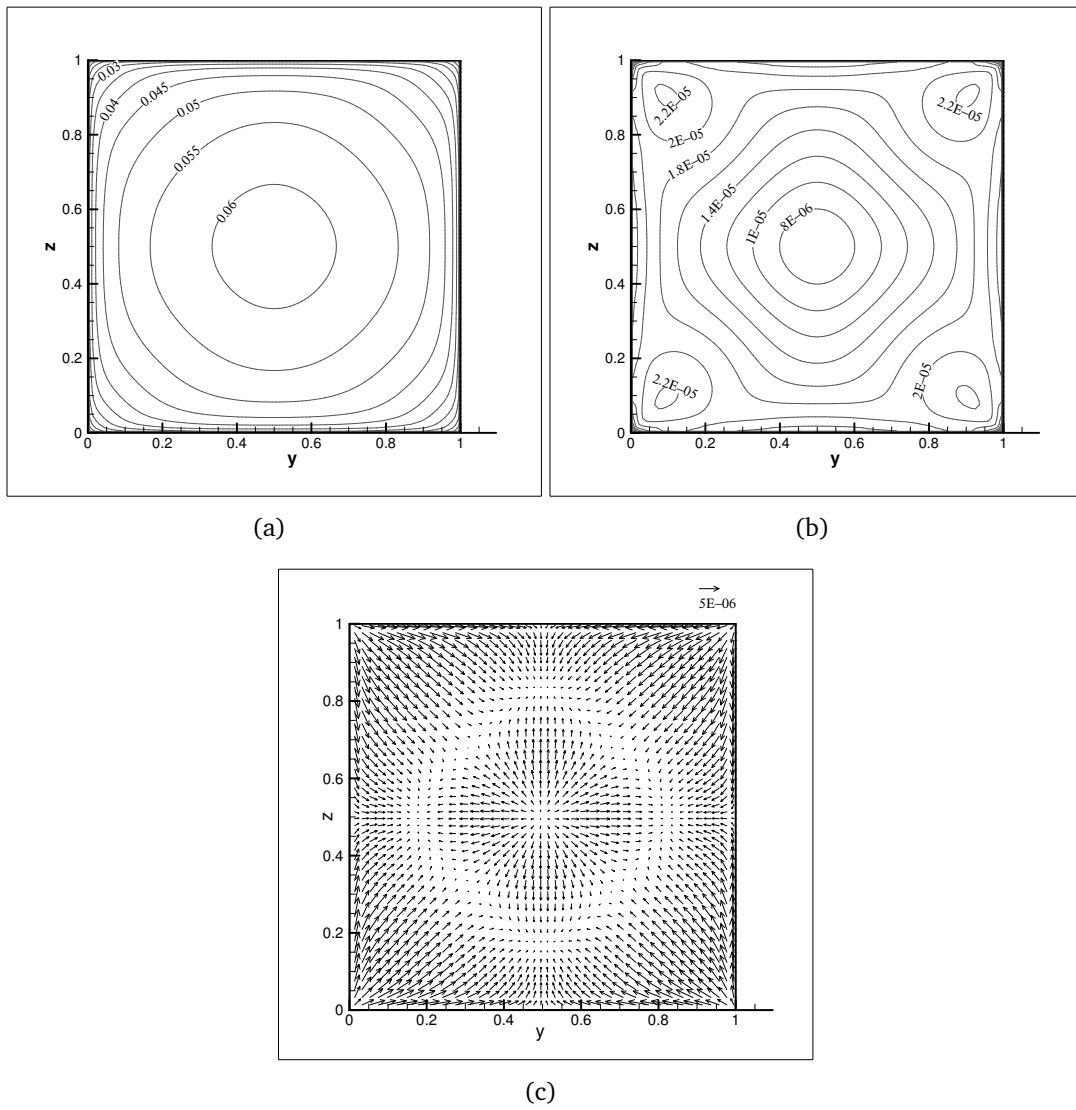


Figure 5.2: Square duct flow results from $k-\epsilon$ model (a) Contours of U and (b) K and (c) Secondary Flow Vectors

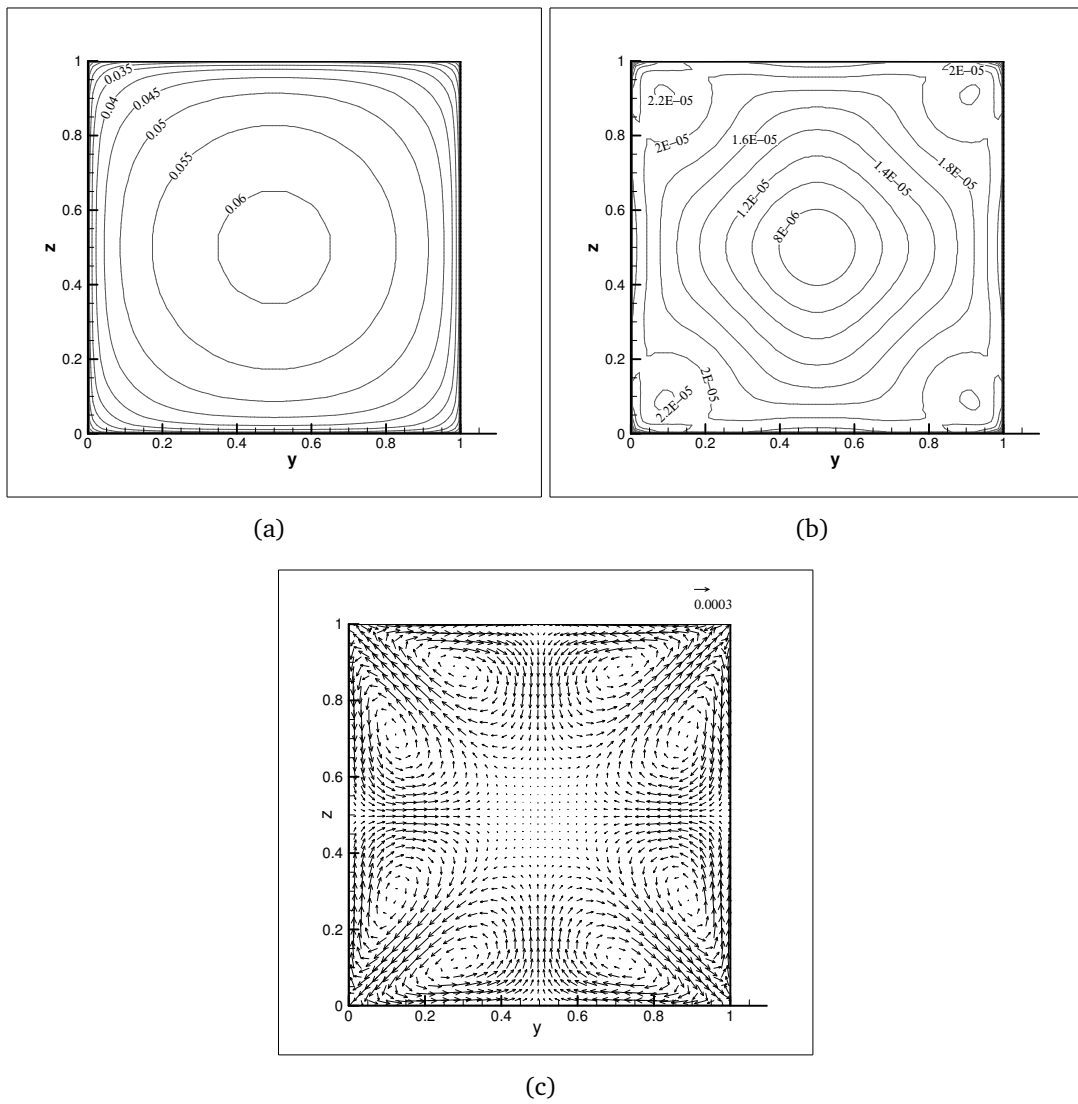


Figure 5.3: Square duct flow results from Speziale model (a) Contours of U , (b) Contours of K and (c) Secondary Flow Vectors

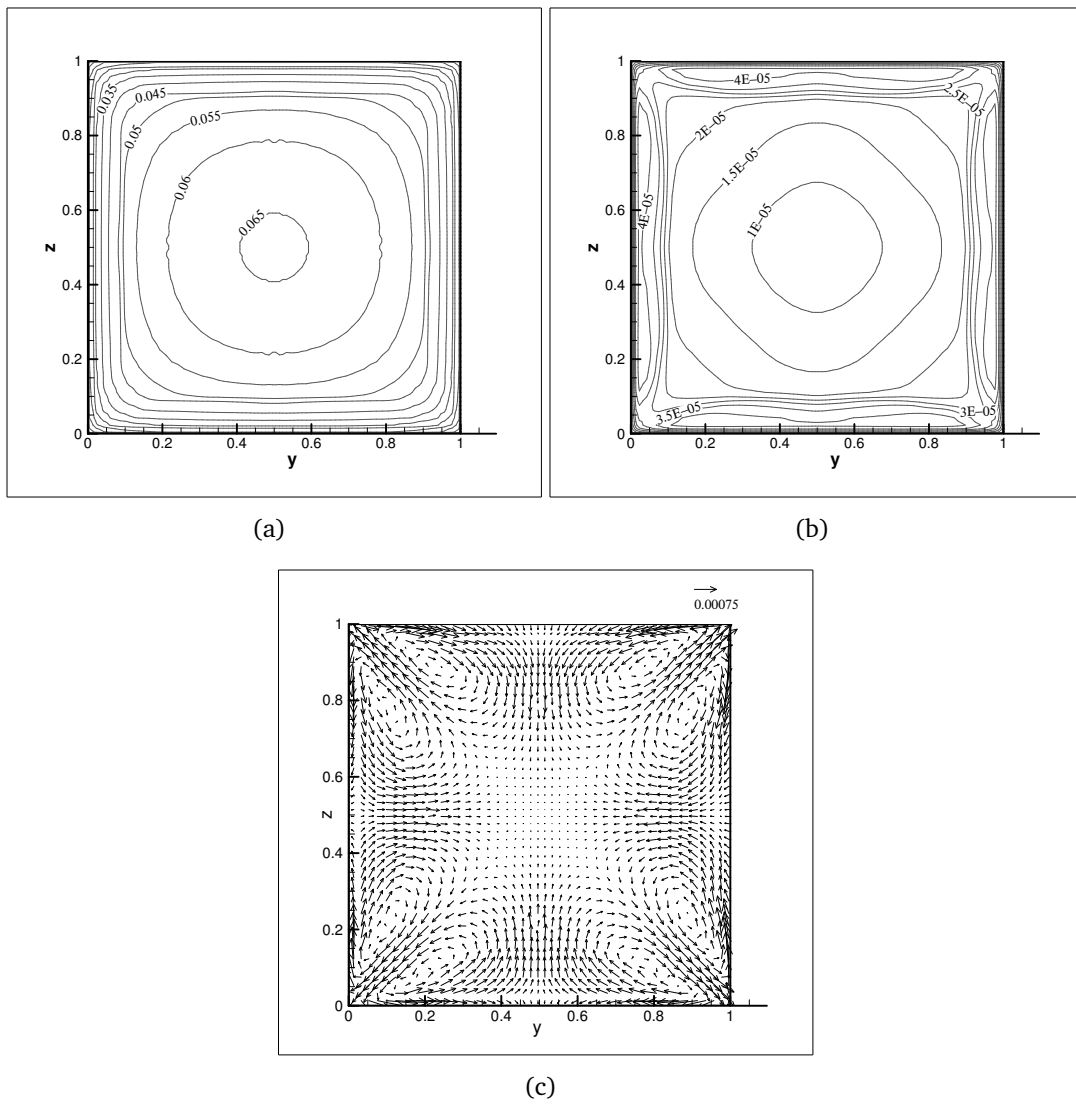
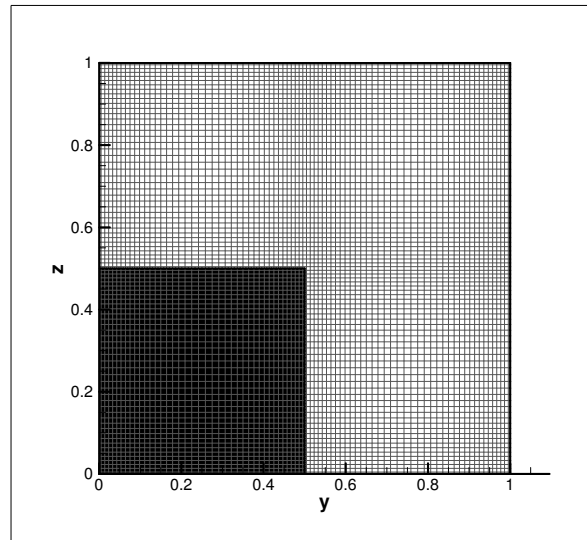
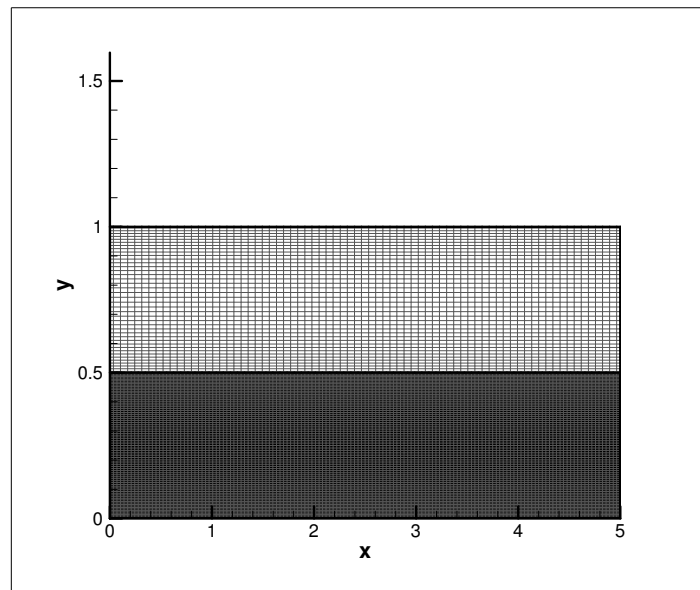


Figure 5.4: Square duct flow results from K&H model (a) Contours of U , (b) Contours of K and (c) Secondary Flow Vectors



(a)



(b)

Figure 5.5: *Compound Channel Simulation - Grid Profile (a) Cross Section (b) Plan Section*

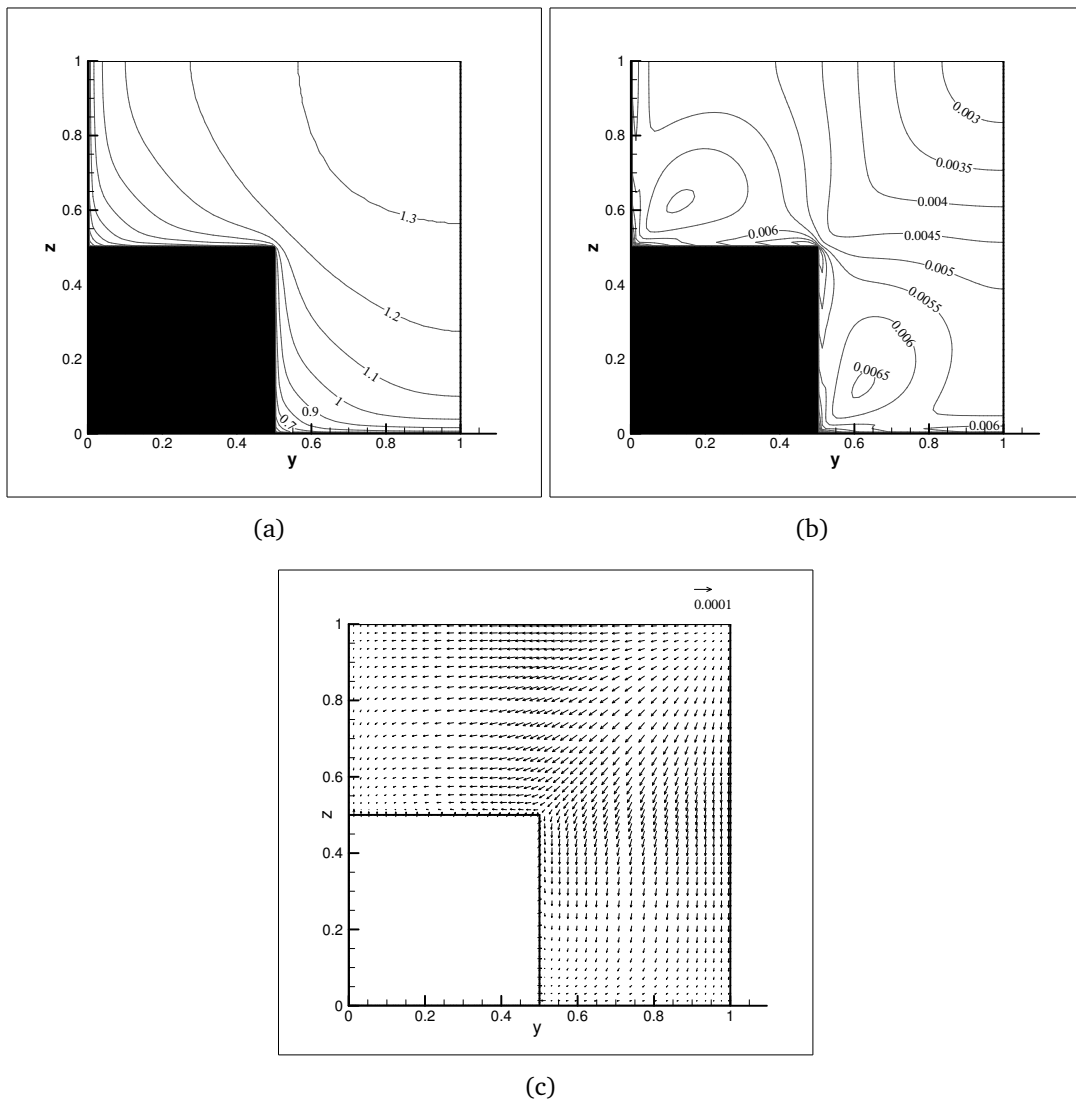


Figure 5.6: Compound channel flow results from $k - \epsilon$ model (a) Contours of U and (b) K and (c) Secondary Flow Vectors

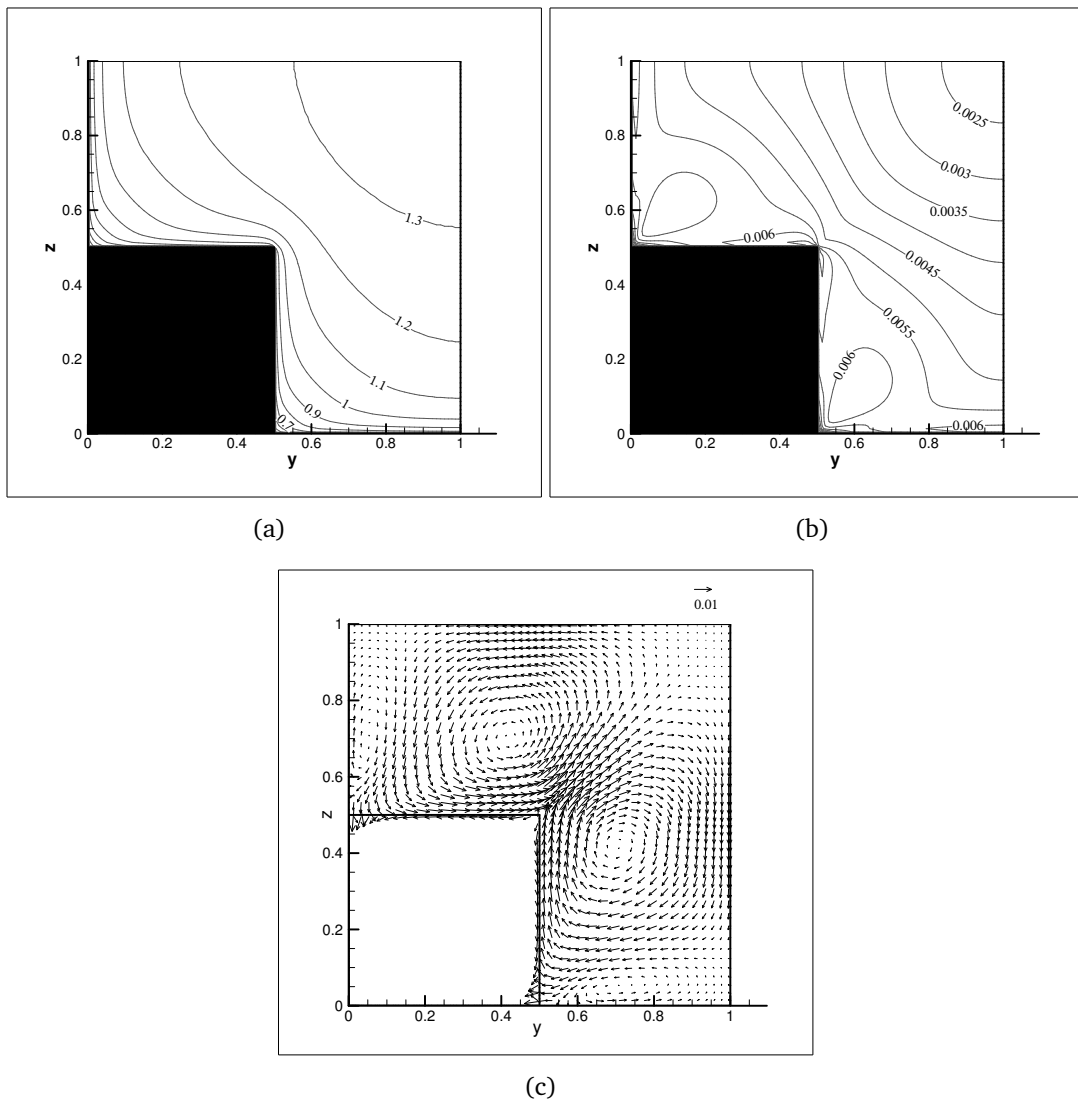


Figure 5.7: Compound channel flow results from K&H model (a) Contours of U , (b) Contours of K and (c) Secondary Flow Vectors

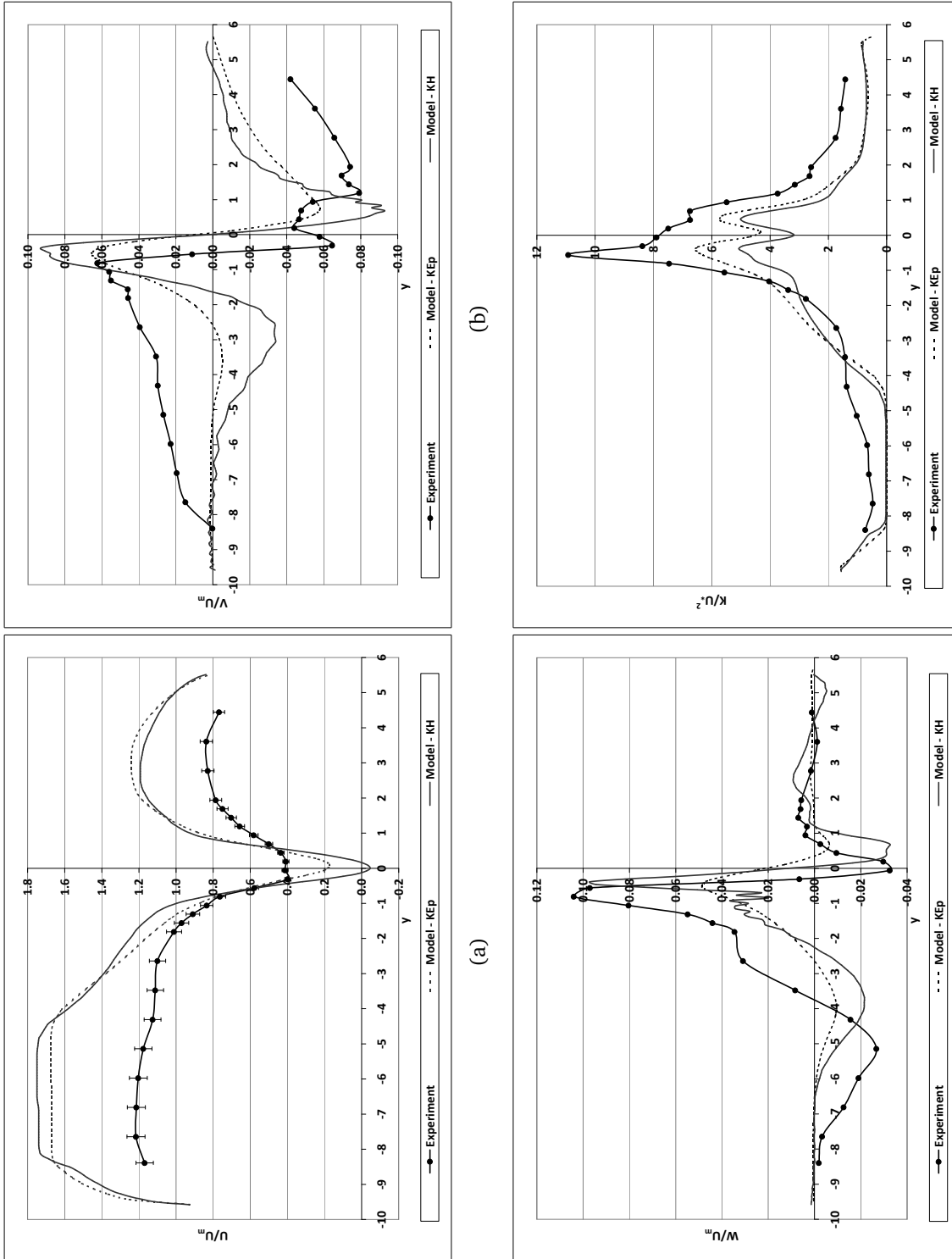


Figure 5.8: Experimental and modelled results for multiple, low aspect ratio, emergent blocks (S1CII), downstream of fourth block at $(x, z) = (+3.5, +0.5)$ (a) U , (b) V , (c) W and (d) K

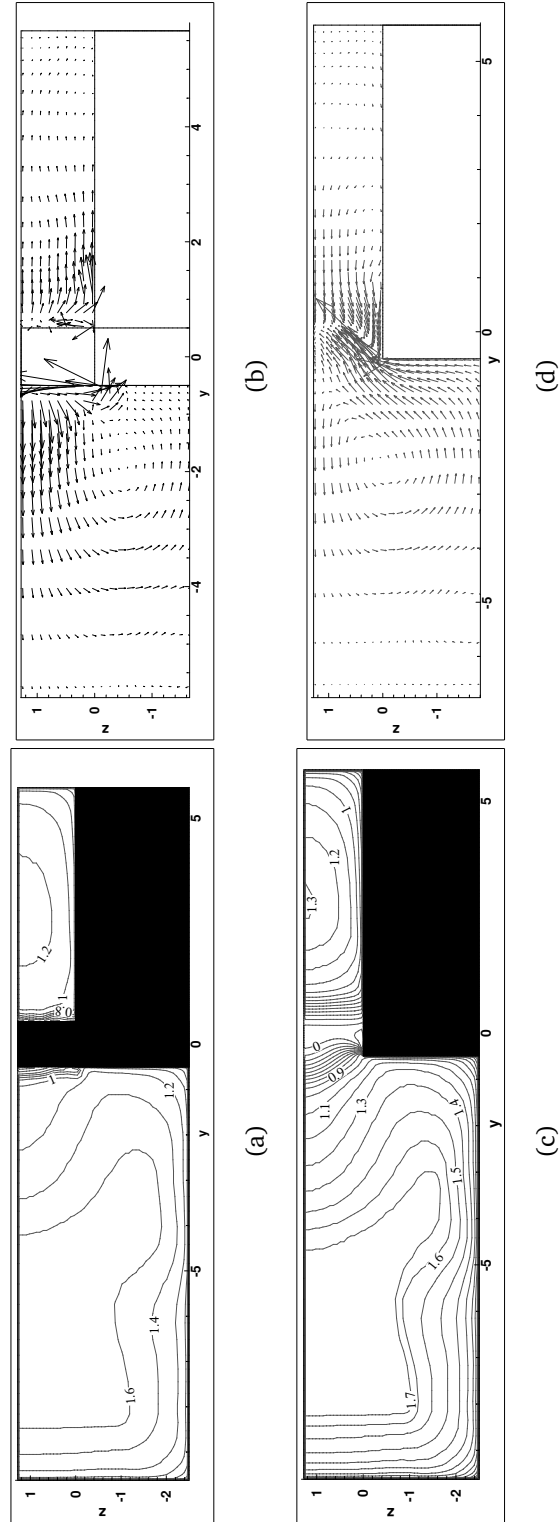


Figure 5.9: Modelled results around fourth emergent low aspect ratio block in series, (S1C1D), Contours of U and secondary flow vectors for (a) & (b) the streamwise block centre and (c) & (d) the downstream station ($x = +3.5$)

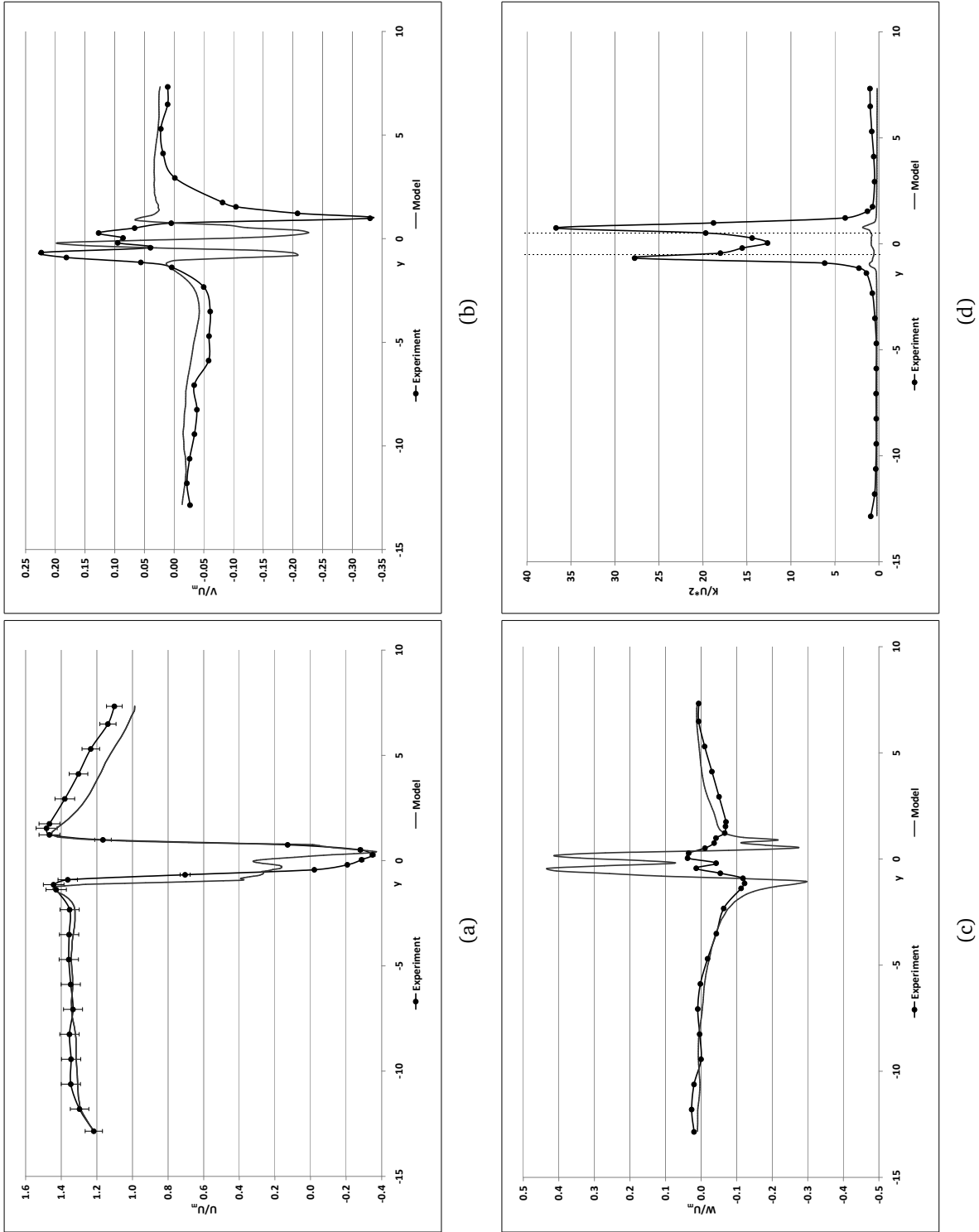


Figure 5.10: Experimental and modelled results at Station Three ($(x, z) = (1.3, 1.0)$), Single, large aspect ratio, emergent block (S2CI) (a) U , (b) V , (c) W and (d) K

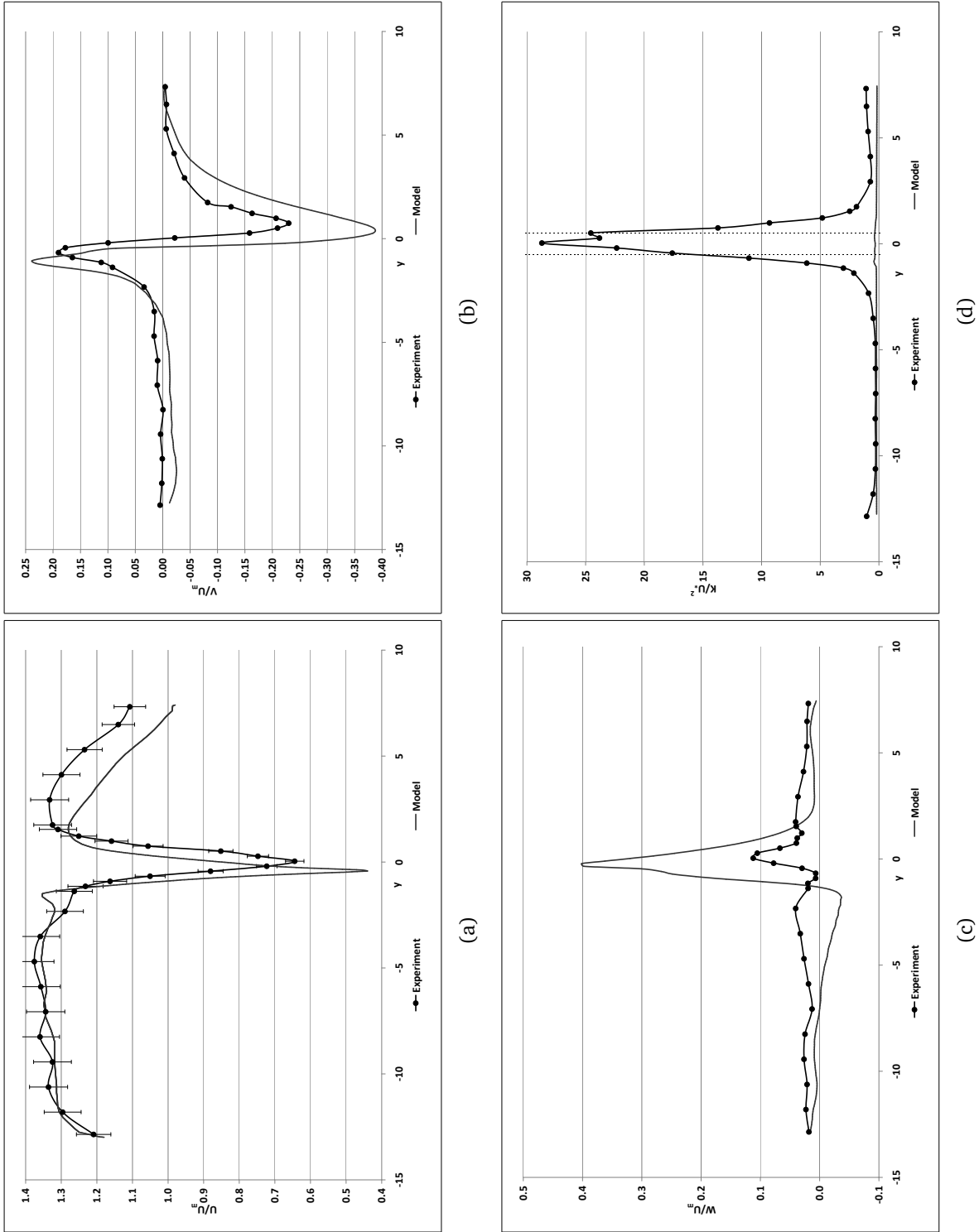


Figure 5.11: Experimental and modelled results at Station Five ($(x, z) = (4.0, 1.0)$), Single, large aspect ratio, emergent block (S2C1) (a) U , (b) V , (c) W and (d) K

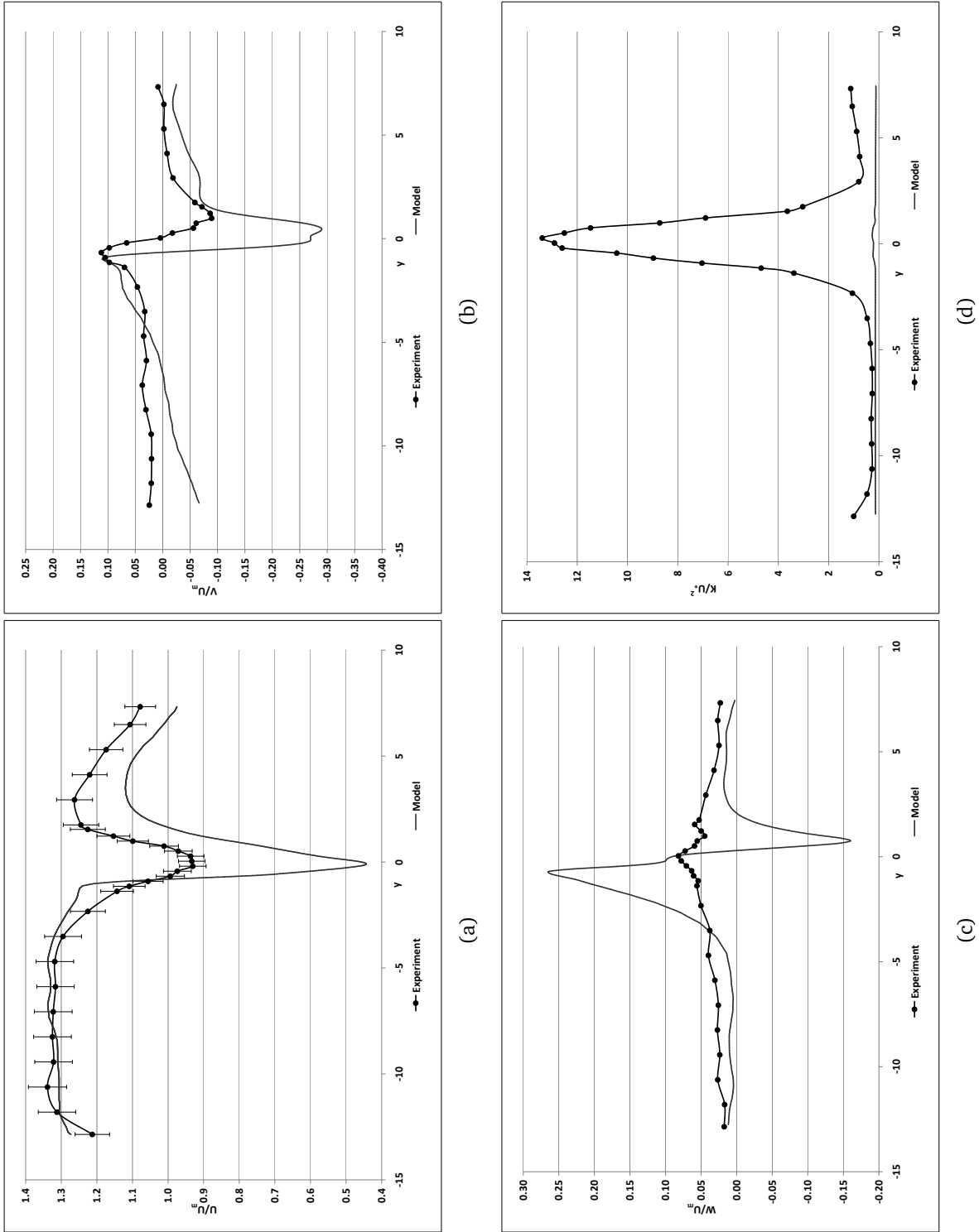


Figure 5.12: Experimental and modelled results at Station Seven $((x, z) = (6.7, 1.0))$, Single, large aspect ratio, emergent block (S2CI) (a) U , (b) V , (c) W and (d) K

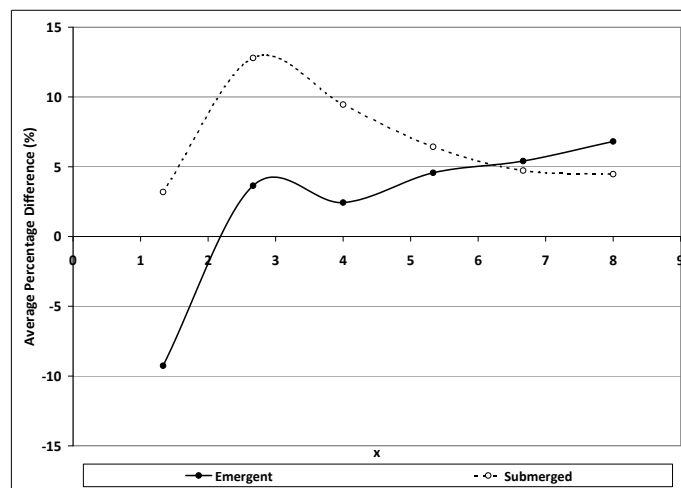


Figure 5.13: Longitudinal variation in the average percentage difference between measured and modelled values of mean streamwise velocity U , Emergent & submerged single, large aspect ratio blocks at the floodplain edge (S2CI&II)

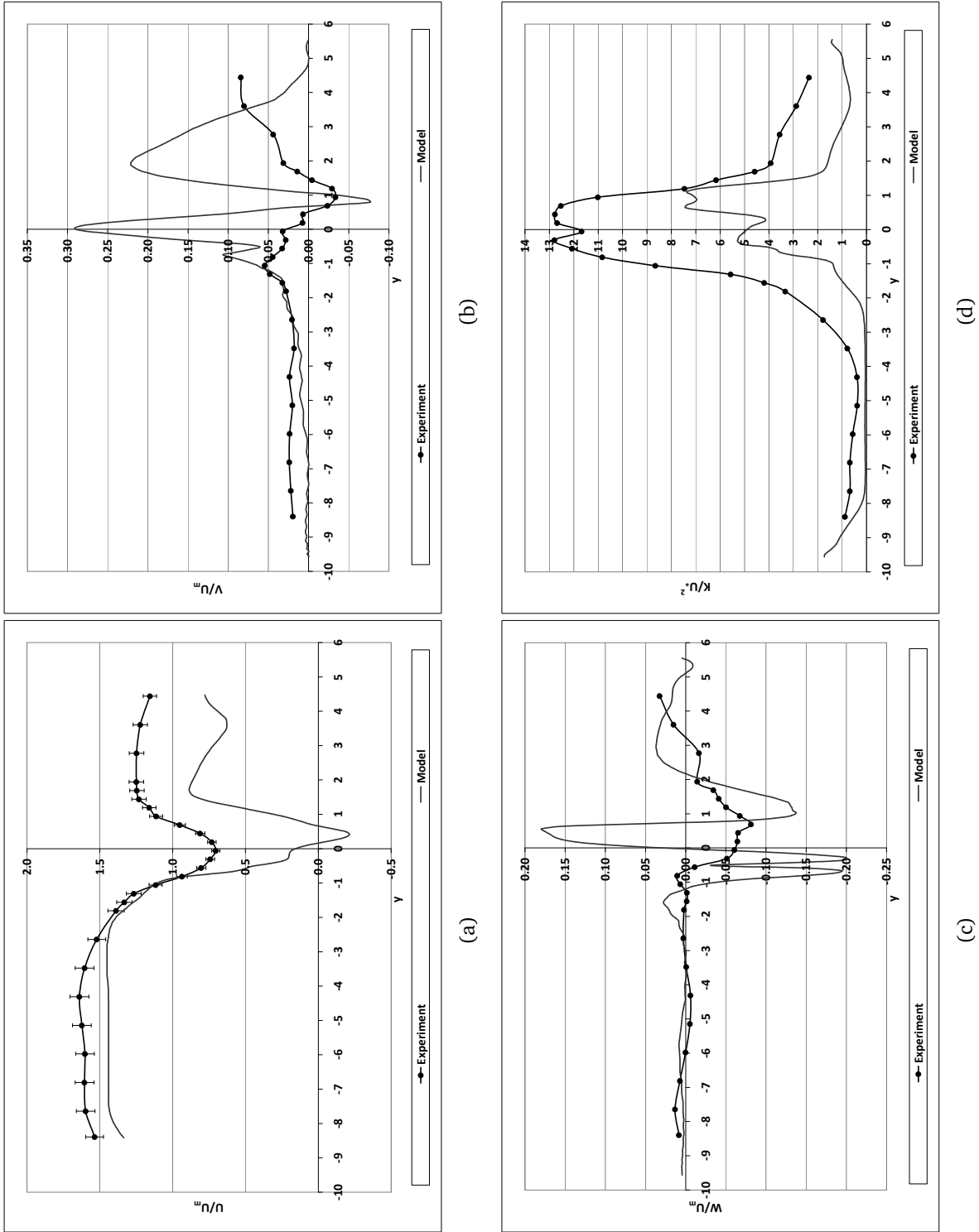


Figure 5.14: Experimental and modelled results for multiple, low aspect ratio, submerged blocks (S1C1), downstream of fourth block at $(x, z) = (+3.5, +0.5)$ (a) U , (b) V , (c) W and (d) K

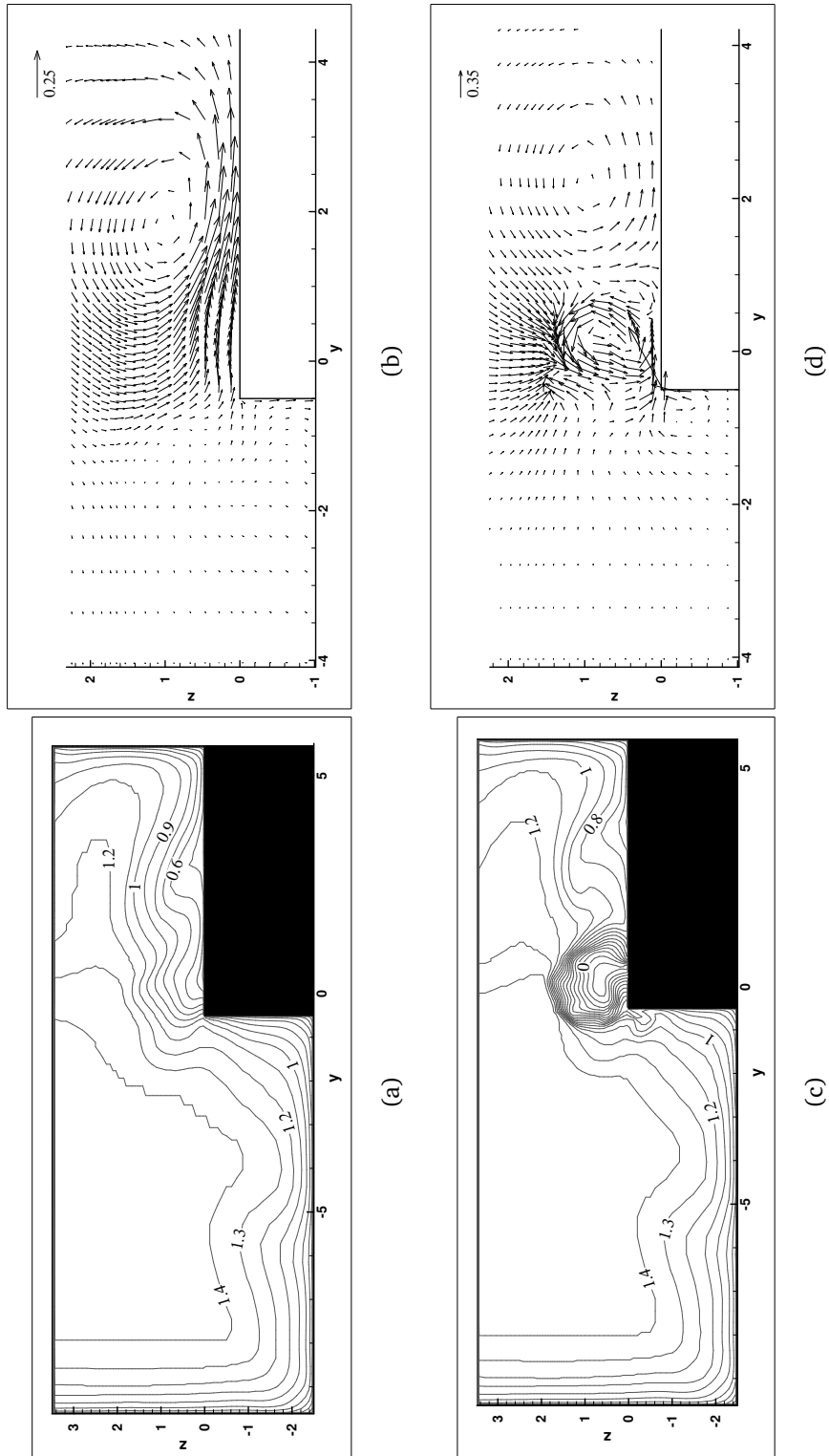


Figure 5.15: Modelled results around fourth submerged, low aspect ratio block in series, (SIC1), Contours of U and secondary flow vectors for (a) & (b) the upstream station ($x = -3.5$) and (c) & (d) the downstream station ($x = +3.5$)

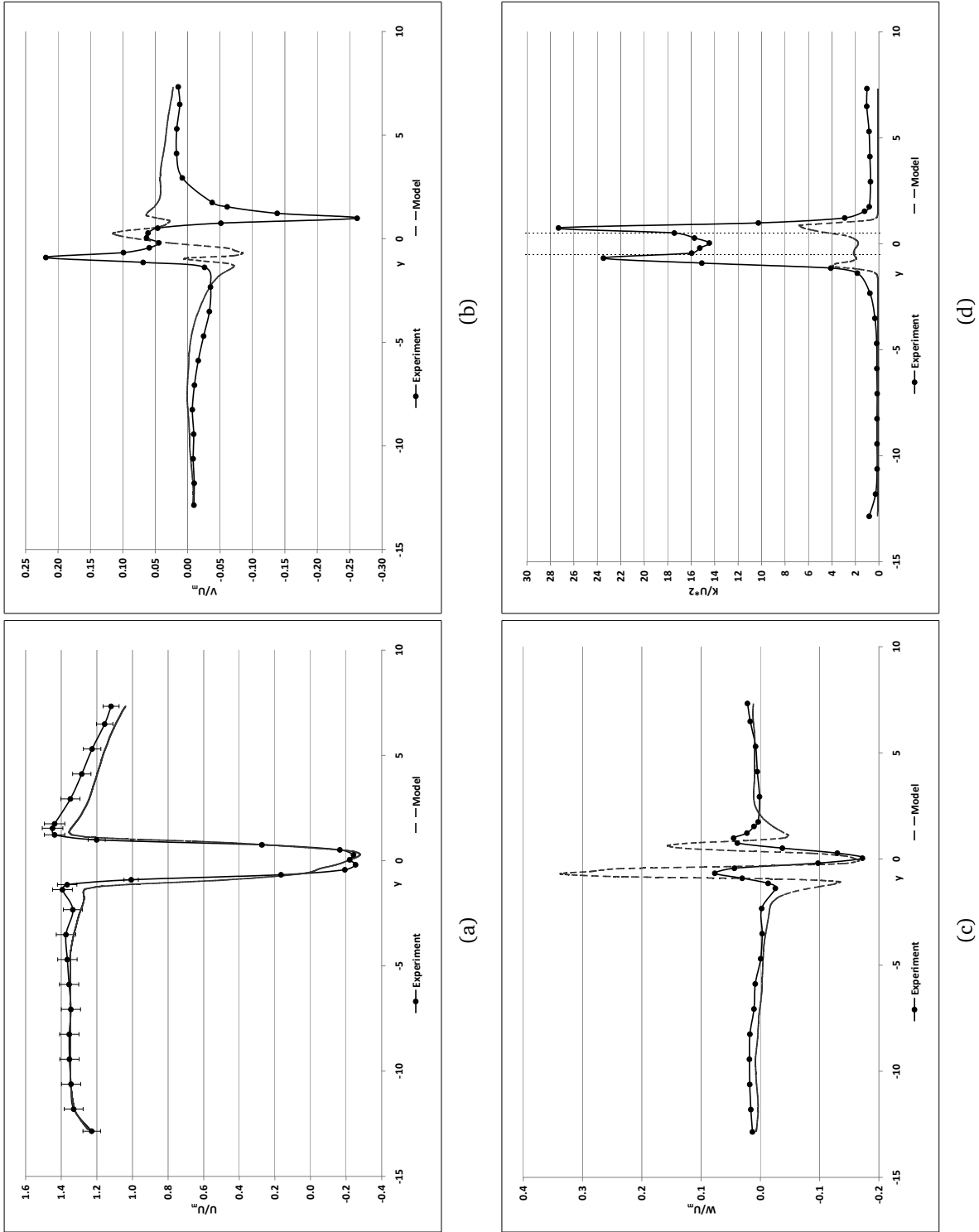


Figure 5.16: Experimental and modelled results at Station Three $((x, z) = (1.3, 1.0))$, Single, large aspect ratio, submerged block (S2CII) (a) U , (b) V , (c) W and (d) K

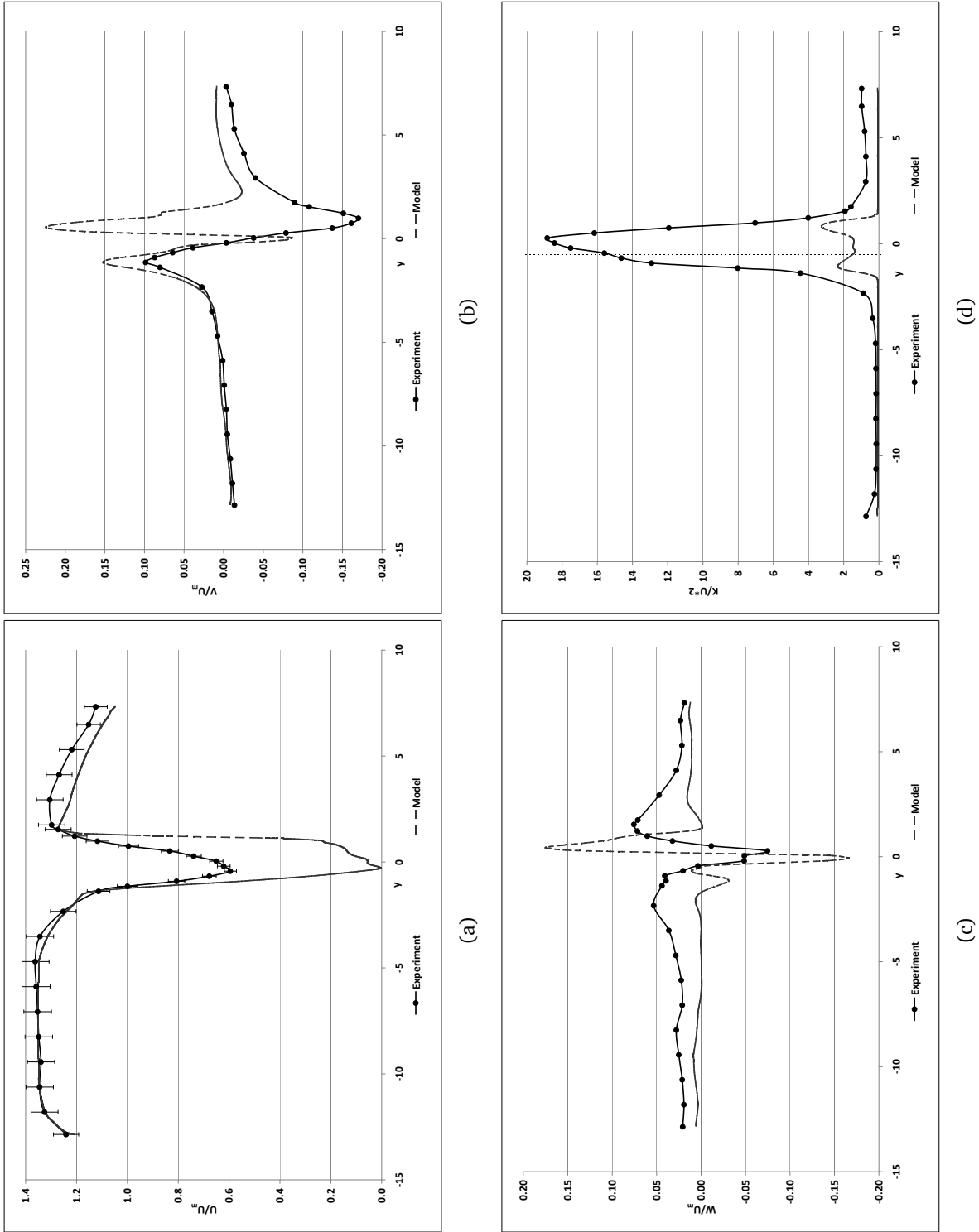


Figure 5.17: Experimental and modelled results at Station Five ($(x, z) = (4.0, 1.0)$), Single, large aspect ratio, submerged block (S2CII) (a) U , (b) V , (c) W and (d) K

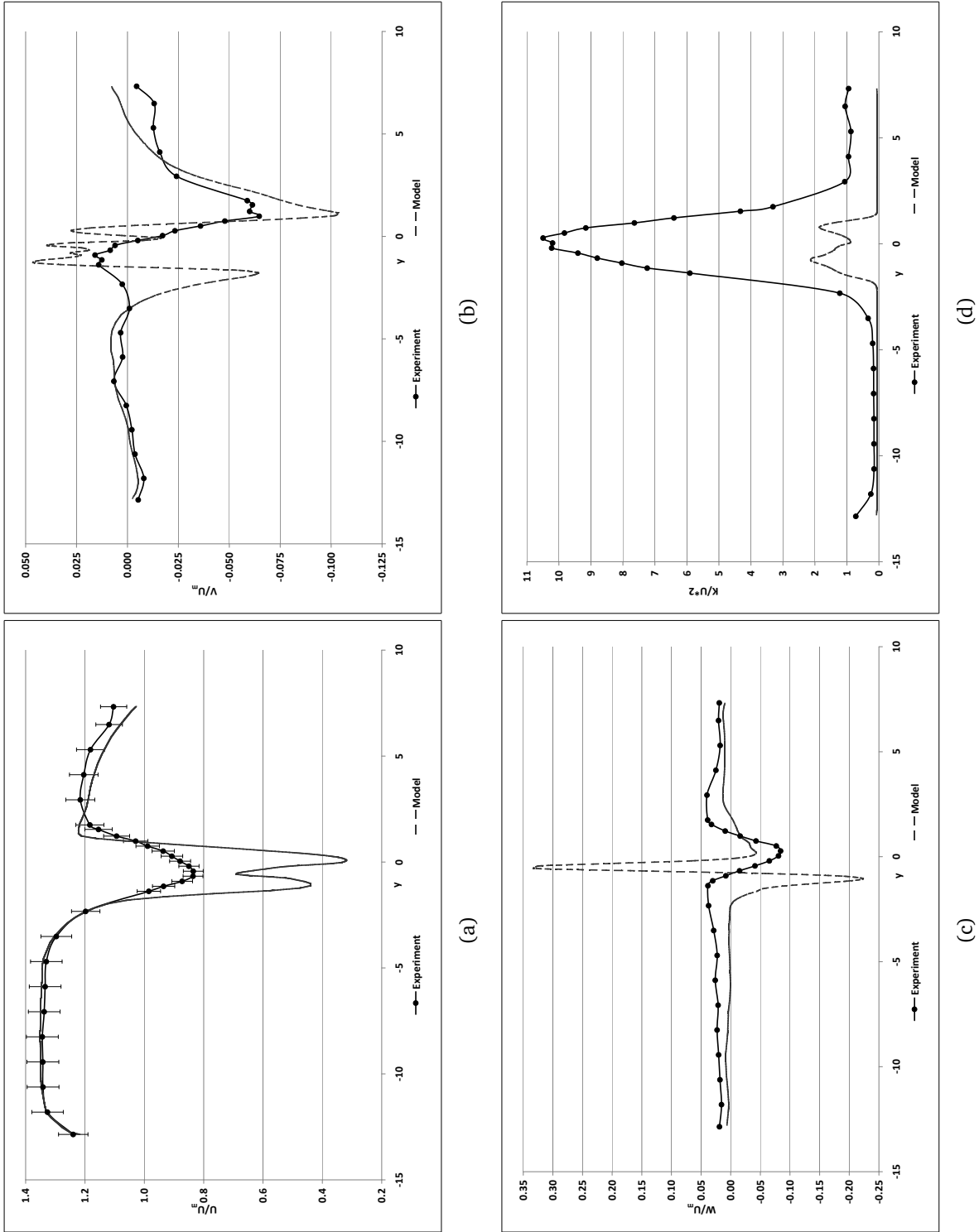
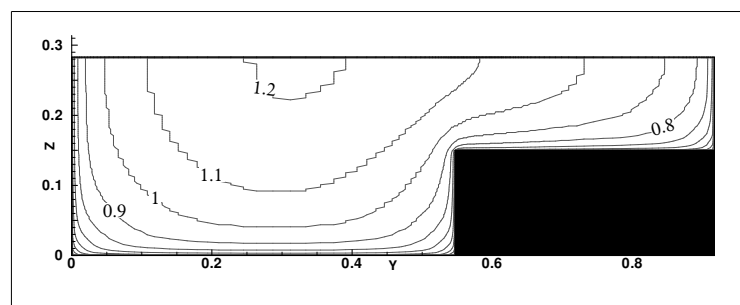
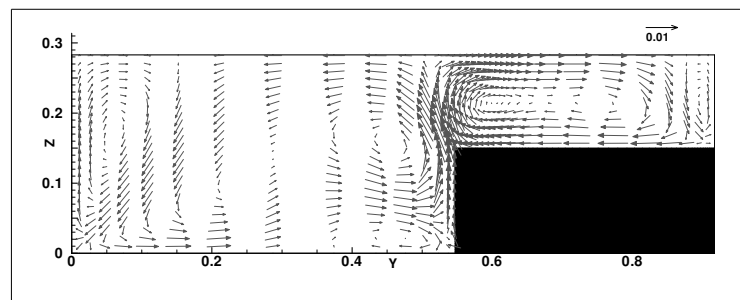


Figure 5.18: Experimental and modelled results at Station Seven ($(x, z) = (6.7, 1.0)$), Single, large aspect ratio, submerged block (S2CII) (a) U , (b) V , (c) W and (d) K



(a)



(b)

Figure 5.19: Variation of Emergent Block Aspect Ratio - Series Inlet Conditions (a) Contours of U and (b) Vectors of Secondary Circulations

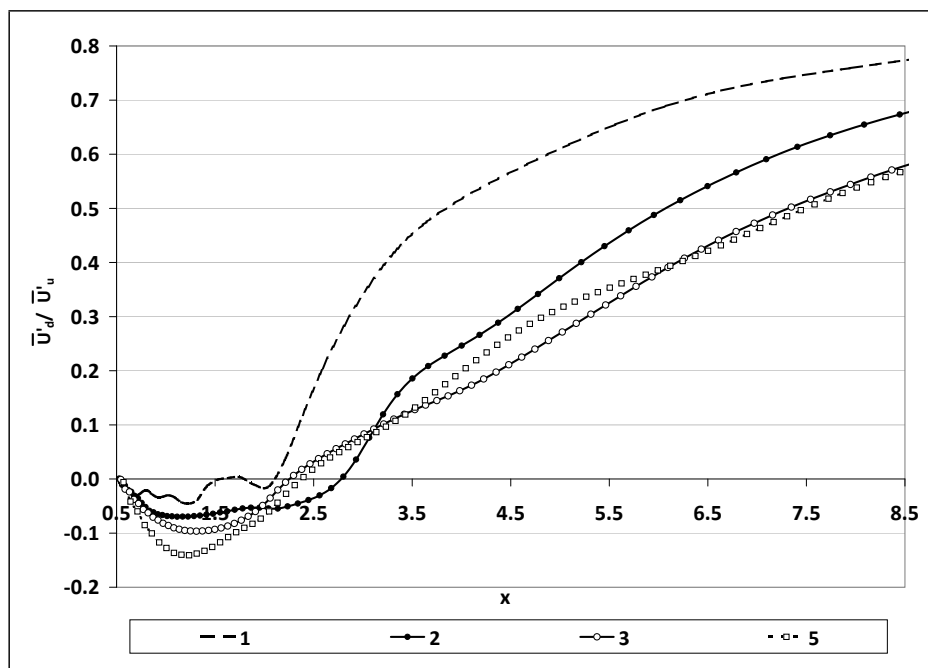


Figure 5.20: Mean streamwise velocity recovery downstream of emergent blocks of varying aspect ratio at floodplain edge

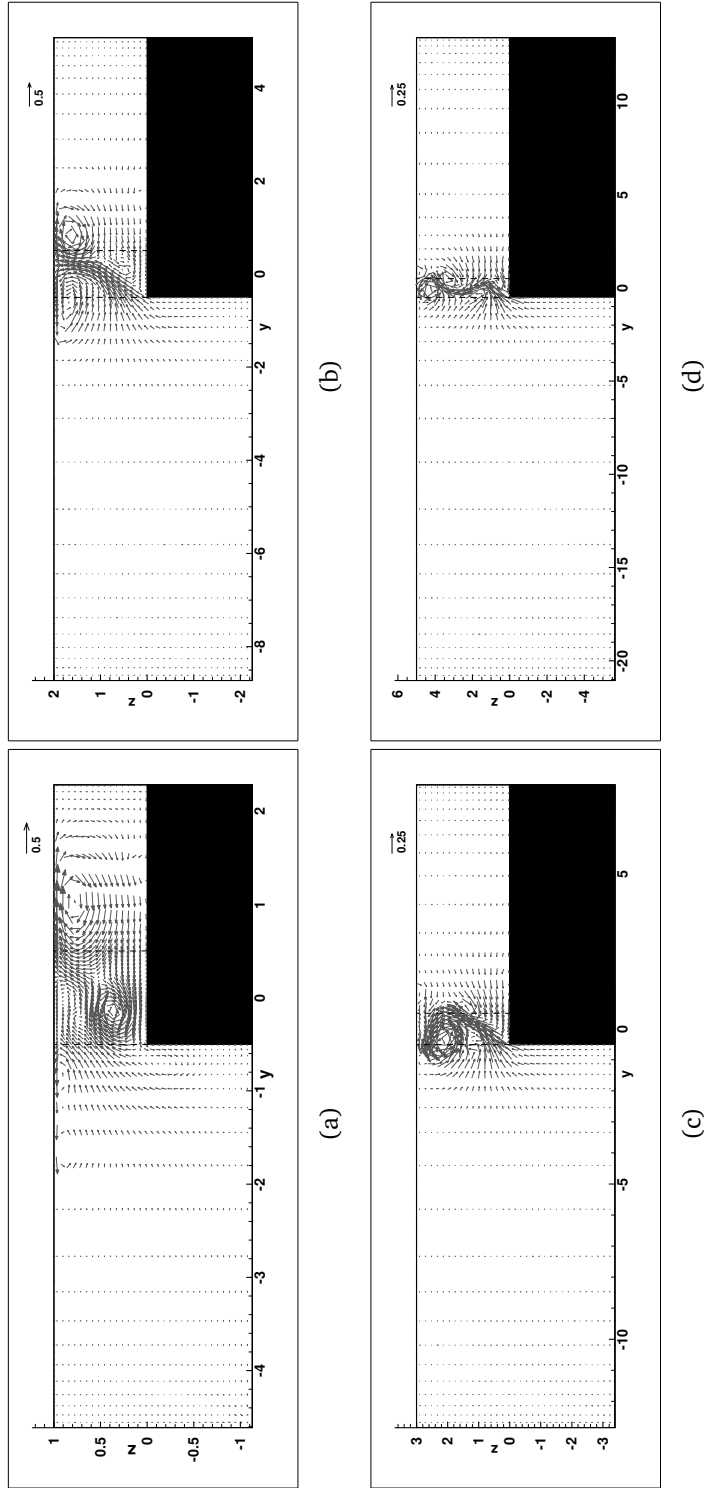
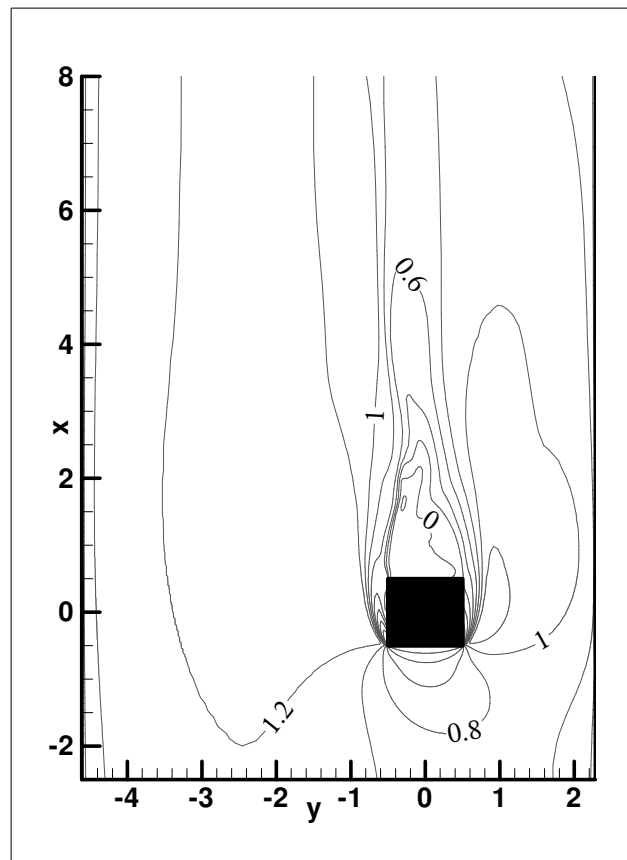
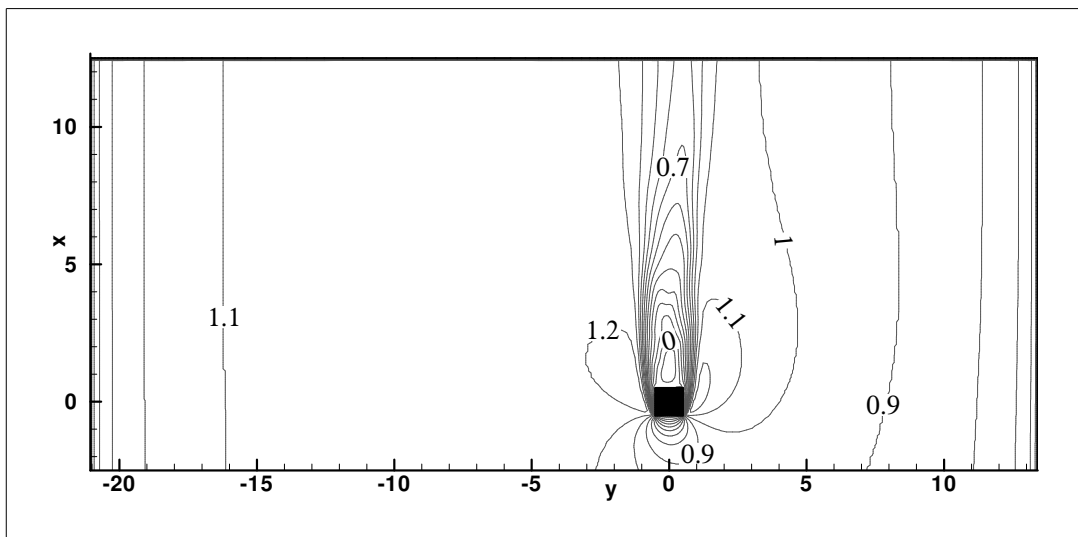


Figure 5.22: Modelled V and W at Station Five ($x = 4$), Single emergent blocks of varying aspect ratio (a) $AR = 1$, (b) $AR = 2$, (c) $AR = 3$ and (d) $AR = 5$

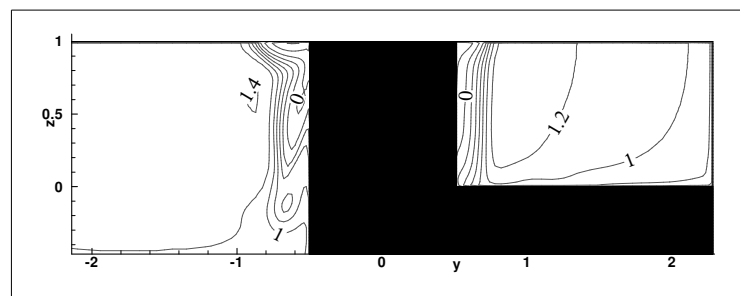


(a)

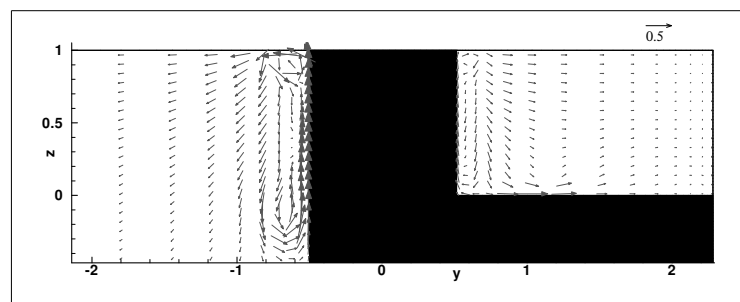


(b)

Figure 5.23: Modelled U at $(z = 1)$, Single emergent blocks of varying aspect ratio (a) $AR = 1$, (b) $AR = 5$

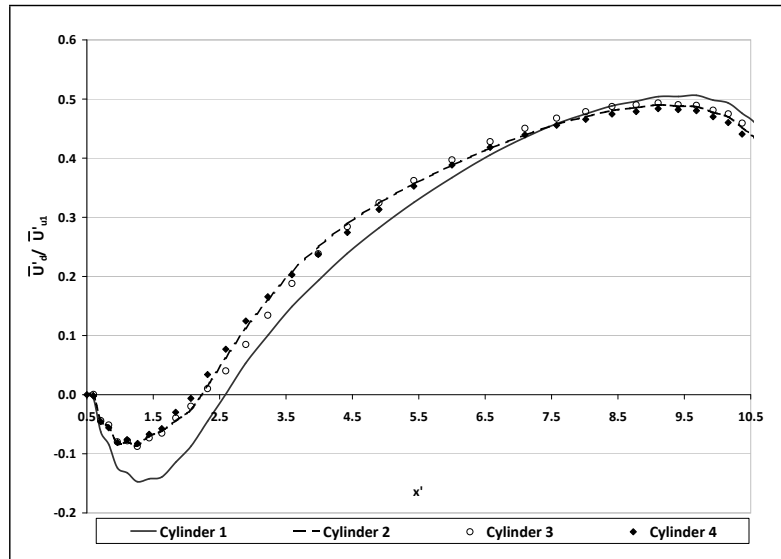


(a)

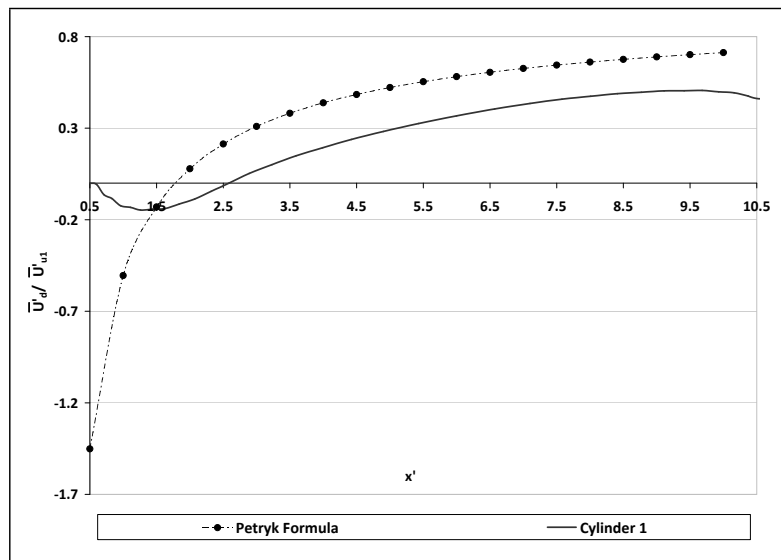


(b)

Figure 5.24: Modelled results for $AR = 1$ at streamwise block centreline (a) U , (b) V and W

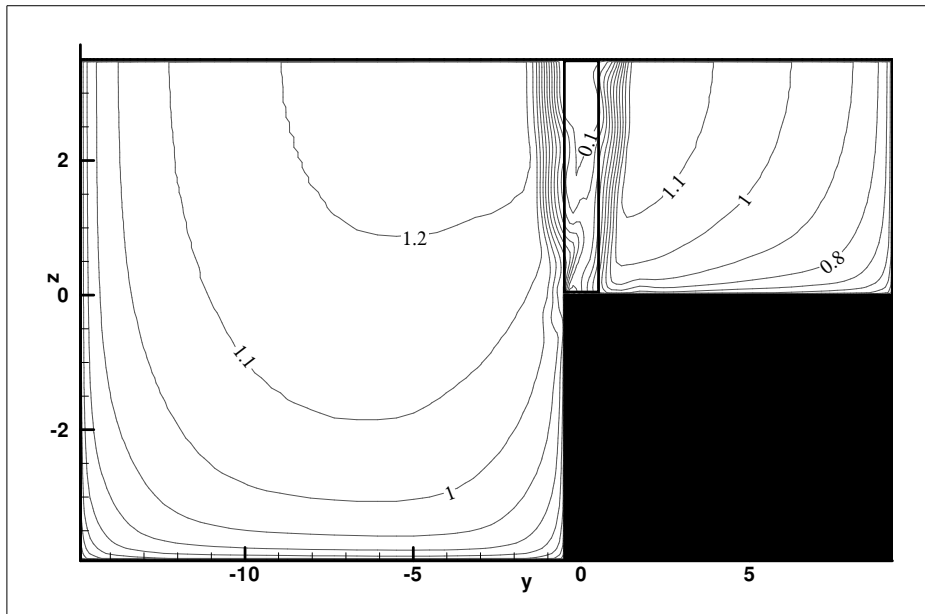


(a)

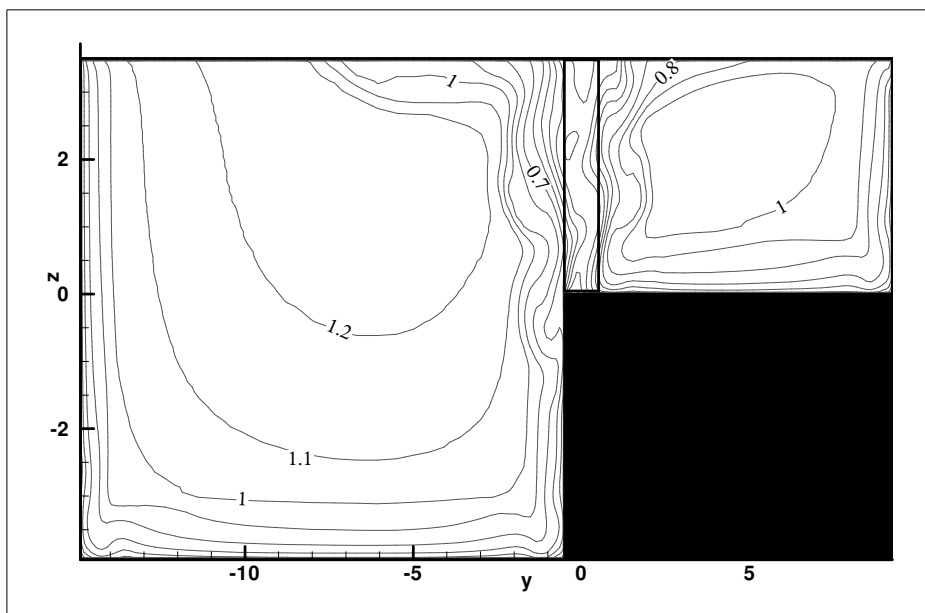


(b)

Figure 5.25: Mean streamwise velocity recovery downstream of first and fourth emergent blocks in multiple block arrangement at the floodplain edge (a) model results only and (b) model results and prediction of Petryk (1969)

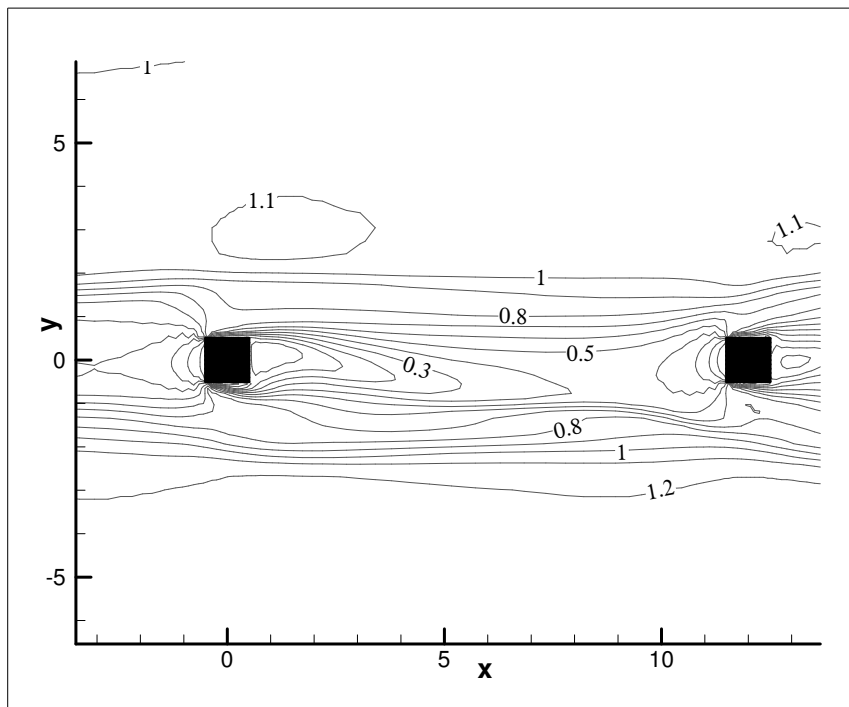


(a)

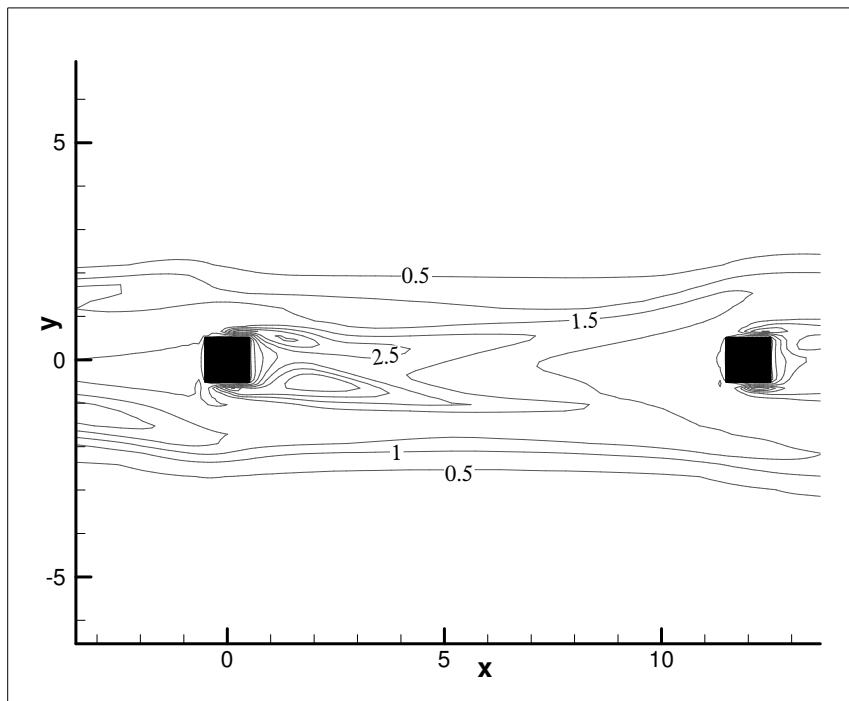


(b)

Figure 5.26: Modelled U for multiple, emergent, high aspect ratio blocks at $x' = 5.5$ for (a) Block 1 and (b) Block 4



(a)



(b)

Figure 5.27: Modelled results at $z = 2.0$ for Block 4 in multiple, emergent, high aspect ratio block case, (a) U and (b) K

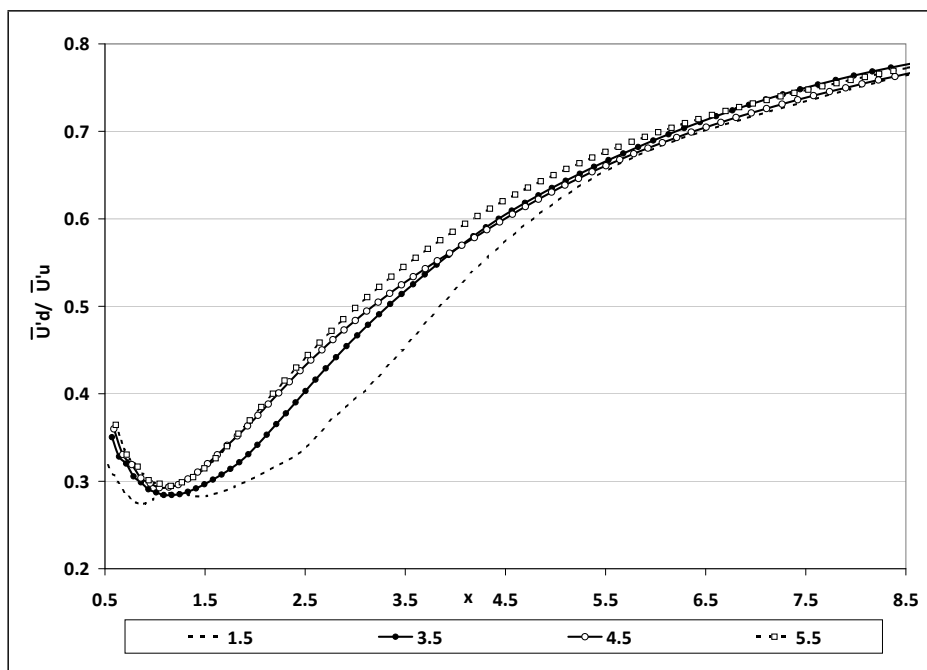


Figure 5.28: Mean streamwise velocity recovery downstream of submerged blocks of varying aspect ratio at floodplain edge

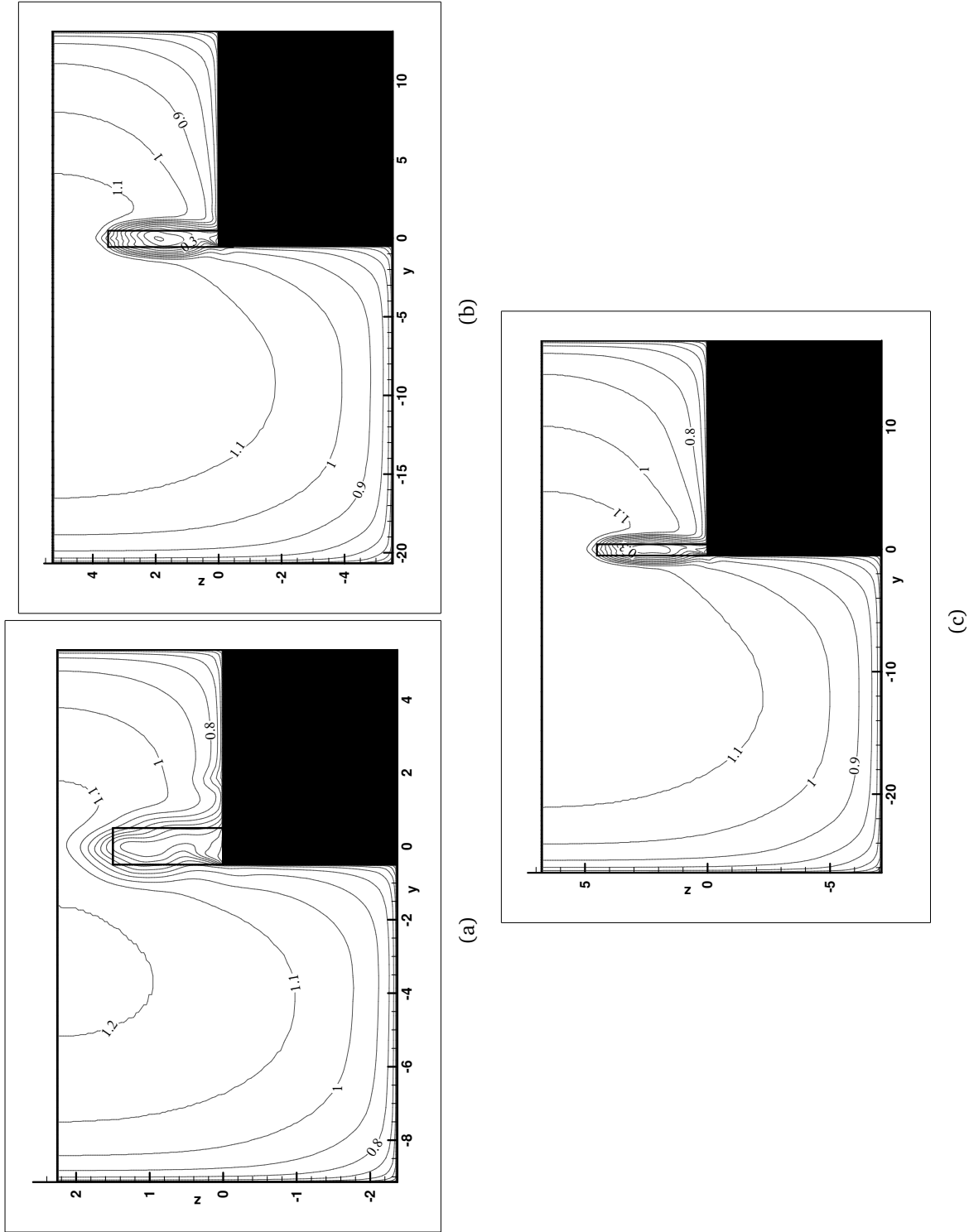


Figure 5.29: Modelled U at Station Five ($x = 4$), Single submerged blocks of varying aspect ratio (a) $AR = 1.5$, (b) $AR = 3.5$ and (c) $AR = 4.5$

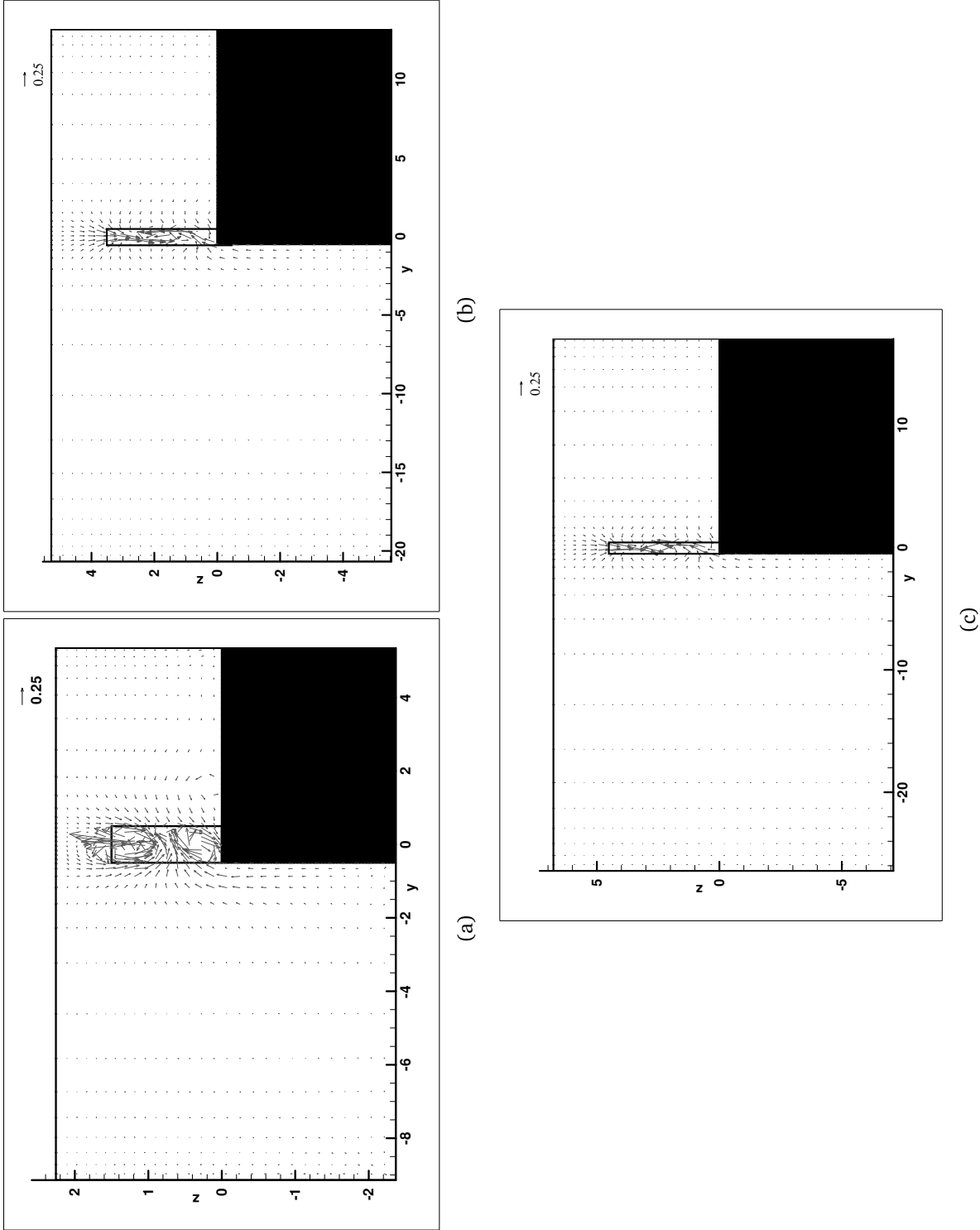


Figure 5.30: Modelled V and W at Station Five ($x = 4$), Single submerged blocks of varying aspect ratio (a) $AR = 1.5$, (b) $AR = 3.5$ and (c) $AR = 4.5$

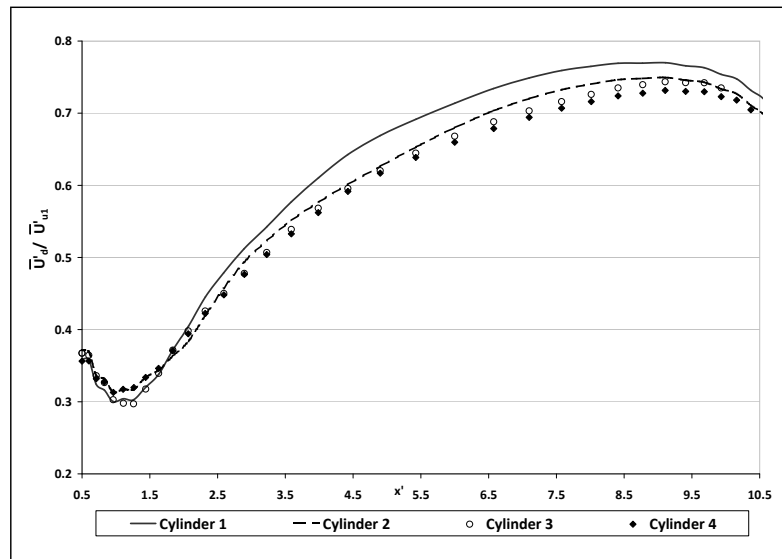
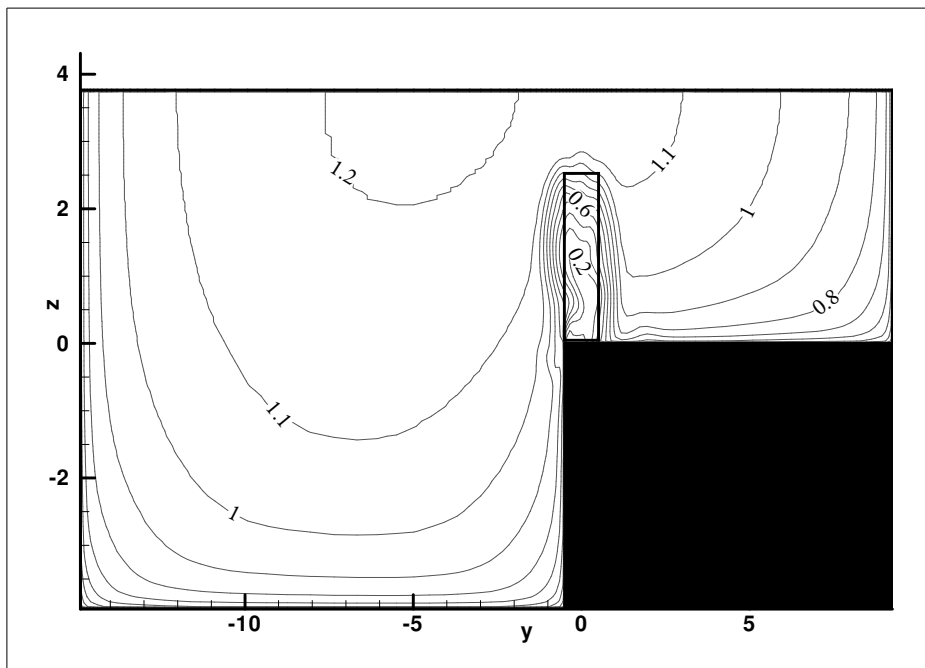
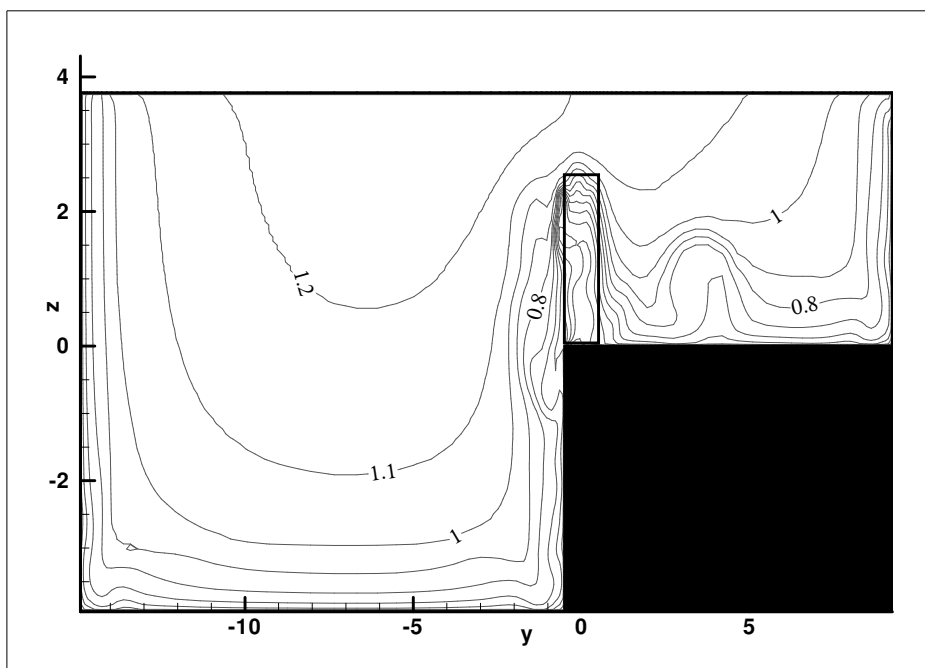


Figure 5.31: Mean streamwise velocity recovery downstream of first and fourth submerged blocks in multiple block arrangement at the floodplain edge



(a)



(b)

Figure 5.32: Modelled U for multiple, submerged, high aspect ratio blocks at $x' = 5.5$ for (a) Block 1 and (b) Block 4

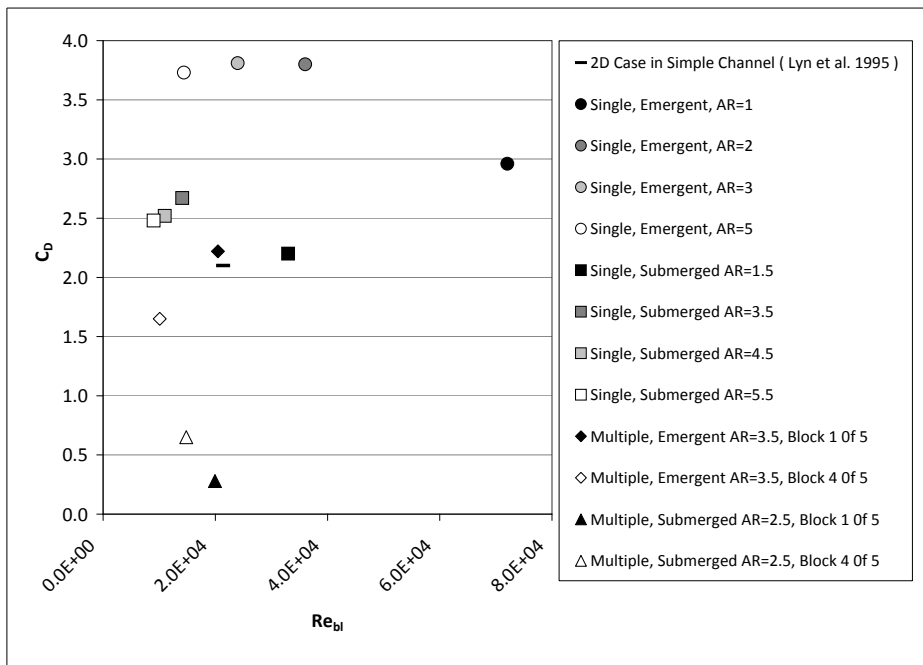


Figure 5.33: Summary of drag coefficient values calculated with numerical model

CHAPTER 6

Conclusion

This chapter summarises the findings of this program of research and includes discussion of their implications and suggestions of new directions for research in this field.

6.1 Summary of Research Findings

In order to elucidate the conclusions that may be drawn from this research project in a systematic manner, bringing together the information gathered from the existing literature, the physical experiments, model development and numerical experiments, they will be summarised here:

- *Holistic Review of Literature on Drag Force*

1. In attempting to include the effects of vegetation in numerical models of open channel flow, two dimensional approaches based on the inclusion of a drag term in the flow equations offer a practical and inexpensive method. However, in order to determine the most appropriate value of drag coefficient to represent the vegetation in such a model, an understanding of how the wider channel flow environment affects the formation and decay of the wakes is essential. The alternative method of

assigning values of C_D in such models, namely by a process of calibrating modelled results against experimental results, must, by definition, be limited in its scope. By expanding the review of relevant literature in this project to include sources of information and data from a range of disciplines, it was shown that the key factors impacting on the structure of the wakes formed behind cylindrical obstacles and therefore, on the final drag force caused by their presence in a flow, are the Reynolds number, Froude number and turbulence intensity of the approaching freestream flow, the blockage ratio of the block's approach area to the channel's cross-sectional area and the geometry of the block and the channel within which it is located. Using this summation of knowledge, it was shown that the location of blocks at the edge of the floodplain in a compound, open channel flow was highly likely to have a significant effect on the drag coefficient and that this effect would vary with the characteristics of both the block and the channel.

- ***Numerical Model Development and Testing***

1. Comparison of the modelled results with the data gleaned from the physical experiments provided a new set of cases to examine the performance of the non-linear turbulence closure of Kimura and Hosoda (2003). In comparison with the linear $k - \epsilon$ turbulence closure, this was shown to offer significantly better performance in simulating the flow around cylindrical obstacles at the floodplain edge.
2. In general, the model was shown to reproduce the mean streamwise velocity profiles particularly well in the near wake region of the blocks. Whilst inaccuracies in the prediction of the magnitudes of the secondary circulations and turbulent kinetic energy were found, such that the secondary circulations tended to be over-predicted whilst the turbulent energy tended to be under-predicted, the model generally also was successful in predicting the shape of these profiles well.

3. Testing the model against the experimentally gathered data also however, demonstrated some of the limiting characteristics of this model for these scenarios. For the low aspect ratio blocks, where the periodic shedding of vortices would be limited, the results suggested that the recognised tendency of the model to under-estimate the truly random component of the turbulence is an important limiting factor. For the high aspect ratio cases, where periodic structures should make much more of an impact on the overall turbulent intensity, the steady nature of the modelling was the limitation as the turbulent energy associated with the shed vortices is not reproduced.
4. The result of these limitations was, in all cases, for the model to predict, particularly in the far wake region, a slower recovery of the mean streamwise velocities than found in the experimental results.

- ***Physical Experiments on Single, Emergent, Large Aspect Ratio Blocks***

1. In comparison with the wake around a similar block at the centre of a simple, rectangular channel, the wake around a large aspect ratio, emergent block at the floodplain edge of a compound, open channel flow is characterised by a slower recovery of the mean streamwise velocities and a faster recovery of the pressure field, resulting in a significantly higher overall drag coefficient.
2. For the compound channel case, the deeper main channel flow was shown to contribute to a reduction in the Froude number of the approaching flow commensurate with the observed reduction in the vertical scale of the axial vortices associated with the free surface deformation. The experimental results also showed, however, that their horizontal scale is larger.
3. The separated regions around the single, emergent block at the floodplain edge were shown to be characterised by differing patterns of reat-

tachment and re-separation on each side of the block due to the differing geometries and freestream conditions to be found there. Over the majority of the height of the block, the balance was such that whilst reattachment was limited on the floodplain side, it was a significant feature on the main channel side, causing the resulting wake to be skewed slightly to the floodplain side of the block centreline. With the vortex shedding process thus compromised on the main channel side of the block, the more energetic vertically orientated vortices being formed and shed from the floodplain side of the block were demonstrated by the asymmetric pattern of turbulent intensity measured across the wake.

4. The axial vorticity formed within the lateral separation zones was shown to be of distinctly different character. Whilst the literature record for surface-mounted blocks in simple channels shows that axial circulations are expected to emerge from these zones such that there is an upward flow at the block centreline, in this case, the vorticity formed within the separated zone on the main channel side of the block was shown to be greater than that formed on the floodplain side. Affecting the secondary circulations in the main channel more widely, the influence of this circulation was observed to reach down to the main channel bed.
5. The rate of decay of the wake structures and the turbulent energy associated with them was shown to be significantly slower on the main channel side of the block, contributing to the overall deceleration of the flow recovery more generally in comparison to that of the equivalent block in the centre of a simple channel geometry.

- ***Numerical Experiments on Single, Emergent Blocks of Varying Aspect Ratios***

1. Through comparison of the results of numerical simulations carried out for a range of values of aspect ratios, it was shown that this geometrical

feature has a strong influence not only on the structure of the wake due to its influence on the shedding process generally but also on the modifications applicable to the wake structure because of the floodplain edge positioning.

2. The premature reattachment of the flow on the main channel side surface of the block was shown to be associated with a clockwise circulation in the floodplain edge region.
3. For low aspect ratio blocks, this circulation and the premature reattachment were shown to be dominant over a larger vertical proportion of the block. On the floodplain side, it was demonstrated that the high blockage ratio associated with the low aspect ratio also promotes reattachment. The combination of these phenomena however, results in the location of the wake on the main channel side of the block centreline for a significant proportion of the block height near the floodplain bed.
4. At the free surface however, the opposite is true so that the wake is characterised by a strong tilt over the depth of the floodplain flow.
5. At high aspect ratios, this tilted region was shown to be limited to a vertical zone very near the floodplain bed. For the majority of the block height for these cases, whilst early reattachment was still a feature on the main channel side, limited or no reattachment was identified on the floodplain side, leading to stronger vortex shedding.
6. For all cases in this series, it was shown that the decrease in the rate of the wake recovery in the deeper water of the main channel identified from the experimental results persists.

- ***Physical Experiments on Single, Submerged, Large Aspect Ratio Blocks***

1. In comparison with the wake around a similar block at the centre of a simple, rectangular channel, the wake around a large aspect ratio, sub-

6.1 Summary of Research Findings

merged block at the floodplain edge of a compound, open channel flow is characterised by a slower recovery of the mean streamwise velocities.

2. The wake structure from a block in this location was shown to be very different to that from a block in an equivalent simple channel flow since the wake tends to bulge very strongly outward into the main channel under the influence of uneven separation, reattachment and re-separation patterns both on the two sides of the block and also on the block top surface.
3. The axial vorticity that is expected in the wake of a submerged block, namely two counter rotating vortices flowing downward at the block centreline, is a result of the domination of the flow coming over the top of the block over the axial vorticity created in the lateral separation zones, which rotates in the opposite direction. It was shown that the asymmetry in the creation of axial vorticity in the lateral separation zones familiar from the emergent case was also found here but that for the submerged block, the strong rotation on the main channel side acts against the flow over the top of the block to diminish the overall vorticity found on the main channel side. The axial circulation on the floodplain side and the overall turbulent intensity associated with all of the periodic and random turbulent structures was shown to be heavily dominant.
4. In common with the emergent case, it was shown that the rate of decay of the wake is slower on the main channel side, so that the bulge of the wake into the main channel tends to be emphasised in the downstream direction.

- *Numerical Experiments on Single, Submerged Blocks of Varying Aspect Ratios*

1. As with the emergent cases, the block aspect ratio was again shown to have a strong influence on the structure of the wake and on the modifications applicable to the wake structure because of the floodplain edge positioning.
2. The greatest impact on the wake structure was found for the low aspect ratio blocks, where the greatest bulging of the wake into the main channel was observed. This may be associated with not only a greater disruption of the separated zone on the main channel side of the block but also with a larger gradient in the position of reattachment on the block top.
3. At high aspect ratios, the bulging phenomenon was shown to be much reduced, along with the upflow at the floodplain edge.

- ***Multiple Block Arrangements***

1. For all cases, the multiple block arrangement was found to promote a larger overall velocity gradient between the main channel and the floodplain.
2. For the emergent blocks, at both low and high aspect ratios, the pattern of axial circulation emanating from the separation zones described for the single block cases is gradually enhanced as the flow past subsequent blocks in the multiple arrangement develops. This acts to alter the distribution of the mean streamwise velocity both on the floodplain and in the main channel. In the main channel in particular, the wake becomes wider and the maximum mean streamwise velocity zone is pushed downward.
3. Despite these changes for the emergent blocks, the evidence also indicated that the asymmetrical separation, reattachment and re-separation characteristics of the lateral separation zones, identified for the single

block cases, persist for the multiple block case, as does the slower recovery on the main channel side.

4. For the submerged cases, the patterns of separation, reattachment and re-separation identified for the single block cases are again seen to persist for the multiple channel arrangements. This ensures that the bulging of the wakes into the main channel and the dominance of the axial circulations on the floodplain also remain. The circulation on the floodplain gradually creates a bulge in the contours of streamwise velocity in this location also, adding to the deceleration of the floodplain flow more generally. The distribution of streamwise velocity in the main channel is much less disturbed.

- ***Manning's Coefficient Conversion and Application of Results***

1. Through conversion of the modelled drag coefficients into contributions to Manning's coefficient, it was shown that the amount to which changes to the Manning's coefficient induced by the floodplain edge location of vegetation should be taken into account is dependent both on the nature of the scenario being modelled and the distribution and geometry of the vegetation.
2. For scenarios in which local reaches of river are to be modelled and particularly where single large trees or other obstacles exist at the floodplain edge, careful consideration of the contribution to the Manning's coefficient made by that obstacle should be made.
3. For scenarios in which less detailed, large scale models of river systems are being created, particularly where there is a multiple arrangement of vegetation or other obstacles at the floodplain edge, less consideration may safely be given to the contribution to Manning's coefficient of those obstacles.

6.2 Suggestions for Future Research

In order to further understand the impacts on compound, open channel flows of the presence of vegetation at the floodplain edge and to extend the applicability of the results reported in this project, the following questions and topics are suggested for examination in future research:

- ***Variation of other important geometrical parameters*** The work of this research project has concentrated on revealing the flow structure of the wakes around two distinct classes of block at the floodplain edge: emergent and submerged blocks. The experimental results collected for the multiple, low aspect ratio, submerged block cases revealed however, the sensitivity of the flow structures to the degree of submergence of the block. For the blocks which experienced only a shallow degree of submergence, the results suggested that the wake structure was more similar to that of the emergent block than to that of the deeply submerged block. In other words, the two states should not be considered in isolation but instead, as two positions in a spectrum. A future question to be addressed therefore would be how the wake structure transitions from one in which the flow over the top of the block is dominant in determining the recovery profile to one in which the flow around the block sides is dominant and how this process is influenced by the floodplain edge positioning. In addition to this geometrical parameter, the spacing between multiple blocks in an in-line arrangement was reported to be an important determinant in controlling separation and reattachment processes and therefore drag coefficients as identified in the literature review. As this project has revealed that the floodplain edge positioning has a significant effect on the recovery profiles of blocks in this location, a future research project could usefully compare the results of for blocks in a simple channel to those at the floodplain edge. By performing such a comparison, the spacings at which the important transitions from linked shedding processes to independence could be identified. As the modifications to the separation zones

and the recovery rates of the wakes around blocks at the floodplain edge have been demonstrated to be strongly linked to the sudden increase in depth on the main channel side of the blocks, in order to determine the limits of the applicability of these modifying factors, an investigation of the diminishing floodplain edge effects as the lateral position of the block is changed would be interesting and useful. Finally, since the variation of aspect ratio examined as part of this work was associated with a fixed floodplain width, it would also be useful to eliminate the relative width of the block in relation to the width of the floodplain as an influencing factor.

- ***Improvement of Numerical Modelling Techniques*** Whilst the numerical modelling undertaken as part of this project was shown to yield useful results for blocks at the floodplain edge, a number of limitations on the accuracy of the results were also identified. Solutions to some of these limitations were worked on, but not resolved, as part of this project. Since an accurate 3D RANS simulation of this flow type could quickly and cheaply yield important results, including analysis of some of the geometrical variations mentioned in the previous paragraph, resolution of these limitations is clearly an important next step. The first improvement that could be made would be to use an unsteady modelling facility, which would be likely to greatly improve the model's performance of the prediction of total turbulent energy, in cases where periodic structures are important. The use of an unsteady model would also allow for confirmation of the analyses of this project with respect to the differences that develop in the vortex shedding processes on the two sides of blocks at the floodplain edge, by clear disaggregation of the periodic and truly turbulent components of the unsteady flow and by examination of the instantaneous wake structures throughout the shedding cycle. The second major improvement that would benefit the results procured from the numerical model would be the inclusion of a moving free surface. Using a volume tracking technique, this would enable a much better representation

of the free surface deformation, the shear layer and associated vorticity at the free surface, and the changes induced in that phenomenon by the sudden increase of depth and change of Froude number experienced at the floodplain edge.

- ***Application of Modified Drag Coefficients*** In order to translate the results of this project into a tool of practical use, it may also be advantageous to use them to develop a generalised 2D approach to the inclusion of one line vegetation at the floodplain edge in models of open channel flows. In a similar vein to the models produced by such researchers as Järvelä (2002) and Wilkerson (2007), as introduced in Section 2.3.2, the creation of a 2D model capable of reproducing the depth-averaged effects of the floodplain edge vegetation would be a route to achieving tangible engineering impact. As opposed to the models suggested in Section 2.3.2 however, any such model would be developed by directly taking into account the underlying physical processes at work and would therefore be of use to engineers facing the gamut of natural scenarios represented by Figure 1.1.

6.3 Final Comment

This research project has shown that the placement of bluff bodies in the shearing flow at the floodplain edge of a compound channel has significant impacts on the wake structures that are formed around them and therefore on the drag force that they exert on the flow. It provides a first glimpse at the nature of these changes, which, despite their potential impact on our understanding of open channel hydraulics and our ability to accurately model the effects of floodplain vegetation, have not been investigated before. The approach taken in this analysis should provide an avenue by which existing data on the bulk behaviour of vegetated, compound channels may be interpreted. Furthermore, detailed study could reveal both the unsteady processes at work in creating these effects and their patterns of

change with channel geometry, finally allowing for the more accurate inclusion of them in engineering models.

References

- BAKER, C. (1980). The turbulent horseshoe vortex. *Journal of Wind Engineering and Industrial Aerodynamics*, **6**, 9–23.
- BEARMAN, P.W. AND MOREL, T. (1984). Effect of freestream turbulence on flow around bluff bodies. *Prog. Aerospace Science*, **20**, 97–123.
- BEARMAN, P.W. AND TRUEMAN, D. (1972). An investigation of the flow around rectangular cylinders. *Aeronautical Quarterly*, **23**, 229–237.
- BOSCH, G. AND RODI, W. (1998). Simulation of vortex shedding past a square cylinder with different turbulence models. *International Journal for Numerical Methods in Fluids*, **28**, 601–616.
- BOUSMAR, D., RIVIÈRE, N., PROUST, S., PAQUIER, A., MOREL, R. AND ZECH, Y. (2005). Upstream discharge distribution in compound-channel flumes. *Journal of Hydraulic Engineering*, **131**(5), 408–412.
- BOUSSINESQ (1887). Esai sur la theories des eaux courantes. *Memories presente par Divers Savants al' Academie des Science*, **23**, 1–680.
- BRUNDRETT, E. AND BAINES, W. (1964). The production and diffusion of vorticity in duct flow. *Annu. Rev. Fluid Mechanics*, **19**, 375–394.
- CASTRO, I. AND ROBINS, A. (1977). The flow around a surface mounted cube in uniform and turbulent streams. *Journal of Fluid Mechanics*, **79**(2), 307–335.

- CHAPLIN, J. AND TEIGEN, P. (2003). Steady flow past a surface-piercing circular. *Journal of Fluids and Structures*, **18**, 271–285.
- DURAO, D., HEITOR, M. AND PEREIRA, J. (1988). Measurements of turbulent and periodic flows around a square cross-section cylinder. *Experiments in Fluids*, **6**, 298–304.
- FISCHER-ANTZE, T., STOESSER, T., BATES, P. AND OLSEN., N. (2001). Les of a circular cylinder of finite height. *Journal of Hydraulic Research*, **39**(3), 303–310.
- FRANKE, R. AND RODI, W. (1993). Calculation of vortex shedding past a square cylinder with various turbulence models. *Turbulent Shear Flows 8*, Springer, New York.
- FRÖHLICH, J. AND RODI, W. (2004). Les of the flow around a circular cylinder of finite height. *International Journal of Heat and Fluid Flow*, **25**, 537–548.
- FUKUOKA, S. AND FUJITA, I. (1989). Predictions of flow resistance in compound channels and its application to design of river courses. *Proc. JSCE (In Japanese)*.
- HANGAN, H. AND VICKERY, B. (1999). Buffeting of a 2d (sharp edged) bluff body. *J. Wind Engineering & Industrial Aerodynamics*, **82**, 173–187.
- HAVEL, B., HANGAN, H. AND MARTINUZZI, R. (2001). Buffeting for 2d and 3d sharp-edged bluff bodies. *J. Wind Engineering & Industrial Aerodynamics*, **89**, 1369–1381.
- HAY, A. (1947). Flow about semi-submerged cylinders of finite length. Princeton University Report, Princeton, NJ.
- HOGBEN, N. (1974). Wave resistance of surface piercing vertical cylinders in uniform currents. NPL Report Ship 183.
- HSEIH, T. (1964). Resistance of cylindrical piers in open channel flow. *Proceedings of the ASCE, Journal of the Hydraulic Division*, **90**, 161–173.

- INOUE, M., BABA, Y. AND HIMENO, Y. (1993). Experimental and numerical study of viscous flow field around an advancing vertical circular cylinder piercing a free-surface. *J. Kansai Soc. Naval Archit. of Japan*, **220**, 57–64.
- JAYATILLEKE, C. (1969). The influence of prandtl number and surface roughness on the resistance of the laminar sub-layer to momentum and heat transfer. *Progress in heat and mass transfer*, **1**, 193–330.
- JORDANOVA, A., JAMES, C. AND BIRKHEAD, A. (2006). Practical estimation of flow resistance through emergent vegetation. *Proceedings of the Institution of Civil Engineers - Water Management*, **159**, 173–181.
- JÄRVELÄ, J. (2002). Determination of flow resistance of vegetated channel banks and floodplains. *River Flow 2002, Bousmar and Zech (eds.), Swets and Zeitlinger*.
- KANG, H. AND CHOI, S. (2004). Reynolds stress modelling of vegetated open channel flows. *Journal of Hydraulic Research*, **42**(1), 3–11.
- KANG, H. AND CHOI, S. (2006). Turbulence modelling of compound open-channel flows with and without vegetation on the floodplain using the reynolds stress model. *Advances in Water Resources*, **29**, 1650–1664.
- KAPPLER, M. (2002). *Experimentelle Untersuchung der Umströmung von Kreiszyllindern mit ausgeprägt dreidimensionalen Effekten*. Ph.D. thesis, University of Karlsruhe.
- KATO, M. AND LAUNDER, B. (1993). The modelling of turbulent flow around stationary and vibrating square cylinders. *Proc. 9th Symp. Turbulent Shear Flows, Kyoto*, vol. 10-4-1.
- KAWAMURA, T., HIWADA, M., HIBINO, T., MABUCHI, I. AND KAMUDA, M. (1984). Flow around a finite circular cylinder on a flat plate. *Bulletin of the JSME*, **27**(232), 2142–2151.

- KAWAMURA, T., MAYER, S., GARAPON, A. AND SORENSON, L. (2002). Large eddy simulation of a flow past a free surface piercing circular cylinder. *Journal of Fluids Engineering*, **124**, 91–101.
- KIMURA, I. AND HOSODA, T. (2003). A non-linear $k - \epsilon$ model with realizability for prediction of flows around bluff bodies. *International Journal for Numerical Methods in Fluids*, **42**, 813–837.
- KNIGHT, D. AND SHIONO, K. (1996). *River Channel and Floodplain Processes*, Anderson, Walling and Bates (Eds), J. Wiley.
- KNIGHT, D., DEMETRIOU, J. AND HAMED, M. (1984). Boundary shear in smooth rectangular channels. *ASCE Journal of Hydraulic Engineering*, **110**, 405–422.
- KOMATSU, T. (2009). *Debris Flow*, Gohoudou.
- LAUNDER, B. AND YING, W. (1973). Prediction of Flow and Heat Transfer in Ducts of Square Cross Section. *Proceedings of the Institution of Mechanical Engineers*, **187**, 455–461.
- LAUNDER, B., REECE, G. AND RODI, W. (1975). Progress in the development of a Reynolds-stress turbulence closure. *Journal of Fluid Mechanics*, **68**(3), 537–566.
- LI, R. AND SHEN, H. (1973). Effect of tall vegetation on flow and sediment. *Proc. Of ASCE Journal of the Hydraulic Division*, **99**, 793–813.
- LIBBY, P. (1996). *Introduction to Turbulence*, Taylor and Francis.
- LINDER, K. (1991). Der strömungswiderstand von pflanzenbeständen. *Mitteilungen Leichtweiss Institut für Wasserbau, TU Braunschweig*, Heft 75.
- LOPEZ, F. AND GARCIA, M. (1997). Open channel flow through simulated vegetation; turbulence modelling and sediment transport. Hydrosystems Laboratory, Department of Civil Engineering, University of Illinois.

- LYN, D., EINAV, S., RODI, W. AND PARK, J. (1995). A laser-doppler velocimetry study of ensemble-averaged characteristics of the turbulent near wake of a square cylinder. *Journal of Fluid Mechanics*, **304**, 285–319.
- MARTINUZZI, R. AND HAVEL, B. (2000). Turbulent flow around two interfering surface-mounted cubic obstacles in tandem arrangement. *Journal of Fluids Engineering*, **122**, 24–31.
- MARTINUZZI, R. AND TROPEA, C. (1993). The flow around surface-mounted, prismatic obstacles in a fully developed channel flow. *Journal of Fluids Engineering*, **115**, 85–92.
- MELLING, A. AND WHITELOW, J. (1976). Turbulent flow in a rectangular duct. *Journal of Fluid Mechanics*, **78**, 289–315.
- MERTENS, W. (1989). Zur frage hydraulischer berechnungen naturnaher fließgewässer. *Wasserwirtschaft*, **79**(4), 170–179.
- NAOT, D. AND RODI, W. (1982). Calculation of secondary currents in channel flow. *Journal of the Hydraulics Division, Proceedings of the American Society of Civil Engineers*, **108**, 948–968.
- NAOT, D., NEZU, I. AND NAKAGAWA, H. (1996). Hydrodynamic behaviour of partly vegetated open channels. *Journal of Hydraulic Engineering*, **122**(11), 625–633.
- NEPE, H. AND VIVONI, E. (2000). Flow structure in depth limited, vegetated flow. *Journal of Geophysical Research*, **105**(12), 28,547–28,557.
- NEZU, I. AND NAKAGAWA, H. (1993). *Turbulence in open channel flows*, IAHR Monograph, Rotterdam, Balkema USA.
- NEZU, I. AND ONITSUKA, K. (2001). Turbulent structures in partly vegetated open channel flows with lda and piv measurements. *Journal of Hydraulic Research*, **39**(6), 629–642.

- NEZU, I. AND RODI, W. (1993). Experimental study on secondary currents in open channel flow. *Journal of Hydraulic Engineering*, **119**, 390–408.
- NIKURADSE, J. (1932). Gesetzmässigkeit der turbulenten strömung in glatten rohren. *Forschungsarbeiten*, **Heft 356**.
- NUDING, A. (1991). Fließwiderstandverhalten in gerinnen mit ufergubüsch. *Wasserbau Mitteilungen*, TH Darnstadt, 35.
- PASCHE, E. AND ROUVÉ, G. (1985). Overbank flow with vegetatively roughened floodplains. *Journal of Hydraulic Engineering*, **111**, 1262–1278.
- PATANKAR, S. AND SPALDING, D. (1972). A calculation procedure for heat, mass and momentum transfer in three-dimensional parabolic flows. *International Journal of Heat and Mass Transfer*, **15**, 1787–1806.
- PATEL, V. (1965). Calibration of the preston tube and limitations on its use in pressure gradients. *Journal of Fluid Mechanics*, **23**, 185–208.
- PETRYK, S. (1969). *Drag on cylinders in open channel flow*. Ph.D. thesis, Colorado State University at Fort Collins.
- PETRYK, S. AND BOSMAJIAN, G. (1975). Analysis of flow through vegetation. *Journal of the Hydraulics Division, Proceedings of the American Society of Civil Engineers*, **101**, 871–884.
- PRANDTL, L. (1927). Über den reibungswiderstand strömenderluft. *Ergeb. Aerodyn. Versuch.*, Göttingen, III Series.
- RAMESH, V., VENGADESAN, S. AND NARASIMHAN, J. (2005). 3d unsteady rans simulation of turbulent flow over bluff body by non-linear model. *International Journal of Numerical Methods for Heat & Fluid Flow*, **166**, 660–673.
- RAMESHWARAN, P. AND SHIONO, K. (2007). A quasi-two-dimensional model for straight overbank flows through emergent vegetation on the floodplain. *Journal of Hydraulic Research*, **45**(3), 302–315.

- RODI, W. (1993). *Turbulence models and their application in hydraulics: a state of the art review*.
- RODI, W. (1997). Comparison of les and rans calculations of the flow around bluff bodies. *Journal of Wind Engineering and Industrial Aerodynamics*, **69-71**, 55–75.
- RUSELLO, P., LOHRMANN, A., SIEGEL, E. AND MADDUX, T. (2006). Improvements in acoustic doppler velocimetry. *The 7th Int. Conf. on Hydroscience and Engineering (ICHE-2006), Sep 10 - Sep 13, Philadelphia, USA*.
- SAKAMOTO, H. AND HANIU, H. (1988). Aerodynamic forces acting on two square prisms placed vertically in a turbulent boundary layer. *J. Wind Engineering & Industrial Aerodynamics*, **31**, 41–66.
- SCHLICHTING, H. (1968). *Boundary Layer Theory*, 6th ed. McGraw-Hill Co., New York.
- SCHOFIELD, W. AND LOGAN, E. (1990). Turbulent shear flow over surface mounted obstacles. *Journal of Fluids Engineering*, **112**, 376–385.
- SCHUMANN, U. (1977). Realizability of reynolds-stress turbulence models. *Physics of Fluids*, **20**, 721–725.
- SELLIN, R. (1964). A laboratory investigation into the interaction between flow in the channel of a river and that of its floodplain. *La Houille Blanche*, **7**, 793–801.
- SELLIN, R. AND BEESTON, D.V. (2002). Berm vegetation and its effect on flow resistance in a two-stage river channel: an analysis of field data. *River Flow 2002, Bousmar and Zech (eds.), Swets and Zeitlinger*.
- SHAH, K. AND FERZIGER, J. (1997). A fluid mechanics view of wind engineering: large eddy simulation of flow over a cubical obstacle. *Computational wind engineering*, **2**, 211–226.

- SHIMIZU, Y. AND TSUJIMOTO, T. (1994). Numerical analysis of turbulent open channel flow over a vegetation layer using a k-epsilon turbulence model. *Journal of Hydroscience and Hydraulic Engineering*, **11**(2), 57–67.
- SHIONO, K. AND KNIGHT, D. (1989). Transverse and vertical reynolds stress measurements in a shear layer region of a compound channel. *Proceedings 7th Symposium on Turbulent Shear Flows, Stanford Univeristy*.
- SHIONO, K. AND KNIGHT, D. (1991). Turbulent open-channel flows with variable depth across the channel. *Journal Of Fluid Mechanics*, **222**, 617–646.
- SIMPSON, R. (2001). Junction flows. *Annual Review of Fluid Mechanics*, **33**, 415–443.
- SPEZEZZY, S. AND BEARMAN, P. (1992). Aspect ratio and end plate effects on vortex shedding from a circular cylinder. *Journal Of Fluid Mechanics*, **234**, 191–217.
- SPEZIALE, C. (1987). On nonlinear $k-l$ and $k-\epsilon$ models of turbulence. *Journal Of Fluid Mechanics*, **178**, 459–475.
- STONE, H. (1968). Iterative solution of implicit approximations of multidimensional partial differential equations. *SIAM Journal of Numerical Analysis*, **5**, 530–538.
- SUN, X. (2006). *Flow characteristics in compound channel with and without vegetation*. Ph.D. thesis, Department of Civil and Building Engineering, Loughborough University.
- TAMAI, N., ASAEDA, T. AND IKEDA, H. (1986). Generation mechanism and periodicity of large surface eddies in a compound channel flow. *Proceedings of 5th congress, APD-IAHR, Seoul, Republic of Korea*, 61–74.
- TOMINAGA, A. AND NEZU, I. (1991). Turbulent structures in compound open channel flows. *Journal of Hydraulic Engineering*, **117**, 21–39.

- TOMINAGA, A., NEZU, I., EZAKI, K. AND NAKAGAWA, H. (1989). Three-dimensional turbulent structure in straight open channel flows. *Journal of Hydraulic Research*, **27**, 149–173.
- TSUJIMOTO, T. (1992a). Spectral analysis of velocity and water surface fluctuations appearing in an open channel with vegetated and non-vegetated regions in a cross-section. *Proc. 6th IAHR International Symposium on Stochastic Hydraulics, Taipei*, 361–368.
- TSUJIMOTO, T. (1992b). Unstable phenomena appearing in open-channel flows with vegetation. *Advances in Hydrosience and Engineering*, vol. 1, 1390–1397.
- TSUJIMOTO, T., SHIMIZU, Y., KITAMURA, T. AND OKADA, T. (1992). Turbulent open channel flow over bed covered by rigid vegetation. *Journal of Hydrosience and Hydraulic Engineering*, **10**(2), 13–25.
- VOULGARIS, G. AND TROWBRIDGE, J. (1998). Evaluation of the acoustic doppler velocimeter (adv) for turbulence measurements. *Journal of Atmospheric and Oceanic Technology*, **15**(1), 272 – 289.
- VYAS, K. (2007). *Modelling of 3D anisotropic turbulent flow in compound channels*. Ph.D. thesis, Department of Civil and Building Engineering, Loughborough University.
- WILKERSON, G. (2007). Flow through trapezoidal and rectangular cylinders with rigid cylinders. *Journal of Hydraulic Engineering*, **133**(5), 521–533.
- WILSON, C., YAGCI, O., RAUCH, H.P AND OLSEN, N. (2006). 3d numerical modelling of a willow vegetated river/floodplain system. *Journal of Hydrology*, **327**, 13–21.
- WU, W., SHIELDS, F., BENNETT, S. AND WANG, S. (2005). A depth-averaged two-dimensional model for flow, sediment transport and bed topography in curved channels with riparian vegetation. *Water Resources Research*, **41**.

REFERENCES

- YANG, K., CAO, S. AND KNIGHT, D. (2007). Flow patterns in compound channels with vegetated floodplains. *Journal of Hydraulic Engineering*, **133**(2), 148–159.
- ZDRAVKOVICH, M. (1997). *Flow around circular cylinders, Volume 1: Fundamentals*, Oxford University Press.